University of Southampton

Faculty of Engineering, Science and Mathematics

Institute of Sound and Vibration Research (ISVR)

A Modal Method for the Simulation of Nonlinear Dynamical Systems with Application to Bowed Musical Instruments

by

Octávio José Patrício Fernandes Inácio

Thesis for the degree of PhD in Sound & Vibration

July 2008

UNIVERSITY OF SOUTHAMPTON

ABSTRACT

Bowed instruments are among the most exciting sound sources in the musical world, mostly because of the expressivity they allow to a musician or the variety of sounds they can generate. From the physical point of view, the complex nature of the nonlinear sound generating mechanism – the friction between two surfaces – is no less stimulating.

In this thesis, a physical modelling computational method based on a modal approach is developed to perform simulations of nonlinear dynamical systems with particular application to friction-excited musical instruments. This computational method is applied here to three types of systems: bowed strings as the violin or cello, bowed bars, such as the vibraphone or marimba, and bowed shells as the Tibetan bowl or the glass harmonica. The successful implementation of the method in these instruments is shown by comparison with measured results and with other simulation methods. This approach is extended from systems with simple modal basis to more complex structures consisting of different sub-structures, which can also be described by their own modal set.

The extensive nonlinear numerical simulations described in this thesis, enabled some important contributions concerning the dynamics of these instruments: for the bowed string an effective simulation of a realistic wolf-note on a cello was obtained, using complex identified body modal data, showing the beating dependence of the wolf-note with bowing velocity and applied bow force, with good qualitative agreement with experimental results; for bowed bars the simulated vibratory regimes emerging from different playing conditions is mapped; for bowed Tibetan bowls, the essential introduction of orthogonal mode pairs of the same family with radial and tangential components characteristic of axi-symmetrical structures is performed, enabling an important clarification on the beating phenomena arising from the rotating behaviour of oscillating modes. Furthermore, a linearized approach to the nonlinear problem is implemented and the results compared with the nonlinear numerical simulations.

Animations and sounds have been produced which enable a good interpretation of the results obtained and understanding of the physical phenomena occurring in these system.

FACULTY OF ENGINEERING, SCIENCE & MATHEMATICS

INSTITUTE OF SOUND AND VIBRATION RESEARCH

Doctor of Philosophy

A Modal Method for the Simulation of Nonlinear Dynamical Systems with Application to Bowed Musical Instruments

by

Octávio José Patrício Fernandes Inácio

CONTENTS

LIST OF FIGURES

LIST OF TABLES

LIST OF ACCOMPANYING MATERIAL

CD including:
- Four animations of the bowed string motion
- .wav files with sounds stemming from the Tibetan bowl simulations

DECLARATION OF AUTHORSHIP

I, Octávio José Patrício Fernandes Inácio declare that the thesis entitled "A Modal Method for the Simulation of Nonlinear Dynamical Systems with Application to Bowed Musical Instruments" and the work presented in it are my own. I confirm that:

- this work was done wholly or mainly while in candidature for a research degree at this University;
- where any part of this thesis has previously been submitted for a degree or any other qualification at this University or any other institution, this has been clearly stated;
- where I have consulted the published work of others, this is always clearly attributed;
- where I have quoted from the work of others, the source is always given. With the exception of such quotations, this thesis is entirely my own work;
- I have acknowledged all main sources of help;
- where the thesis is based on work done by myself jointly with others, I have made clear exactly what was done by others and what I have contributed myself;
- parts of this work have been published as:
    - INÁCIO, Octávio, ANTUNES, José, WRIGHT, Matthew (2007), "Computational modelling of string-body interaction for the violin family and simulation of wolf notes", Journal of Sound and Vibration, Vol. 310/1-2 pp 260-286.
    - INÁCIO, Octávio, HENRIQUE, Luís, ANTUNES, José, (2006), "The Dynamics of Tibetan Singing Bowls", Acta Acústica 92, n.º 4, pp. 637-653, Hirzel-Verlag.
    - INÁCIO, Octávio, HENRIQUE, Luís, ANTUNES, José, (2003), "Simulation of the Oscillation Regimes of Bowed Bars: A Nonlinear Modal Approach", Communications in Nonlinear Science and Numerical Simulation 8, pp. 77-95, Elsevier.

Signed: …………………………………………………………………..

Date:……………………………………………………………………

ACKNOWLEDGEMENTS

DEFINITIONS AND ABBREVIATIONS USED

Variables

a	Number of bow hairs assumed in contact with the string
A	Cross-sectional area of a bow hair
b	Number of modelled bow hairs
c	Wave speed in string
C	Friction decay parameter
C_a	Lumped adherence damping of the total modelled bow hairs
$\bar{C}_a$	Adherence damping of a single bow hair
$\mathcal{C}$	Linear dissipative factor
E	Young’s modulus
F	Force
F_{fD}	Dynamical friction force
F_{fS}	Static force limit
F_N	Normal force
F_0	Peak sliding friction force
$\mathfrak{I}_n(t)$	Modal force
$g(t)$	String impulse response
h	Bridge impulse response
H	Length of the bow hair
i	Time step index
J_i	Product of contact point velocities at successive time steps
K	Modal stiffness matrix
K_B	Body parameter
K_{bs}	Bridge–string stiffness

K_a	Lumped adherence stiffness of the total modelled bow hairs
$\bar{K}_a$	Adherence stiffness of a single bow hair
$\mathcal{K}$	Linear stiffness restoring force
l_b	Bow width
L	Length of string
m_a^B	Body parameter
m_n	Modal mass
M	Modal mass matrix
n	Mode number
N	Maximum *n*
q_n	Modal response
Q	Modal response matrix
t	Time
R	String radius
S	Cross-sectional area of string
T	Tension
v_c	String velocity
$v_h(t)$	Velocity time-history
V_{bow}	Bow velocity
V_r	Relative velocity
x	Axial position
y	Transverse displacement
Z	Wave impedance
α	Ratio of propagation wave speeds
β	Inharmonicity coefficient
ε	Regularization interval amplitude

γ	Stiffness constant for the Dahl model
ζ_n	Modal damping
η	Dissipation coefficient
μ	Friction coefficient
μ_D	Dynamical friction coefficient
μ_S	Static friction coefficient
σ	Linear density
θ	Angular displacement
ρ	Density
Ξ	Modal force matrix
ϕ_n	Modeshape
φ_n	Modeshape
ω_n	Circular eigenfrequency

Subscripts

A, a	Adherence
$a1$	Related to the left side of the bow hair in relation to the contact point
$a2$	Related to the right side of the bow hair in relation to the contact point
b	Bridge
B	Body
bow	Bow
bs	Bridge–string
c	Contact point
d	Dynamic
D	Asymptotic dynamic
f	Frictional

N	Normal
s	Slip
S	*Static*
tan	tangencial
$trans$	transverse
tor	torsional

Superscripts

A	Family of modes
B	Family of modes
h	Single bow hair
p	Body mode index
P	Number of body modes

PRESENTATION

In Acoustics, as in most other fields of Science, the simulation of physical phenomena is the endeavour of most researchers. The main objective is to reproduce an acoustical event under controlled conditions in order to understand, modify, control or simply mimic system behaviour. The applications are immense: from noise control to musical sound synthesis, room acoustics design, high-fidelity sound reproduction or environmental noise predictions, among many others.

Almost as numbered as the applications are the simulation methods. Experimental, analytical or numerical, based on physical understanding or phenomenological in nature, the diverse methodologies have different validities but generally with the same underlying goal: to determine the effect of changing one ore more variables, in order to comprehend the system dynamics. From these systems, musical instruments represent a rather interesting case, since the pleasantness of sounds produced and the physical analogy to non-musical systems make them perfect objects of study.

Researchers in Musical Acoustics have devoted more than 100 years (see Helmholtz (1877), Rayleigh (1894), amongst others) to the study of musical instruments and, particularly in the past decades to the simulation of their dynamical behaviour in order to establish reliable models for sound reproduction or physical understanding.

As a contribution to this field of study, this thesis describes a computational method based on a modal approach for the simulation of nonlinear dynamical systems with particular application to bowed (friction-excited) musical instruments: bowed bars, bowed strings and bowed bowls.

The introductory chapter, which includes the literature review, presents three fundamental aspects to the contents of the thesis: 1) friction-excited vibrations, exploring some of the different areas where friction induced self-sustained oscillations have a predominant role; 2) a literature review of research work on bowed musical instruments, establishing the context where the present method fits and 3) the aims and contributions of this thesis to scientific knowledge.

In Chapter 2 the general simulation methodology is presented, common to all three instruments, together with a short description of their main characteristics, relevant to the computational method. The friction model used in the simulations is then described, followed by a reference to other approaches, found in the literature, to the description of friction phenomena in these instruments. Since other alternative methods have also been developed by different authors to simulate the dynamics of bowed instruments, a comparison with one of the most reliable is made regarding bowed strings. As a conclusion to this chapter, the main advantages and disadvantages of the method when compared to the alternatives are described.

The following three chapters describe the application of the simulation methodology to each of the three instruments studied: Chapter 3 addresses one the most studied systems in Musical Acoustics – the bowed string; Chapter 4 describes the application of the method bowed bars as an example of a two dimensional, dispersive system;; and Chapter 5 concludes the applications with axi-symmetrical structures, such as the bowed Tibetan bowls. The results of the simulations are presented in each of these three chapters followed by the experimental work performed.

In Chapter 6, a linearized analysis of the dynamical equations described in the previous chapters is developed, with application to the bowed bar and the bowed string. After presenting the linearized formulation and the steady and oscillating solution, a brief comparison with the results obtained from the nonlinear computations is made. Chapter 7 concludes the thesis, with a summary of the contents and a description of the main achievements. Finally, the perspectives for future work are described.

CHAPTER 1

INTRODUCTION

1. INTRODUCTION

1.1. Friction-excited vibrations and sound

A large proportion of sound sources radiate acoustical energy through the action of vibrating solid surfaces upon a surrounding fluid (Fahy, 2007). The source of these vibrations can be various, from transient impacts (as a press hammer or a xylophone mallet) to continuous oscillatory forces (such as rotating shaft on a turbine or a electromagnetic field in loudspeakers), amongst others. When referring to sound emanating from a violin or the brake noise from an automobile, friction is the main mechanism of vibratory energy.

Friction is defined as a force that resists relative motion between two contacting surfaces (Ibrahim, 1994a) and develops between the sliding surfaces regardless of the magnitude of that motion (Akay, 2002). Tabor (1981) represents the friction force as the resistance which develops during the deformation of thin surface layers by penetrated irregularities (see Figure 1.1) and by atomic and molecular interactions on the portions of contacting solids separated by a distance close to 10 Å (Å = Angstrom = 10-8 cm).

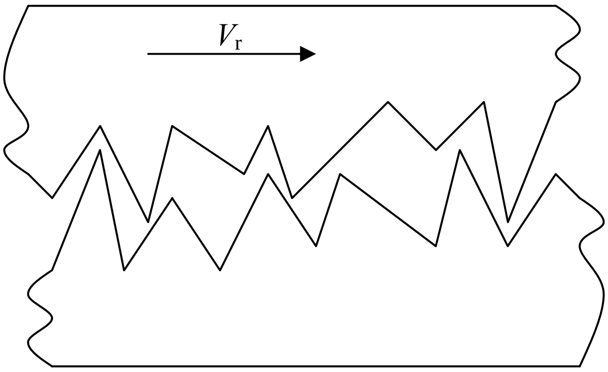

Figure 1.1 – Schematic representation of two sliding surfaces on the microscopic level (V_r is the relative velocity between the surfaces).

Friction fulfils a dual role by transmitting energy from one surface to the other and by dissipating energy of relative motion (Akay, 2002). As a result from this energy exchange mechanisms, friction can generate waves and oscillations within the solids which, depending on their geometrical and dynamical characteristics, usually lead to the radiation of sound. It is therefore important to understand not only the microscopic and macroscopic mechanisms underlying the generation of friction, one of the subjects of Tribology[1], but also the dynamics of the bodies whose surfaces are in motion.

The study of contact and friction phenomena has been pioneered by the historical works of Leonardo da Vinci (1452-1519), Amontons (1699), J.T. Desaguliers (1725), Euler (1749) and Coulomb (1785); an interesting overview is given by Fenny et al (1998) and Tabor (1981). Coulomb recognized that frictional resistance occurs at localized asperity contacts and, together with Amontons, that the friction force is proportional to the normal load between the surfaces, independent of the apparent contact area and sliding speed (Ibrahim, 1994a). However, the friction force is dependent or much further aspects: the overall shapes of the contacting surfaces and its surface texture; whether the surface deformation is elastic and/or plastic; the presence of wear particles or of lubricating films; the environmental conditions (Ibrahim, 1994a)[2], as well as the contact and dynamical properties of the moving solids, amongst others.

The classic friction laws, usually referred to as Coulomb laws, apply to dry (non-lubricated) contacts and can be summarized as:

- The friction force is independent of the apparent area of contact.
- The friction force is proportional to the normal contact force.
- The friction force is independent of the sliding velocity.

Although the first two laws are generally observed in most systems, the third law is known to be invalid for some systems. Martins, *et al*. (1990) have provided a distinction between static and kinetic friction (when both surfaces are in motion), in that kinetic friction depends on the sliding velocity while the static friction depends on the time of repose. This notion supports some conclusions by Euler (1748) in which the fact that the kinetic coefficient of friction is less than the static one could be attributed to the fact that asperities on one surface could jump part of the way over the gap between asperities on the other (Ibrahim, 1994a). In fact, depending on the system

---

[1] Tribology is the science and technology of interacting surfaces in relative motion. It includes the study and application of the principles of friction, lubrication and wear.

[2] For the purposes of this thesis, lubricated contacts as described by fluid dynamic equations will not be addressed (usually relevant for mechanical components); only dry friction is of interest since it is the most relevant for bowed musical instruments. If appropriate to the explanation of certain phenomena in bowed strings, lubricated contacts will be addressed briefly.

in question (e.g. the nature of the solids in contact), the static and kinetic (or dynamical) friction coefficient can either be very different of extremely similar.

These and other descriptions of frictional behaviour mainly associated with the characteristics of the surfaces are now prolific and have resulted in profound knowledge on the micro-scale surface interaction mechanisms. However, the dynamics of solid interfaces and its relation with the theory of frictional forces at solid interfaces in relative motion have a recent history in the engineering and applied mechanics research (see Bowden & Tabor, 1964; Suh, 1986; Johnson, 1985; Rice & Ruina, 1983; Singer & Pollack, 1992). Friction is a complex process and depends on several parameters, some of which are relevant to the present discussion. In friction-excited vibrations, the dependence of friction on the relative velocity and the normal force between sliding surfaces is paramount. Other factors can also impose an important influence, such as temperature and time-dependence of the friction parameters (see Ibrahim, 1994a).

1.2. Simulation Methods and Dry Friction Models

Computer simulations of the motion of mechanical systems usually imply finding the solutions of the governing inhomogeneous partial differential equations either by analytical or numerical methods. Among these methods, some have been applied with success to musical instruments, from the simple lumped networks of masses and springs to time-domain numerical methods such as finite difference schemes, digital waveguides models and wave digital filters, among others.

When dry friction excitation is present, calculations face the difficulty of the strongly nonlinear characteristic of the friction force near zero velocity. The Coulomb friction laws, described in the previous section, imply the well-known friction model represented in Figure 1.2a or Figure 1.2b, where the sliding (dynamical) friction force, F_{fD} – Coulomb friction –, is independent of the relative velocity between sliding surfaces.It is now widely understood that in order to establish motion a static force limit, F_{fS} , higher than the Coulomb sliding friction is required (Figure 1.1b). Equation (1.1) expresses this latest model, where μ_D is a kinetic (or dynamical) friction coefficient and μ_S is the static friction coefficient, and F_N is the normal load.

$$\begin{cases} F_{fD} = \mu_D F_N \,\mathrm{sgn}(\dot{y}) & ;\ \text{if}\ \ |\dot{y}| > 0 \\ |F_{fS}| < \mu_S F_N & ;\ \text{if}\ \ |\dot{y}| = 0 \end{cases} \tag{1.1}$$

The discontinuity of this step function expresses the extreme nonlinearity of the excitation friction force, which – together with the indeterminate friction force during adherence – are the major difficulties for simple simulation methods. In order to properly integrate the ordinary differential equations that describe the motion of the system, the appropriate value of the derivative must be used on each side of the discontinuity, which can be a problem since the discontinuity can occur inside the integration subintervals (Armstrong-Hélouvry *et al.* 1994).

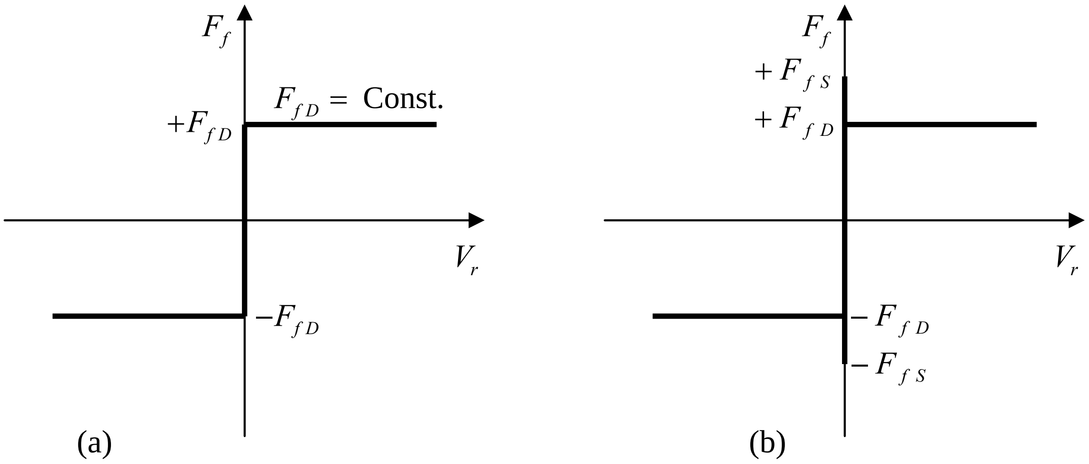

Figure 1.2 – Friction force as a function of the relative velocity between surfaces: (a) the Coulomb model with $F_{fS} = F_{fD}$ and (b) the Coulomb + static model with $F_{fS} \geq F_{fD}$.

Furthermore, for most systems, the change of the dynamical friction coefficient with the relative velocity between surfaces is not constant. This dependency has been the subject of several studies: Sampson, *et al.* (1943), Burwell & Rabinowicz (1953), Grosh (1963), Rabinowicz (1958, 1965), to mention a few. Tolstoi *et al.* (1971) suggested that the decrease of the dynamical friction with increasing sliding velocity can be explained by the effect of normal contact oscillation between the bodies; Sampson, *et al.* (1943), referred a difference on the friction coefficient during acceleration and deceleration which is responsible for the hysteretic effect observed in some systems; this behaviour was also observed by Sakamoto (1985, 1987), Hunt *et al.* (1965), Bell & Burdekin (1969), Brockley & Ko (1970), Antoniou et al. (1976), and Martins *et al.* (1990), suggesting that the loops in the frequency-velocity plots were greatly affected by the experimental model. Several analytical relations for the friction-velocity curve have been developed, most of them showing some type of exponential decay (Brockley & Ko, 1970; Bo & Pavalescu, 1982; Hess & Soom, 1990)[3].

As an example, Figure 1.3 represents a typical variation of the dynamical friction coefficient with the relative velocity (for continuous sliding) between two surfaces. Indeed, the instantaneous change between the sliding friction force to the static friction value represented in Figure 1.2b is unrealistic, and some kind of approximation to the static value has to occur when motion approaches $V_r = 0$. For continuous sliding, this variation is approximately a decaying exponential function (Smith, 2000).

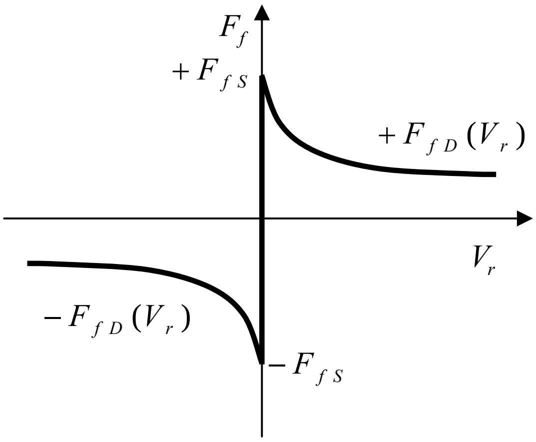

Figure 1.3 – Typical variation of the friction coefficient with relative velocity between surfaces (only non-lubricated contact is considered).

Several approaches have been used by different authors to overcome the problem of the discontinuity at the origin, usually recurring to a regularization method (Martins *et al.* 1990; Oden & Martins, 1985; Tworzydlo & Becker, 1991) or employing switching functions which detect the presence of the discontinuity in the last integration sub-interval (Dupond, 1993). To detect zero velocity crossing one possible switching function is $\text{sgn}(\dot{x})$. For the integration of discontinuous equations, small integration steps must be adopted, especially to capture transients that can occur near the

---

[3] The references given in this paragraph state investigation carried from an industrial perspective. Also in the field of Musical Acoustics, the description of the friction laws governing the interaction between two bodies (the bow and the string of a violin, for example) has led to interesting findings. Being specific to the core of this thesis, they will be discussed in section 1.3.

discontinuity, but variable-step size and variable-order methods are also adequate (Armstrong-Hélouvry *et al.* 1994).

One possible regularization method, which overcomes the need for the switching functions, is the approximation of the sticking part of the friction law by a linear region (Haessig & Friedland, 1991; Threlfall, 1978; Bernard, 1980), like the one represented in Figure 1.4.

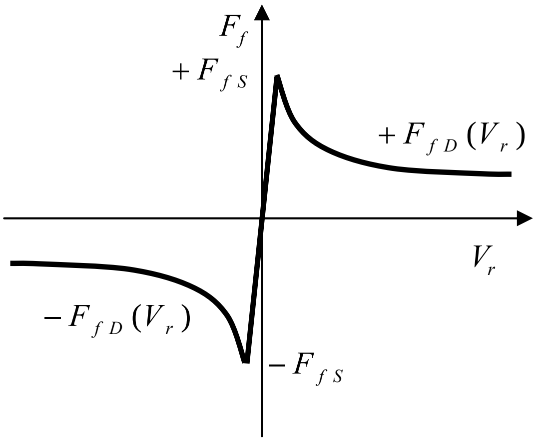

Figure 1.4 – Variation of the friction coefficient with relative velocity with a linear approximation simulating a pseudo-sticking state.

The sticking stage of the friction law is better approximated as steeper is the slope across the origin. This imposes the need for very short time integration steps, which can be a difficulty in some simulation methods. Other improvements on this law have been suggested by Bo & Pavalescu (1982) and Klamechi (1985), which still face the problem of not being able to represent the friction force at zero relative velocity. In other words, such approach is unable to simulate true adherence.

Karnopp (1985) developed an alternative approach in which the zero velocity detection was surpassed by defining a zero velocity interval within which the velocity of the system may change but the output is locked to zero, therefore simulating the sticking stage. In this interval the friction force exactly cancels the driving force and only when the driving force exceeds the “break-free” force, the body accelerates and the magnitude of the relative velocity will surpass the interval limits and switch to slip mode. Some of the drawbacks of this model are that the friction force within this interval does not agree well with real friction and the system complexity increases greatly with the number of degrees of freedom.

Other models have been proposed, such as the Dahl model (Dahl, 1968; 1976) developed from the stress-strain curve in classical solid mechanics, in which the friction force F_f is a function of the displacement and the sign of the sliding velocity V_r. Equation (1.2) represents the Dahl model, where γ is a stiffness constant and F_0 determines the peak sliding friction force. These constants can be selected according to the system in question.

$$\frac{dF_f}{dx} = V_r \gamma \left(F_f - F_0 \operatorname{sgn}\left(V_r \right) \right)^2 \tag{1.2}$$

This particular model, however, will not generate a static friction force higher than the sliding friction force, unless F_0 is a function of the sliding velocity.

These and other models, such as the “bristle model” and the Reset Integrator Model (Haessig & Friedland, 1991) or the Bliman and Sorine models (Bliman, 1992; Bliman & Sorine, 1991), have been able to simulate relevant aspects of friction induced-vibrations, particularly the important stick-slip phenomenon.

1.2.1 The Stick-Slip Phenomenon

Resulting from the contact between the atomic scale random asperities of solids in contact, friction is characteristically aperiod in nature. However, in certain conditions, the vibrations or sound generated by friction can become periodic. There are several mechanisms that can lead to this particular situation; however the stick-slip phenomenon is one of the most important and characteristic of friction-induced self-sustained oscillations[4].

In a single-degree-of-freedom system, a necessary condition for self-excited vibrations to exist is a negative slope of the friction-force speed curve. This negative slope is responsible for the energy that is supplied to the vibrations (Ibrahim, 1994b). If one of the sliding surfaces has a certain degree of elasticity it is possible that both surfaces experience relative sliding or sticking in different times of their interaction. When this occurs, their relative motion is not continuous but intermittent, with oscillations occurring by the process of stick-slip. In multi-degree-of-freedom

---

[4] These particular types of oscillations are originated when a steady (non-oscillatory) flow of energy is transformed into an oscillatory motion through some kind of nonlinear mechanism (see section 1.2.3).

systems, the phase differences between the coupled modes can supply energy to induce vibrations (Ibrahim, 1994b).

In most contexts where stick-slip vibration can occur, it is an undesired effect. For example, in machining it is likely to impair the surface finish of the cut, and in braking systems it may increase wear while reducing braking efficiency. (Smith & Woodhouse, 2000)

1.2.2 Friction vibrations in Industrial components

Many mechanical systems and components use friction as the dominating force for their functioning, such as brake systems, transmission systems (pulleys) or friction damping mechanisms, amongst others. However, if friction is beneficial for most applications it also generates some detrimental effects, which can be a serious problem in many industrial applications. Friction-induced vibration, chatter and squeal can impose functioning difficulties and ultimately failure in turning blade joints, electric motor drives, water-lubricated bearings in ships and submarines, wheel/rail of mass transit systems, machine tool/work piece systems and brake systems (Ibrahim, 1994).

Apart some of the common every-day life noises generated by friction (such as the squeal of sneakers on parquet floors, the squeak of snow when walking on it, moving door hinges, scratching chalk on a blackboard) there are several examples of noises that result from friction-excited vibrations: squeaks and squeals in the interior of automobiles, aircraft and automotive brake squeals, belts on pulleys or rail-wheel noise (Akay, 2002), amongst others.

1.2.3 Friction vibrations in Musical Instruments

If the examples of the previous section are annoying to the ear, bowed musical instruments use friction to induce further more pleasant sounds. Apart from the well known violin family instruments (violin, viola, cello and double bass), friction is the sound producing mechanism of many others, from Medieval to Contemporary music. The Tromba Marina, the viola da gamba, the bowed vibraphone and marimba, the nail violin, the musical saw, musical glasses, the glass harmonica, the brazilian cuica or the Portuguese *sarronca* as well as Tibetan bowls are some important examples (see Figure 1.5, Figure 1.6 and Figure 1.7).

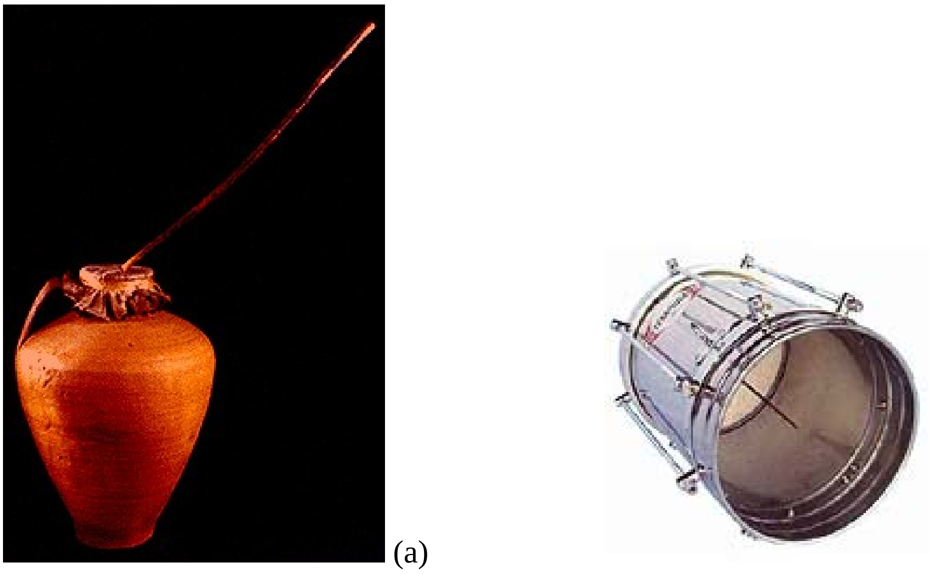

(a) (b)

Figure 1.5 – Examples of bowed membranophones: (a) the Portuguese sarronca and (b) the Brazilian cuica.

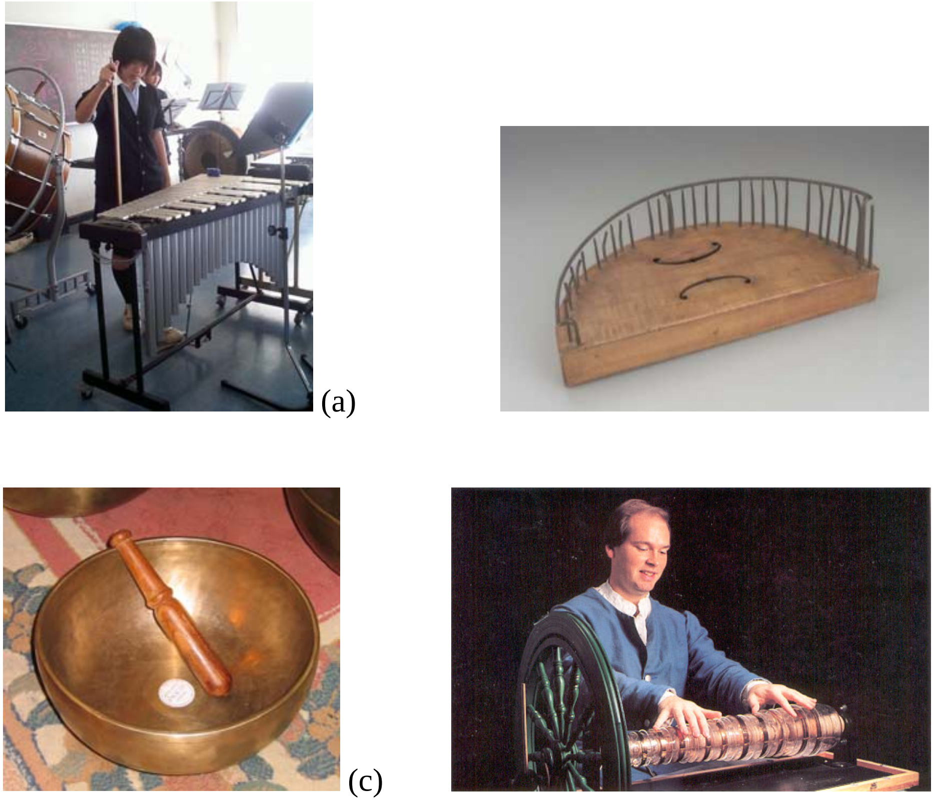

(a) (b)

(c) (d)

Figure 1.6 – Examples of bowed idiophones: (a) the bowed vibraphone; (b) the nail violin; (c) the Tibetan bowl and d) the glass harmonica.

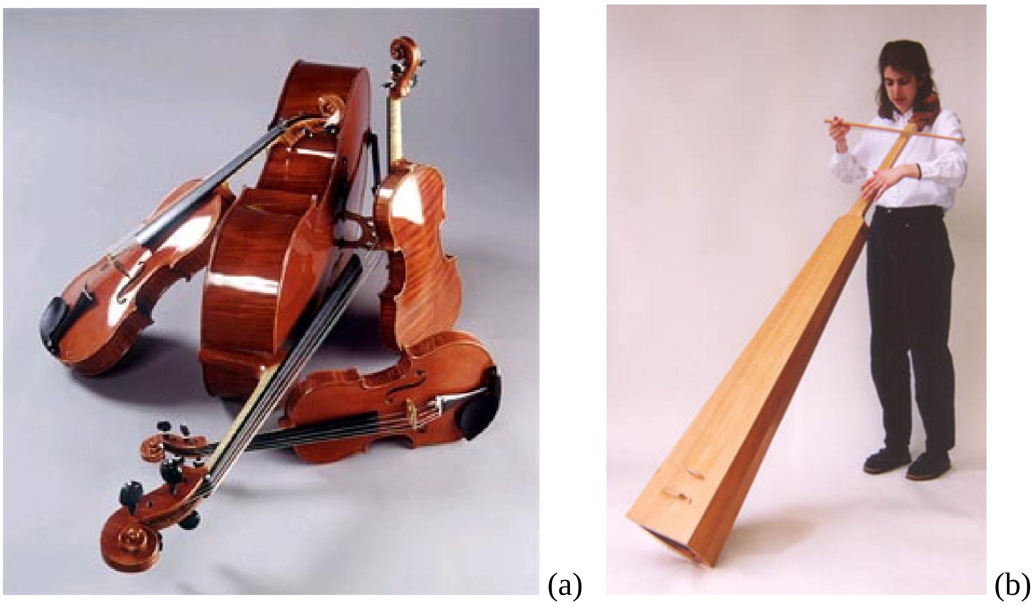

Figure 1.7 – Examples of bowed chordophones: (a) the violin family instruments; (b) the medieval tromba marina.

Of all the examples presented, three main components to the production of sound can be found: a source of energy (the player), a mechanism for generating friction (by the sliding contact of two surfaces), a tuned resonator and a component that modifies, amplifies and/or radiates the frictional energy (usually referred to as a resonator and/or radiator). In contrast to plucked string or percussion musical instruments (but in harmony with most wind instruments) friction excited instruments are essentially nonlinear in nature[5]. This nonlinearity allows for a self-sustained oscillation to be generated while the stationary source of energy is available. Figure 1.8 represents an energy flow diagram common to all self-sustained musical instruments where these and other components are represented.

This energy transfer and transformation process can be used to describe the principles of functioning of musical instruments. A steady sound source (usually the player's muscles when bowing or breath when blowing, or even a mechanical ventilator in the case of organs) generates the energy necessary to start the system. This energy is converted into vibratory energy through a nonlinear interface (friction, reed, etc.) between the musician's gesture and the primary resonating component (string, air column, plate or membrane, etc.). In all self-excited instruments (violin, clarinet, tuba, etc.), the nonlinear interface will react in synchrony with the resonator, due to feed-

---

[5] It is important to state that some exceptions occur where percussion musical instruments have also significant nonlinear characteristics of geometrical nature (see Rossing, 2000).

back phenomena from the later (vibration or pressure pulse). In fact, coupling between the nonlinear generator and the primary resonator is so close that they cannot be considered separately (Fletcher, 1999). Under suitable conditions of the control parameters (bow normal force and tangential velocity, blow pressure, etc.), the instrument will become linearly unstable. Then vibratory or acoustic responses will grow until saturating nonlinear effects limits the oscillating amplitude, usually leading to limit-cycle regimes. The primary resonator can, in some instruments, interact with other nonlinear mechanisms and with a secondary resonator (such as the body of a cello) which can act also as a radiator of sound.

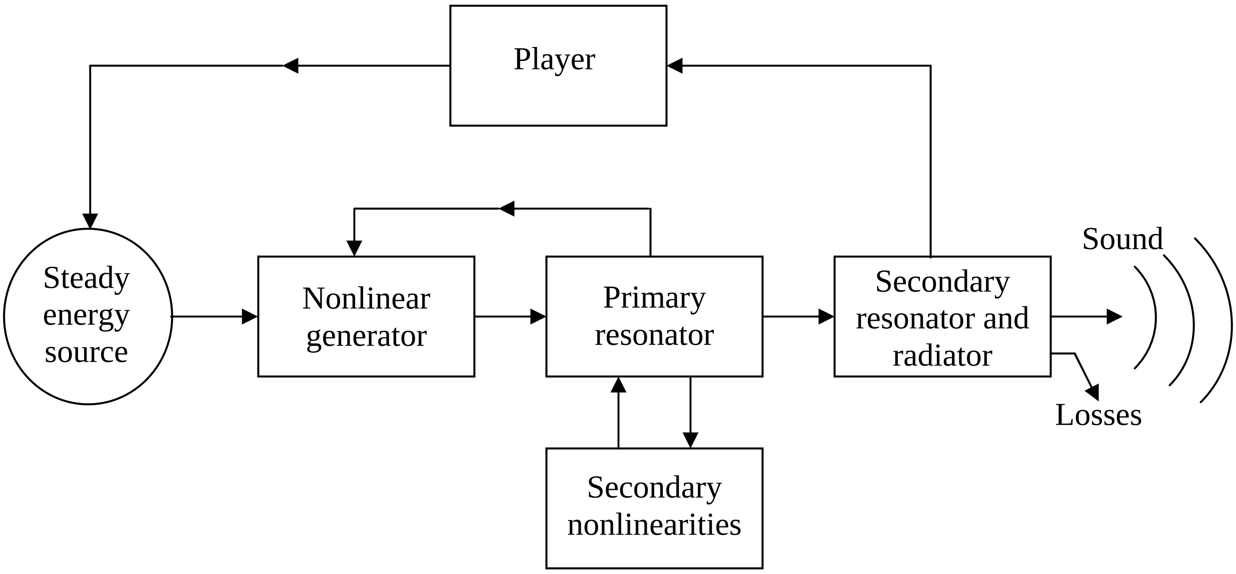

Figure 1.8 – Diagram representing the components and the energy flow in a self-sustained musical instrument.

1.3. Research on Bowed Musical Instruments

Apart from bowed strings, which have been the subjects of most scientific research in Musical Acoustics, other bowed instruments haven't received such a notorious attention. Bars, plates and shells, which are the main components of most idiophones, have been extensively studied, but generally only when impact (either linear or non-linear) excitation is present.

Several friction-excited idiophones are familiar to western musical culture, such as bowed vibraphone and marimba bars, the nail violin, the musical saw, musical glasses and the glass harmonica, as well as some natural objects rubbed against each other, like sea shells, bones, stones or pine-cones. In an interesting tutorial paper, Akay (2002) presents an overview of the acoustics phenomena related to friction, which is the main sound-generating mechanism for such systems. Some of these musical instruments have been experimentally studied, in particular by Rossing (2000). Nevertheless, the analysis of idiophones excited by friction is comparatively rare in the literature and mostly recent – see French (1983), Rossing (1994), Chapuis (2000) and Essl & Cook (2000). Among these studies, only French (1983) and Essl & Cook (2000) aim at physical modelling, respectively of rubbed glasses and bowed bars.

On the modelling techniques of such instruments, the developments of McIntyre and Woodhouse (1979), with the now classic digital waveguide method, have been paramount for the knowledge of their behaviour and for the development of real-time synthesis methods for musical purposes (Smith, 2003). Other applications for musical purposes aiming particularly on the creation of new sounds based on physical modelling were developed in IRCAM. The software Modalys developed in this institute is based on a modal representation of the systems, similarly to the method developed in this thesis. However, the nonlinear interactions between the instruments components are treated in a totally different approach from the one presented here (see Bensoam, 2006).

In this section, a review is made of some of the most important references to the three types of instruments studied in this thesis: bowed bars, bowed shells and bowed strings.

1.3.1 Bowed bars

In spite of the increasing application of bowed idiophones, as vibraphones or marimbas, in contemporary music making, it is only recently that the scientific community started working on the dynamic processes behind this sound-producing technique — see Rossing (1994, 2000) and Essl & Cook (2000). Friction-induced vibrations in bowed bars present several interesting aspects: In the first place, it is still a challenge to properly simulate the complex stick-slip behaviour of multi-degree-of-freedom systems; Secondly, the much studied and now well understood synchronization mechanism provided by the back-and-forth travelling waves in bowed string instruments (McIntyre & Woodhouse, 1979) does not apply to bowed bars. Indeed, the harmonic relationship between the modal frequencies of string transverse modes is not typically found in bending bars. This is connected to the fact that string waves are non-dispersive (or, at most, weakly dispersive), whereas flexural waves are strongly dispersive. Hence, the classical Helmholtz-type excitation mechanism (Fletcher & Rossing, 1998) found in bowed strings does not apply to bowed bars.

In 2000, Essl & Cook published the results of an investigation in which several experimental measurements of bars of bar percussion instruments bowed by a double bass bow and by a bowing machine were presented. They examined the relationships between performance and perception parameters which are relevant for musical performance and presented a simulation method using a banded waveguide time-domain approach. Their results stated the increase of the bar vibration amplitude with increasing bow velocity and the independence on bowing force, as also seen in bowed strings. Their simulation results lacked information on the spatial details of the bar vibratory behaviour, but presented qualitative good agreement with measurements.

1.3.2 Bowed shells

Recently, some researchers became interested in the physical modelling of singing bowls, using waveguide synthesis techniques for performing numerical simulations (Cook, 2002; Serafin *et al*, 2002; Young & Essl, 2003). Their efforts aimed particularly at achieving real-time synthesis. Therefore, understandably, several aspects of the physics of these instruments do not appear to be clarified in the published formulations and results. For instance, an account of the radial and tangential vibratory motion components of the bowl shell – and their dynamical coupling – has been ignored in the published literature. Also, how these motion components relate to the travelling position of the excitation stick (called *puja*) contact point is not clear at the present time. Details of the contact/friction interaction models used in simulations have been seldom provided, and the significance of the various model parameters has not been asserted. On the other hand, experiments clearly show that beating phenomena arises even for near-perfectly symmetrical bowls, an important aspect which the published modelling techniques seem to miss (although beating from closely mistuned modes has been addressed – not without some difficulty (Young & Essl, 2003) – but this is a quite different aspect). Therefore, it appears that several important aspects of the excitation mechanism in singing bowls still lack clarification.

1.3.3 Bowed strings

Raman's seminal paper (Raman, 1918) was a landmark study of the dynamics of bowed strings. Since then, a plethora of research papers has been published on bowed-string instruments, including enlightening work by Friedlander (1953), Schelleng (1973), McIntyre, Schumacher and Woodhouse (1983), to name just a few – see Cremer's book (Cremer, 1984) – for an extensive account of the field).

In most published work, simulations assumed a string pinned at the bridge and the nut, and therefore decoupled from the instrument body. This approach proved adequate to obtain the typical motion patterns displayed by bowed-strings. However, because the bridge is assumed motionless, such computations are obviously unable to cope with more subtle phenomena related to the coupling of string and body motions.

A crude approach to incorporate body effects, when simulating string sounds, is to start by computing the vibratory response of an "isolated" (bowed or plucked) string, and then use the resulting string/bridge interaction force to drive a given body vibro-acoustic transfer function. However this simple approach is quite limited and cannot account for any energy feedback from the body into the string – such as is found in wolf notes – because the full string/body coupling is not modelled.

Apparently only a few authors have attempted to address this string/body coupling problem. McIntyre (1983) incorporated in their wave-propagation computational algorithm a bridge-reflection function which encapsulates the dynamical behaviour of a given body resonance, enabling them to simulate the coupled dynamics between the string and the chosen body resonance. Similarly, Puaud et al (1991) used (in connection with a so-called “numerical bow”) a mass-stiffness bridge-resonator, therefore also emulating a chosen body-resonance coupled to the string dynamics. Recently, a different approach has been pursued by several authors to simulate instrument bodies and cavities – see Huang et al (2000), for instance – by using 2D or 3D waveguides to compute simplified multi-degree-of-freedom resonating systems. However, until now, this modelling technique has only been used to simulate the body-filtering effects on string/bridge dynamical forces, with no feedback coupling. In relation to other stringed instruments, Derveaux et al (2003) achieved fully coupled string/soundboard computations for a modelled guitar.

1.4. Aims and contributions

The aim of this thesis is to present a robust computational method, based on a modal approach, for the simulation of three different types of bowed musical instruments: bowed strings, bowed bars and bowed shells. Although the dynamical and frictional behaviour can be quite different for each system, it is proposed to use the same general friction model for the three types of instruments, although using two different implementations for simulating the adherence state. The objective is to perform simulations which exhibit results with the same global vibratory behaviour when compared to the real instruments.

Most of the work presented in this thesis has already been published by the author in refereed scientific journals. All these publications have been co-authored by other researchers whose contributions were related to supervision of the work carried by the author of this thesis.

1.4.1 Contributions on the modelling techniques

Several methods have been used by different authors to simulate different vibratory aspects of musical instruments, as already described in the previous sections. The main contribution of this thesis is the implementation of a computational method, mainly originated in industrial applications, to the simulation of the vibratory behaviour of two types of bowed musical instruments: strings and idiophones (divided into one dimensional and axi-symmetric structures – bars and bowls, respectively), utilizing the same underlying friction model. The modal approach and the friction modelling developed in this thesis allows great versatility for incorporating different components of the instrument in the simulations, when compared with other methods. Some of these contributions of this method are summarized in the following paragraphs and further detailed in the respective chapters:

Bowed Bars

- Numerical model including the force generated by the supports and acting on the nodal points of the first flexural mode of the bar;

- Numerical model allowing the introduction of a bar of arbitrary shape and pre-defined (calculated or identified) modal basis.

Bowed Tibetan Bowls

- Numerical model introducing orthogonal vibratory modes pairs, with both tangential and radial components, coupled by the nonlinear friction force, for symmetrical and slightly asymmetrical shapes;

Bowed Strings

- Numerical model incorporating the measured dynamics of real-life instrument bodies, coupled to the string motions. Two different approaches to account for the coupled string/body dynamics are proposed.

1.4.2 Contributions on the results

The implementation of the simulation method presented in this thesis has contributed to new results, not only because some of the instruments had never been simulated with the level of physical detail provided by this method, but mainly from the new findings in relation to what was common knowledge on the vibratory behaviour of some musical instrument components. The new results are summarized in the following paragraphs and further detailed in the respective chapters:

Bowed Bars

- Simulation of the time history of the vibration of bowed bars with good agreement with measured time-history;

- Simulation of different vibratory regimes of bowed bars for different playing conditions of either bow velocity and applied force;

- Interpretation of the self-excited regimes based on a linearized analysis of the system before nonlinear effects emerge.

Bowed Shells

- Simulation of the time-history of the vibrations of bowed Tibetan bowls with good agreement with measured time-history;

- Simulation of different vibratory transients and self-sustained regimes of bowed Tibetan bowls for different playing conditions of either bow velocity and applied force;

- Clarification of the radial and tangential vibratory behaviour of bowed Tibetan bowls and of the beating phenomena associated with perfectly axi-symmetrical instruments;

- Demonstration of the strong dependence of the Tibetan bowls self-sustained regime order of oscillation on the contact/friction parameters;

Bowed Strings

- Presentation of the effect of torsion modes on the string dynamics for a wide range of torsion to transverse frequency ratios;

- Demonstration that differences between point-model and finite-width simulations can be more pronounced outside the range of bowing parameters leading to the Helmholtz motion;

- Effective simulation of the wolf-note on a cello, establishing the range of the playing parameters where this phenomenon emerges;

- Demonstration of the beating dependence of the wolf-note with bowing velocity and applied bow force, with good agreement with measured results;

- Interpretation of the self-excited regimes based on a linearized analysis of the system before nonlinear effects emerge.

For all cases validating qualitative experiments are presented, as well as realistic “sounds” and original animations of both transients and steady-state regimes which are illuminating and pedagogic.

Chapter 2

GENERIC SIMULATION METHODOLOGY

2. GENERIC SIMULATION METHODOLOGY

2.1. *Introduction*

The modelling approach developed in this thesis is not tied to a specific system, but has been devised to be used with any kind of dynamical problem, in this case bowed musical instrument vibratory behaviour, where localized frictional forces couple different vibrating subsystems. For this reason, a generic description of the computation method is made in this chapter, which is common to the three systems studied. The details of the implementation for each of the three instruments are presented in the corresponding chapters.

2.2. *Nonlinear computations in the time domain using a modal basis*

The mathematical description of vibrating systems like tensioned strings or rigid bars is usually performed by means of one or several linear partial differential equations in both time and space domain. Although torsional and axial vibrations are also present in the dynamics of these systems, a focus will be placed on transverse displacement only, for matter of simplicity in describing the basis of this computational method.

If linear dissipation is assumed, the small-amplitude motions $y(x,t)$ of the system subject to a force distribution $F(x,t)$ can be described by an equation of the type:

$$\sigma \frac{\partial^2 y}{\partial t^2} + \mathcal{C}\left(\frac{\partial y}{\partial t}\right) + \mathcal{K}\left(y\right) = F(x,t) \tag{2.1}$$

where σ is the linear density of the system inertia, $\mathcal{C}\left(\frac{\partial y}{\partial t}\right)$ is a linear dissipative term and $\mathcal{K}\left(y\right)$ is the linear stiffness restoring force which depends on the particular kind of system in study. For the present work, the external force field $F(x,t)$ is originated by the friction between a violin or cello bow or a rubber or wooden stick, and one or more points of the vibrating body.

Any solution of (2.1) can be formulated in terms of the unconstrained system modal parameters: modal masses m_n, circular frequencies ω_n, damping values ζ_n and mode shapes $\varphi_n(x)$, with $n = 1,2, \ldots, N$. The order N of modal truncation is problem dependent and must be asserted by physical reasoning. On the modal space the forced response of the damped string is formulated by (2.2), which follows from (2.1) by writing the solution of this partial-differential equation with the separation approach (2.4):

$$\left[M\right]\left\{\ddot{Q}(t)\right\}+\left[C\right]\left\{\dot{Q}(t)\right\}+\left[K\right]\left\{Q(t)\right\}=\left\{\Xi(t)\right\} \tag{2.2}$$

where: $\left[M\right]=\text{Diag}(m_1,\cdots,m_N)$, $\left[C\right]=\text{Diag}(2m_1\omega_1\zeta_1,\cdots,2m_N\omega_N\zeta_N)$, and $\left[K\right]=\text{Diag}(m_1\omega_1^2,\cdots,m_N\omega_N^2)$, are the matrices of modal parameters, while $\left\{Q(t)\right\}=\left\langle q_1(t),\cdots,q_N(t)\right\rangle^T$ and $\left\{\Xi(t)\right\}=\left\langle \Im_1(t),\cdots,\Im_N(t)\right\rangle^T$ are the vectors of modal responses and generalised forces, respectively. In the modal Equation (2.2) proportional damping is postulated. The modal damping values ζ_n are usually identified from experiments; however, they may eventually be theoretically estimated (Fletcher & Rossing, 1998). Moreover, it is assumed that the system uncontrained modeshapes are real. The modal forces $\Im_n(t)$ are obtained by projecting the external force field on the modal basis:

$$\Im_n(t)=\int_0^L F(x,t)\;\varphi_n(x)\;dx\;,(n=1,2,...,N) \tag{2.3}$$

The physical motions at any point of the system can be computed from the modal amplitudes $q_n(t)$ by superposition:

$$y(x,t)=\sum_{n=1}^{N}\varphi_n(x)\,q_n(t) \tag{2.4}$$

and similarly concerning the velocities and accelerations. For given external excitation and initial conditions, the previous system of equations can be integrated using any adequate time-step integration algorithm. Explicit integration methods are well suited for the friction models developed here, as will be explained in section 2.3 and 2.4. In these implementations, a simple Verlet integration algorithm is used (Beeman, 1976), which is a second order explicit scheme. Note that, although (2.2)-(2.4) obviously pertain to a linear formulation, nothing prevent us from including in $\Im_n(t)$ all nonlinear effects arising in the system. Accordingly, the system modes become coupled by the nonlinear effects, as will be shown later.

The definition of the modal basis to use in the computations is of paramount importance to obtain results which can be comparable to the behaviour of real-life instruments. In the next sections a short description is made of the different modal basis used for each instrument studied, to allow a clear understanding of their different natures.

2.2.1 Strings

Consider a string with a uniform linear density μ, length L and fixed at both ends stretched to a tension T. Assuming negligible bending stiffness in the string, the restoring force $\mathcal{K}(y)$ is equal to $c^2(\partial^2 y / \partial x^2)$ turning (2.1) into the classic damped wave equation, where the wave speed c is given by $c^2=T/\mu$. Since c is constant, waves of different frequencies travel with the same phase speed and the modal frequencies are then given by $\omega_n = n\pi c/L$, and mode shapes $\varphi_n(x) = \sin(n\pi x/L)$, with $n = 1,2, \ldots, N$. This harmonic relation of the circular frequencies, characteristic of non-dispersive systems, originates naturally consonant sounds which are traditionally sough for in musical instruments making or tuning.

2.2.2 Bars with constant cross section

In clear contrast with the perfectly flexible string, the constant cross section bar exhibits considerable bending stiffness, $EI(x)$, where E is the Young Modulus and $I(x)$ the local moment of inertia. The restoring force $\mathcal{K}(y)$ in (2.1) is now dependent on a fourth spatial derivative, which results in a different phase speed for different wave frequencies. This dispersive behaviour originates modal frequencies with values far from any harmonic relation as can be seen in (2.5), for free-free boundary conditions.

$$\omega_n = \frac{\pi^2 K_r}{4L^2}\sqrt{\frac{E}{\rho}}\left[3.011^2, 5^2, 7^2, \ldots, (2n+1)^2\right] \tag{2.5}$$

where K_r is the radius of gyration of the cross section of the bar and ρ is the specific mass of the bar material (Fletcher & Rossing, 1998).

Although this formulation is essentially correct for long and thin bars, the model used in this work considers the effects of rotary inertia and shear stress, which occur in thick bars, by use of the Timoshenko beam model (Graff, 1975). As a result, the high inharmonicity is still present but there is a slight decrease in the value of the higher modal frequencies (Fletcher & Rossing, 1998).

The sound originated by the vibration of these objects tends to be somewhat unpleasant, unless the inharmonic frequencies are very high in the spectrum and decay so rapidly not to be clearly discriminated by the human ear, such as the bars used in the glockenspiel.

2.2.3 Bars with variable cross section

In order to obtain more pleasing sounds in the whole register of instruments such as the marimba or the vibraphone, makers usually tune these instruments by giving the bars a variable cross section. Following years of craftsmanship, instrument makers arrived to bar profiles which have natural frequencies in the approximate relation $f_2 = 3f_1$ and $f_3 = 9f_1$ (1-3-9) or $f_2 = 4f_1$ and $f_3 = 10f_1$ (1-4-10) of the first three bending modes, allowing for more harmonious sounds to be produced.

Although those are the most used relations it is possible to tune a bar to quite distinct sets of modal frequencies. Henrique *et al* (2002a, 2002b, 2002c), have developed optimization procedures to find the optimal bar profile for any given set of desired natural frequencies relations (f_n/f_1), for example 1-2-3, which is similar to the one obtained in the ideal string as far as the first three bending modes are concerned. This unorthodox tuning of the bars can lead to dynamical responses to friction excitation which behave midway between the ideal bowed string and the constant cross section bowed bar.

2.2.4 Axi-symmetric structures (bodies of revolution)

Perfectly axi-symmetrical structures, such as bells or round glasses, exhibit double vibrational modes occurring in orthogonal pairs with identical frequencies (Rossing, 1994). These vibratory modes exhibit modeshapes which are usually labelled as (j,k) (where j relates to the number of nodal meridians and k to the number of nodal circles).

When excited by impact, the different partials (usually with a great emphasis on the first few modes) give rise to a long stable decaying transient. However, if a slight alteration of this symmetry is introduced, the natural frequencies of these two degenerate modal families deviate from identical values by a certain amount. In this situation, the slight frequency difference will generate beating between the two modal families. Furthermore, shell modeshapes present both radial and tangential components which are extremely important for the correct simulation of bowing in these instruments since the radial and tangential motions and contact forces are coupled. Furthermore, the friction excitation acts on the tangential modes of the system and sound radiation mainly stems from its radial motion.

2.3. *Friction model*

The relation between the force acting on a bowed system and its resulting motion is governed by a friction law which can be have different behaviours depending on the surface properties of the bodies in contact. As seen in Chapter 1, several authors have developed friction models to define this relation, taking different assumptions in consideration.

In bowed instruments research, a great emphasis is obviously given to this problem, and different models have arisen in the past decade attempting to emulate as accurately as possible the real contact relation between the friction force and the motion of the system. Particularly, the bowed string friction law has been the subject of the more various models, with more or less complexity (see Woodhouse & Galluzzo, 2004).

For the computational method described in this thesis, a classical Coulomb model is used. Not being devised for a specific system, this model allows good versatility when used with the three different instruments analysed in this thesis. The implementation of this friction law in the computational method is described in the following section.

2.3.1 Classical Coulomb model

Consider a Coulomb-type friction force arising when the bow is applied at location x_c of the system:

$$\begin{cases} F_s(x_c,t) = -\mu_d(\dot{y}_c)F_N \operatorname{sgn}(\dot{y}\ ) \; ; \text{ if } \; |\dot{y}_c| > 0 \\ |F_a(x_c,t)| < \mu_S F_N \qquad\qquad\qquad ; \text{ if } \; |\dot{y}_c| = 0 \end{cases} \tag{2.6}$$

Here, the relative transverse velocity between the bow and the system is given by (see Figure 1.8):

$$\dot{y}_c = \dot{y}(x_c,t) - \dot{y}_{bow}(t) = \sum_{n=1}^{N} \varphi_n(x_c)\,\dot{q}_n(t) - \dot{y}_{bow}(t) \tag{2.7}$$

where $F_N(t)$ is the normal force between the bow and the bar, μ_S is a “static” friction coefficient (used during surface adherence) and $\mu_d(\dot{y}_c)$ is a “dynamic” friction coefficient (used for sliding regimes).

It is assumed here that μ_d is an instantaneous function of the relative bow/bar velocity, and use the following model:

$$\mu_d(\dot{y}_c) = \mu_D + (\mu_S - \mu_D)\,\mathrm{e}^{-C|\dot{y}_c|} \tag{2.8}$$

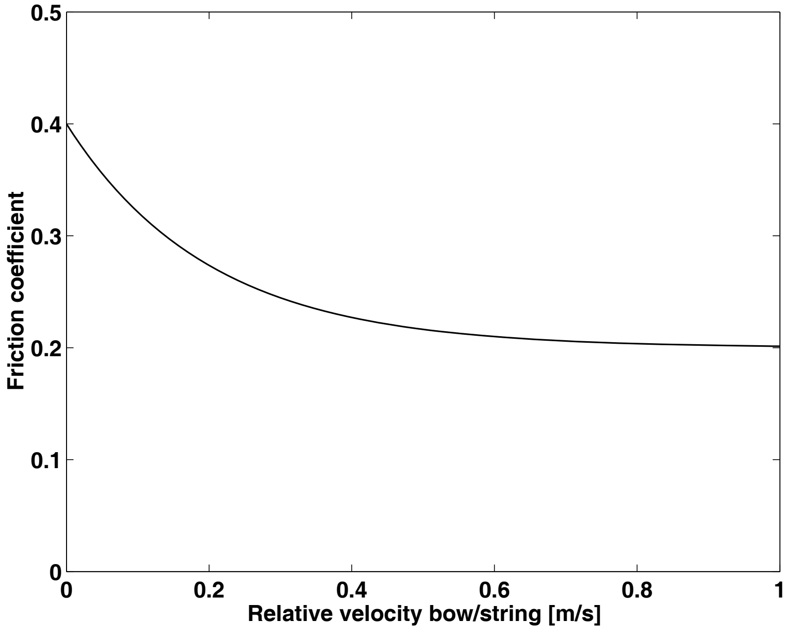

Figure 2.1 – Typical evolution of the friction coefficient with the relative sliding velocity ($\mu_S = 0.4$, $\mu_D = 0.2$, $C = 5$).

where, $0 \le \mu_D \le \mu_S$ is an asymptotic lower limit of the friction coefficient when $|\dot{y}_c| \to \infty$, and parameter C controls the decay rate of the friction coefficient with the relative bow/bar sliding velocity. The friction model (2.8) can be readily fitted to typical experimental data (see for example, Lazarus, 1972), by adjusting the empirical constants μ_S, μ_D and C.

The sliding behaviour, described by the first equation (2.6), does not cause problems for simulations, as this equation explicitly shows how the sliding force should be computed as a function of the sliding velocity. However, during adherence, simulation becomes much more difficult. Indeed, the second equation (2.6), merely states a limiting value for the friction force, during adherence, and gives no hint on how $F(\dot{y}_c, t)$ may be actually computed. This is because the adherence force depends on the overall balance of external and internal forces acting upon the system, which is quite complex for multi-degree of freedom problems. Most friction algorithms deal with this problem through implicit approaches, which can be very expensive to run.

The implementation of this friction model, mainly in what concerns the adherence state, can be made in different ways. Depending on the sliding/sticking time ratio during each period, a real adherence state (zero relative velocity between the bow and the system) might be more or less relevant to establish the proper motion of the system. For this reason, two implementations of the friction model which will be used in the subsequent chapters are described in the following paragraphs.

2.3.2 Spring-dashpot true adherence model

In this approach, adherence is simulated through a spring-dashpot model which enables zero relative velocity between the friction exciter and the analyzed system.

The following explicit *procedure* is used at each time-step i:

(1) If in the previous time-step the system was sliding, a possible adherence between the friction exciter (hereby named generically as *bow*) and the system is detected by computing $J_i = \dot{y}_c(t_i)\,\dot{y}_c(t_{i-1})$. Then, if $J_i > 0$, the system is still sliding in the same direction. Computation of $F_s(\dot{y}_c, t_i)$ is made according to the first equation (2.6), with $\dot{y}_c(t_i)$ given by (2.7) and $\mu_d(t_i)$ by (2.8).

(2) However, if $J \leq 0$, then a reversal of the relative motion is occurring and adherence will arise. Then, the sticking force is computed using the following model:

$$F_a(x_c, t_i) = -K_f\ y_c(t_i) - C_f\ \dot{y}_c(t_i) \tag{2.9}$$

which will be used during the complete duration of the adherence state. The idea in (2.9) is to “attach” the system to the bow at point x_c using a suitable “adherence stiffness” and to damp-out any residual bow/system relative motion during sticking using an “adherence damping” term. At any time during adherence, the relative velocity $\dot{y}_c$ at the attachment point is given by (2.7) and the relative displacement y_c is given as:

$$y_c = y(x_c, t) - y^a_{bow}(t) = \sum_{n=1}^{N} \varphi_n(x_c)\, q_n(t) - y^a_{bow}(t) \tag{2.10}$$

where $y^a_{bow}(t)$ is the current position of the bow “attachment point”. For a given constant bow speed, this changes as $y^a_{bow}(t) = (t - t_a)\,\dot{y}_{bow}$, where t_a is the time value when adherence was detected. As discussed by Antunes *et al* (2000), the parameter K_f can be approximated by the axial stiffness of the bow hair, while C_f is chosen in order to obtain an almost-critical damping of the “adherence oscillator”.

(3) After computing the adherence force, $F_a(\dot{y}_c, t_i)$ is compared with the maximum allowable value $\mu_S F_N$. If $|F_a| \le \mu_S F_N$, the current estimate is accepted and simulation continues assuming a sticking state. On the contrary, when $|F_a| > \mu_S F_N$, sliding will arise and the friction force is recomputed according to the first equation (2.6). Then, the procedure continues with the next time-step.

By virtue of (2.7) and (2.10), all the modes of the system become coupled when the nonlinear friction forces are computed and projected on the modal basis (2.4) and then incorporated in (2.3).

2.3.3 Pseudo-adherance with a regularized near-zero velocity model

In this section, a simpler approach is taken to model friction interaction, which allows for faster computation times, although it lacks the capability to emulate true friction adherence. The friction force will be formulated as:

$$\begin{cases} F_t(\theta_c,t) = -\left|F_r(\theta_c,t)\right| \mu_d\left(\dot{\tilde{y}}_t(\theta_c,t)\right) sgn\left(\dot{\tilde{y}}_t(\theta_c,t)\right) \\ \qquad\qquad\qquad\qquad\qquad\qquad , \text{ if } \left|\dot{\tilde{y}}_t(\theta_c,t)\right| \ge \varepsilon \\ \\ F_t(\theta_c,t) = -\left|F_r(\theta_c,t)\right| \mu_s\, \dot{\tilde{y}}_t(\theta_c,t)\big/\varepsilon \quad , \text{ if } \left|\dot{\tilde{y}}_t(\theta_c,t)\right| < \varepsilon \end{cases} \tag{2.11}$$

where μ_s is a “static” friction coefficient and $\mu_d(\dot{\tilde{y}}_t)$ is a “dynamic” friction coefficient, which depends on the relative surface velocity $\dot{\tilde{y}}_t$. The following model is used:

$$\mu_d(\dot{\tilde{y}}_t) = \mu_\infty + (\mu_s - \mu_\infty)\exp\left(-C\left|\dot{\tilde{y}}_t(\theta_c,t)\right|\right) \tag{2.12}$$

where, $0 \le \mu_\infty \le \mu_s$ is an asymptotic lower limit of the friction coefficient when $\left|\dot{y}_t\right| \to \infty$, and parameter C controls the decay rate of the friction coefficient with the relative sliding velocity, as shown in the typical plot of Figure 2.2(a). This model can be fitted to the available experimental friction data (obtained under the assumption of instantaneous velocity-dependence), by adjusting the empirical constants μ_s, μ_∞ and C.

Notice that both equations (2.11) correspond to velocity-controlled friction forces. For values of $\dot{y}_t$ outside the interval $[-\varepsilon, \varepsilon]$, the first equation simply states Coulomb's model for sliding. Inside the interval $[-\varepsilon, \varepsilon]$, the second equation models a state of *pseudo-adherence* at very low tangential velocities. Obviously, ε acts as a regularization parameter for the friction force law, replacing the "zero-velocity" discontinuity (which renders the adherence state numerically tricky), as shown in Figure 2.2 (b). This regularization method, extensively developed in Oden & Martins (1985), has been often used as a pragmatic way to deal with friction phenomena in the context of dynamic problems. However, using this model, the friction force will always be zero at zero sliding velocity, inducing a relaxation on the "adherence" state (dependent on the magnitude of ε), and therefore disabling a true sticking behaviour. How pernicious this effect may be is problem-dependent – systems involving a prolonged adherence will obviously suffer more from the relaxation effect than systems which are sliding most of the time. For the problem addressed here, realistic results have been obtained using formulation (2.11), for small enough values of the regularization domain ($\pm\varepsilon \approx 10^{-4}\,\mathrm{ms}^{-1}$) – results which do not seem to critically depend on ε, within reasonable limits.

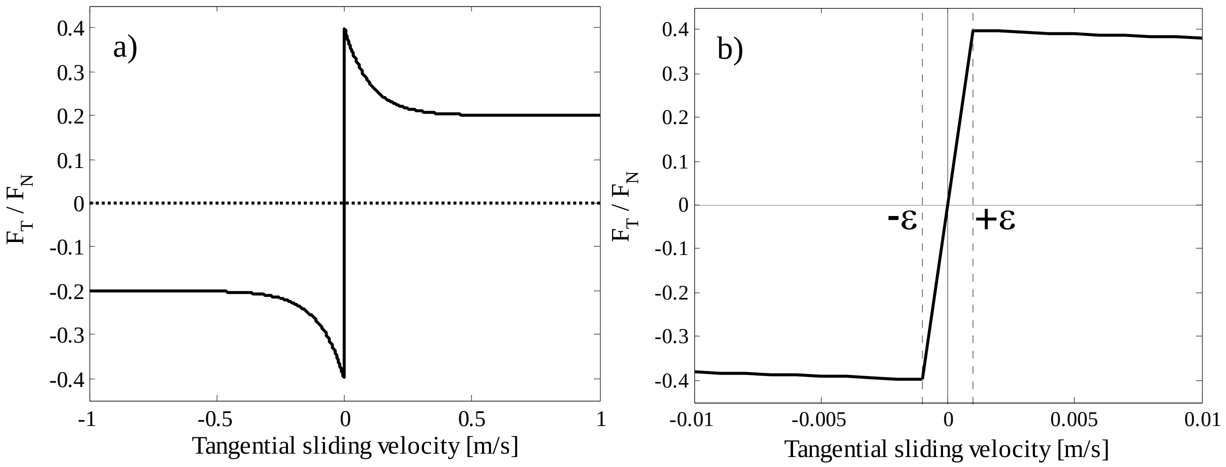

Figure 2.2 – Friction coefficient as a function of the contact relative tangential velocity (μ_∞ = 0.2, μ_s = 0.4, C = 10): For -1< $\dot{y}_t$ <1; (b) For -0.01< $\dot{y}_t$ <0.01.

2.3.4 Other friction models

As mentioned in the previous sections, different friction models have been explored over the past decade, mainly in relation to the study of the bowed string. The most common models relate the friction force only with the relative velocity between the bow and the string. This is the case of the model previously described, as well as the "Hyperbolic Friction Function" (Guettler, 2002) where the friction coefficient is an hyperbolic function of the relative bow/string velocity.

In a recent study, Smith and Woodhouse (2000) measured the friction and relative sliding speed between a rosined rod and a vibrating cantilever system. This analysis showed a hysteresis loop in the friction-velocity relationship, which doesn't find explanation on the classical friction models referred before. The authors suspected that this behaviour is related to the temperature dependence of the rosin characteristics used in the bow. In pursuing this effect two different friction models were devised: a "thermal viscous model" and a "thermal plastic model". For both of these models, the authors claim that their implementation on the simulation of the bowed string dynamics give results consistent with measurements in steady sliding tests (Woodhouse & Galluzzo, 2004), representing an alternative to the classical friction model used in this thesis. This is a very active research area at the present time.

2.4. *Numerical aspects*

2.4.1 Integration algorithm

The modal equations (2.2), coupled through the right hand-side force terms, may be numerically integrated using either an explicit or implicit approach, meaning that the dynamical force balance may be based on the state of the system at either the last computed time-step t_i or the next time-step $t_{i+1} = t_i + \Delta t$ under computation. Both approaches have merits and disadvantages as, in broad terms, explicit algorithms are simpler and faster per time-step than implicit algorithms, which must iterate until convergence. However, the latter typically enable the use of larger integration time-steps Δt, which may compensate the previous disadvantage, the best option being problem dependent. Previous experience with vibro-impacting and friction-excited systems (see Antunes & Tafasca, 2000; Tafasca *et al*, 2000; Antunes *et al*, 2001; Inácio, 2002; Inácio *et al*, 2006]) suggests that explicit algorithms are well suited for such problems. Among other possible choices the so-called "Velocity-Verlet" method introduced by Swope *et al* (1982) is used here. This is a simple explicit algorithm of second order. Although not frequently found in structural dynamics computations, this algorithm has been widely used by researchers dealing with granular flow and molecular dynamics computations – see Deuflhard *et al* (1999), for instance. However, other methods such as Newmark's algorithm (Newmark, 1959; Bathe & Wilson, 1973) might be used as well.

Notice that because numerical efficiency is not an issue here, it is not claimed that the time-step integration algorithm presented is the most efficient approach for the problem.

For each modal equation, the Velocity-Verlet algorithm is expressed as:

$$\begin{aligned} q_n(t_{i+1}) &= q_n(t_i) + \dot{q}_n(t_i)\Delta t + \frac{\Delta t^2}{2}\frac{\Im_n(t_i)}{m_n} + O(\Delta t^3) \\ \dot{q}_n(t_{i+1}) &= \dot{q}_n(t_i) + \frac{\Delta t}{2}\frac{\Im_n(t_i) + \Im_n(t_{i+1})}{m_n} + O(\Delta t^3) \end{aligned} \tag{2.13}$$

where, because the interaction forces depend on the system response, $\Im_n(t_i) = \Im_n\left[q_j(t_i), \dot{q}_j(t_i)\right]$ and, strictly speaking, $\Im_n(t_{i+1}) = \Im_n\left[q_j(t_{i+1}), \dot{q}_j(t_{i+1})\right]$ (where the index j stands for all modes in the range $j = 1, ..., N$). The use of such an expression for $\Im_n(t_{i+1})$ can be solved by an implicit scheme. However, formulation (2.13) may be split as follows:

$$\begin{aligned} \dot{q}_n(t_{i+1/2}) &= \dot{q}_n(t_i) + \frac{\Delta t}{2}\frac{\Im_n(t_i)}{m_n} \\ q_n(t_{i+1}) &= q_n(t_i) + \dot{q}_n(t_{i+1/2})\Delta t \\ \dot{q}_n(t_{i+1}) &= \dot{q}_n(t_{i+1/2}) + \frac{\Delta t}{2}\frac{\tilde{\Im}_n(t_{i+1})}{m_n} \end{aligned} \tag{2.14}$$

with $\Im_n(t_i) = \Im_n\left[q_j(t_i), \dot{q}_j(t_i)\right]$ and the approximation $\tilde{\Im}_n(t_{i+1}) = \Im_n\left[q_j(t_{i+1}), \dot{q}_j(t_{i+1/2})\right]$ is used instead of the unknown value $\Im_n(t_{i+1})$.

2.4.2 Comparison with a classical approach

Several computational approaches to the simulation of bowed musical instruments have been developed by other authors. Bowed string research, for example, has led to some of the most important developments on simulation methods, which are today recognized as trustworthy (Woodhouse & Galluzzo, 2004). Therefore, in order to establish consistent comparisons between the present approach and an already established and thoroughly published simulation method, the digital waveguide model for bowed strings motion developed by McIntyre & Woodhouse (1979) was chosen.

In this method, considering a point bow model, two dynamical quantities are required in the digital waveguide model: the velocity $v_c(t)$ of the string at the bowing point, and the friction force $F(t)$ at the same point. The calculation of these quantities is performed by two equations: one relating $F(t)$ and $v_c(t)$ by a chosen friction law and the other emerging from the dynamical response of the string when excited by a given force $F(t)$. This last relation is usually referred as the “Friedlander construction” (Friedlander, 1953).

One of the most important features of the Friedlander scheme is that the calculation of the string velocity $v_c(t)$ is dependent on the friction force $F(t)$, the velocity time-history $v_h(t)$ stemming from reflected waves, and on the string’s wave impedance Z, as in equation (2.15)

$$v_c(t) = \frac{F(t)}{2Z} + v_h(t) \tag{2.15}$$

Equation (2.15) is a direct consequence of decomposing the string (velocity) impulse response $g(t)$ in two terms:

$$g(t) = \frac{1}{2Z}\delta(t) + g_h(t) \tag{2.16}$$

where the Dirac term applies at $t = 0$ and (as would happen in an infinite string) is independent of the pulse-reflections at the boundary conditions, while the second term $g_h(t)$ is solely the result of the reflected waves. To allow for physically sound computations the calculation of the friction force should account not only for the term $g_h(t)$ in the string dynamics but also on the term which embeds the string's wave impedance. In the present approach, in contrast to most researchers, the dynamics of the string is not treated through a (modified) convolutional approach, but using instead a modal formulation. In the now-classic convolution approach developed by McIntyre, Schumacher and Woodhouse, the decomposition (2.16) of the string impulse response is useful, because it allows a very fast computation of the string response: in order to obtain $v_c(t)$, the slow convolution using the "full" impulse response $g(t)$ is replaced by the bow load term $\frac{F(t)}{2Z}$ plus a second term stemming solely from the reflected waves, $g_h(t)$, which can be computed fast by formulating the reflected waves in terms of "short-lived" reflexion functions at the string ends. Such decomposition leads naturally to the Friedlander construct for the string dynamical equilibrium.

However, it is important to notice that even if the decomposition (2.15) and (2.16) are useful in the framework of the above-mentioned approach, they are certainly not the only possible way to solve the problem. In the modal approach such decomposition is not needed nor used. Working with the string modal basis, which is equivalent to the "full" impulse response $g(t)$, the full velocity $v_c(t)$ at the bow location is obtained from the dynamical time-step integration, and not only the reflections-generated term $v_h(t)$. Therefore, the wave impedance of the string is encapsulated in the modal basis, in the same way that it is encapsulated in the "full" impulse response $g(t)$.

This is clearly shown in Figure 2.3, below, where the initial 0.05 s of the string velocity impulse response at the bow location ($x_{bow}/L = 0.09$) is plotted, obtained from the summation of 100 modal contributions ($f_n = 196\,n$ Hz , modal damping $\zeta_n = 0.001, \forall n$). It is clear that all the pulses contained in $g(t)$ – including the initial Dirac term – are rightly displayed (apart from the unavoidable Gibbs phenomenon and the filtering effect of modal truncation). Therefore all the terms in equation (2.16) are reflected in the modal basis used by these computations, as should be.

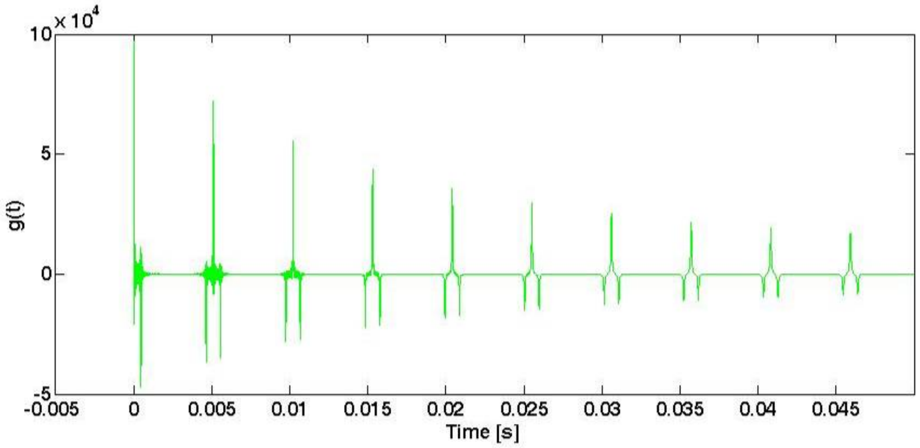

Figure 2.3 – Impulse response $g(t)$ obtained by modal summation

For the needs of the demonstrative computations presented in the following, Figure 2.4 shows the impulse response pertaining to the delayed reflections, $g_h(t)$. This was obtained from $g(t)$, by replacing the first spike by zeros.

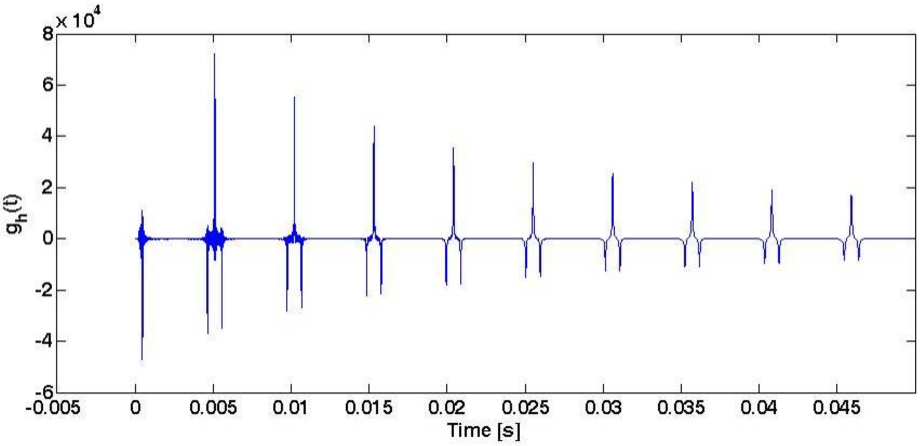

Figure 2.4 – Impulse response $g_h(t)$ pertaining to the delayed reflections

In order to illustrate the validity of the preceding arguments a few demonstrative computations are described in the following chapters, using three computational approaches:

a) The modal method, using the friction model and a time-step integration of the modal equations, as explained in the preceding sections of this thesis.

b) An equivalent method, but with the string response computed from the convolution

$$v_c(t) = \int_0^t F(\tau) g(t-\tau) d\tau \tag{2.17}$$

and the friction force also computed using the friction model presented in section 2.3.1.

c) Another convolution approach, basically analogous to the classic McIntyre, Schumacher and Woodhouse method, except that $v_h(t)$ is computed from the "long" convolution,

$$v_h(t) = \int_0^t F(\tau) g_h(t-\tau) d\tau \tag{2.18}$$

instead of their rapid scheme using reflexion functions. For the computation of the friction force, Friedlander's construct has been implemented

$$\begin{cases} \text{Sticking}: \quad v_c(t) = v_{bow} \quad ; \quad F(t) = 2Z\left(v_{bow} - v_h(t)\right) \\ \text{Sliding}: \quad v_c(t) \ \text{ such that } \ 2Z\left(v_c(t) - v_h(t)\right) = \mathrm{F}_{\mathrm{NL}}\left[v_{bow} - v_c(t)\right] \end{cases} \tag{2.19}$$

The computational approach (b) serves here as a convenient "bridge" between method (a) and the classic convolution approach (c). For this method, the "long" convolution is computed using $g_h(t)$ (instead of using reflexion functions) to maintain compatibility of model (c) with the modal parameters used in computation (a) and with the corresponding impulse response $g(t)$ used in (b). Indeed, understanding and not computation time is the issue here. Note that, concerning the previous nonlinear computations, (a) and (b) are explicit methods, meaning that the friction force at time t_{i+1} is computed based on the string response (at location x_{bow}) at the previous time-step, e.g. $y_c(t_i)$ and $v_c(t_i)$. On the contrary, for computations (c) a fully implicit scheme has been implemented, such that the second equation (2.19) is solved in an iterative manner. The physical parameters used here for a simple point model are those of the system studied in the paper, including the exponential sliding friction curve. Finally, for all simulations, and independently of the fact that it is needed or not, the reflections-generated response $v_h(t)$ is also computed from the convolution:

$$v_h(t) = \int_0^t F(\tau) g_h(t-\tau) d\tau \tag{2.20}$$

Figure 2.5 shows the initial transient of the string, acted by the bow at normal force $F_{bow} = 1\ \mathrm{N}$ and tangential velocity $v_{bow} = 0.15\ \mathrm{m/s}$, computed using approach (a).

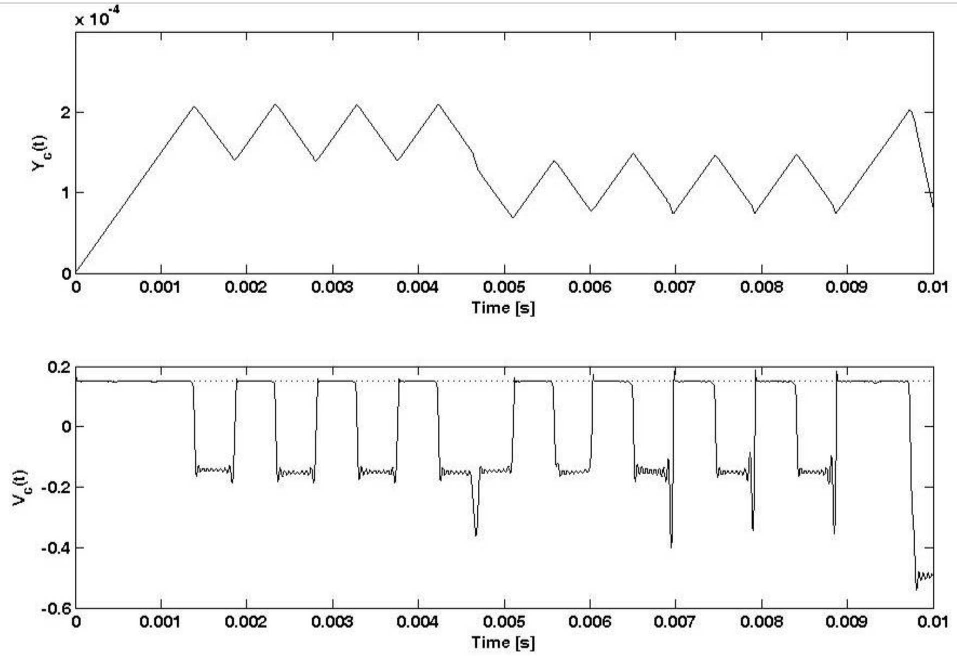

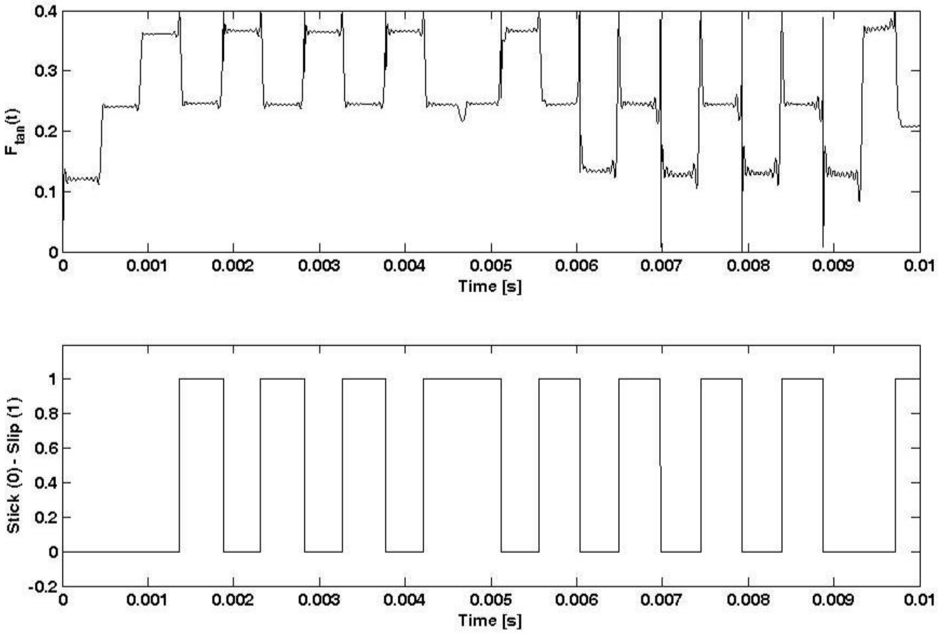

Figure 2.5 – Starting transient computed according to model (a).

The plots show the string displacement $y_c(t)$ and velocity $v_c(t)$, at the bowing location, the friction force, as well as a logical indicator of the friction state (stick/slip). One may notice at the start that the string sticks to the bow, while secondary waves (between the bridge and the bow) can be seen in the friction force plot. For a large enough amplitude, the friction force reaches the limit value $\mu_S F_N$ and a complex sequence of sliding/sticking states follows.

Figure 2.6 shows the same computation, but using now approach (b) – the time-step integration of the modal equations was replaced by convolution (2.17). It is clear from the results that the two approaches are equivalent.

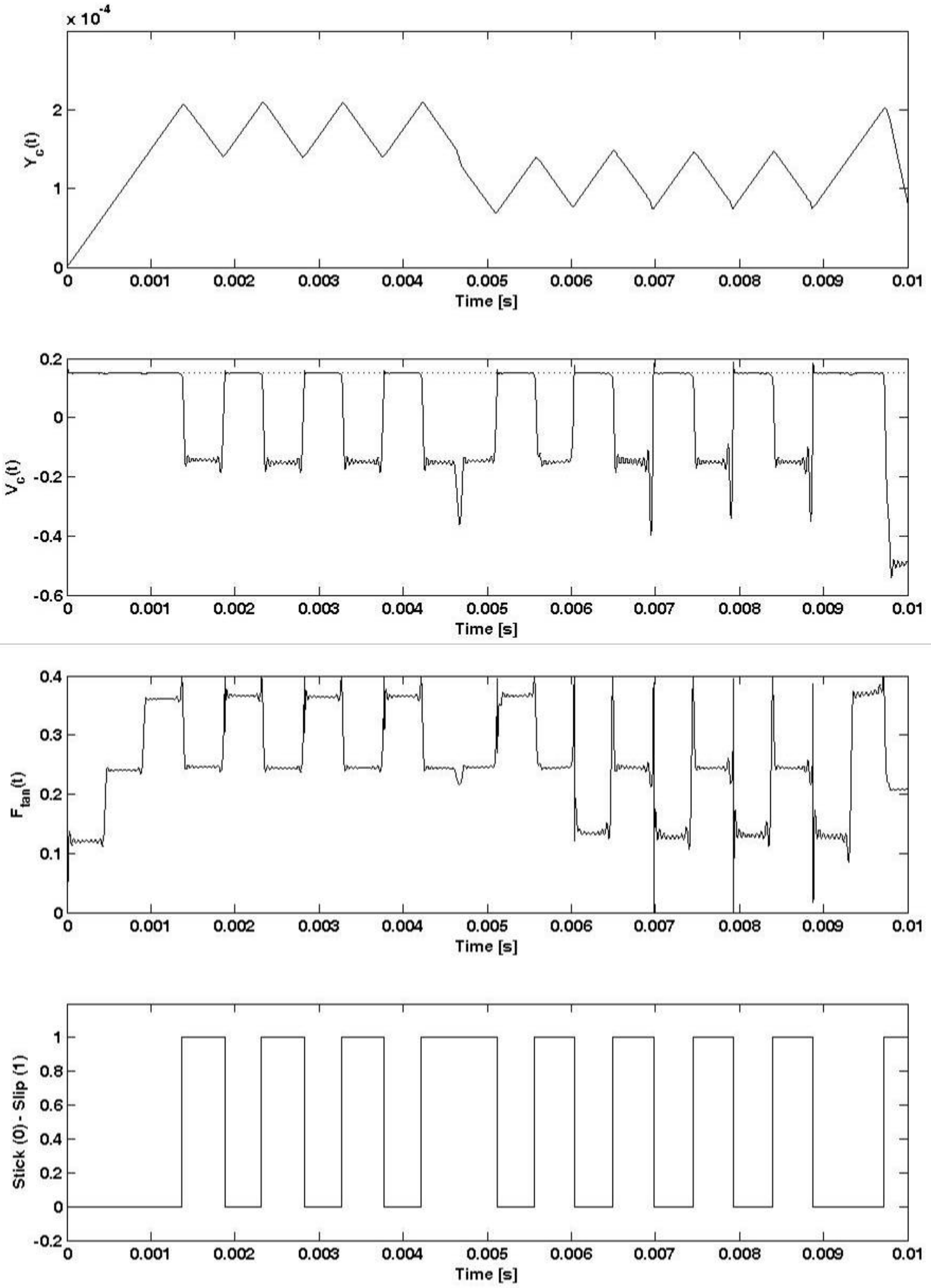

Figure 2.6 – Starting transient computed according to model (b).

Figure 2.7 shows $v_c(t)$ as well as the reflection-generated velocity component $v_h(t)$, which was computed from equation (2.20), using the friction force $F(t)$ generated in the computation (b), Figure 2.6.

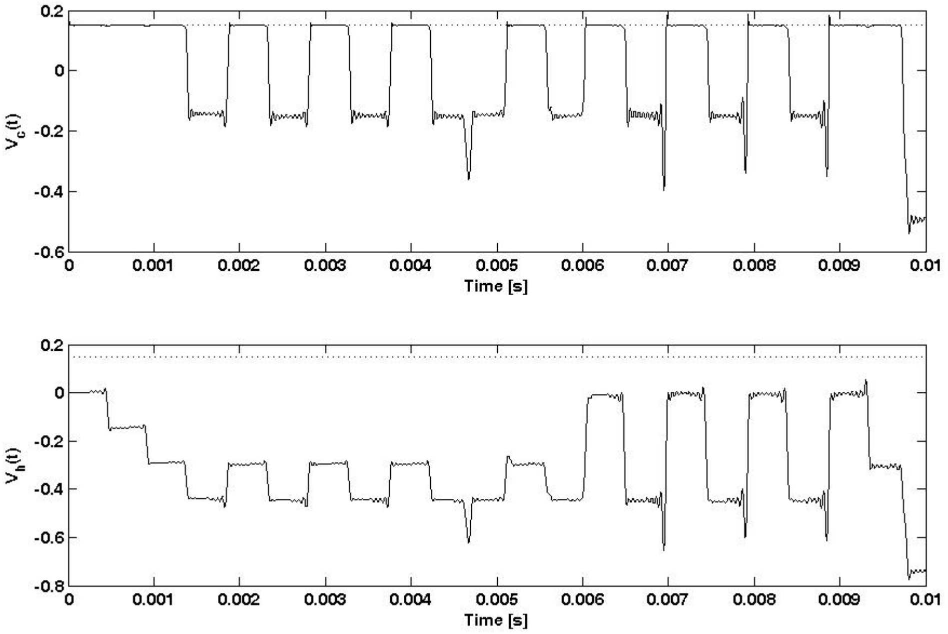

Figure 2.7 – Total velocity $v_c(t)$ and the reflection-connected component $v_h(t)$ generated from computation (b).

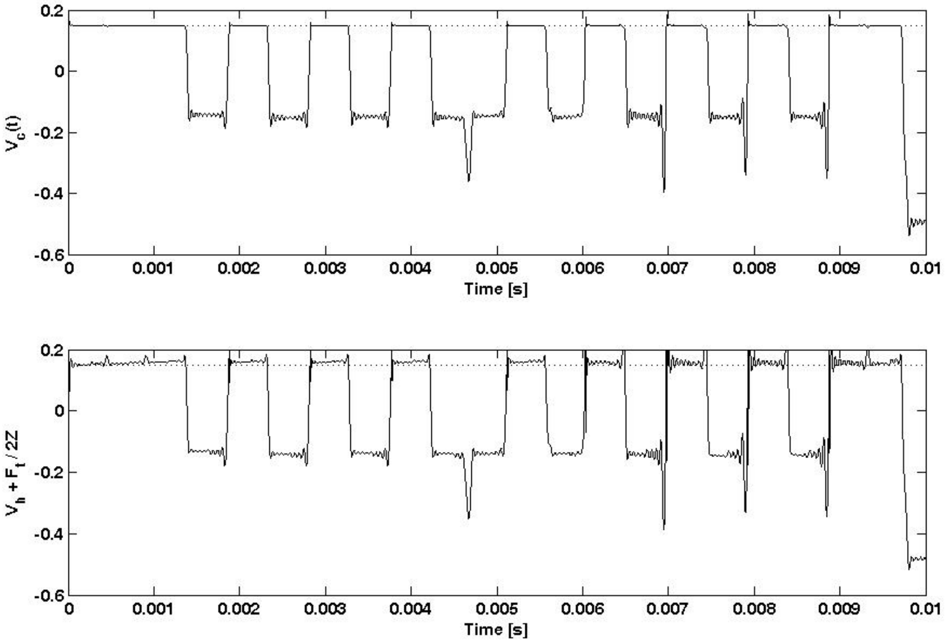

Figure 2.8 – Total velocity $v_c(t)$ and the quantity $\frac{F(t)}{2Z} + v_h(t)$ generated from computation (b).

Notice that $v_h(t)$ is quite different from $v_c(t)$. In particular, as it should, $v_h(t) = 0$ at the very beginning of the motion, until the first reflection arrives to the bowing point. On the other hand, during all the sticking motion-start, $v_c(t) \cong v_{bow}$, while $v_h(t)$ reflects the "coming and going" of the reflected waves between the bridge and the bow. The main point is highlighted in Figure 2.8: when comparing the computed velocity $v_c(t)$ with the quantity $\frac{F(t)}{2Z}+v_h(t)$, these two quantities well fulfil equation (2.15) – which was never used for performing this nonlinear simulation.

One may notice, however, that the two plots shown in Figure 2.8 are not absolutely identical, but present some minute differences, which are mostly due to the fact that in equation (2.15) the impedance Z of the string is used, without any correction to account for the compliance of the bow-hairs. Indeed, because in computations (a) and (b) a bowing model with a finite impedance Z_b is used, equation (2.15) is not strictly applicable. No effort was made, however, to produce a correction for the bow compliance in these demonstrative computations.

It is interesting to compare the previous computations (a) and (b) with the corresponding results from method (c), where the Friedlander construct is implemented as explained before. Results are shown in Figure 2.9, and their similarity with those presented in Figure 2.5 and Figure 2.6 pertaining to the present computational model, is unmistakable. Again, some differences can be pointed, essentially because computation (c) is related to a bow with infinite impedance, while (a) and (b) present a more "flexible" behaviour at the contact point due to the bow compliance implemented in the present contact model. Accounting for the fact that, strictly speaking, the system in computation (c) is not exactly the same as the one in computations (a) and (b), a comparison between all these results is quite satisfying. As a last illustration, Figure 2.10 shows the string displacement at the contact point, for the three computational models, when the transient computation is extended for 0.1 second. Again the results (a) and (b) present slight differences when compared with those of the classical approach (c), which reflect the bow-hair compliance effect, as discussed before.

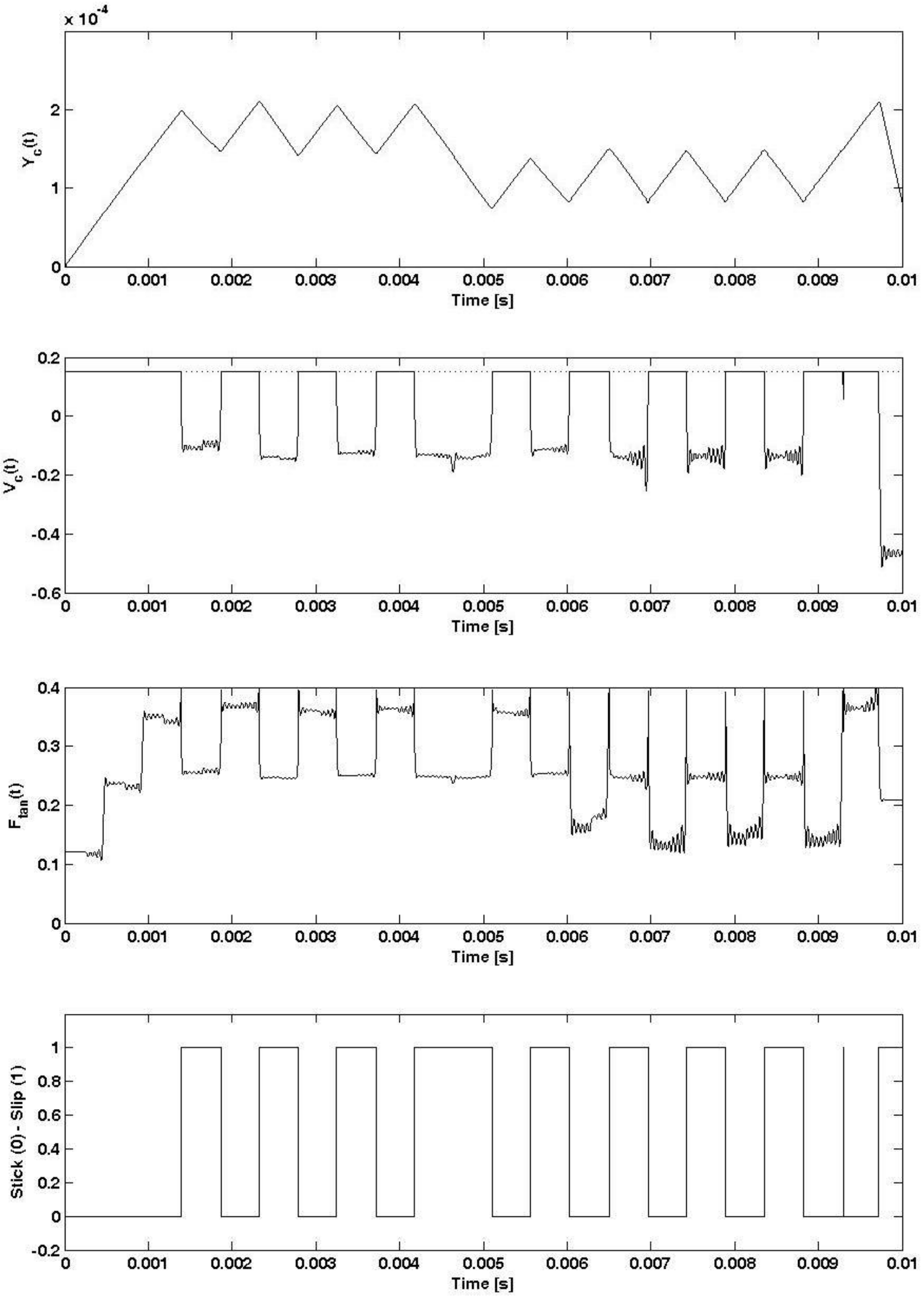

Figure 2.9 – Starting transient computed according to model (c).

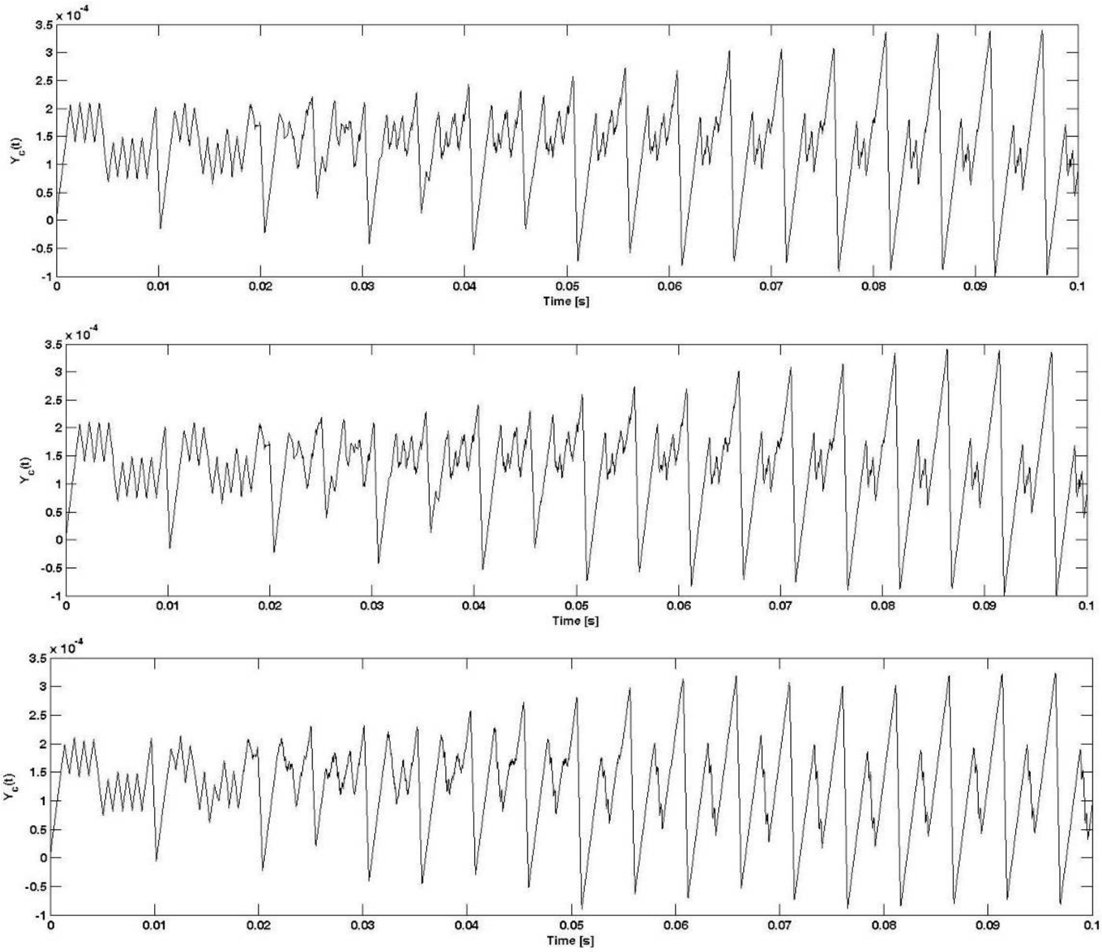

Figure 2.10 – Transient computed for 0.1 s according to models (a), (b) and (c).

2.5. *Advantages and disadvantages of the method*

The computation method presented in this thesis has clear advantages and disadvantages when compared with others already referred, such as the digital waveguide model or other time-domain methods.

The modal approach is able of very detailed simulations, leading to very realistic space-domain and time-domain dynamics. On the other hand, contrasting the efficient approach of McIntyre *et al* (1983), the modal method is well suited to deal with systems presenting both harmonic (e.g., with modal frequencies such as $f_n = m\,f_1$ with m integer) and non-harmonic modal relationships.

Although this method implies a linear formulation, it allows the inclusion of nonlinear interaction forces without disrupting the physical principles that sustain it.

At the present time, with the high-level non-compiled MATLAB implementation used, this computational method is unable to perform real-time simulations, which is a definite advantage of the classic approach developed by McIntyre *et al* (1983), who cleverly exploits the non-dispersive nature of string and acoustic waves arising in most musical instruments. Real-time implementation was never an objective of this thesis, so no effort whatsoever was input in such direction. However, this modal approach allows the introduction of several components of the instrument, without any important additional of “code building” effort. This possibility of component addition is one of the major advantages of the method. As long as the interconnections are physically sound it is possible to introduce several features of the musical instrument to be simulated. For example, in the case of the bowed string, the presence of a moving finger performing glissandos along the arm of a cello is easy to simulate because the respective interaction force is projected on the string unconstrained modal basis at the finger position for each time-step. Moreover, including the effect of a “compliant” component, such as the body of the instrument, with its own possibly rich modal basis, is possible as will be demonstrated in this thesis. Obviously, as the number of components of the instrument grow, so will the size of the problem to be solved which will inevitably decrease the computation times. However, this increase of computation time will also increase for other methods for the same problem complexity, which do not share the ease of introduction of these components.

A note on numerical stability is need at this stage when referring to the construction of a virtual instrument with its several components. Apart from the ease of introduction of these instrument parts, the modal method preserves very high numerical stability of the coupled system, in contrast with other methods. The finite difference scheme, for example, does not insure that stable isolated components computations will perform numerically sound once coupled (Bilbao, 2007).

This possibility of composing an instrument with its several features allows also the computation of energy flow between the various components. Although this aspect will not be treated in this thesis, several computations performed along the research carried showed that this has an advantage, not only to better understand the behaviour of the instrument, but also to check numerical stability. Even if the system is nonconservative it is possible to check whether energy was dissipated by any component or by any numerical problem.

One of the aspects that can lead to a time-consuming model construction is the definition of the modal basis. If for simple systems such as the string, this modal basis can be easily calculated, for more complex systems a careful modal identification or a “heavy” eigenvalue problem solution is needed, in order to obtain realistic results. However, the modal description allows for a non-local method of solving the governing partial differential equations of the system, in contrast with the local description (grid-point) of the explicit finite difference methods, digital waveguide and lumped network models.

Apart from the definition of the modal basis, which can be more or less easy to obtain, the modal truncation order is a very important aspect. Any continuous system presents an infinite number of theoretical modes (degrees-of-freedom). The choice of the number of modes to be used in computations has to be based on the knowledge of the real system, and the larger the number of modes, the longer will the computation perform and heavier will be the amount of information processed. This is also a problem for other methods, such as the finite difference methods where the spatial discretization of the system must be high enough to allow an accurate computation of the detailed dynamics. In practice, all modes significantly excited through the nonlinear excitation mechanisms must be included in the computational modal basis. This should be asserted by analysing the convergence of results for incresisng number of modes, as well as by confrontation with experiments.

Another clear advantage of this method, by contrast with the finite difference method for example, is the preservation of the frequency relations between modal frequencies, along the calculation, independently of the number of modes used. This aspect is one of the main problems with finite-difference methods where numerical dispersion can easily occur. Although this can be controlled to a certain extent by the degree of discretization of the system, this will always have as a consequence a higher computation effort.

Chapter 3

BOWED STRINGS

3. BOWED STRINGS

3.1. Introduction

Raman’s seminal paper (Raman, 1918) was a landmark study of the dynamics of bowed strings. Since then, a plethora of research papers has been published on bowed-string instruments, including enlightening work by Friedlander (1953), Schelleng (1973), McIntyre, Schumacher and Woodhouse (1983), to name just a few – see Cremer’s book (Cremer, 1984) – for an extensive account of the field.

In this Chapter, a detailed description of the implementation of the modal simulation method is given, with application to bowed string motion.

3.1.1 Bow Width

Although computationally more expensive – for ideal non-dispersive systems – than the now classical and widely used approach developed by McIntyre & Woodhouse (1979) and McIntyre *et al* (1983), this method finds its most usefulness as more complex physical features are incorporated in the numerical simulations – such as frequency-dependent or space-dependent system parameters, coupling of the transverse and torsion string motions (Inácio *et al*, 2001, Antunes *et al*, 2001; Inácio *et al*, 2002a), dispersive effects connected to bending stiffness in non-ideal inharmonic strings (or even beams or shells) – Inácio *et al*, 2003a, 2003b; Inácio *et al*, 2004a, 2004b –, as well as the complex coupling of strings and the instrument body, through the moving bridge (Inácio *et al*, 2004c, 2004d; Inácio *et al*, 2005).

Unlike other computational techniques, the effectiveness of the modal method is not affected by dispersive effects in the system dynamical equations. Furthermore, the computational strategy and workload of the modal approach are practically not affected as one considers further intricacies in the bow/string interaction model. Such is not the case for the wave-propagation (coupled with reflection functions) simulation method (McIntyre & Woodhouse, 1979; McIntyre *et al*, 1983) which, although extremely efficient when addressing basic configurations (e.g. ideal strings under point-excitations), is hardly amenable to deal directly with significant dispersive phenomena and/or distributed loading – hence the need to couple it with a much “slower” finite-difference scheme in Pitteroff & Woodhouse (1998a, 1998b, 1998c), in order to accommodate the space-distributed bow/string interaction.

The work presented in this chapter evolved from preliminary results presented in Inácio *et al* (2002b). Here, finite-width bows are simulated by a set of evenly-distributed contact points (which define a given bow-width, l_b), instead of a single bow/string contact point. The frictional forces resulting from the multiple bow/string interaction points are simultaneously projected on the string modes, and the modal differential equations are solved using an explicit time-step integration algorithm. This simple approach proved effective and convergence results, shown in section 3.3.3.1, suggest that modelling using one contact point per millimetre of contact width is adequate to enable realistic simulations.

As a first approximation, the bow-hair is modelled here in a quasi-static manner, such that only the axial flexibility and damping of the contacting hairs are accounted for. As in Pitteroff & Woodhouse (1998a, 1998b, 1998c), inertial effects in the hair ribbon have been neglected. However, a true dynamical model of the bow, such that the hair ribbon is modelled by a number of its axial (and other) modes, should present no difficulties whatsoever.

Also, although debatable, it was decided not to incorporate, in the simulations related to the bow width, phenomena such as the string inharmonicity and torsion modes. Finally, in spite of the considerable interest and promising results of recent and more advanced physically-based friction models (thermally-controlled, elasto-plastic) – Smith & Woodhouse (2000), Woodhouse (2003), Galluzzo & Woodhouse (2003), Serafin *et al* (2003) –, it was chosen to use in the present computations a conventional velocity-dependent Coulomb friction model. Indeed, the on-going research on the tribology of rosin interfaces is far from resolved, and – recalling the words of J. Woodhouse (*in* Woodhouse & Galluzzo, 2004) – “recent results have shown that none of the friction models used in the existing literature is entirely credible”. Therefore, the conventional approach is still justified in the context of this work, enabling an easier assessment of the present results with respect to others on both point-bowing and finite-width bowing, which were also obtained using simple velocity-dependent friction laws.

Finally, it is postulated here that the normal bow/string interaction force and transverse velocity can be externally controlled, independently of the string vibratory responses, which are only computed along the transverse direction. Extension of this computational model to deal with two-dimensional motions, incorporating the string modes along the normal direction as well as the bow-hair dynamics, presents no difficulties in principle and will be also addressed elsewhere.

In this section, other dynamical regimes beyond the classic Helmholtz motion are analysed. Many researchers in this field associate musically interesting tone with this regime only. For instance, a recent communication (Serafin & Young, 2003) states that "In the case of the bowed string, *good tone* refers to the Helmholtz motion", a view which echoes the feeling of most researchers in the field. However, inspiring violin playing often makes a significant use of higher-order (multiple slides-per-cycle) regimes to capture different musical atmospheres – for example the strings are played *sul ponticello* in almost every musical work. Therefore the effects of finite-width bowing are explored on various dynamical regimes which arise in the range of playing parameters explored.

In many cases, a qualitative comparison with the results obtained by Pitterof & Woodhouse (1998a, 1998b, 1998c) is possible. However, when attempting quantitative comparisons, one should bear in mind that a violin G string (196 Hz) is used, using comparatively low friction bow/string interaction forces ($\mu_S = 0.4$, $\mu_D = 0.2$), while those authors simulated an A string (440 Hz) subjected to higher frictional forces ($\mu_S = 0.8$, $\mu_D = 0.3$). Also as pointed, in contrast to Pitterof & Woodhouse (1998a, 1998b, 1998c), the present computations pertain to an ideal string with torsion motions neglected. Finally, note that adherence parameters are assumed here independent of the contact bow width (in order to focus on the effect of l_b) while in Pitterof & Woodhouse (1998a, 1998b, 1998c) they are taken proportional to l_b.

Finite-width bowing simulations are compared to those of a point-excited string, and the main features stemming from the multiple contact points are highlighted. The results obtained are presented in the form of parameter-space maps which show the influence of bowing parameters – such as the applied normal force F_N, bow velocity $\dot{y}_{bow}$, bowing bridge-distance x_c, and bow-width l_b – on the self-excited vibratory regimes, as well as their corresponding steady amplitudes. In agreement with previous authors (McIntyre *et al*, 1981; 1982; (Pitterof & Woodhouse, 1998a; 1998b; 1998c) the finite-width model reveals the existence of backward and forward "partial" differential slips of individual hairs, occurring between the main slip phases of the Helmholtz (or other more complex) motions, which lead to an increase of broadband high-frequency content in the spectrum of the string/bridge interaction force. The range of input parameters explored also allowed observation of the flattening effect, which was found in the point-model as well as in the finite-width cases, although in a lesser degree for finite-width bowing.

3.1.2 String/Body Coupling

A crude approach to incorporate body effects, when simulating string sounds, is to start by computing the vibratory response of an "isolated" (bowed or plucked) string, and then use the resulting string/bridge interaction force to drive a given body vibro-acoustic transfer function. However this simple approach is quite limited and cannot account for any energy feedback from the body into the string – such as is found in wolf notes – because the full string/body coupling is not modelled.

Apparently only a few authors have attempted to address this string/body coupling problem. McIntyre (1983) incorporated in their wave-propagation computational algorithm a bridge-reflection function which encapsulates the dynamical behaviour of a given body resonance, enabling them to simulate the coupled dynamics between the string and the chosen body resonance. Similarly, Puaud *et al* (1991) used (in connection with a so-called "numerical bow") a mass-stiffness bridge-resonator, therefore also emulating a chosen body-resonance coupled to the string dynamics. Recently, a different approach has been pursued by several authors to simulate instrument bodies and cavities – see Huang *et al* (2000), for instance – by using 2D or 3D waveguides to compute simplified multi-degree-of-freedom resonating systems. However, until now, this modelling technique has only been used to simulate the body-filtering effects on string/bridge dynamical forces, with no feedback coupling. In relation to other stringed instruments, Derveaux *et al* (2003) achieved fully coupled string/soundboard computations for a modelled guitar.

The aim of the present work is to simulate the interaction between strings and real-life instrument bodies, where the present computational method is extended to incorporate the multi-modal dynamics of a violin and cello body, fully coupled to the string motions. A hybrid approach is taken, in the sense that a theoretical model of the string is coupled with dynamical body data, obtained either from simplified models or real-life experiments.

The string is modelled using its unconstrained modes assuming, pinned-pinned boundary conditions at the tailpiece and the nut. Then, at the bridge location, the string/body coupling is enforced using the body impulse-response or modal data (as measured at the bridge). At each time step, the system motion is computed by integrating the string modal equations, excited by the modally-projected values of the frictional bow force and also of the string/bridge contact force. The latter is obtained from the body motion at each time-step, as computed either (a) using the body impulse-response, or (b) from a modal model of the body. In the first method, the body dynamics are obtained through incremental convolution, a costly procedure which however enables the direct simulation of real bodies without any further modelling assumptions or simplifications. The second method allows for faster computations, but demands a computed or identified modal model of the instrument body.

It should be mentioned here that the modal basis unconstrained at the bridge location (coupling point) is not the only option available to solve this problem. Indeed the interested reader may refer to the recent work by Woodhouse (2004), who deals with body-string coupling in guitars by modelling the string as pinned-pinned at the nut and the bridge, and then complements such basis with a so-called “constraint mode” which can be shown to be the static response of the string when the bridge extremity is moved (Craig, 1981). Similar issues arise when dealing with sub-structure synthesis where the analyst may choose between several families of the basis functions used to represent each substructure – refer, for instance to Meirovich (1997). The merits of the various approaches will be reflected on the number of basis terms used to achieve convergence, however, a comparison of these different methods is a matter for future work.

After a few demonstrative experiments and a detailed presentation, the computational approach is illustrated for both violin and cello typical self-excited string motion regimes. These are compared for “isolated” strings and for the string/body coupled model, based here on synthetic body dynamical data. In particular, interesting simulations pertaining to the so-called wolf notes are presented.

3.2. *Computational Model*

3.2.1 Formulation of the string dynamics

Consider a string of length L with linear density μ and bending stiffness EI, subject to a axial tension T and an external force distribution $F(x,t)$. If a dissipation parameter η is assumed, the small-amplitude transverse motions $y(x,t)$ are described by a fourth order differential equation:

$$\mu\frac{\partial^2 y}{\partial t^2}-T\frac{\partial^2 y}{\partial x^2}+\eta\frac{\partial y}{\partial t}+\frac{\partial^2}{\partial x^2}\left(EI\frac{\partial^2 y}{\partial x^2}\right)=F(x,t) \qquad (3.1)$$

However, the interaction between the bow and the string also generates torsional motion (Cremer, 1984). The bow induces a moment distribution $M(x,t)$ on the string, whose small-amplitude angular displacement $\theta(x,t)$ can be described by:

$$J\rho\frac{\partial^2\theta}{\partial t^2}-JG\frac{\partial^2\theta}{\partial x^2}+\nu\frac{\partial\theta}{\partial t}=M(x,t) \qquad (3.2)$$

where G is the shear modulus of the string, ρ is its mass density and J the polar moment of inertia. A dissipation parameter ν is also included to allow for damping of the string’s torsional motion. The transverse and torsional wave speeds are respectively given by:

$$c_{trans}=\sqrt{\frac{T}{\mu}} \qquad (3.3)$$

$$c_{tor}=\sqrt{\frac{G}{\rho}} \qquad (3.4)$$

Consider point C in Figure 3.1 as the contact point between the bow and the string when the bow is at rest. Once some velocity, V_{bow}, is applied by the player, the string describes a transverse motion, y_c between point C and C' (equal to $\overline{OO'}$), and a torsional motion θ_c, between point C' and point C''. The total displacement of point C is the sum of the transversal displacement, y_c, with the cord $C'C''$. As the same motion occurs for all the points of the surface of the string at the cross-section of contact with the bow, the tangential motion of the string's surface, $y_{tan}(t)$, can be described by:

$$y_{tan}(t) = y^O_{tran}(t) + R\theta(t) \tag{3.5}$$

where $y^O_{tran}(t)$ is the transverse displacement of the centre of the string and R its radius. The previous equation describes the coupling between transverse and torsional motion of the string.

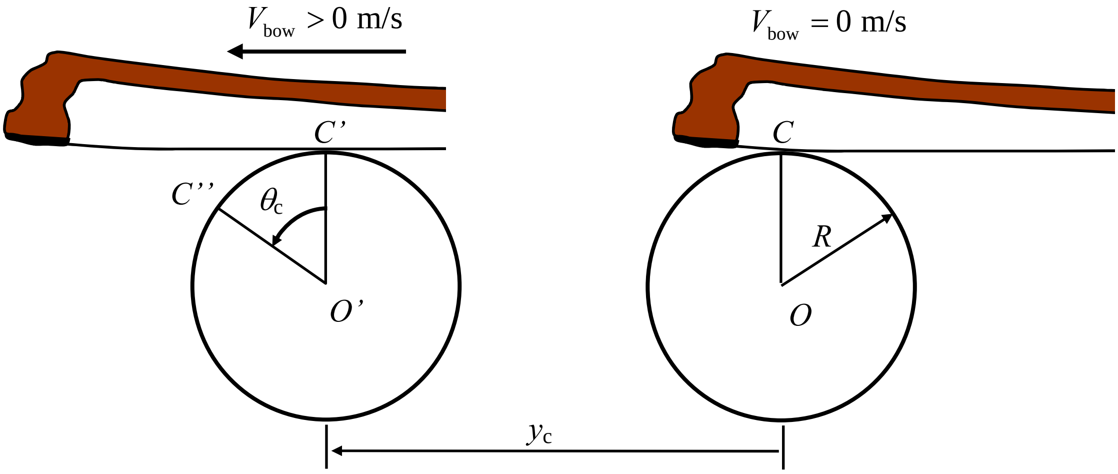

Figure 3.1 – Geometric scheme of the translational and rotational motion of the bowed string

Any solution of (3.1) can be formulated in terms of the string's transverse modal parameters m_n, ω_n, ζ_n and modeshapes $\varphi_n(x)$, $n = 1, 2, \cdots, N$. The order N of modal truncation is problem dependent and must be asserted by physical reasoning, supported by the convergence of computational results. The forced transverse response of a damped string can then be formulated as:

$$[M]\{\ddot{Q}(t)\} + [C]\{\dot{Q}(t)\} + [K]\{Q(t)\} = \{\Xi(t)\} \tag{3.6}$$

where: $[M] = \text{Diag}(m_1, \cdots, m_N)$, $[C] = \text{Diag}(2m_1\omega_1\zeta_1, \cdots, 2m_N\omega_N\zeta_N)$,

$[K] = \text{Diag}(m_1\omega_1^2, \cdots, m_N\omega_N^2)$

$\{Q(t)\} = \langle q_1(t), \cdots, q_N(t)\rangle^T$, $\{\Xi(t)\} = \langle \Im_1(t), \cdots, \Im_N(t)\rangle^T$.

The modal damping values ζ_n are usually identified from experiments; however, they may eventually be theoretically estimated (see Fletcher & Rossing, 1998). The modal forces $\Im_n(t)$ are obtained by projecting the external force field on the modal basis:

$$\Im_n(t) = \int_0^L F(x,t)\, \varphi_n(x)\, dx \qquad (3.7)$$

In a similar way, the torsional motions described by equation (4.1) can have a modal formulation.

$$[I]\left\{\ddot{Q}_{Tor}(t)\right\} + [C_{Tor}]\left\{\dot{Q}_{Tor}(t)\right\} + [K_{Tor}]\left\{Q_{Tor}(t)\right\} = \left\{\Psi(t)\right\} \qquad (3.8)$$

where: $[I] = \mathrm{Diag}(I_1, \cdots, I_N)$, $[C_{Tor}] = \mathrm{Diag}(2I_1\varpi_1\xi_N, \cdots, 2I_N\varpi_N\xi_N)$,

$[K_{Tor}] = \mathrm{Diag}(I_1\varpi_1^2, \cdots, I_N\varpi_N^2)$; $\left\{Q_{Tor}(t)\right\} = \left\langle q_1^{Tor}(t), \cdots, q_N^{Tor}(t)\right\rangle^T$,

$\left\{\Psi(t)\right\} = \left\langle \Upsilon_1(t), \cdots, \Upsilon_N(t)\right\rangle^T$.

where I_N are the modal moments of inertia, and ϖ_N and ξ_N are the angular natural frequencies and modal damping for torsional motion, respectively.

Torsional vibrations in strings are usually quite difficult to measure. The scarce available data indicates that the ratio of torsional to transverse wave speeds lies in a range from 2.6 to 7.6 depending on the material and construction of the string and damping values ξ_n that vary from 1% to 7.7% (Gillan & Elliot, 1989). The modal moments $\Upsilon_n(t)$ are obtained by projecting the external force field on the modal basis:

$$\Upsilon_n(t) = \int_0^L M(x,t)\ \varphi_n^{Tor}(x)\ dx \qquad (3.9)$$

where $M(x,t) = F(x,t)\cdot R$.

The modal shapes φ_n and φ_m^{Tor} are calculated by solving the homogeneous form of the second order undamped transverse and torsional wave equations:

$$\mu\frac{\partial^2 y}{\partial t^2} = T\frac{\partial^2 y}{\partial x^2} \qquad \text{and} \qquad J\rho\frac{\partial^2\theta}{\partial t^2} = JG\frac{\partial^2\theta}{\partial x^2} \qquad (3.10)$$

The physical motions can then be computed from the modal amplitudes $q_n(t)$ and $q_n^{Tor}(t)$ by superposition:

$$y_{Tan}(x,t) = \sum_{n=1}^{N} \varphi_n(x)\, q_n(t) + R \sum_{m=1}^{M} \varphi_m^{Tor}(x)\, q_m^{Tor}(t) \tag{3.11}$$

and similarly concerning the velocities and accelerations. For given external excitation and initial conditions, the previous system of equations can be integrated using an adequate time-step integration algorithm. Explicit integration methods are well suited for the friction model developed here. In this implementation, a simple Verlet integration algorithm is used (Beeman, 1976), which is a second-order explicit scheme. Note that, although (3.6)–(3.9) obviously pertain to a linear formulation, nothing prevent us from including in $\Im_n(t)$ and $\Upsilon_n(t)$ all nonlinear effects arising in the system. Accordingly, the system modes become coupled by the nonlinear effects.

Considering rigid terminations at the nut and tailpiece extremities of the string, the external force field $F(x,t)$ is due to three applied forces (see Figure 3.2):

- The excitation friction force $F_{s,a}(x_c,t)$ due to the friction-induced transverse excitation provided by the moving bow hairs;
- The interaction force $F_b(x_b,t)$ between the body and the string at the bridge;
- The possible presence of a finger on the fingerboard, applying a force $F_f(x_f,t)$.

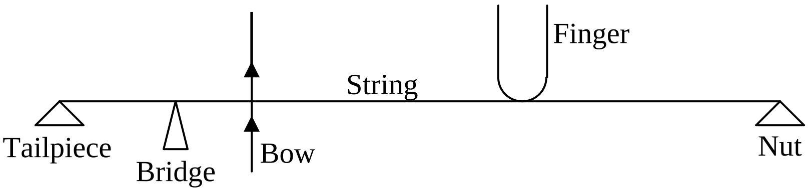

Figure 3.2 – Idealized model of the bowed string

In this model, the finite width of the bow is simulated by considering a given number, *b*, of contact points between the string and the bow, distributed along a width l_b on the string length L', measured between the nut and the bridge. Each contact point is located at a distance x_C^h from the bridge, as shown in Figure 3.3.

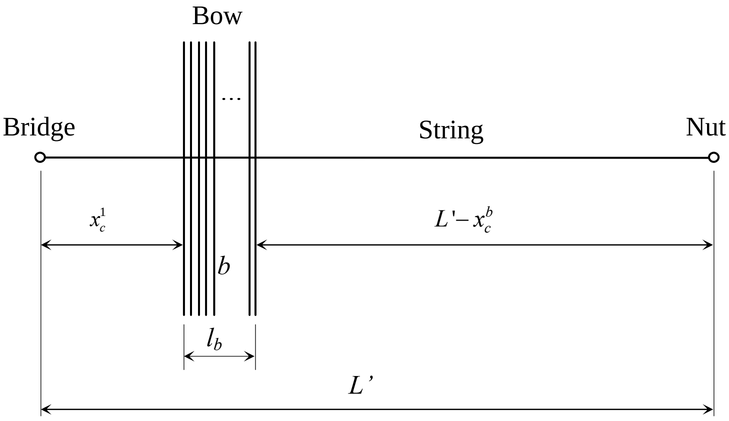

Figure 3.3 – Configuration of the bow/string interaction

In the next sections, a description of the models of the previously mentioned excitation forces are given.

3.2.2 Friction Model

As seen in the introductory chapter, friction related phenomena have been subject of a considerable amount of research, and several models have emerged to address a number of related problems. Due to the complexity of the interaction between contacting surfaces and of the associated high nonlinearity, most models are of an empirical nature. A survey of the experimental and analytical knowledge in this field can be found in Rabinowicz, 1965; Kragelsky *et al*, 1982; Oden & Martins, 1985; Haessig & Friedland, 1985; Karnopp, 1983; Leine *et al*, 1998.

In this chapter, adherence is modelled using the concept of spring/damping attachment point, while sliding is modelled by fitting an empirical formulation to experimental published data (Lazarus, 1972), as described in section 2.3.2. The implementation of the friction model is described once again in this chapter since it includes specific additional details of the application to the bowed string, namely related to the width of the bow.

The friction force arising between the string and one individual bow contact point *h* at location x_C^h of the string is given by equation (3.12), where F_s^h and F_a^h pertain to the friction force during sliding and adherence, stemming from the Coulomb model, respectively:

$$\begin{cases} F_s^h(x_c^h,t) = -\mu_d(\dot{y}_c^h)\dfrac{F_N}{b}\operatorname{sgn}(\dot{y}_c^h)\ ;\ \text{if}\ \left|\dot{y}_c^h\right| > 0 \\ \left|F_a^h(x_c^h,t)\right| < \mu_S\dfrac{F_N}{b}\ ;\ \text{if}\ \left|\dot{y}_c^h\right| = 0 \end{cases} \tag{3.12}$$

where F_N is the normal force between the bow and the string, μ_S is a "static" friction coefficient (used during surface adherence), $\mu_d(\dot{y}_c^h)$ is a "dynamic" friction coefficient (used for sliding regimes) and b is the number of bow hairs used in the model. Here, the relative transverse velocity between the bow and the string is given by:

$$\dot{y}_c^h(x_c^h,t) = \dot{y}(x_c^h,t) - \dot{y}_{bow}(t) = \sum_{n=1}^{N}\varphi_n(x_c^h)\dot{q}_n(t) - \dot{y}_{bow}(t) \tag{3.13}$$

In this work it is assumed that $\mu_d(\dot{y}_c)$ is a function of the relative bow/string velocity, and use the following model:

$$\mu_d(\dot{y}_c^h) = \mu_D + (\mu_S - \mu_D)e^{(-C\left|\dot{y}_c^h\right|)} \tag{3.14}$$

where, $0 \le \mu_D \le \mu_S$ is an asymptotic lower limit of the friction coefficient when $\left|\dot{y}_c^h\right| \to \infty$, and parameter C controls the decay rate of the friction coefficient with the relative bow/string sliding velocity. The friction model (3.14) can be readily fitted to typical experimental data, by adjusting the empirical constants μ_S, μ_D and C (see Figure 3.4).

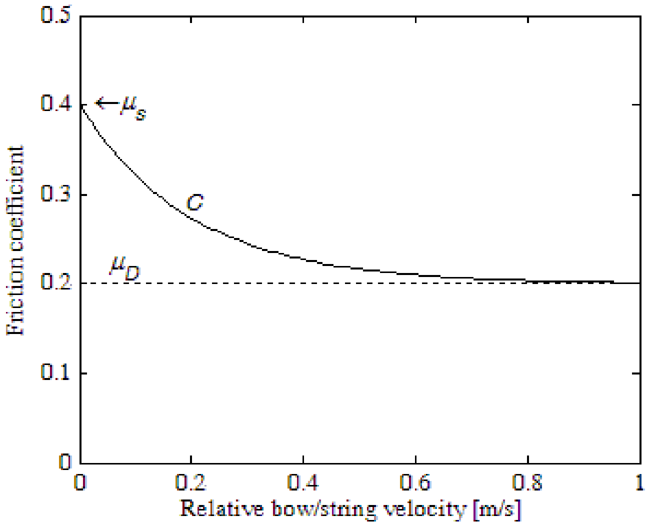

Figure 3.4 – Change of the friction coefficient with the bow/string relative velocity

The sliding behaviour, described by the first equation (3.12), does not cause problems for simulations, as this equation explicitly shows how the sliding force should be computed as a function of the sliding velocity. However, during adherence, simulation becomes more difficult. Indeed, the second equation (3.12) merely states a limiting value for the friction force, during adherence, and gives no hint on how $F_a^h(\dot{y}_c^h, t)$ may be actually computed. This is because the adherence force depends on the overall balance of all internal and external forces acting upon the system, which are quite complex for multi-degree of freedom problems. Most friction algorithms deal with this problem through implicit numerical schemes. In the present approach, the following explicit procedure is used at each time-step i, for each bow hair, h:

(1) If in the previous time-step the system was sliding, detecting of a possible bow-hair/string adherence is made, by computing $J_i^h = \dot{y}_c^h(t_i)\dot{y}_c^h(t_{i-1})$. Then, if $J_i^h > 0$, the system is still sliding in the same direction. $F_s^h(\dot{y}_c^h, t_i)$ is computed according to the first equation (3.12), with $\dot{y}_c^h(t_i)$ given by equation (3.13) and $\mu_d(t_i)$ by equation (3.14);

(2) However, if $J_i^h \leq 0$, then a reversal of the relative motion is occurring and adherence will arise. Then, the sticking force is computed using the following model:

$$F_a^h(x_c^h, t_i) = -K_a\, y_c^h(x_c^h, t_i) - C_a\, \dot{y}_c^h(x_c^h, t_i) \qquad (3.15)$$

which will be used during the complete duration of the adherence state. The idea in equation (3.15) is to "attach" the string to the bow at point x_c using a suitable "adherence stiffness" and to damp-out any residual bow/string relative motion during sticking using an "adherence damping" term in equation (3.15). y_c is the relative displacement between the string and the bow hair, at any time during adherence, given as:

$$y_c^h(x_c^h,t) = y(x_c^h,t) - y_{bow}^a(t) = \sum_{n=1}^{N} \varphi_n(x_c^h) q_n(t) - y_{bow}^a(x_c^h,t) \qquad (3.16)$$

where $y_{bow}^a(x_c^h,t)$ is the current position of the bow contact point. For a given constant bow speed, this changes as $y_{bow}^a(x_c^h,t) = [t - t_a(x_c^h)]\,\dot{y}_{bow}$, where $t_a(x_c^h)$ is the time value when adherence was detected for the contact point modelled at location x_c^h.

As stated before, in this work the axial vibration modes of the bow hairs are not taken into account and, as a first approximation, each bow hair is modelled as a spring-dashpot attachment on each side of the contact point between the string and the bow hair. The adherence stiffness K_a in equation (3.15) is computed as described in the following paragraphs. Consider an axial stiffness coefficient $\bar{K}_a$ of a single bow hair given by:

The adherence stiffness K_a in equation (3.15) is computed from:

$$\bar{K}_a = \bar{K}_{a1} + \bar{K}_{a2} \qquad (3.17)$$

where $\bar{K}_{a1}$ and $\bar{K}_{a2}$ are related to the axial stiffness of the bow hair on each side of the contact point. Although the real axial stiffness will change as the contact point moves along the bow, $\bar{K}_{a1}$ and $\bar{K}_{a2}$ are here assumed to be equal and given by:

$$\bar{K}_{a1} = \bar{K}_{a2} = \frac{EA}{H/2} \qquad (3.18)$$

where E is the Young Modulus, A the cross section of one individual bow hair and H the total length of the bow hair. The adherence stiffness of each contact point is given by

$$K_a = \bar{K}_a \, {}^{a}\!/\!{}_{b} \tag{3.19}$$

where a is the number of bow hairs assumed in contact with the string, and b is the number of pseudo bow hairs (contact points) used in the numerical model. Similarly, $C_a = \bar{C}_a \, {}^{a}\!/\!{}_{b}$, where $\bar{C}_a$ is the adherence damping of a single bow hair.

(3) After computing the adherence force, $F_a^h(x_c^h, t_i)$ is compared with the maximum allowable value $\mu_S F_N / b$. If $\left|F_a^h\right| \le \mu_S F_N / b$, the current estimate is accepted and simulation continues assuming a sticking state. On the contrary, when $\left|F_a^h\right| > \mu_S F_N / b$, sliding will arise and the friction force is recomputed according to the first equation (3.12). Then, the procedure continues with the next time-step. By virtue of (3.13) and (3.16), all the string modes become coupled when the nonlinear friction force is projected on the modal basis, equations (3.7) and (3.9), and then incorporated in equations (3.6) and (3.8).

3.2.3 Formulation of the Body Dynamics

As previously explained, the present method can be implemented to simulate the influence of the string/body coupling using two different procedures: incremental convolution of a measured impulse response or through a modal model of the body dynamics.

3.2.3.1 Incremental Convolution Formulation

At the bridge, the string motion forces the violin body into vibration. The response of the body can be computed, at each time step i, by the incremental convolution of the time-history of the interaction force between the bridge and the string $F_b(x_b, t)$ and the body impulse response function $h_b(t)$ at the same point x_b, according to equation (3.20).

$$y_b(x_b, t) = \int_0^t F_b(x_b, \tau) h_b(t - \tau) d\tau \tag{3.20}$$

where $y_b(x_b, t)$ is the displacement of the bridge at the contact point with the string, while $h_b(t)$ is the displacement/force impulse response functions of the instrument body, measured at the bridge, along the horizontal direction (see Figure 3.5).

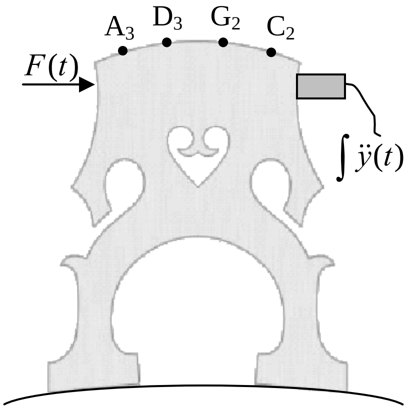

Figure 3.5 –Setup used for the transfer function measurements

3.2.3.2 Modal Formulation

As for the string, it is assumed that in the instrument body damping is proportional and hence body modes are also real. This assumption is debatable, as discussed in (Woodhouse, 2004), but will be adopted here to avoid the additional burden of using a complex modal basis. Notice, however, that if the direct convolution formulation **(3.20)** is used, the possible complexity of body modes is already embedded in the body impulse response $h_b(t)$ and introduces no further difficulty. The response of the body of the instrument can be represented by a simplified modal model:

$$\left[M_B\right]\left\{\ddot{Q}_B(t)\right\}+\left[C_B\right]\left\{\dot{Q}_B(t)\right\}+\left[K_B\right]\left\{Q_B(t)\right\}=\left\{\Xi_B(t)\right\} \tag{3.21}$$

where $\left[M_B\right]=\mathrm{diag}(m_1^B,\cdots,m_P^B)$, $\left[\,C_B\,\right]=\mathrm{diag}(2\,m_1^B\omega_1^B\,\zeta_1^B,\cdots,2\,m_P^B\omega_P^B\,\zeta_P^B)$, $\left[\,K_B\,\right]=\mathrm{diag}\left(m_1^B(\omega_1^B)^2,\cdots,m_P(\omega_P^B)^2\right)$, are the matrices of the body modal parameters, $\left\{Q_B(t)\right\}=\left\langle q_1^B(t),\cdots,q_P^B(t)\right\rangle^T$ and $\left\{\Xi_B(t)\right\}=\left\langle \Im_1^B(t),\cdots,\Im_P^B(t)\right\rangle^T$ are the vectors of modal responses and generalized forces, respectively. The modal forces $\Im_p^B(t)$ are obtained by projecting the string/body coupling force $F_b(x_b,t)$ (see section 3.2.4), on the body modal basis. The modal parameters are identified from a single transfer function measurement ($H_b(\omega)=\mathscr{F}\left[h_b(t)\right]$) at the bridge. This fact leads to a requirement that the modal mass matrix should be normalised by postulating that all modeshapes $\varphi_p^B(x_b)$ are unitary at the bridge location. The physical motions at the bridge are then computed from the modal amplitudes $q_p^B(t)$ by superposition:

$$y_b(x_b,t) = \sum_{p=1}^{P} q_p^B(t)\,; \tag{3.22}$$

3.2.3.3 Discussion of the Body Dynamics Formulation Methods

Both methods described before have advantages and disadvantages from the computational point of view. The incremental convolution method allows the use of measured impulse response functions of real-life instruments, without any other assumptions other than linearity, nor does it require the use of any modal identification procedure. It allows the most accurate representation of the body dynamics, but has the great disadvantage of requiring long computation times due to the direct convolution formulation (3.20). On the other hand, the modal approach of the body allows for much lower computation times (at least by one order of magnitude), but requires a careful modal identification to be performed. Furthermore, the modal representation is less than ideal to cope with the body dynamics at higher-frequency modal densities because of the large number of modes that would be required. Computation times are proportional to the number of modes used in the model. In contrast, the incremental convolution procedure's computation time does not depend on the modal order but only on the duration of the impulse response function. Finally, it should be emphasised that although not discussed in this thesis, vertical motion of the string and bridge can be easily implemented with this computational method.

3.2.4 Formulation of the String/Body Coupling

The coupling between the string and the body of the violin arises from the bridge/string contact force $F_b(x_b,t)$ which is used in equations (3.6), (3.20) and (3.21). This interaction is modelled by connecting the string to the bridge through a very stiff spring and a dashpot to prevent parasitic oscillations:

$$F_b(x_b,t) = K_{bs}\left[y_b(x_b,t) - y_s(x_b,t)\right] + C_{bs}\left[\dot{y}_b(x_b,t) - \dot{y}_s(x_b,t)\right] \tag{3.23}$$

where K_{bs} is the stiffness coupling coefficient between the bridge and the string, C_{bs} is the damping coupling coefficient between the bridge and the string and $y_s(x_b,t)$ and $y_s(x_b,t)$ are the displacement and velocity of the string at the bridge, respectively.

3.3. Numerical Results

3.3.1 Influence of the string inharmonicity

Wave propagation in non-ideal (rigid) strings is dispersive. This effect is most easily simulated using a modal model, as the bending stiffness effect is automatically incorporated in the string modes, with modified frequencies $\omega_n = n\omega_1\left(1+\beta n^2\right)^{1/2}$, for $n \geq 2$, where β is an inharmonicity coefficient (Cremer, 1984). Computations show that an increase in the string bending stiffness leads to progressive “rounding” of the Helmholtz corner and, in general, to a deterioration of the response spectrum, as illustrated in Figure 3.6. The results are compatible with previous investigations (see, Cremer, 1984; Pitteroff & Woodhouse, 1998; Serafin *et al*, 1999).

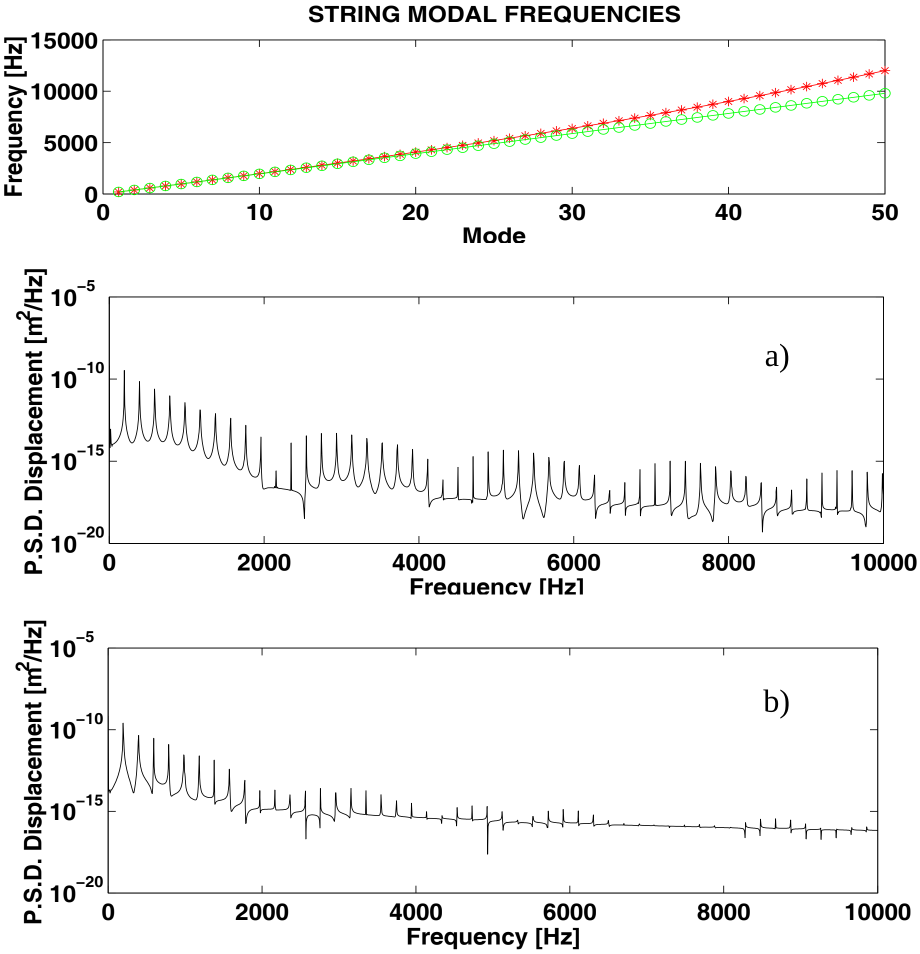

Fig **ım;**

I)

3.3.2 Influence of the string torsion

Transverse and torsion modes are heavily coupled by the friction forces. Beyond the additional damping, inclusion of the string torsion modes can affect both the transient durations and the steady state regimes, depending on the ratio of propagation wave-speeds $\alpha = c_{tor} / c_{tran}$. Indeed, opposing a conclusion from the analysis in (Serafin *et al*, 1999), the systematic simulations presented suggest that torsion should not be neglected if α < 4 gut strings should then be particularly prone to torsion effects. Figure 3.7 to Figure 3.10 show the influence of the inclusion of the torsion coupling in various aspects of the string's motion.

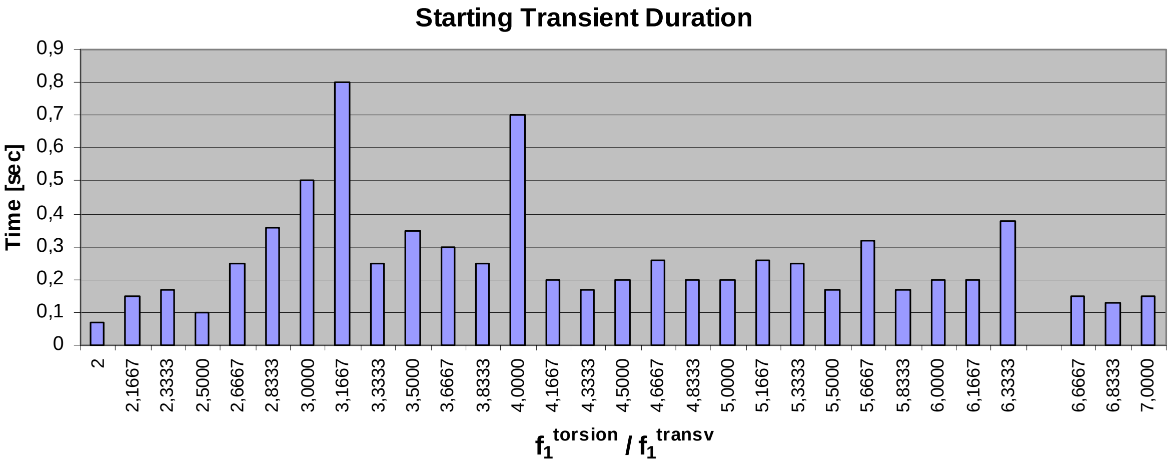

Figure 3.7 – Starting transient duration for a violin G string as a function of the ratio of torsional to transverse wave speeds (x_c = 30 mm, F_N = 1N, $\dot{y}_{bow}$ = 0.1 m/s)

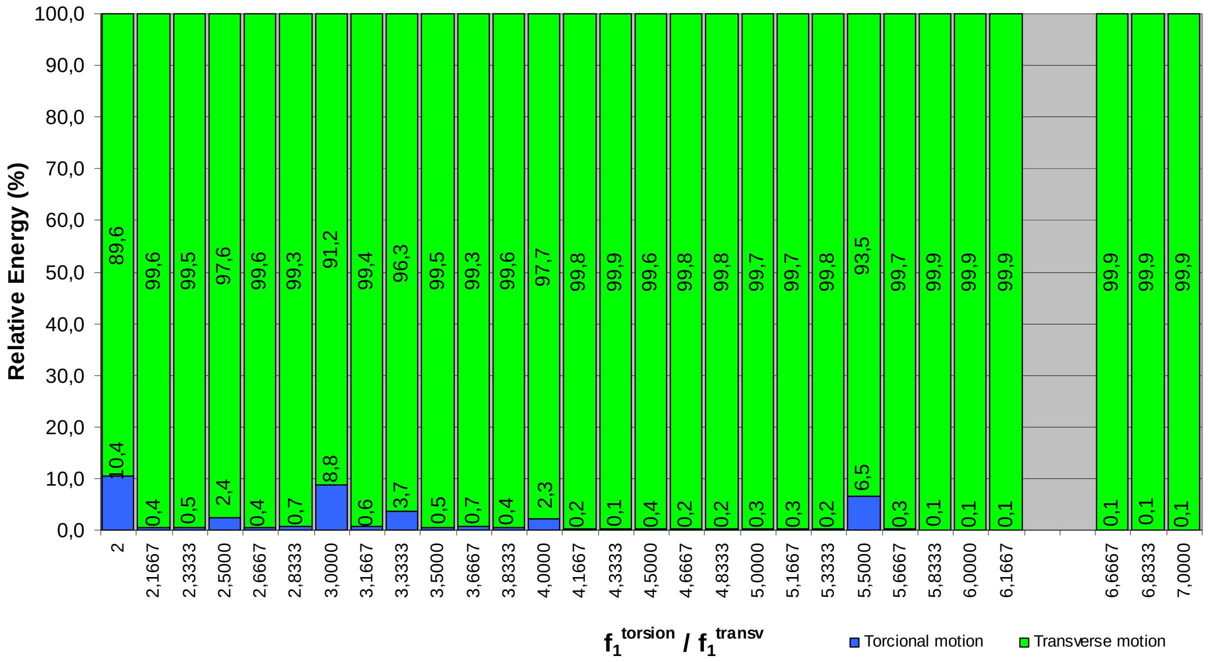

Figure 3.8 – Distribution of the total mechanical energy between torsional and transverse motion as a function of the ratio of torsional to transverse wave speeds (x_c = 30 mm, F_N = 1N, $\dot{y}_{bow}$ = 0.1 m/s)

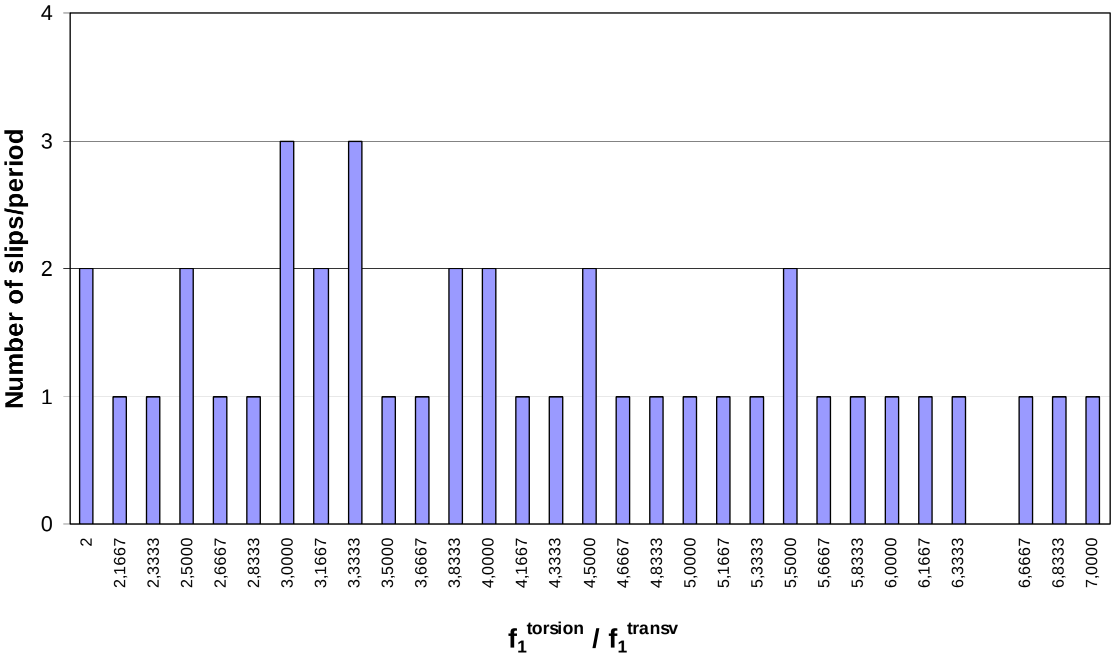

Figure 3.9 – Number of main slips per period as a function of the ratio of torsional to transverse wave speeds (x_c = 30 mm, F_N = 1N, $\dot{y}_{bow}$ = 0.1 m/s)

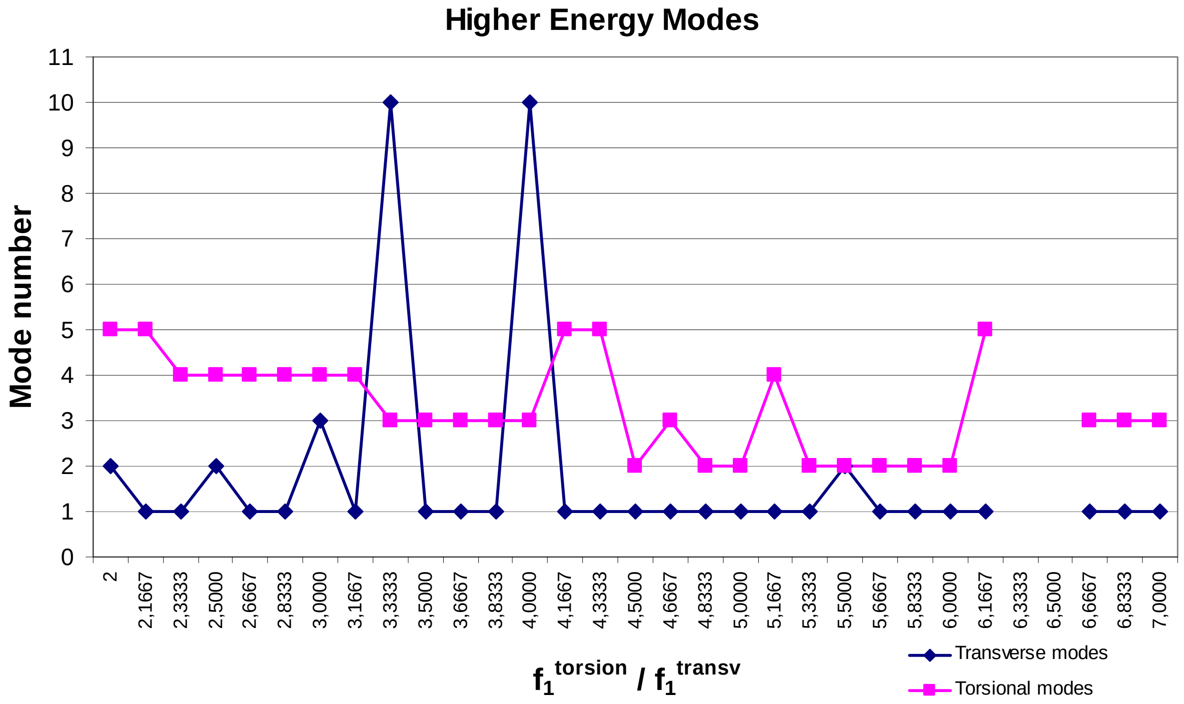

Figure 3.10 – Number of the mode with highest energy as a function of the ratio of torsional to transverse wave speeds (x_c = 30 mm, F_N = 1N, $\dot{y}_{bow}$ = 0.1 m/s)

3.3.3 Influence of the bow width

In the following simulations, a G-string was implemented with a fundamental frequency of 196 Hz, length L = 0.33 m and linear density of $\sigma = 3.1\times10^{-3}$ kg/m. In order to achieve adequate computational convergence 50 modes were used – enough to emulate the relevant phenomena excited by the bow string interaction; a modal damping value of 0.1% was used for all modes (however, frequency-dependent damping could be easily introduced using this computational method).

Concerning the friction model, the scarce experimental data available (Schumacher, 1994; Askenfelt, 1989) led to a sliding law such as the one represented in Figure 3.4, using μ_S = 0.4, μ_D = 0.2 and C = 5. For the adherence model a total value of $K_a\ b = 10^5$ N/m has been used, following calculations from equations **(3.17)** to **(3.19)** considering a = 50 hairs, $A = 3.8\text{x}10^{-8}$ m^2, $E = 8.5\text{x}10^9$ Pa and H = 65 cm which agree with the values measured by Pitteroff and Woodhouse (1998a). Similarly, the adherence damping value $\bar{C}_a$ of a single bow hair used is 0.2 Ns/m, in accordance with their measurements. In order to focus on the sole effects of changing the bow width l_b, it was decided to use here the same global adherence coefficients $K_a\ b$ and $C_a\ b$, irrespectively of the number of contact points b used in the numerical model to simulate the bow width.

A large range of excitation parameters was explored: F_N = 0.1~10 N and $\dot{y}_{bow}$ = 0.01~1 m/s. In most calculations the middle point of the contact line was located at a distance of 30 mm from the bridge; however results when bowing at 10 mm are also reported.

3.3.3.1 Influence of the number of bow pseudo-hairs

Figure 3.11 shows the reaction forces at the bridge obtained by bowing with a normal force of 1 N and a bow velocity of 0.1 m/s, for a different number of pseudo bow hairs (contact points b = 1, 2, 10, 20 and 50), the bow width being 10 mm for all cases. The point-bow model (b = 1) reaction force represented in the first graph clearly shows the well-known Shelleng's ripples caused by well-defined secondary waves that travel back and forth between the bow and the bridge during the sticking part of the fundamental period.

However, as a finite-width of the bow is introduced, a clear difference is seen in the reaction force curve. The ripple's staircase pattern is attenuated giving rise to a lower amplitude higher frequency ripple, which lacks the regularity of the point-model response. These effects are more pronounced as the number of contact pseudo hairs increases. However, increasing this number beyond 10 does not alter the reaction force curve significantly, which lead us to the conclusion that a minimum number of one pseudo hair (contact point) per millimetre of bow width is necessary to perform a realistic analysis of the influence of the finite width of the bow.

The differences in the reaction forces shown in Figure 3.12 are due to the phenomenon known as *partial slipping* well explained by McIntyre *et al* (1981), by which some of the bow hairs slip while other continue to stick to the string during the adherence phase of the Helmholtz motion. Each partial slip generates a new wave in the string that propagates between the bridge and the nut. The attenuation of the Shelleng's ripples is due to interference between these multiple waves.

3.3.3.2 Influence of the width of the bow

The influence of the finite width of the bow on the sound produced by violin synthesis algorithms can be seen in Figure 3.12. The spectrum of the bridge reaction force (which ultimately drives the body of the instrument) for the same conditions as in Figure 3.11 shows the emergence of high-frequency broadband noise, compared to the one generated by the ideal point-bow model (b=1). This difference can be heard in the sounds generated by these simulations. Additionally, as the number of hairs is increased, the amplitude differences between the harmonics generated are less pronounced, something that can also be seen in the results published by Schoonderwaldt *et al* (2003). This effect is particularly evident in the vicinity of the string partials which have nodal points at the bowing location, disappearing for bows with more than 5 bow hairs.

The effect of changing the bow width (while maintaining constant the number of bow hairs per millimeter width) is depicted in Figure 3.13 and Figure 3.14. The increase in broadband energy content above 2000 Hz is also present. For small bow widths this energy increment is present mainly in the vicinity of the string partials having nodal points at the bowing location.

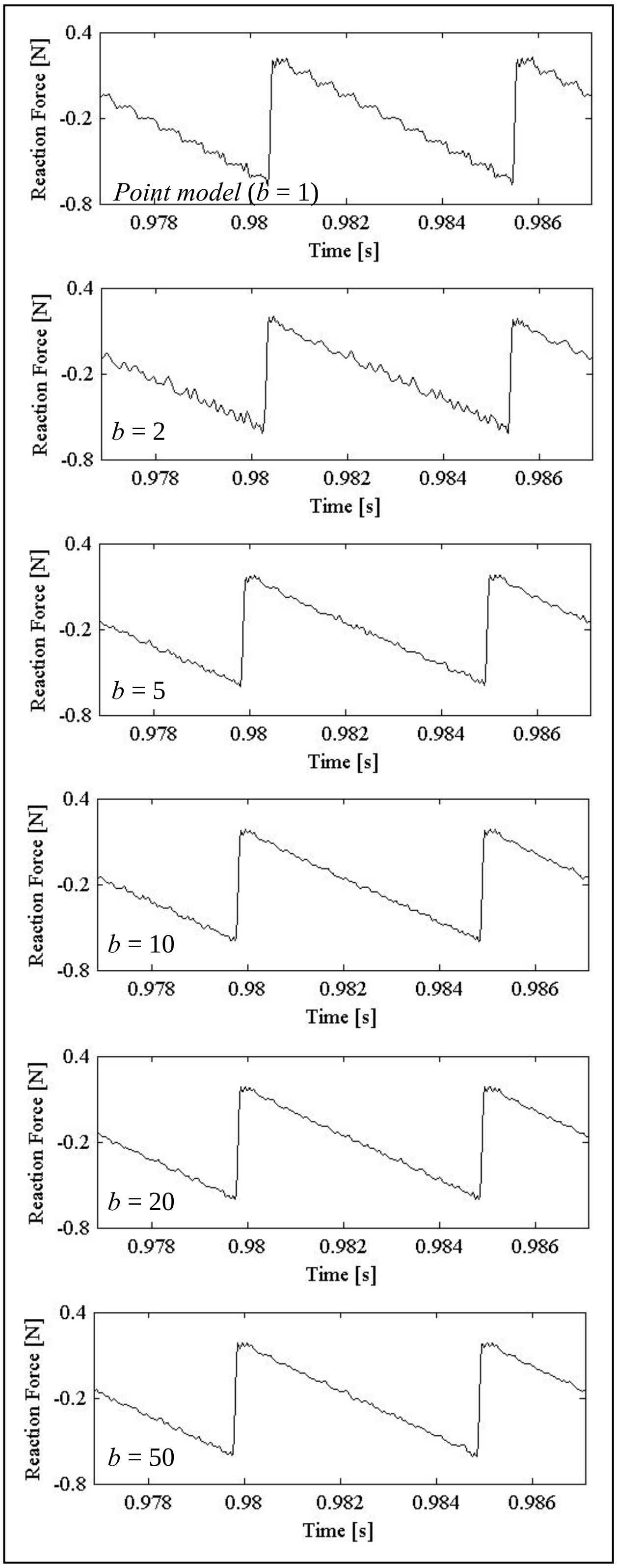

Figure 3.11 - Reaction force at the bridge for a point model and five bows with 10 mm width and different number of bow contact points *b* for $F_N = 1\,\mathrm{N}$**,** $\dot{y}_{bow} = 0.1\,\mathrm{m/s}$**.**

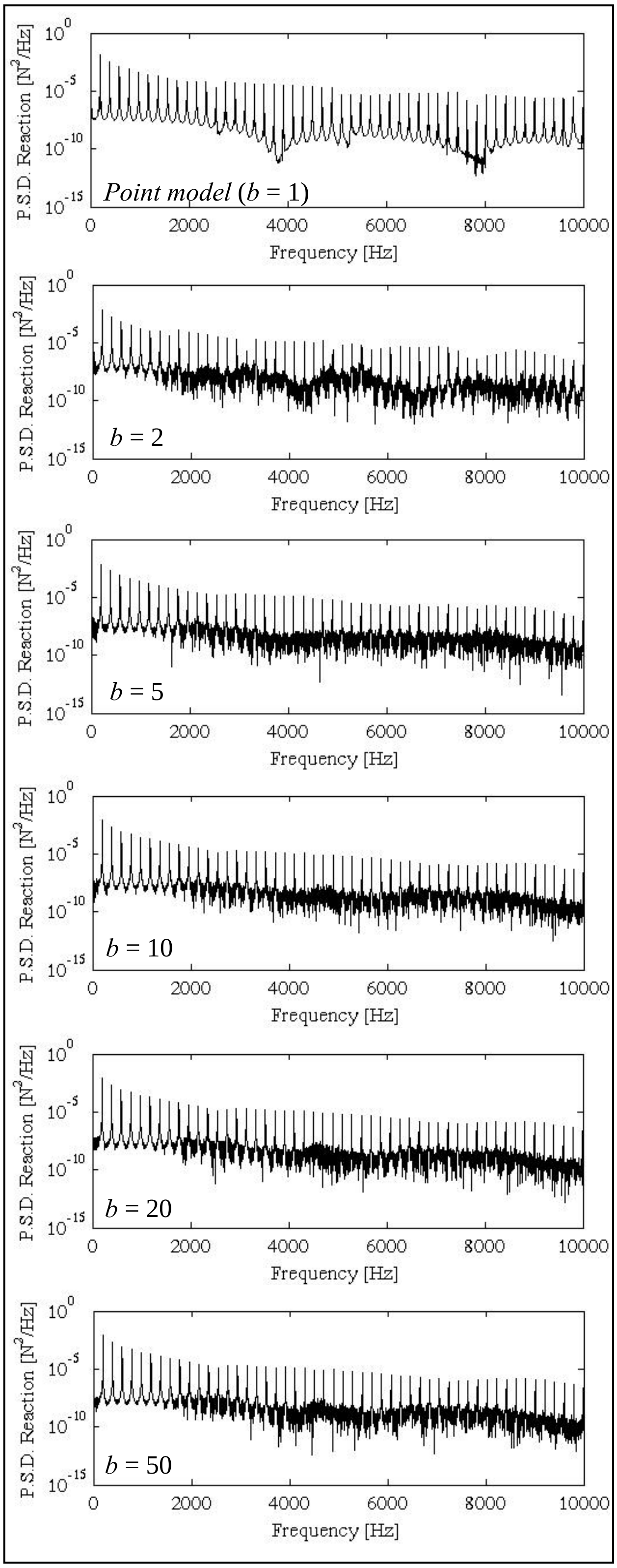

Figure 3.12 - Power spectral density of the reaction force at the bridge for a point model and five bows with 10 mm width and different number of bow contact points *b* for $F_N = 1\,\mathrm{N}$**,** $\dot{y}_{bow} = 0.1\,\mathrm{m/s}$**.**

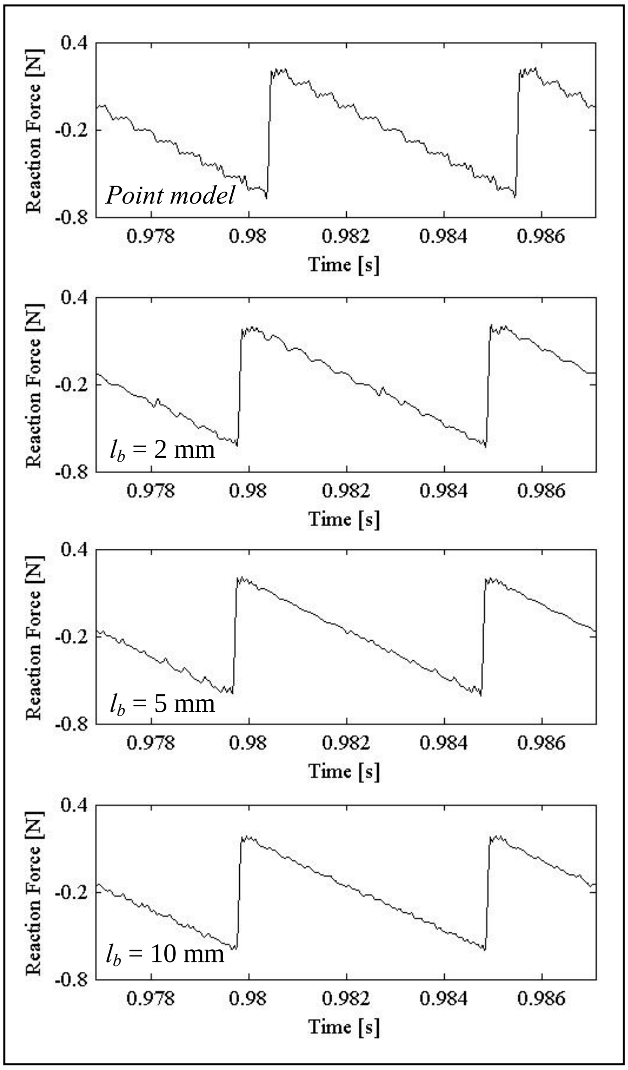

Figure 3.13 - Reaction force at the bridge for four different bow widths l_b and 1 bow contact point per millimetre

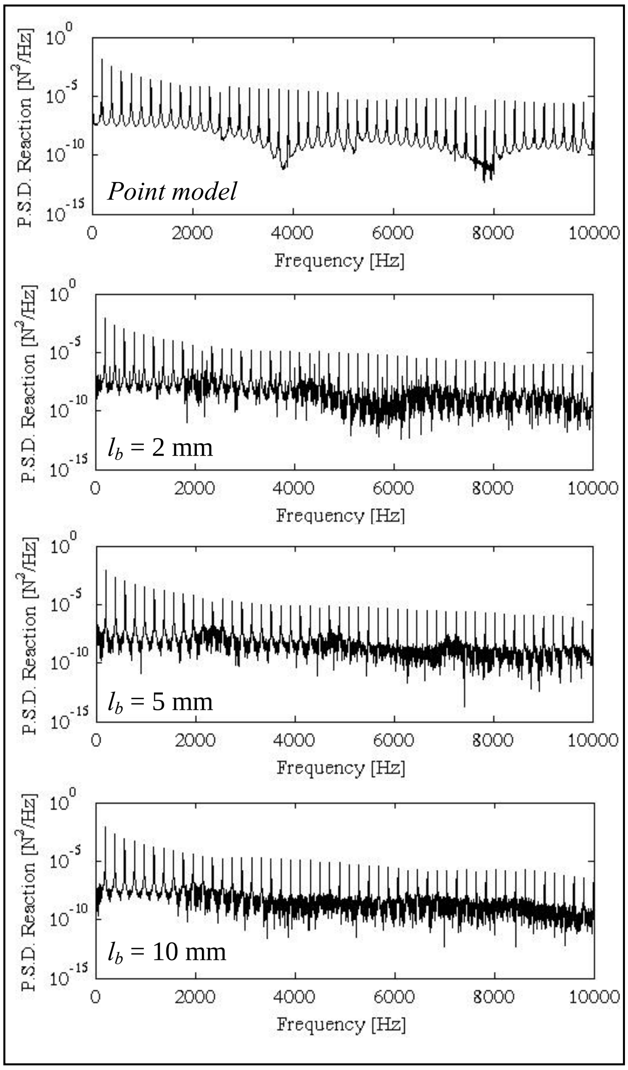

Figure 3.14 - Power spectral density of the reaction force at the bridge for different bow widths l_b and 1 bow contact point/mm

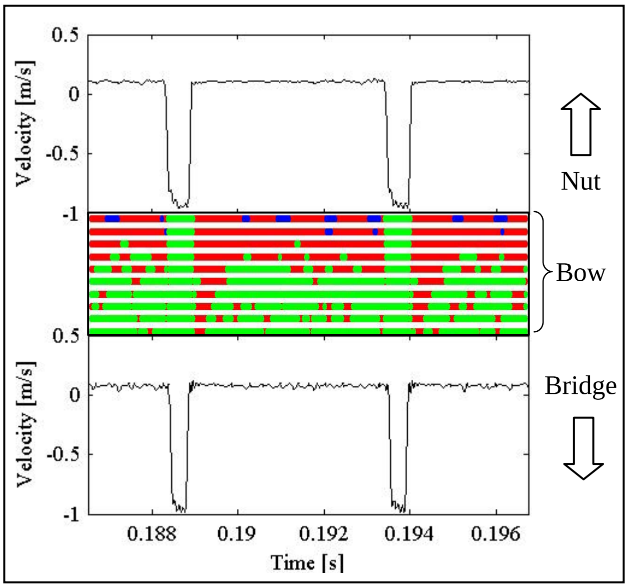

Figure 3.15 - Velocity waveforms of the string at x_c^1 (bottom trace) and x_c^{10} (top trace). The colours stand for: adherence (red); backward slip (green); forward slip (blue).

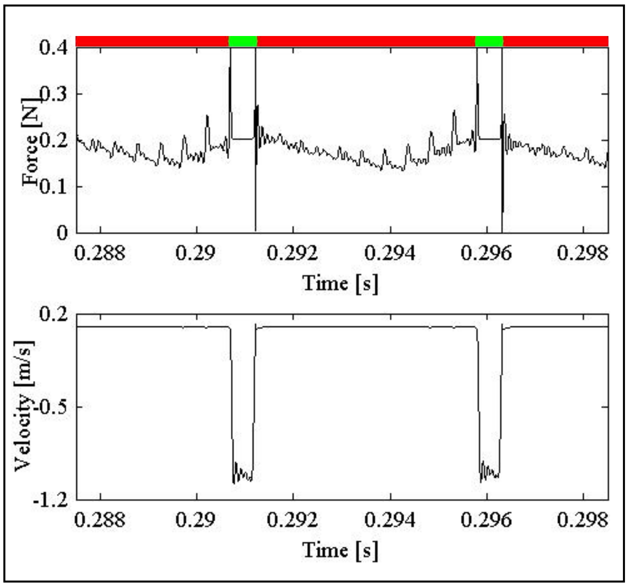

Figure 3.16 - Total friction force time-history, stick/slip time-space diagram and velocity waveform for F_N = 1 N, $\dot{y}_{bow} = 0.1\,\mathrm{m/s}$, using point bowing ($b$ = 1).

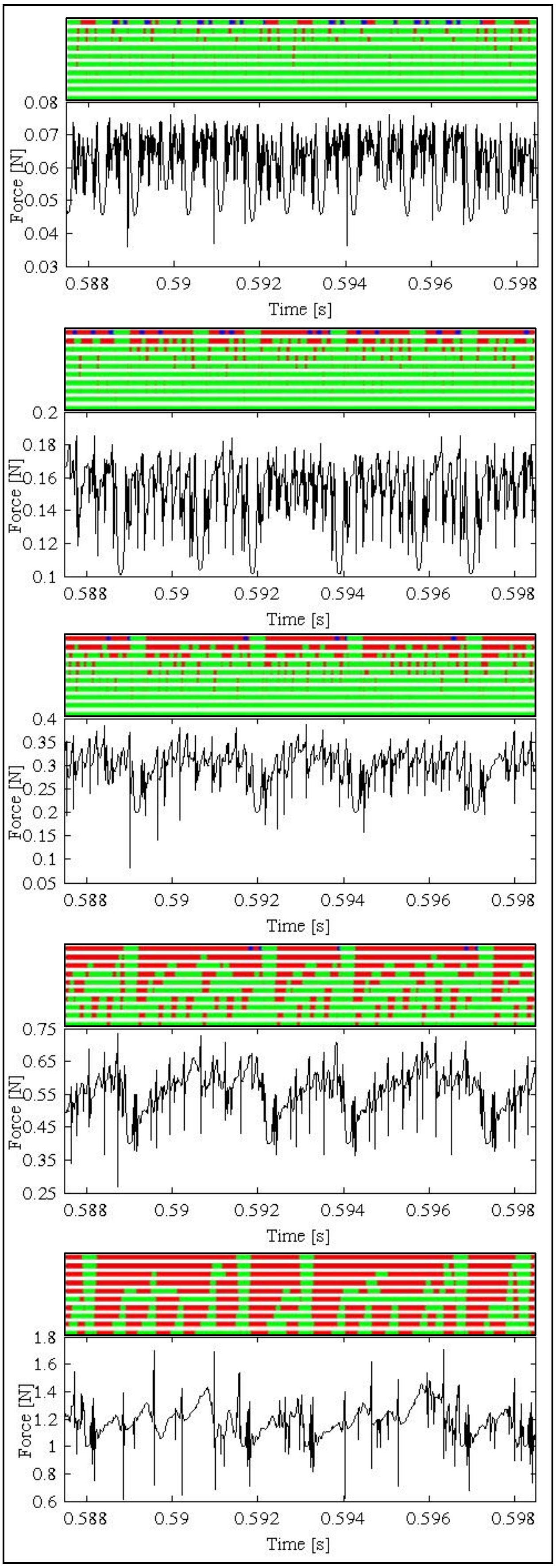

Figure 3.17 - Total friction force time-histories and stick/slip time-space diagram for x_c = 10 mm, F_N = 0.2, 0.5, 1, 2 and 5 N, $\dot{y}_{bow} = 0.1\,\mathrm{m/s}$, l_b= 10 mm and b = 10

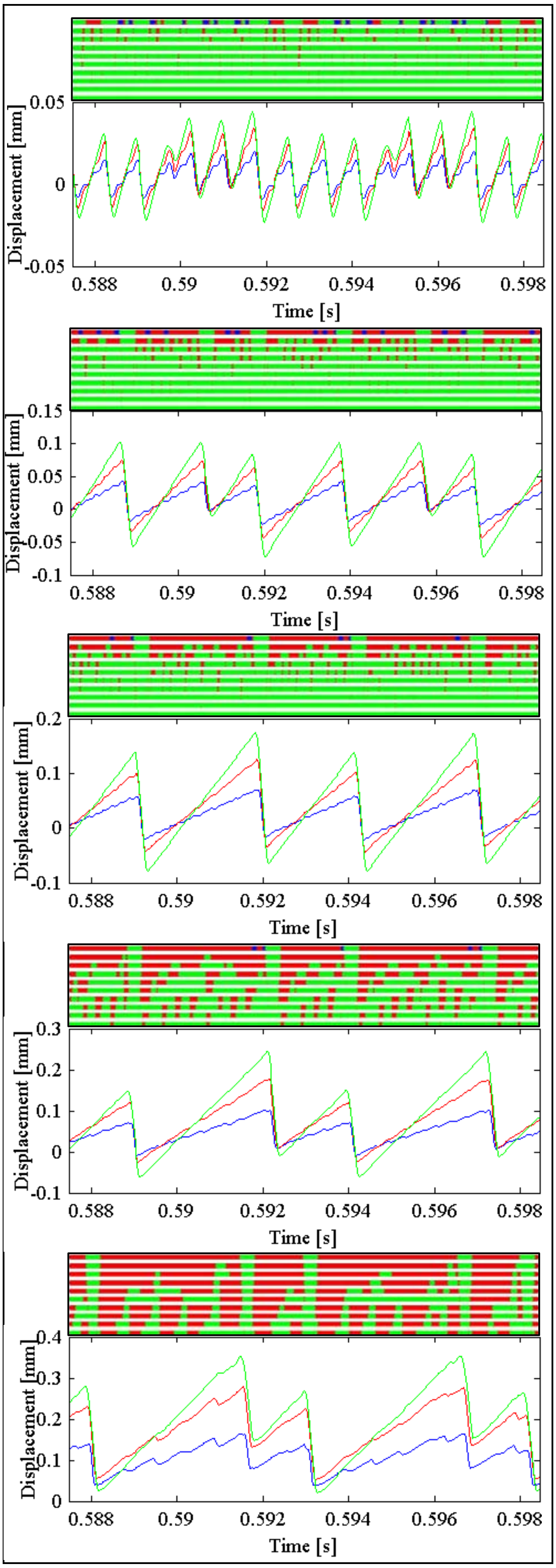

Figure 3.18 - Displacement time-histories and stick/slip time-space diagram for three bow pseudo-hairs (x_c^1 - blue, x_c^5 - red, and x_c^{10} - green) for the same playing conditions as in Figure 9.

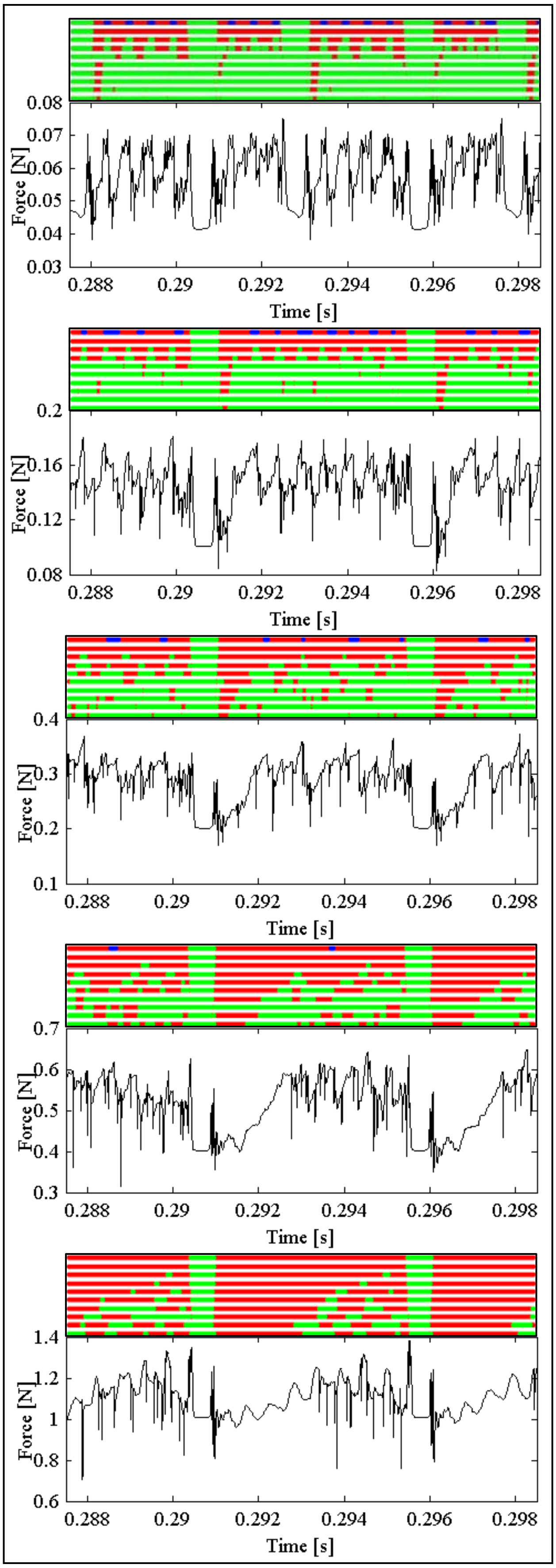

Figure 3.19 - Total friction force time-histories and stick/slip time-space diagram for x_c = 30 mm, F_N = 0.2, 0.5, 1, 2 and 5 N, $\dot{y}_{bow} = 0.1\,\mathrm{m/s}$, l_b= 10 mm and b = 10.

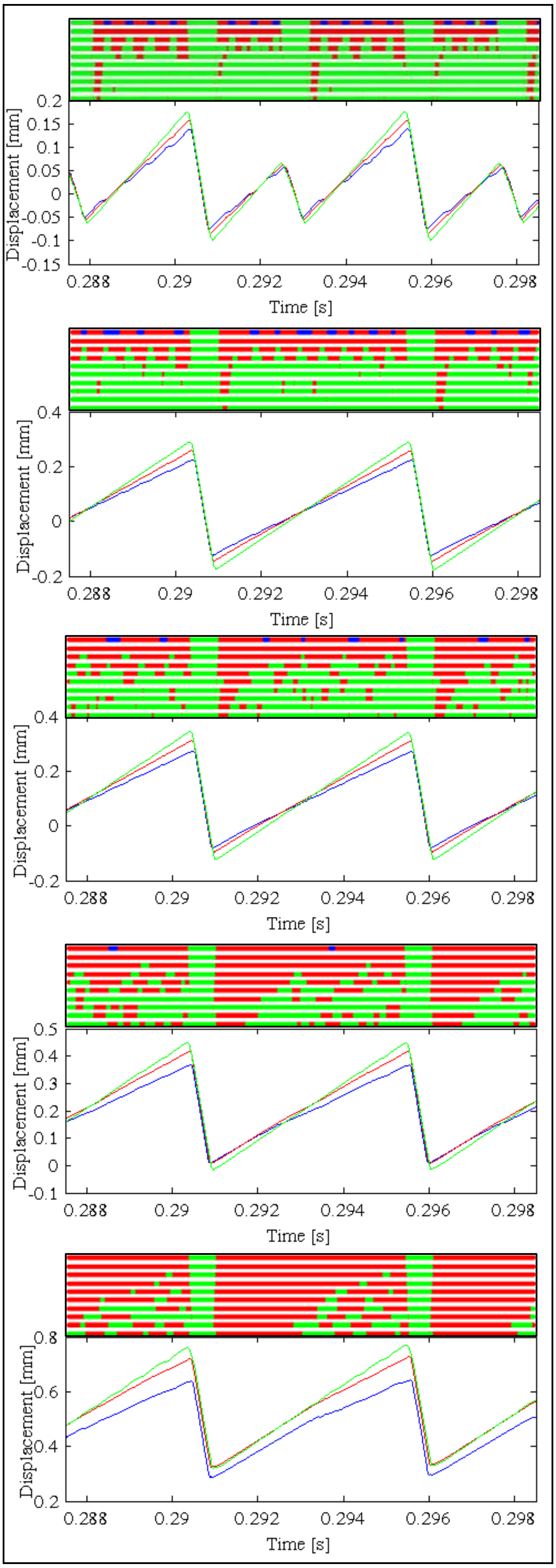

Figure 3.20 - Displacement time-histories and stick/slip time-space diagram for three bow pseudo-hairs (x_c^1 - blue, x_c^5 - red, and x_c^{10} - green) for the same playing conditions as in Figure 11

3.3.3.3 *Input parameter dependence*

Another interesting aspect, also mentioned by Pitteroff and Woodhouse (1998a), is the spatial pattern of this differential slipping phenomenon which denotes both backward (against the direction of bowing) and sometimes also forward (in the direction of bowing) slips of individual hairs in different parts of the bow's width. Figure 3.15 shows the velocity of the string bowed by a 10 mm (with 10 pseudo-hairs) bow at the contact points with the first and tenth bow hair, together with a spatial representation of the stick/slip state of each individual bow hair as a function of time; the excitation parameters are $F_N = 1\text{N}$ and $\dot{y}_{bow} = 0.1 \text{m}/\text{s}$. In this spatial representation, the green colour represents backwards sliding, the blue colour represents forward sliding and the adherence state is represented in red. The velocity waveform of the string contact point at the inner edge of the bow (closer to the bridge) shows more "activity" than at its outer edge. In fact, at x_c^1 the string slides during most of the oscillation period being more sensitive to the secondary waves generated between capture and release of the string. At the outer edge of the bow (x_c^{10}), the string is sticking during most of the motion, only interrupted by partial forward slips which can be understood in terms of the geometrical distortion of the string due to the finite width of the bow, as will be seen later. For comparison a similar diagram is shown in Figure 8 for the point model case under the same playing conditions ($F_N = 1\text{N}$ and $\dot{y}_{bow} = 0.1 \text{m}/\text{s}$), together with the friction force time-history. The secondary waves that travel between the bow and the bridge result in peaks of the friction force increasing in amplitude until slip occurs.

Figure 3.17 and Figure 3.19 show the variation of the stick-slip spatial pattern, together with the total friction force (sum of the friction force at the 10 bow hairs) with the increase of the normal force applied by the bow, for two different bowing positions x_c = 10 mm and x_c = 30 mm. An interesting aspect that arises from the analysis of these diagrams is that although the global string motion is periodic, as can bee seen from the regularly spaced “full” slips that characterize the Helmholtz and higher-order regimes, the local slip/stick dynamics are only quasi-periodic, but with a clear spatial resemblance between periods. For a detailed view of the string behaviour under the action of the bow, Figure 3.18 and Figure 3.20 represent the string motions at three different contact points with the bow – x_c^1, x_c^5, and x_c^{10} – for the same playing conditions of Figure 3.17 and Figure 3.19. This representation clearly shows that the displacement of the string during adherence is not uniform over the width of the bow, with the string at x_c^1 (bridge side) having smaller displacement amplitudes than x_c^5 and x_c^{10}, as implied by the geometry of the deformed string. Indeed, this difference in the displacement waveforms of the different contact points demonstrates the previously mentioned geometrical distortion of the string under the bow, as was also demonstrated by Pitterof and Woodhouse (1998a) in Figure 12. Despite the forward slips occurring in the outer hair (x_c^{10}), it seems clear that an effective bowing area exists located near the outer edge of the bow (nut side) that sticks to the string during most of the motion. Increasing the normal force increases this effective bowing area while the number of forward slips decreases.

Comparing Figure 3.17 and Figure 3.18 (x_c = 10 mm) position with Figure 3.19 and Figure 3.20 (x_c = 30 mm), it is clear that bowing closer to the bridge implies a larger mostly sliding section of the string and therefore it is easier for inter-period slips to occur and originate the higher order regimes characteristic of *sul ponticello* playing. Even for high normal forces ($F_N = 5$ N) it is difficult to impose a Helmholtz regime at this bowing position. When bowing at x_c = 30 mm with low normal forces, for instance $F_N = 0.2$ N, more than one slip occurs at each period while for higher bowing forces the Helmholtz regime dominates. As expected, changes in this effective bowing area influence the fluctuations of the total friction force applied by the bow on the string.

3.3.3.4 Motion Regimes

The playing parameter-space explored was $F_N = 0.1 \sim 10\ \mathrm{N}$ and $\dot{y}_{bow} = 0.01 \sim 1\ \mathrm{m/s}$, in 7 increasing steps proportional to 2 and 5. This analysis shows greatest interest when studying the effects of finite-width bowing on the various dynamical regimes which may arise for a significant range of playing parameters.

The main dynamical regimes found in the simulations are illustrated in Figure 3.21 to Figure 3.28. In the following paragraphs a description of these dynamical regimes is made associating them with a colour scheme for use in further discussions:

- *decaying regime* – light yellow – in which a self-sustained oscillation does not arise and the bridge reaction force is negligible or continuously decaying after a transient displacement of the string originated by the initial motion of the bow (Figure 3.21).
- *Helmholtz regime* – green (Figure 3.22);
- *higher-order regime* – blue – representing motions with more than one slip per period, usually associated with *sul ponticello* sounds (Figure 3.23);
- *raucous regime* – red – in which broadband, chaotic oscillations are present (Figure 3.24);
- *anomalous low-frequency regime* – magenta – for which low frequency periodicity occurs well below the string fundamental (Figure 3.25).

Other peculiar regimes were also found that show interesting characteristics: Figure 3.26 depicts a regime (A) common to all the bow widths simulations which is the only periodic oscillation without a sawtooth waveform, (cyan); Figure 3.27 represents a regime (B) visible only in the point model simulations which, in contrast with the higher-order regime mentioned previously, develops multiple slips as the bow normal force and velocity are increased setting a transition regime to raucous motion (orange); finally, in Figure 3.28, a self-sustained regime (C) is depicted obtained with an initial transient of increasing amplitude above 2 seconds (yellow).

Figure 3.29 and Figure 3.30 show the variation of the *root mean square* reaction force at the bridge for different values of the bow width, normal force and bow velocity, at two different bowing locations: x_c = 10 m and x_c = 30 mm.

Comparing the results for both bowing positions it is clear the expected dominance of higher-order regimes (blue area) when bowing closer to the bridge than at the "normal" location x_c = 30 mm where the green area (Helmholtz regime) dominates. Considering both these regimes as "musically acceptable", the wider blue+green area suggests that playing near the bridge gives more control over the playing parameters that result in "usable" sounds. Globally, a trend is seen for higher amplitudes as either the normal force or bow velocity are increased. For low normal forces the increase in bow velocity originates higher reaction forces until a limiting value after which no oscillation or a decaying oscillation occurs. For higher values of the normal force, low velocities do not allow regular bow/string slips and raucous motion arises. As the bow velocity increases the reaction force rises and the motion eventually evolves to periodic regimes.

The results of the simulations using a point model bow (Figure 3.29a and Figure 3.30a) show a higher diversity of regimes comparing to the finite bow width results, particularly when bowing at 30 mm from the bridge. An interesting aspect is the presence of anomalous low frequency regimes, in contrast to finite-width bowing, with a single exception seen in Figure 3.30c. Figure 3.29a and Figure 3.30a show globally higher amplitudes of the reaction force in comparison with the finite-width case. This is probably the reason for the emergence of these anomalous low frequencies since they require the action of high bow normal forces (Hanson *et al*, 1994).

Considering the simulations using a finite-width model, the increase of bow width between 5 mm to 10 mm suggest a higher control of the musically acceptable playing range, with the Helmholtz motion being more easily obtained for the 10 mm width bow, when bowing with high normal forces and low bow velocities. However, the differences in the global behaviour are less significant than in comparison with the point-model simulations, which also stems from the analysis of Figure 3.11 to Figure 3.14.

Four animations of the string motion corresponding to the four curves in Figure 3.13 are appended to this thesis. These animations pertain to the first 0.5 s of the movement of a free G violin string with F_N = 1 N, $\dot{y}_{bow} = 0.1\,\mathrm{m}/\mathrm{s}$ and x_c = 30 mm, under the action of bows of different widths. Animation 1 depicts a point bow model (b = 1), while in animations 2 to 4 the bow widths are respectively l_b= 2 mm, l_b= 5 mm and l_b= 10 mm, with one contact point per millimetre. In these animations, the nature of the stick/slip state between the bow and the string is represented by the colours of the dots at each contact point: *red* indicates stick; *green* indicates backwards slip and *blue* indicates forward slip. The displacement time history of the contact point closest to the nut is also shown, in which a moving dot with the same colour scheme as before is used for describing the stick/slip states.

In all simulations, the bowing parameters chosen trigger the Helmholtz motion after a short initial transient. One of the most elucidating aspects of these animations is the visualization of the passage from the initial transient, in which a double slip regime predominates, to the regular Helmholtz motion. Regarding the animation pertaining to the 10 mm bow width, the emergence of forward slips in the contact points closer to the nut is clearly seen, and seems to originate from the forward ‘push’ given by secondary waves travelling in advance or behind the Helmholtz corner.

3.3.3.5 Flattening effect

Exploring the range of input parameters already mentioned allowed the study of the *flattening effect* phenomenon, characterized by a decrease on a note fundamental frequency as the bow force is increased. This effect has been first discussed on the basis of numerical simulations by McIntyre & Woodhouse (1979) and McIntyre *et al* (1983), and parametrically studied thoroughly by Schumacher (1979), Boutillon (1991) and Faure & Boutillon (1991). Basically, the flattening effect results from the net delay occurring during capture and release transitions of the Helmholtz motion, for F_N above a minimum value. As mentioned in Schumacher (1994), the flattening effect can only be accounted for if a realistic (rounded) Helmholtz corner is implemented. In contrast with the algorithms used by other authors, such as McIntyre & Woodhouse (1979) and McIntyre *et al* (1983) (in which the rounded corner is simulated by the introduction of narrow-width reflection functions, instead of the idealized ones), in the present method the realistic rounded Helmholtz corner naturally emerges from the finite number of string modes excited by the bow-string nonlinear interaction. The compliant bow is only capable of effectively exciting the string up to a limiting cut-off frequency which is dependent on the longitudinal stiffness of the bow hairs. Therefore, the perfectly sharp Helmholtz corner which could only be reconstructed by an infinite number of modes, will be as round as the reconstruction from the finite number of effectively excited modes allows. It should be noted that, in this results now presented, the rounding of the Helmholtz corner is not a result of inharmonicity effects, since no bending stiffness was used in these calculations.

More recently the flattening effect has been revisited by Pitterof and Woodhouse (1998b) and Woodhouse (2003). In the latter work, the author compares the influence of the use of two different friction models, thermal and velocity-dependent, on the flattening effect. Although this comparison is an interesting matter for future work, some conclusions relating the evolution of a note fundamental frequency with increasing bow force are relevant. For the case of the velocity-dependent friction model (similar to the one used here) these authors state the existence of a threshold for flattening, below which the fundamental frequency is not altered for a specific range of bow forces. After this threshold the frequency decreases until a maximum bow force is reached beyond which the Helmholtz oscillation regime disrupts.

Figure 3.31 and Figure 3.32 show the variation of the fundamental frequency (f_1) with increasing normal force and bowing velocity for three different bow widths at different distances from the bridge, 10 mm and 30 mm. The fundamental frequency was calculated by inspection of the main oscillation period, for all periodic regimes. The different regimes are represented using the same colour scheme as in Figure 3.29 and Figure 3.30.

The decreasing values of f_1 with increasing F_N reach 99.5% of the nominal frequency (196 Hz). These values seem lower than those measured and predicted by other authors – Schumacher (1994) (which state a flattening of the fundamental frequency roughly between 1% and 3%), however comparisons should be made with care since their results do not pertain to a G string and the simulation friction parameters are significantly different. However, as also stated by Woodhouse (2003) these results show a limit value for F_N below which the flattening effect is not significant, in contrast to results obtained using thermal friction models. As the present results show, this value seems to increase for higher bow velocities and is markedly affected by considering point-bowing instead of finite-width bows, which seem to be less prone to flattening.

Additionally, Figure 3.31 and Figure 3.32 show a limiting value as F_N is increased, beyond which the motion jumps to the so-called raucous sounds (in the figures, the points not represented correspond to the raucous regime or to the anomalous low-frequency regime). This maximum bow force is, for most of the bowing velocities considered, higher for the finite width bow than for the point bow model.

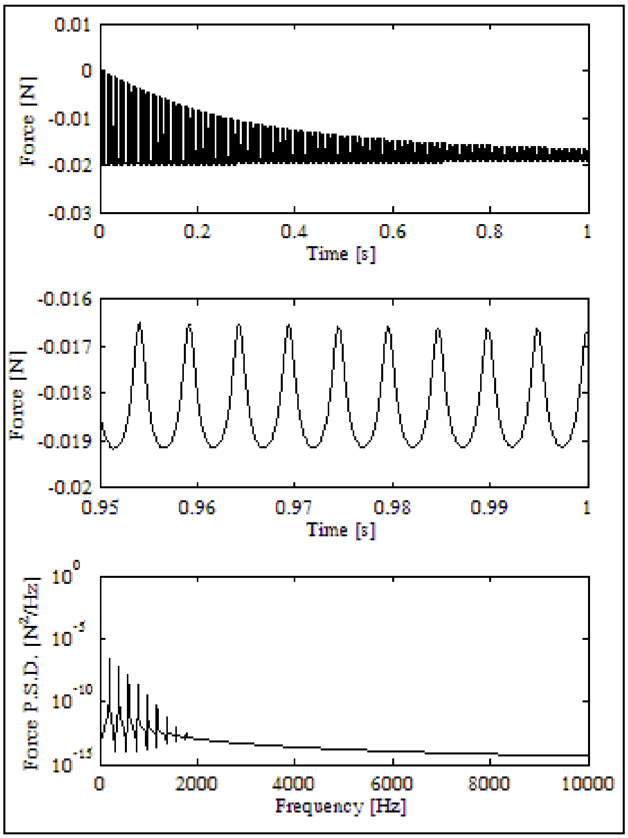

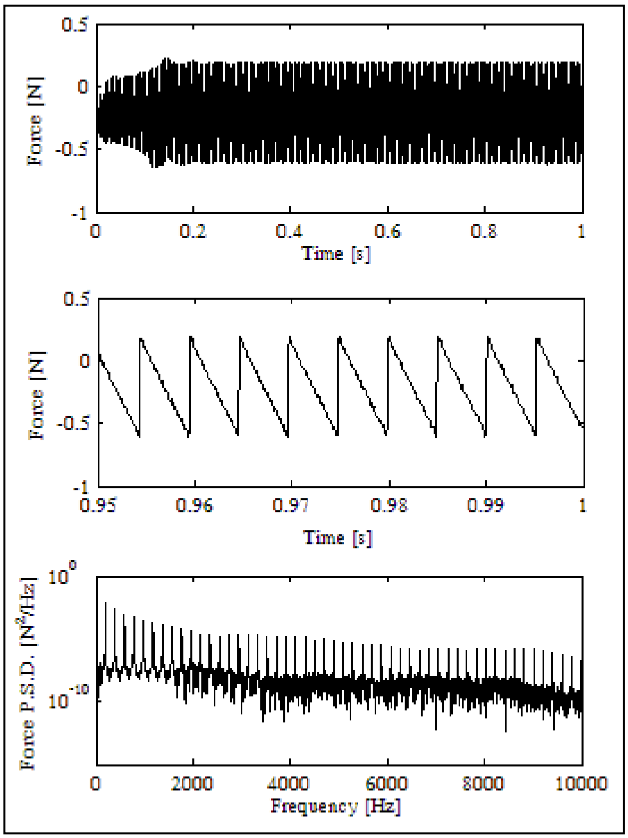

Figure 3.21 - Time-histories and spectra of the *decaying regime* (light yellow)

Figure 3.22 - Time-histories and spectra of the *Helmholtz regime* (light yellow)

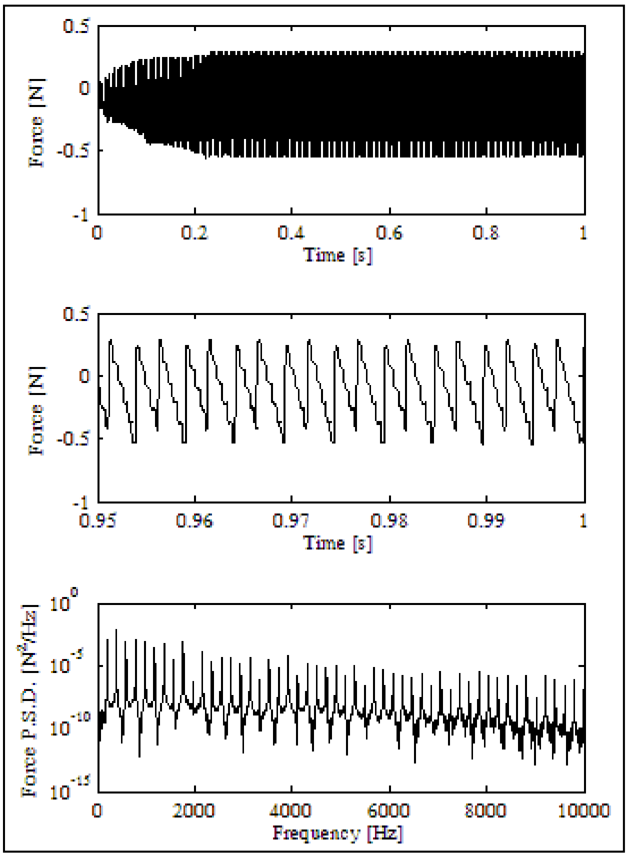

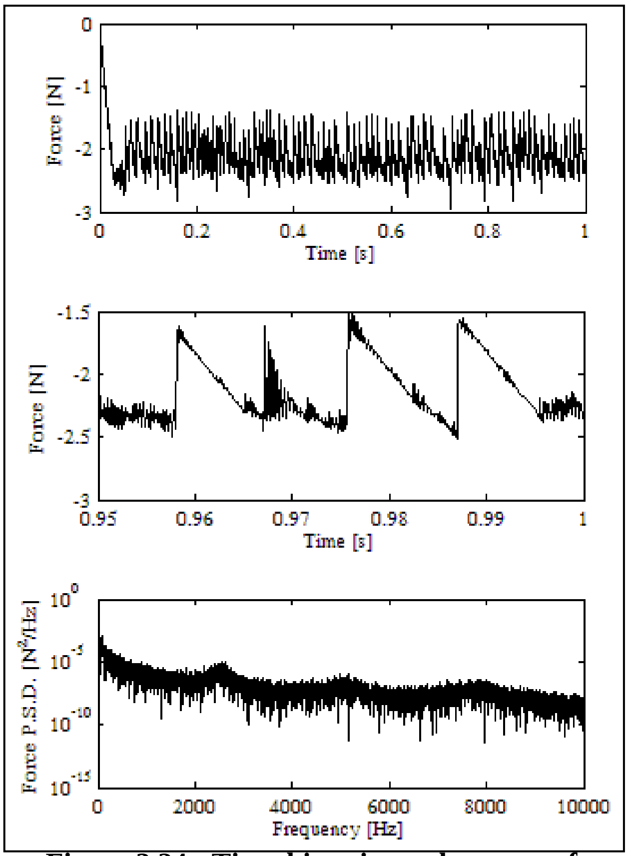

Figure 3.23 - Time-histories and spectra of the *higher-order regimes* (blue)

Figure 3.24 - Time-histories and spectra of the *raucous regime* (red)

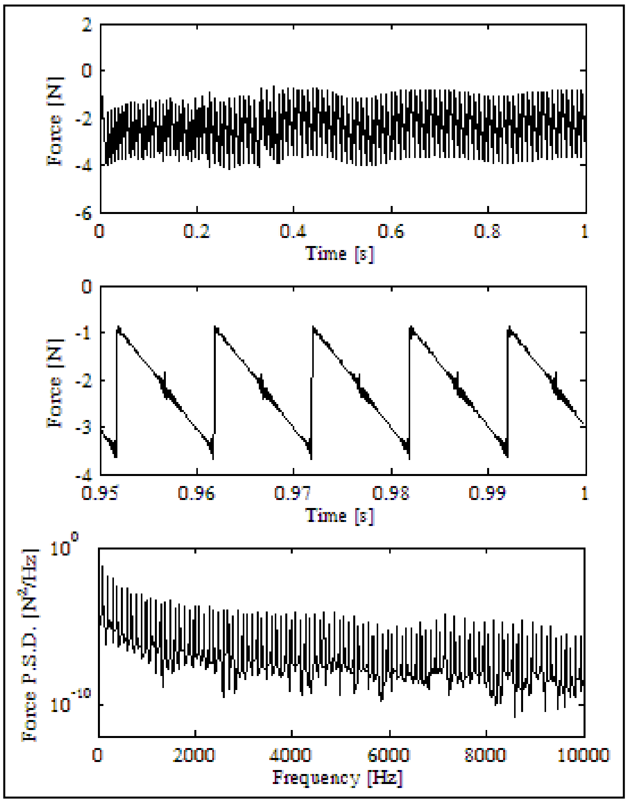

Figure 3.25 - Time-histories and spectra of the *anomalous low-frequency regime* (magenta)

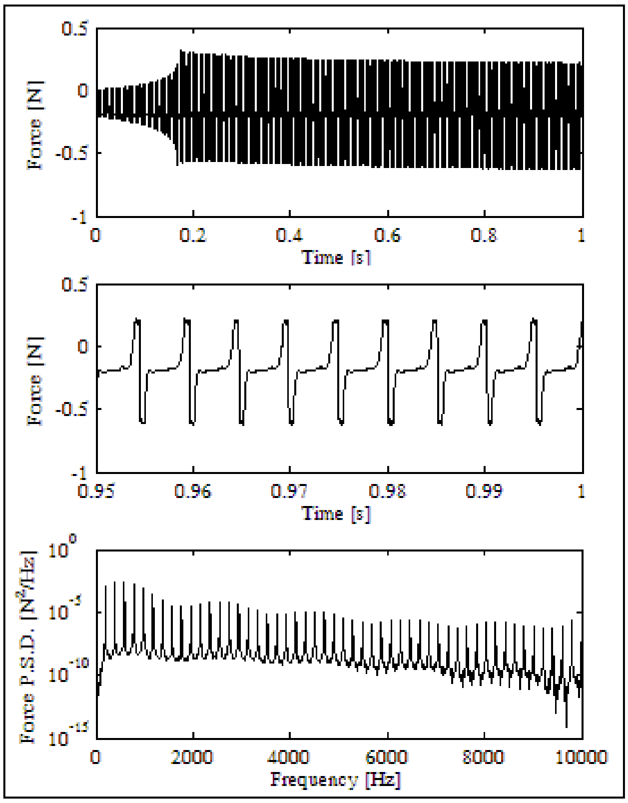

Figure 3.26 - Time-histories and spectra of the particular regime A (cyan)

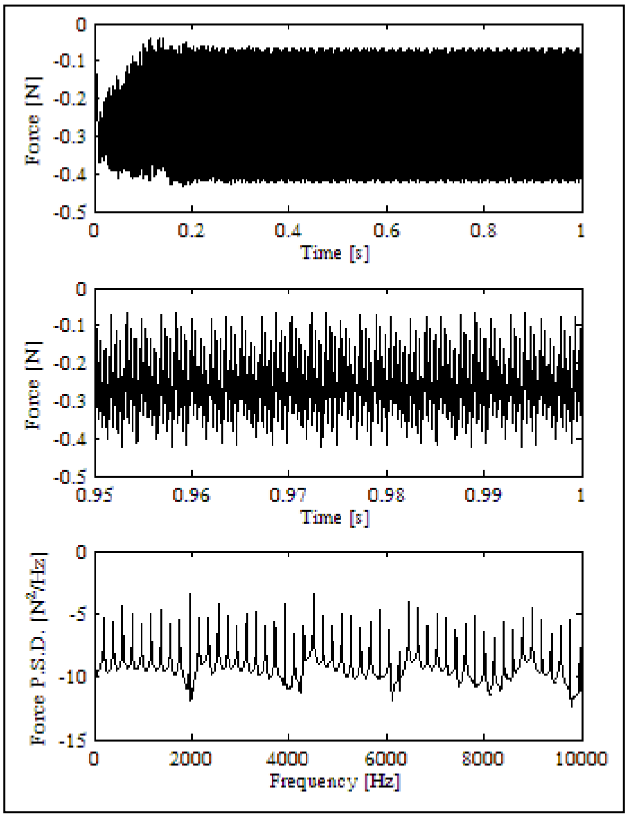

Figure 3.27 - Time-histories and spectra of the particular regime B (orange)

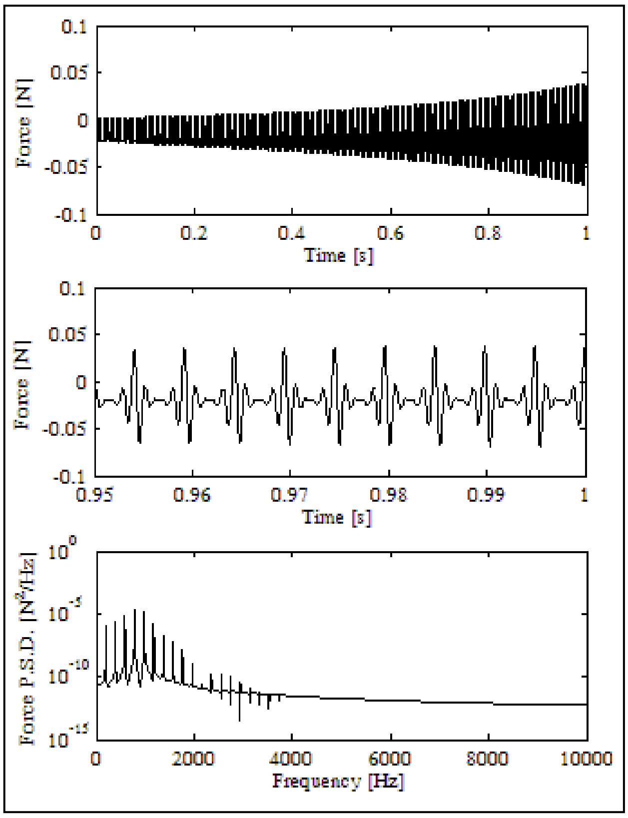

Figure 3.28 - Time-histories and spectra of the particular regime C (yellow)

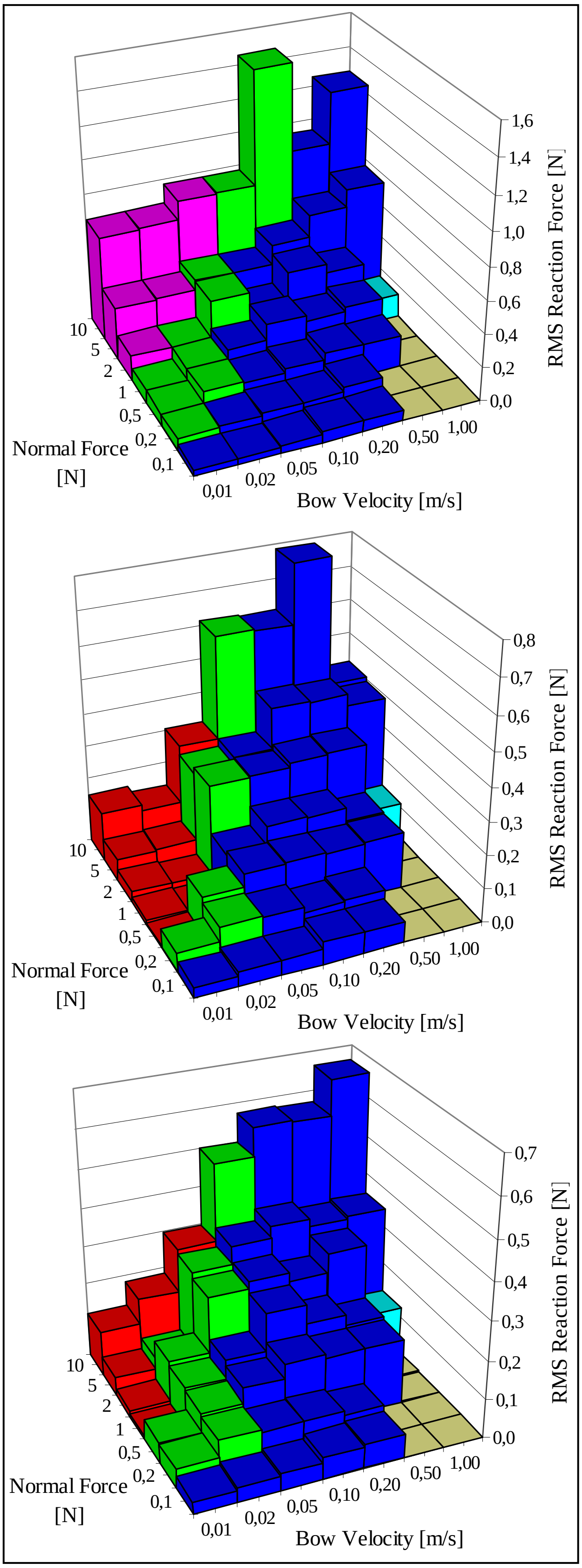

Figure 3.29 - Variation of the RMS reaction force at the bridge with F_N and $\dot{y}_{bow}$ for x_c = 10 mm and different bow widths: a) Point model; b) l_b= 5 mm (b = 5); c) l_b = 10 mm (b = 10).

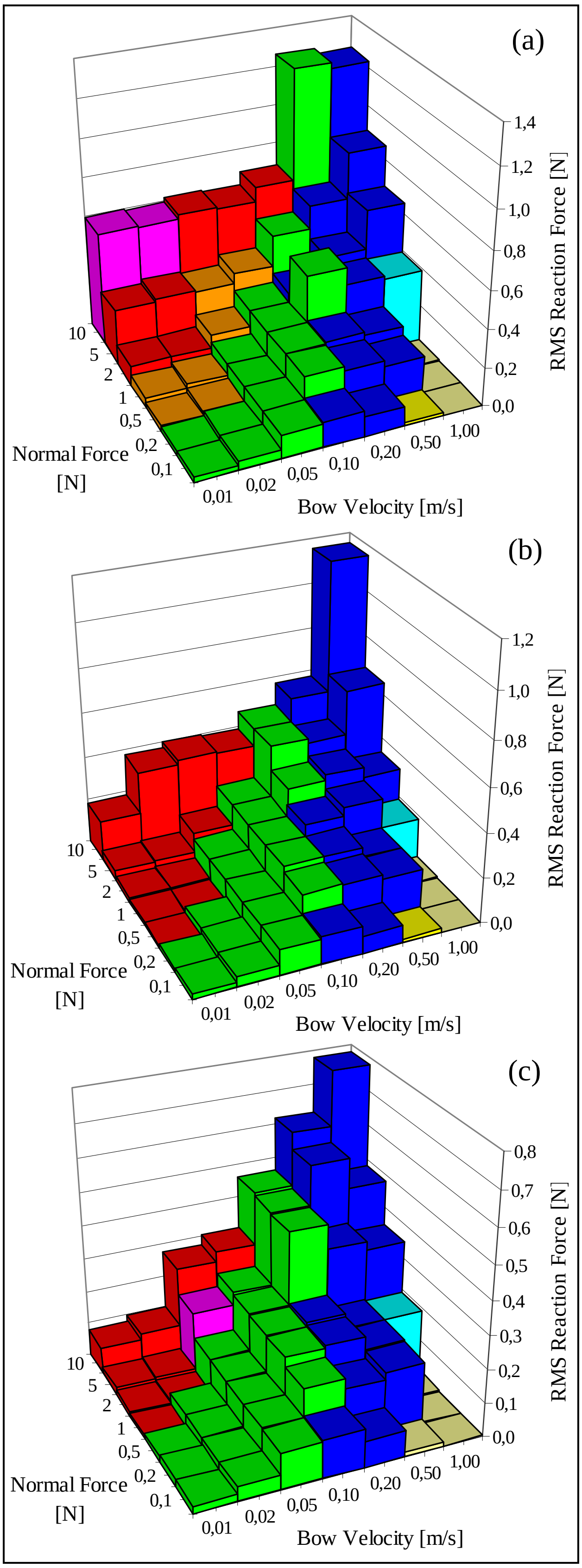

Figure 3.30 - Variation of the RMS reaction force at the bridge with F_N and $\dot{y}_{bow}$ for x_c

= 30 mm and different bow widths: a) Point model; b) *l_b*= 5 mm (*b* = 5); c) *l_b* = 10 mm (*b*

= 10).

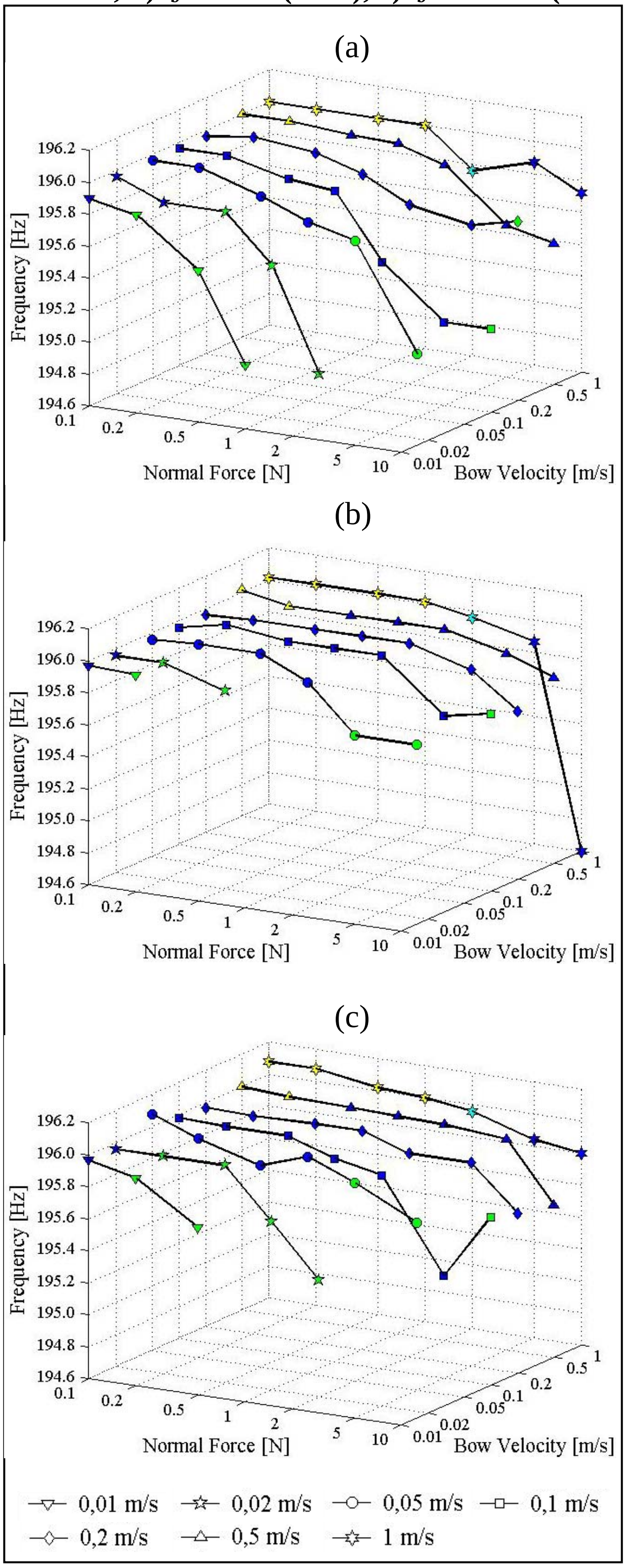

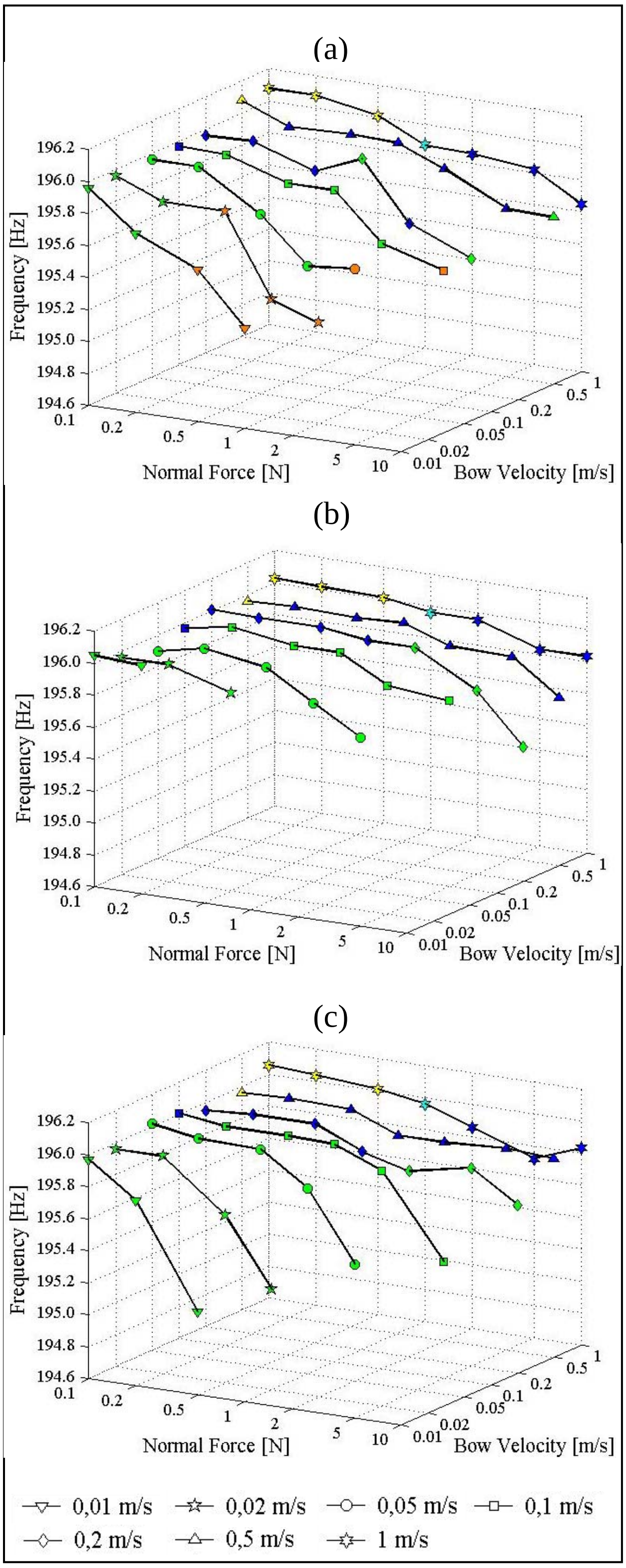

Figure 3.31 - Variation of *f_1* with *F_N* and $\dot{y}_{bow}$ for x_c = 10 mm and different bow widths: a) Point model; b) *l_b*= 5 mm (*b* = 5); c) *l_b* = 10 mm (*b* = 10).

Figure 3.32 - Variation of f1 with FN and for = 30 mm and different bow widths: a) Point model; b) lb= 5 mm (b = 5); c) lb = 10 mm (b = 10).

In this chapter, the influence of the finite width of the bow on the dynamical regimes of the bowed string has been modelled and analyzed using a modal method. This method enables accounting the finite width of the bow with only a modest increase in computing effort and code development. Comparisons between the use of a point-bow and bows with several contact points (hairs) suggest a minimum number of 10 contact points (pseudo-hairs) for a realistic simulation of the bowed string dynamics. In fact, the finite width model predicts reaction forces that are different from the point model case, leading to an increase of broadband high frequency content in the reaction force spectrum. In agreement with other authors Pitteroff & Woodhouse (1998a) the modal model reveals the existence of backward and sometimes forward slips (partial slipping) of individual hairs, occurring between the main slip phases of the Helmholtz motion. This partial slipping phenomenon has a complex spatial pattern denoting an effective adherence area that increases with the bowing force F_N.

As can be easily understood, the effects of the partial-slipping mechanism connected to finite-width bowing become comparatively more significant when the bow/bridge distance is decreased, when the very sensitive higher-order (multiple slip per period motion) regimes are more the rule than the exception.

Finally, the range of input parameters explored allowed us to quantify the well-known flattening effect, which – in agreement with Pitteroff & Woodhouse (1998b) – was found more significant for the point-model than for the finite-width case. This is connected with the apparent decrease of the “effective” static friction coefficient pointed in Pitteroff & Woodhouse (1998b), which is also reflected in the present results. The computed vibratory levels are (at comparable bowing parameters) consistently higher for the point-model than for the finite-width bow.

At the end of their most important series of papers, Pitteroff & Woodhouse Pitteroff & Woodhouse (1998a, 1998b, 1998c) state that “The overall conclusion is that point-bow and finite-width models produce distinctly but not fundamentally different behaviour.”, and furthermore that “Many physical effects can be generated with both models but these effects appear in different parts of the parameter space. Other effects are only accessible with finite-width modelling” (Pitteroff & Woodhouse, 1998b). The results stemming from the modal computational model also support these conclusions. Furthermore, the numerical simulations presented here suggest that differences between point-model and finite-width simulations can be more pronounced outside the range of bowing parameters leading to the Helmholtz motion, which is typically more robust to modelling (or playing) details than the sensitive higher-type or near-raucous responses. In particular, at higher bow normal forces, it appears that the so-called “anomalous low frequency” responses Hanson *et al* (1994) may be more easily obtained under bowing conditions close to the point-model idealisation than under the large contacting interface of a non-tilted bow.

Several animations of the bowed string motion are appended to this thesis, which highlight interesting aspects discussed in this work.

3.3.4 Influence of the string/body coupling

Simulations were performed for both a violin and a cello. The movement of a violin G-string with a fundamental frequency of 196 Hz is simulated, with an effective length L = 0.33 m and a linear density of $\rho S = 3.1\times10^{-3}$ kg m^{-1}, in order to test the behaviour of the coupled computation method described above. The cello C-string simulated has a total length of 0.83 m from the nut to the tailpiece with 0.7 m and a linear density of $\rho S = 14\times10^{-3}$ kg m^{-1} from the bridge to the nut, giving a fundamental frequency of 65.4 Hz. In order to achieve adequate computational convergence 60 modes were used for the violin string and 80 modes for the cello string, with a recorded sampling frequency of 20000 Hz. A modal damping value of 0.1% was used for all modes (however, frequency dependent damping can be easily introduced with this method) and a string inharmonicity coefficient β was introduced to provide more realistic simulations (Schelleng, 1973; McIntyre *et al*, 1983). This effect is easily simulated using the modal approach, as the bending stiffness influence is automatically incorporated in the string modes, with modified frequencies according to:

$$\omega_n = n\omega_1\sqrt{1+\beta n^2}\ \text{, for } n \geq 2 \tag{3.24}$$

where $\beta = \pi E\phi^4 / 64L^2T$ for homogeneous strings. However, the lower strings for the violin or cello are usually wound and therefore non-homogeneous, so a value of β = 2.3×10^{-4} was used, which was inferred from Table 4.9 of (Jansson, 2002).

The body of the violin and the cello were simulated using a modal basis whose parameters were identified from measured input admittances. In the case of the violin a very crude model was used comprising only 13 modes covering the frequency range between 200 Hz and 3500 Hz. In the case of the cello a thorough modal identification procedure was carried and 53 modes were chosen leading to the synthesized input admittance shown in Figure 3.33.

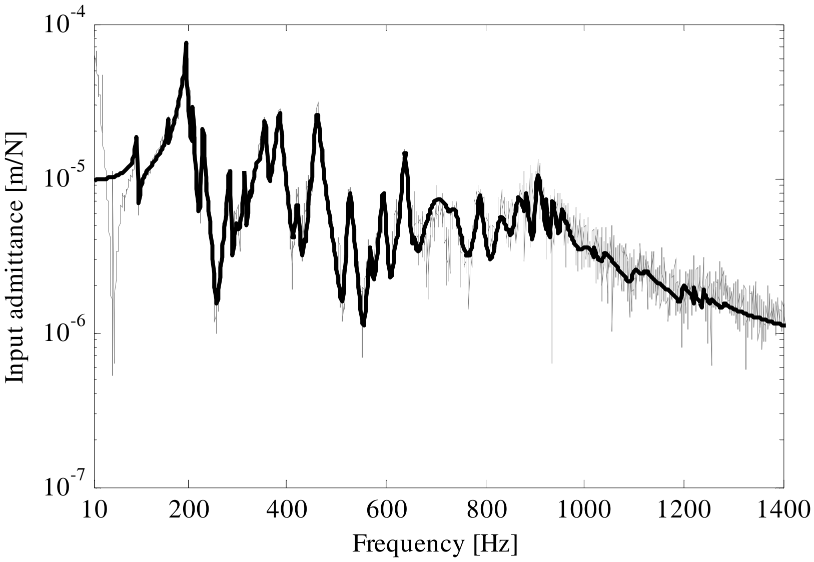

Figure 3.33 – Measured (light line) and synthesized (heavy line) input admittance of the cello used in the simulations.

A classic sliding law friction model, such as the one presented in equation (7), with μ_S = 0.4, μ_D = 0.2 and C = 5, was chosen, which produced realistic results. For the adherence model a total value of $K_a = 10^5$ N/m as been used. As previously discussed, a near-critical value of the adherence damping term C_a was adopted (Tafasca et al, 2000; Antunes *et al*, 2001). In this context, it should be mentioned that recent research results (Smith & Woodhouse, 2000; Woodhouse, 2003) suggest the relevance of dynamical thermal phenomena in the tribology of rosin, which may induce hysteretic effects in the friction-velocity dependence. In spite of the unquestionable interest of such findings, the classical approach for sliding behaviour was used.

The stiffness constant value, K_{bs}, used for the string/body coupling was chosen in order to enable a very stiff connection, while keeping a satisfactory computational convergence. As demonstrated in Section 3.5 a value equal or higher than 10^6 N/m is enough. Concerning the damping constant a value $C_{bs} = 10$ Nsm^{-1} proved adequate. As also shown in Section 3.5 of this thesis, for K_{bs} equal or higher that 10^6 N/m the modal damping of the string/body coupled modes is not affected by this value of C_{bs}.

3.3.4.1 Violin Simulation Results

Figure 3.34 to Figure 3.36 show simulations of the violin string and bridge dynamics for different boundary conditions, when applying a normal bow force (F_N) of 1 N and bow velocity ($\dot{y}_{\text{bow}}$) of 0.1 m/s, at 0.030 m (approximately $L/10$) from the bridge. Figure 3.34 shows the most widely simulated case of a string pinned at the bridge and the nut (with a length of 0.330 m). Perfect reflections arise from these extremities and the Helmholtz motion is clearly perceptible. The force at the bridge is easily computed from the modal time responses $q_n(t)$, through a superposition of the modal reaction forces, (3.25), where f_1 is the fundamental frequency of the string.

$$F_b(t) = -4\pi \frac{\rho}{S} L f_1^2 \sum_{n=1}^{N} n\, q_n(t) \tag{3.25}$$

Figure 3.35 represents the case of a string pinned at the tailpiece and the nut, with a total length of 0.385 m, a rigid bridge being placed at 0.330 m from the nut. The same overall behaviour as in the previous example could be expected, since there is no movement of the bridge. However, note that the string inharmonicity enables some energy to pass to the tailpiece-side of the string, leading to low-amplitude waves at higher frequency. These parasitic oscillations are clearly perceptible in the string/bridge coupling force shown in Figure 3.35, superimposed on the well known bow-bridge secondary waves shown in Figure 3.34. This effect, noted by Puaud *et al* (1991), can be seen very clearly on the computed animations of the string motion. Nevertheless, and not unexpectedly, a Helmholtz motion similar to the previous example developed. Notice that the overall behaviour of the string-bridge contact force is similar for the computations in Figure 3.34 and Figure 3.35. This is a reassuring feature, given that in Figure 3.34 the contact force is computed from the modal summation of (3.25), while in Figure 3.35 the interaction force stems from the totally different approach stated in (3.23).

Figure 3.36 shows the results obtained from the simulations computed through the implementation of the string/body coupling by application of the modal model of a violin body (Figure 3.33). A modal identification was performed, as pointed before, on a mass-produced violin and 13 modes were chosen to represent the gross features of its dynamical behaviour. The corresponding synthesized impulse response function was also calculated and used in the incremental convolution method, leading exactly to the same results. As in the previous example, the oscillations of the tailpiece side of the string can also be seen in the string/bridge coupling force.

The similarity of the plots depicted in Figure 3.35 and Figure 3.36 is due to the high impedance presented by the violin bridge to the string waves, which are – in this computation – hardly affected by the comparatively negligible bridge motion. However it is important to emphasise that this result was obtained when bowing an open G-string, with a fundamental frequency significantly lower than the first body resonance (at about 276 Hz). However, in contrast to this situation, interaction between the string and the body can be much stronger when playing notes with frequencies close to body resonances. Then, bridge motion amplitude (and energy string/body interplaying) may become very significant, as typically experienced in cellos when playing wolf notes.

Simulations of plucked violin strings were also performed using a rigidly supported bridge and a flexible (compliant) bridge. Figure 3.37 (a) and (b) depict the velocity of the string at the plucking point for these two conditions. Using a rigid bridge, case (a), the string motion decreases in a simple exponential manner, while with the compliant bridge, case (b), the interaction with the body dynamics can be clearly seen. In this later case, energy is transferred from the string and dissipated by the body through the bridge originating a higher motion decay rate. An accurate identification of the damping factor of the individual modal responses of the plucked string, using the modal identification ERA method (Juang & Pappa, 1985; Juang, 1994), showed that the 0.1% damping of the string modes is unaltered when the string's modal frequencies are not close to a body resonance (the same conclusion applies to the body modes' damping factors). However, in the case of the compliant bridge, when the string and body resonances are close (a few Hertz apart) the string mode damping values become higher, as expected. As an example, the modal damping of the string's second mode (at 392 Hz) couples well to the body's second mode (at 404 Hz) changing the damping value from 0.1% to 0.37%. The correctness of the damping values identified from the time domain simulations was verified by the complex eigenvalues of a coupled system model, as shown in Section 3.5.

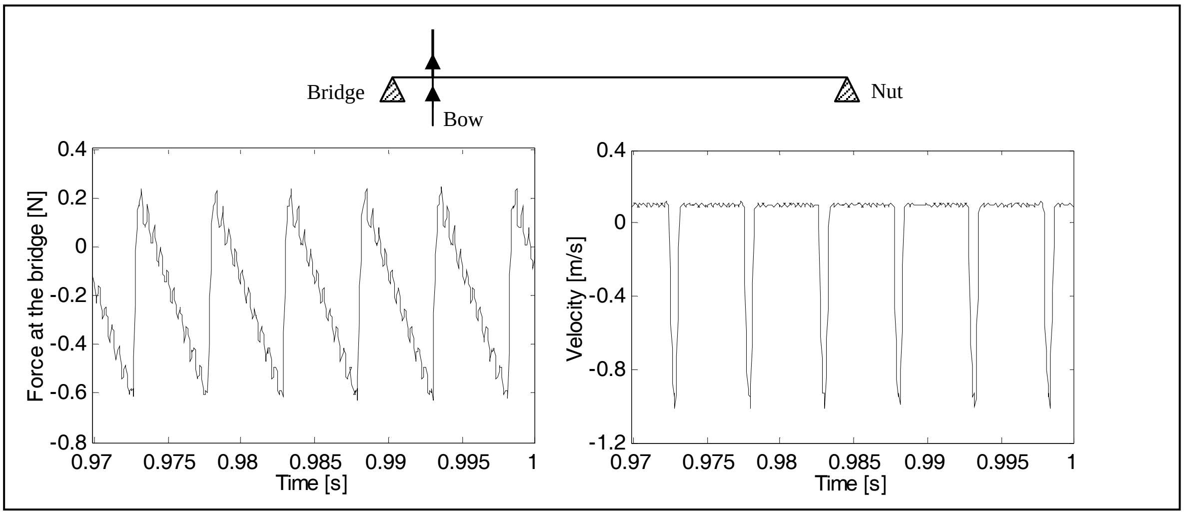

Figure 3.34 – Force at the bridge and string velocity at the bow contact point for a 0.330 m string pinned at both extremities (F_N = 1 N, $\dot{y}_{bow}$ = 0.1 m/s).

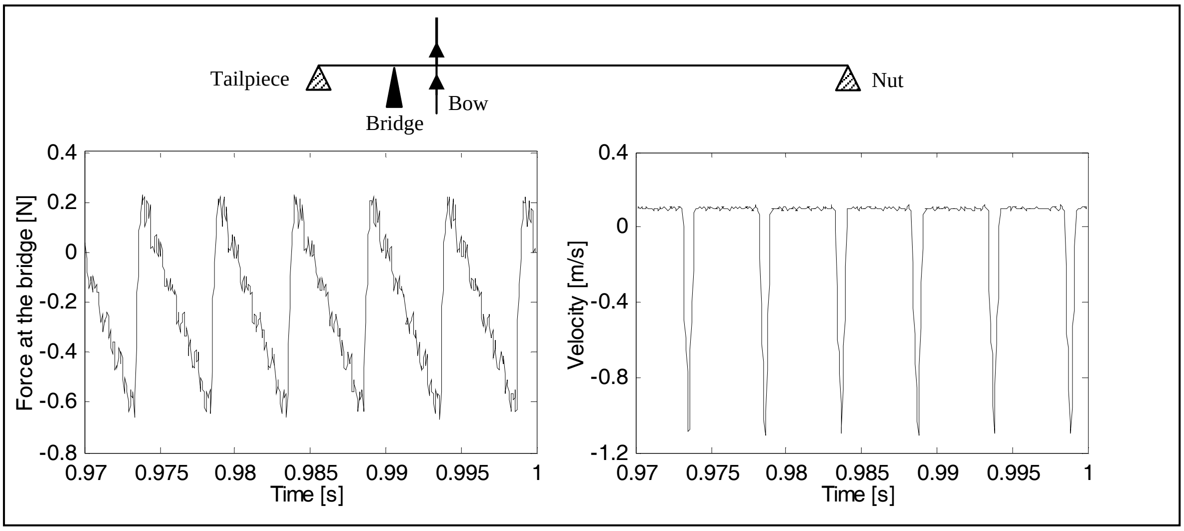

Figure 3.35 – Force at the bridge and string velocity at the bow contact point for a 0.385 m string pinned at the nut and tailpiece (rigidly supported bridge at 0.330 m, F_N = 1 N, $\dot{y}_{bow}$ = 0.1 m/s).

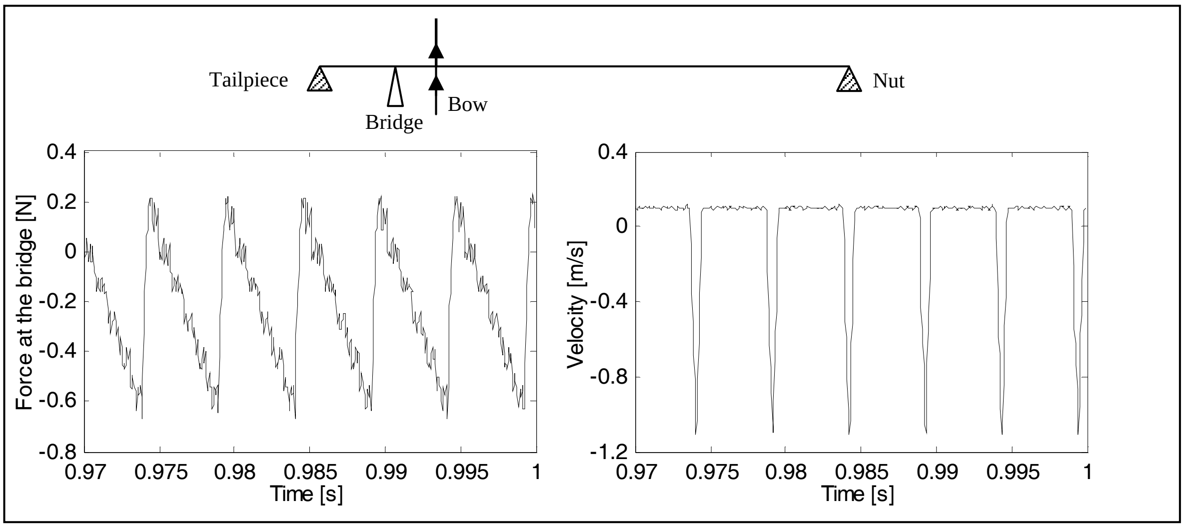

Figure 3.36 – Force at the bridge and string velocity at the bow contact point for a 0.385 m string pinned at the nut and tailpiece (flexible bridge at 0.330 m, F_N = 1 N, $\dot{y}_{bow}$ = 0.1 m/s).

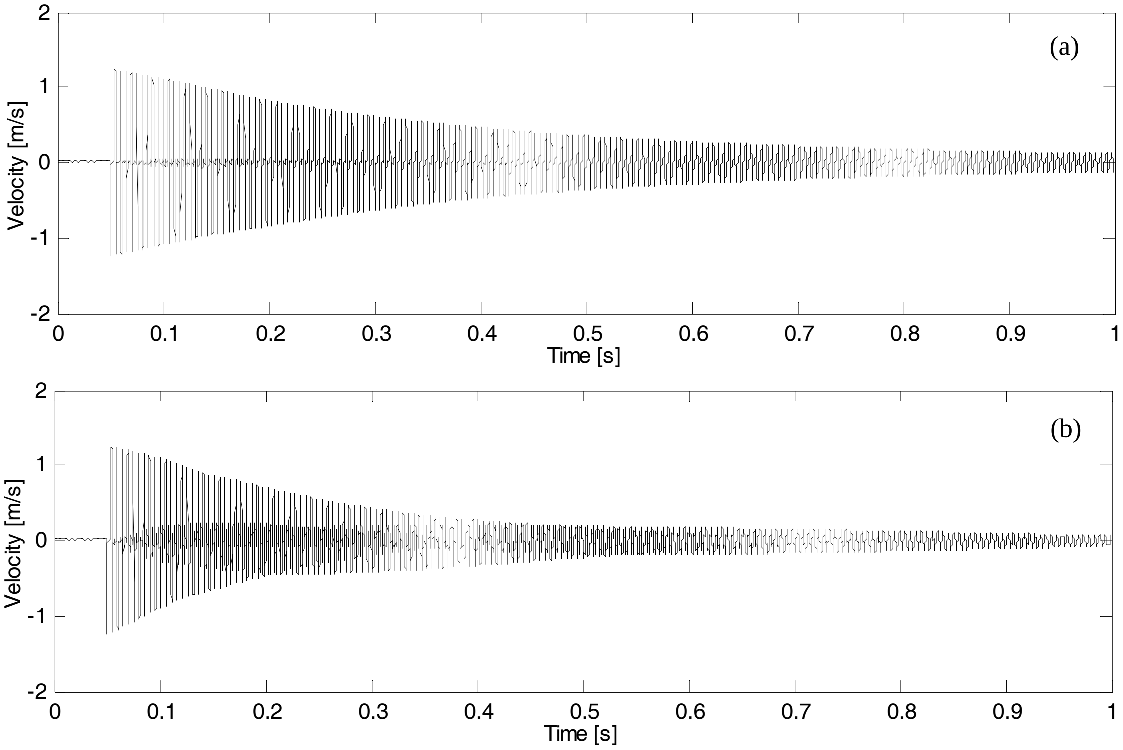

Figure 3.37 – Simulation of a plucked G-string uncoupled (a) and coupled (b) to the instrument body.

3.3.4.2 Cello Simulation Results

3.3.4.2.1 The problem of wolf notes

The wolf note is a particular effect to which bowed string instruments (bad or good) are known to be very susceptible. It is an unpopular phenomenon among musicians since it gives rise to harsh and beating-like sounds, making proper musical execution extremely difficult at some positions along the fingerboard. Although unpleasant for the listener, the emergence of this effect is paradigmatic of the importance of the body/string interaction.

The wolf phenomenon has been the subject of several studies – Raman, (1918), Puaud (1991), Schelleng (1963), Firth & Buchanan (1973), Benade (1975), McIntyre, J. Woodhouse (1979), Gough (1980), Woodhouse (1993b) – the most generally accepted explanation being the one suggested by Schelleng (1963), forty years ago. More recently the basis of this explanation has been revisited and further discussed by Woodhouse (1993b). However, there are still a few aspects deserving exploration, such as the influence of the string dynamics in the portion between the tailpiece and the bridge (see Derveaux *et al* (2003) for an interesting experimental account). On the other hand, a dependence of the wolf beating frequency on the bowing parameters was experienced, an aspect which seems almost absent from the literature, other than in McIntyre *et al* (1983), where two simulations of a wolf note played with different bow forces are shown, exhibiting different wolf beating frequencies. Also, the emergence of wolf phenomena appears to depend somewhat on the time-history of the bowing parameters, a fact which has also been noted in Derveaux *et al* (2003).

3.3.4.2.2 Wolf-note simulation

As the influence of the cello body on the dynamics of its C_2 string was so apparent during the preliminary experiments, several coupled simulations for this instrument using a modal representation of this instrument body (see Figure 3.33) were performed. To easily detect the emergence of a possible wolf note, a glissando was implemented in the simulation-scheme by moving a finger along the fingerboard in the range x_f = 260~210 mm relatively to the bridge – *upward glissando* – or x_f = 210~260 mm – *downward glissando*. In this case, the bow was placed at 40 mm from the bridge. To simulate the force exerted by a moving finger on the string, the “finger” was pragmatically modelled using three spring/dashpots of adequate stiffness/dissipation at coordinates [x_f - 5 mm, x_f , x_f + 5 mm].

The results are presented in Figs. Figure 3.38 to Figure 3.41, which represent the bridge displacement, for different bowing conditions. The wolf note emerges approximately between positions 243 mm to 237 mm for the upward glissando, however it does not arise at exactly the same range for the downward glissando as can be seen in Figure 3.39.

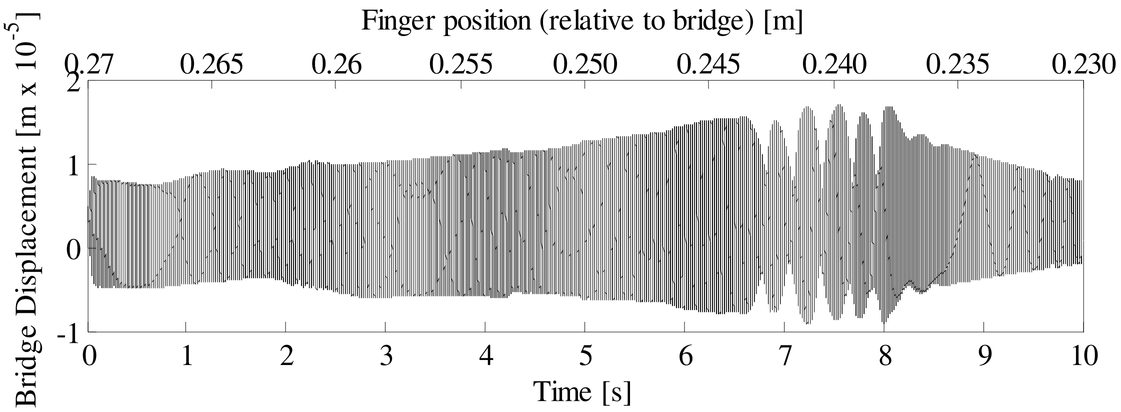

Figure 3.38 – Simulation of an upward glissando on a cello C-string with F_N = 1 N and $\dot{y}_{\text{bow}}$ = 0.05 m/s.

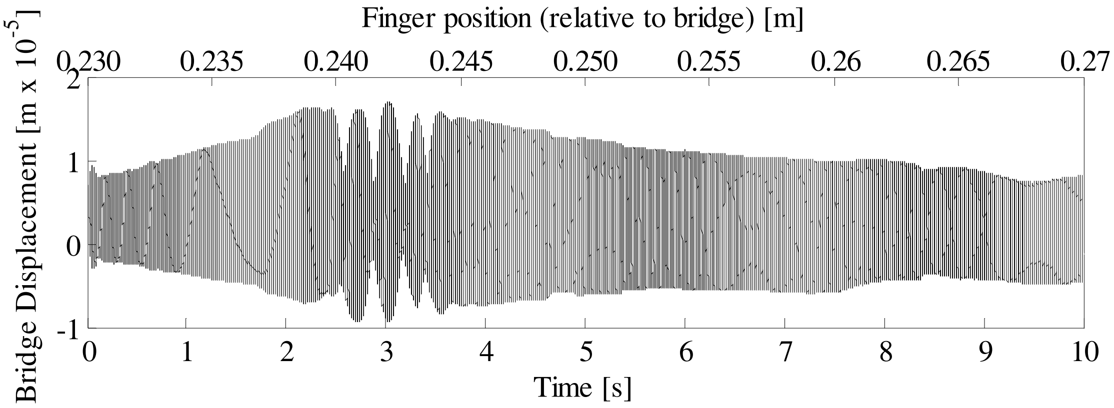

Figure 3.39 – Simulation of a downward glissando on a cello C-string with F_N = 1 N and $\dot{y}_{\text{bow}}$ = 0.05 m/s.

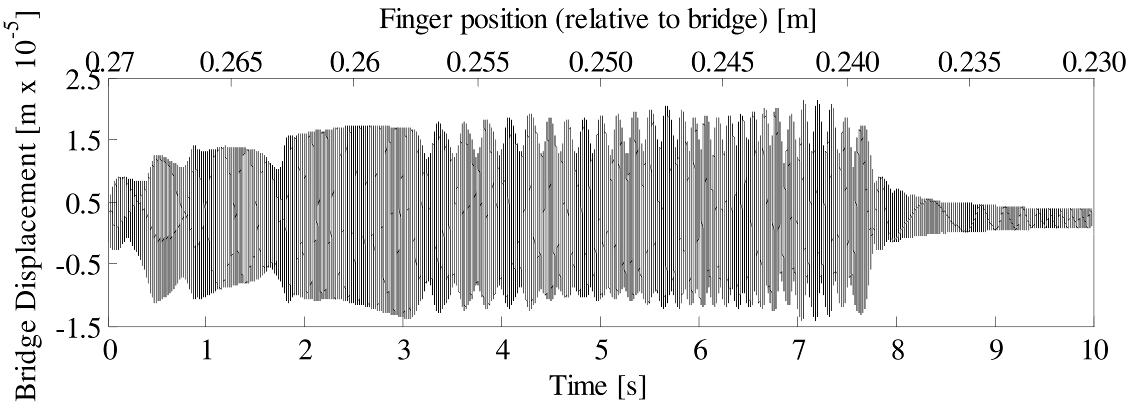

Figure 3.40 – Simulation of an upward glissando on a cello C-string with F_N = 1 N and $\dot{y}_{\text{bow}}$ = 0.1 m/s.

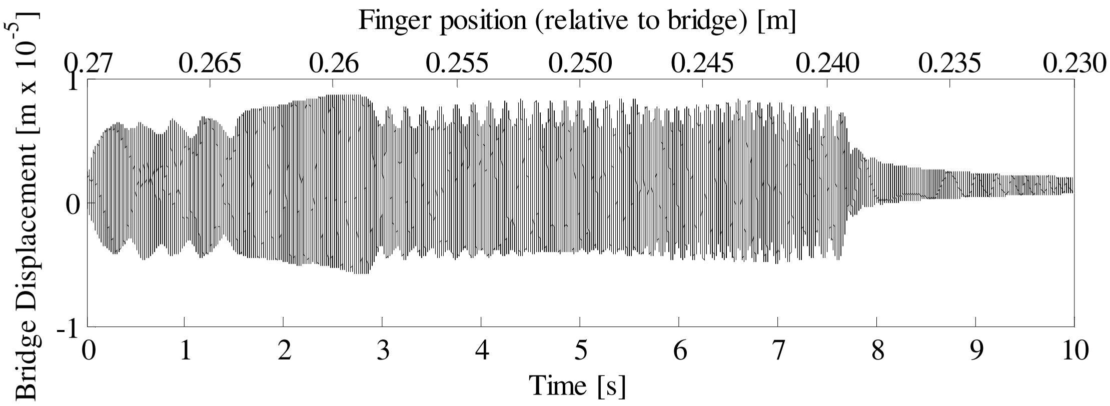

Figure 3.41 – Simulation of an upward glissando on a cello C-string with F_N = 0.5 N and $\dot{y}_{\text{bow}}$ = 0.05 m/s.

Another interesting aspect is the fact that the wolf note beating frequency changes for different bowing conditions. Increasing the bowing velocity causes an increase of the beating frequency (Figure 3.40), while higher bow normal forces tend to reduce this value. Reducing the bow normal force obviously increases the beating frequency as can be seen in Figure 3.41. This latter dependence of the beating frequency on the applied normal force was already briefly numerically demonstrated in McIntyre *et al* (1983), however no account has been found in the literature on the bow velocity-dependent beating frequency.

An interesting aspect is that the playing conditions in Figure 3.40 and Figure 3.41 seem to extend the range in which the wolf note emerges, probably associated with the complexity of the body modal response. This feature is also apparent in real-life playing in which musicians denote high difficulty in obtaining clear and repeatable wolf notes.

The explanation of the wolf note formation was first stated by Raman (1918), and later revisited by McIntyre & Woodhouse (1979), which mentions the connection between their time-domain explanation and the frequency-domain explanation by Schelleng. They explain the emergence of the wolf note in the light of the concept of minimum bow force: the continual increase of energy loss from the string due to the build-up of energy in the coupled body implies an increase in the minimum bow force necessary to establish Helmholtz motion.

If the minimum bow force needed exceeds the actual bow force, the Helmholtz motion gives way to a “double slip” regime, during which the two slips gradually get out of phase and the new slip takes over as the new Helmholtz motion. This cycle repeats itself giving origin to the characteristic wolf note sound (McIntyre & Woodhouse, 1979).

It is then tempting to link the wolf beating frequency to the conditions enabling the emergence of the double slip regime. By increasing the normal force double slips will be triggered later (or even suppressed), leading to a lower beating frequency. However, by increasing the bow velocity, double slip motions will be triggered more easily (as shown in Figure 3.49 in this section) causing an increase of the wolf beating frequency. Nevertheless, this tentative reasoning should be supported by a detailed analysis.

In order to map the space of dynamical regimes obtainable with different playing conditions, F_N and $\dot{y}_{\text{bow}}$, at the wolf note finger position, one of these input parameters was successively set to a wide range of discrete values while the other parameter values were continuously increased in an exponential time sweep. It should be clear that this approach does not intend to represent real transient behaviour, but simply parametric changes over a determined range of values (for details on bowed-string musical transients, refer to Guettler, 1997).

Figure 3.42 shows the instrument bridge displacement time-histories resulting from an exponential sweep of the bow velocity between 0.01 m/s and 1 m/s while the bow normal force is varied between 0.2 N and 10 N in discrete steps proportional to 1, 2 and 5. Figure 3.43 represents also the bridge displacement time-histories but now resulting from an exponential sweep of the bow normal force between 0.1 N and 10 N while the bow velocity is varied between 0.01 m/s and 0.5 m/s in the same proportion as in Figure 3.42. A colour scheme is used to represent the oscillation regimes that arise for different values of the input parameters.

Six regimes were found during the exponential sweeps performed: a low amplitude or inexistent oscillation; the wolf note regime; the familiar Helmholtz regime; higher order regimes characterized by multiple slips within one fundamental period; a raucous regime of chaotic oscillations; and, for a small range of input parameters, the anomalous low frequency regime (see Hanson *et al*, 1994).

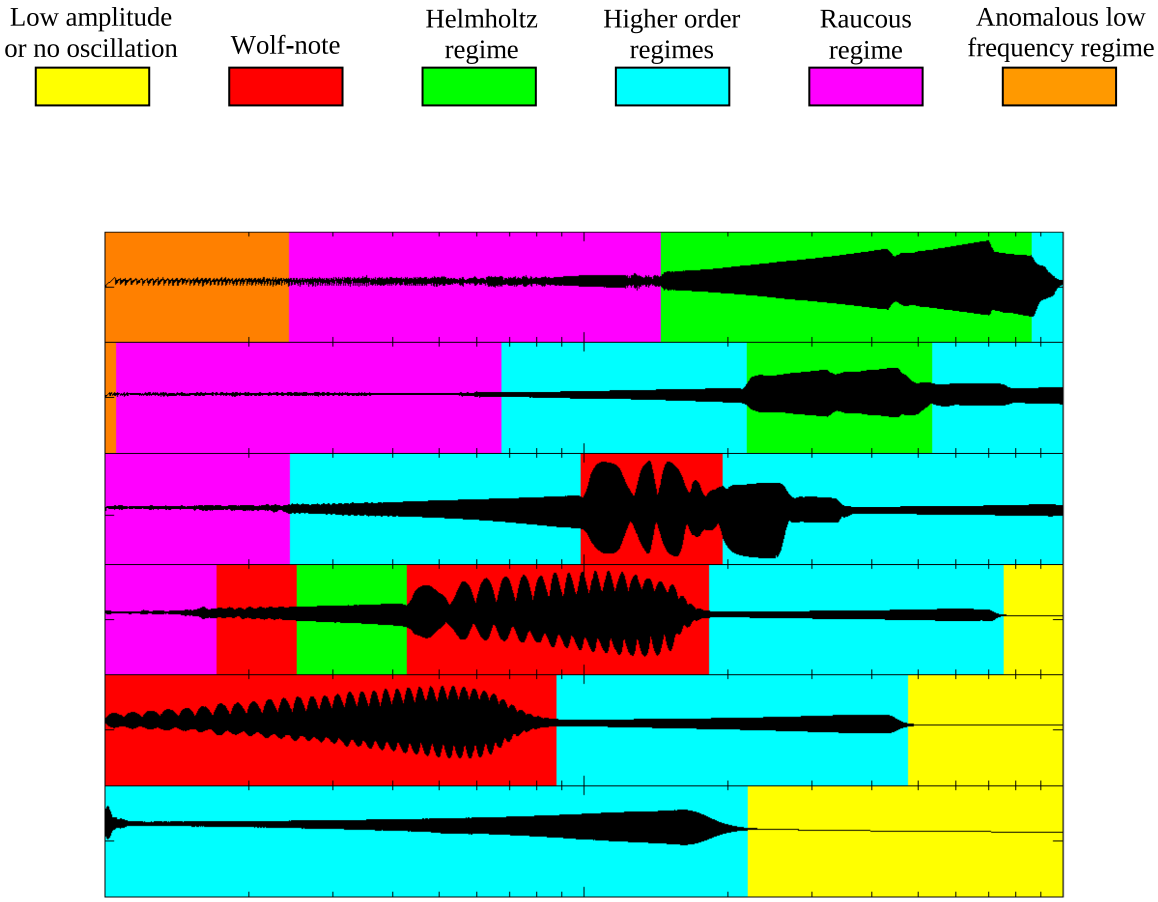

Figure 3.42 – Map of the oscillation regimes (see legend below) of a cello string bowed at the wolf note position, for discrete values of F_N and an exponential sweep of $\dot{y}_{\text{bow}}$.

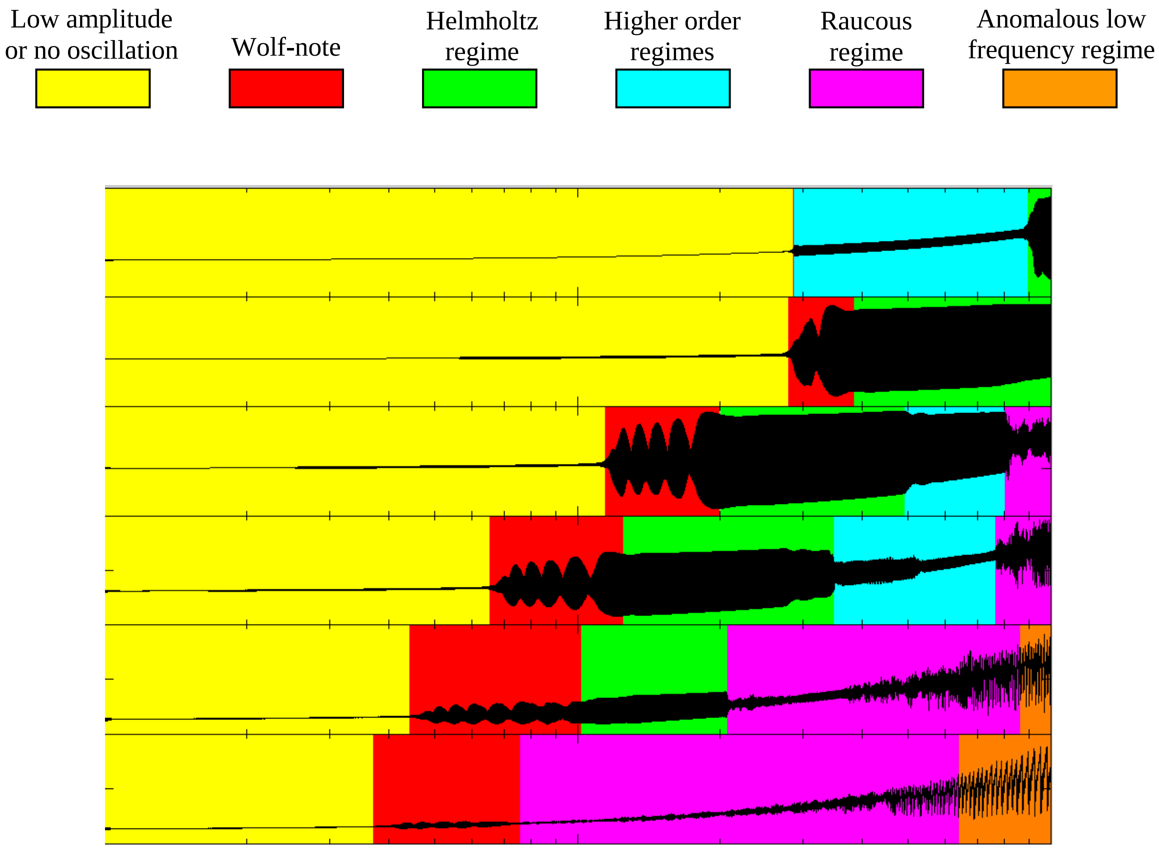

Figure 3.43 – Map of the oscillation regimes (see legend below) of a cello string bowed at the wolf note position, for discrete values of $\dot{y}_{\text{bow}}$ and an exponential sweep of F_N.

A detailed analysis of the previous figures can give some insight on the mechanism through which musicians usually try to avoid the wolf note by varying the bow playing conditions. According to these simulations, and as can be seen in Figure 3.42 and Figure 3.43, the wolf note can emerge over a large range of bow velocities and normal forces. Nevertheless, from Figure 3.42, if a bow force of 1 N is applied with a bow velocity around 0.03 m/s, Helmholtz motion is possible, as well as for higher bow velocities and normal forces. Interestingly, Figure 3.43 shows a somewhat different picture, with a large range of playing conditions leading to a very low amplitude or even non-existent oscillation, for values where in Figure 3.42 a self-sustained regime would appear. As in many nonlinear systems, various response regimes may arise, for the same driving parameter values, depending on the initial conditions of the motion. Even so, the global behaviour is similar in both figures, with other regimes, such as the anomalous low-frequency, emerging or being less excited, such as the higher-order regime. Thus, it seems probable that musicians try to escape the wolf note by using playing conditions of bow velocity or normal force outside the “wolf” range represented in the previous figures.

Another interesting and expected result is the appearance of the flattening effect (Cremer, 1984) when increasing bow normal force is applied. This feature is particularly clear in the results from the force exponential sweep. A detailed analysis (or simply listening to the sound resulting from these simulations) shows that Helmholtz motion is maintained in some regions (see Figure 3.43) but as the force increases the fundamental frequency decreases, until chaotic (raucous) motion establishes.

The dependence of the wolf beating frequency on the playing conditions, is also evident in the simulations represented in Figure 3.42 and Figure 3.43. The continuous “sweep” of bow velocity or normal force shows very clearly this dependence. Figure 3.49 and Figure 3.50 depict a detail of the time-history of bridge displacement, in which this continuous change in the wolf note frequency is apparent. Values of this frequency are shown for clarity in Figure 3.49 and Figure 3.50.

The values of the wolf note “beating” frequency were identified over short time intervals containing two “beating” periods, represented by the shaded areas in Figure 3.49 and Figure 3.50. As can be seen from the values presented and by inspection of the figures, there is a clear trend for increasing “beating” frequency as the bow velocity increases. Also, as stated before, the opposite effect occurs as the bow normal force is increased.

3.4. *Experimental results*

3.4.1 Experimental bridge responses of a cello

In order to explore the coupling between the body of the instrument and the strings, some preliminary measurements were made on a cello. Figure 3.44 shows a typical mobility frequency response function measured at the bridge in the horizontal direction as shown in Figure 3.45, through impact excitation, the bridge response being sensed by an accelerometer. The main body resonance occurs at approximately 196 Hz with a relatively low damping ratio (ζ = 0.7%) when compared with the majority of the other peaks which reveal damping ratios of the order of 2%. This high amplitude mobility peak (1.6×10^{-1} $\mathrm{ms^{-1}N^{-1}}$) is responsible for the wolf note.

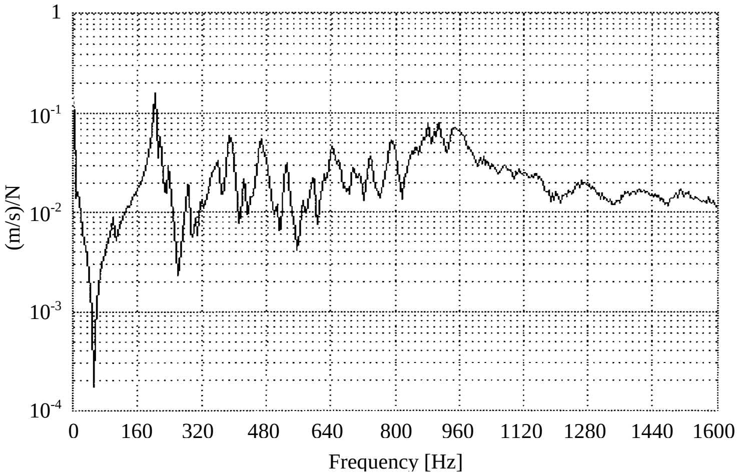

Figure 3.44 – Mobility transfer function of the cello measured at the bridge.

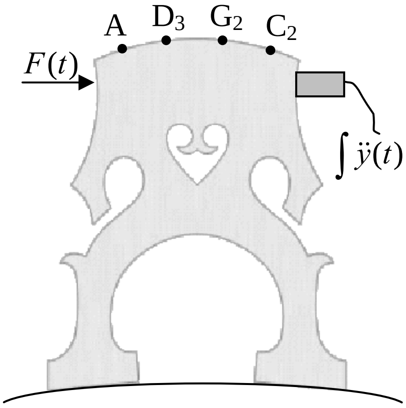

Figure 3.45 – Setup used for the transfer function measurements.

Figure 3.46 to Figure 3.48 show several typical bridge velocity responses, and corresponding spectra, to excitation by bowing on the C_2 open string (tuned to 65.4 Hz) at different notes on the fingerboard. Typical velocity amplitudes for the vibration of the bridge at the C_2 open string are shown to be of the order of 0.1~0.2 m/s. At a bowing position of approximately 40 mm from the bridge (Figure 3.46), the third harmonic is prevalent relative to the lower order partials. The proximity of its frequency to the main body resonance (3×65.4 Hz = 196.2 Hz) enhances this particular harmonic, revealing the importance of string/body coupling for normal musical regimes.

Figure 3.47 depicts the typical amplitude-modulated waveform that characterizes the wolf note. In order to achieve this sound, the C_2 string was stopped at a distance approximately $L/3$ from the bridge (where L is the length of the string), and the G_3 note was played at approximately 196 Hz. Clearly, the beating phenomena displayed is the result of strong coupling between the string vibration and the main body resonance, which is related to the proximity of their frequencies. Shortening the effective length of the string by a small amount is enough to prevent the wolf note to develop as can be seen in Figure 3.48. In this case the finger moved along the fingerboard in the direction of the bridge a few millimetres, which was enough to alter the fundamental frequency of the stopped string to 218 Hz which prevented the strong string/body coupled response.

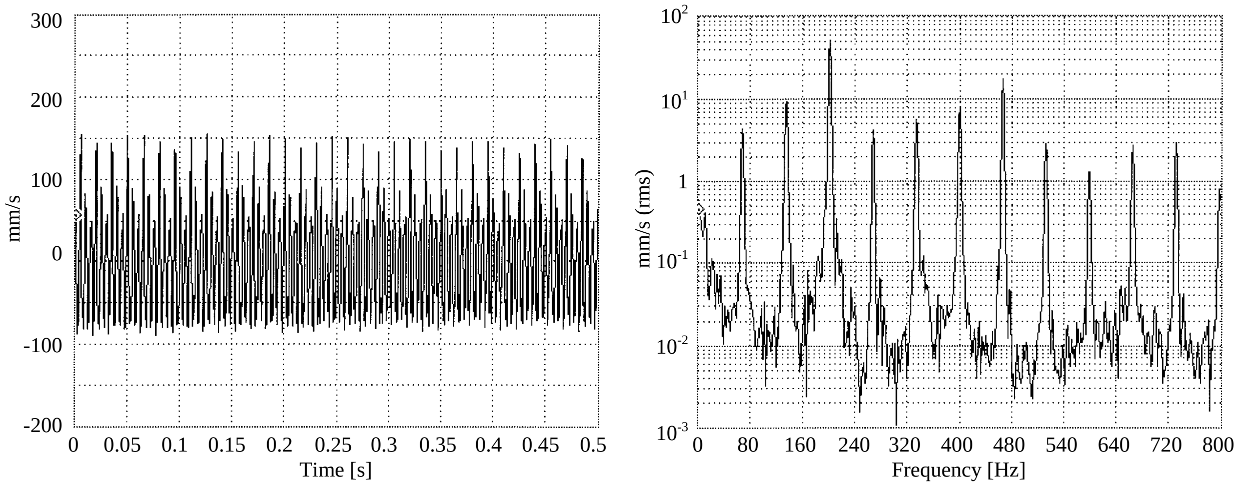

Figure 3.46 – Velocity time-history and spectrum of the bridge vibration, resulting from bowing on the C_2 open string.

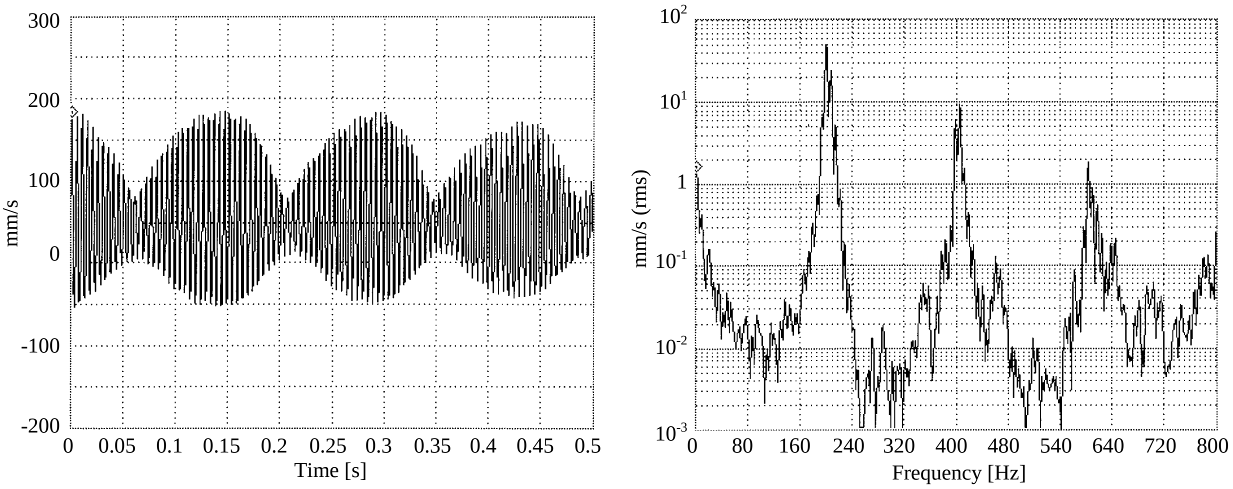

Figure 3.47 – Velocity time-history and spectrum of the bridge vibration, resulting from bowing on the C_2 string at a fingerboard position approximately *L*/3 from the bridge (generating here a wolf note).

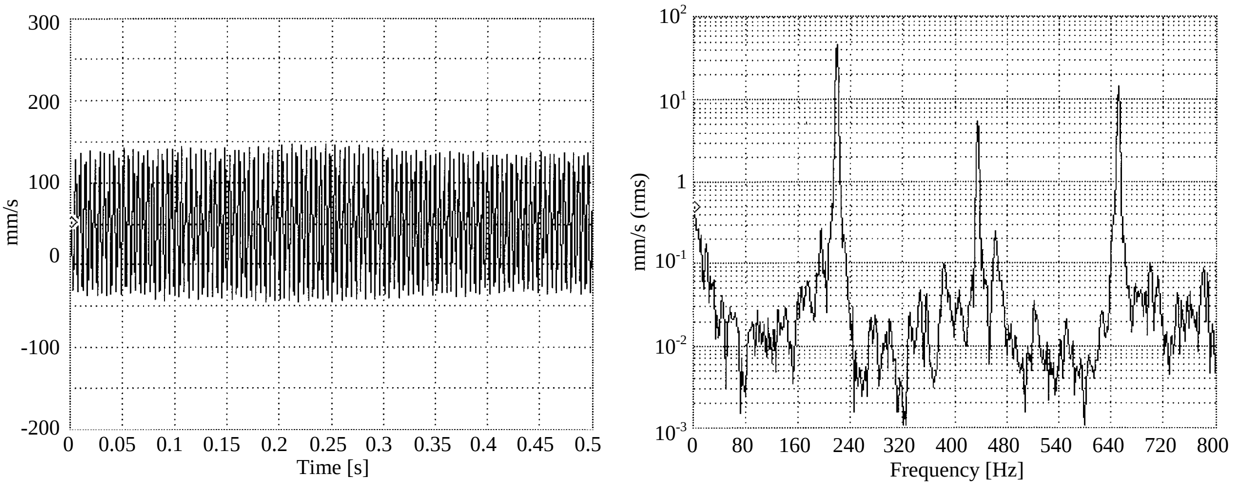

Figure 3.48 – Velocity time-history and spectrum of the bridge vibration, resulting from bowing on the C_2 string at a fingerboard position about one semitone above the wolf note (compare with Figure 3.46).

3.4.2 Experimental self-excited motions in a cello

This variation was also clearly heard in real bowing experience, and for that reason an attempt was made to obtain preliminary experimental results that could qualitatively substantiate the previous numerical simulations. Obtaining similar controlled playing conditions as the ones numerically implemented was not possible for the scope of this work. Therefore, a human playing approach was followed, and for that reason the qualitative results shown in the figures should be regarded in this light.

Figure 3.51 and Figure 3.52 show the time history of the uncalibrated sound pressure measured at 40 cm from the bridge of a cello (the same that was used to obtain the frequency response in Figure 3.33), when playing a wolf note under varying playing conditions. For the results of Figure 3.51 an attempt was made to keep the applied normal force constant and continuously increasing (as steady as possible) the bow velocity, while in Figure 3.52 the normal force was increased and the velocity kept approximately constant. These results are clear in showing the same trend as in Figure 3.49 and Figure 3.50, apart from some deviations due to the difficulties in accurately controlling the playing parameters.

From the various bow strokes realized during these experiments, other aspects were found which are in accordance (at least qualitatively) with the change in regimes depicted in Figure 3.42 and Figure 3.43. During most of the strokes in which the bow velocity was continuously increased, the wolf note would change to a higher order regime after a limiting bow velocity (as also seen Figure 3.42). On the other hand, the increase of normal force also showed the emergence of the Hemholtz regime after the wolf note, and if the bow force was further increased, the Helmholtz regime would give rise, as expected, to a raucous regime.

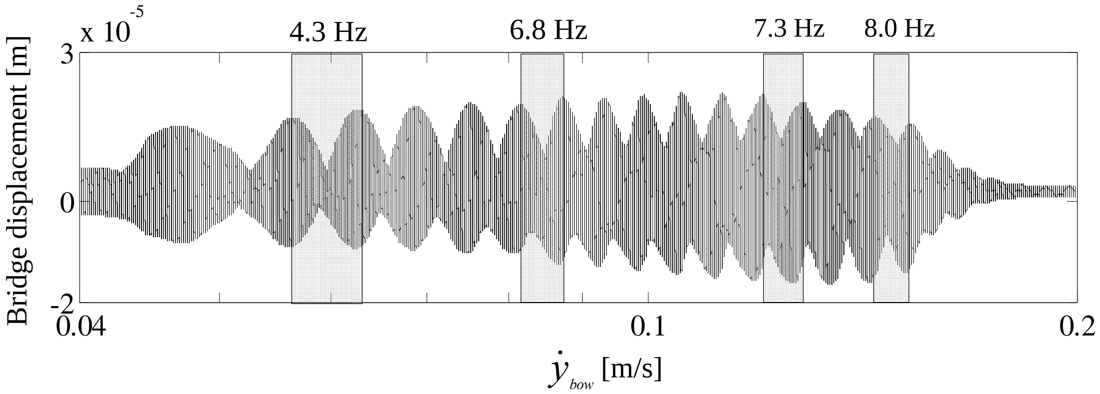

Figure 3.49 – Detail of the time-history of the cello string oscillation during the wolf note regime played with F_N = 1 N with increasing $\dot{y}_{\text{bow}}$

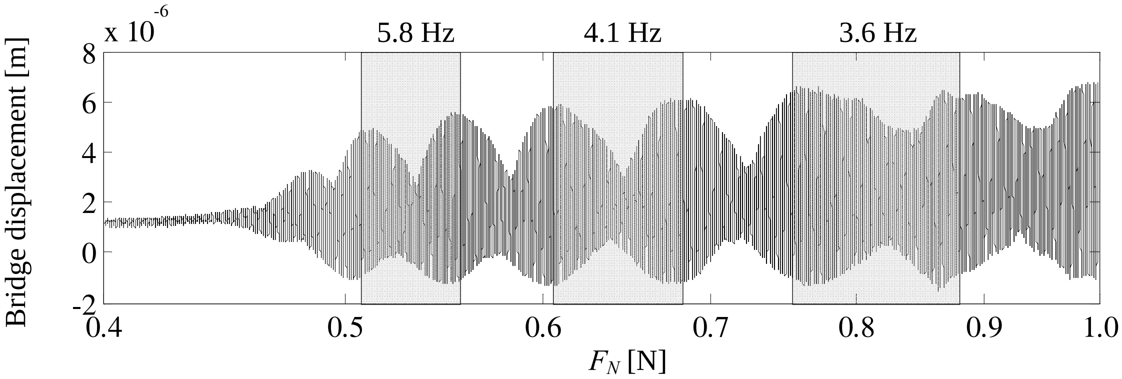

Figure 3.50 – Detail of the time-history of the cello string oscillation during the wolf note regime played with $\dot{y}_{\text{bow}}$ = 0.1 m/s, with increasing F_N.

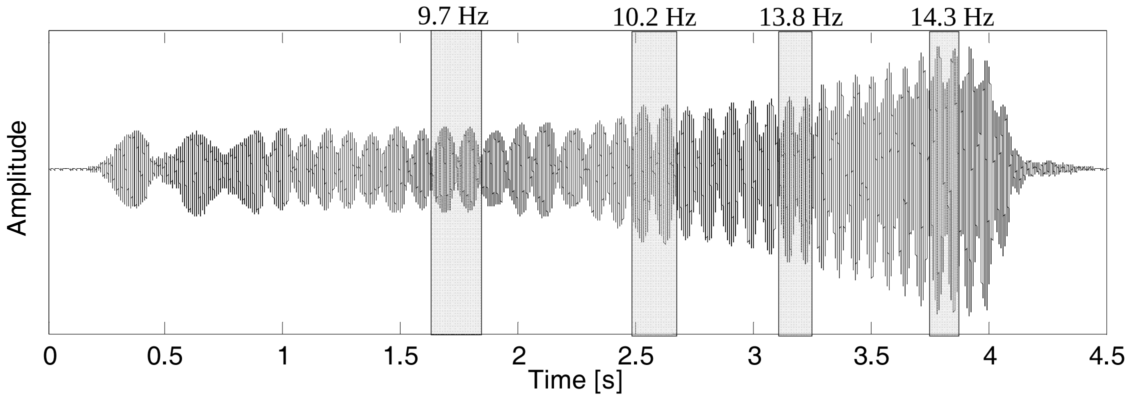

Figure 3.51 – Measured sound pressure time-history of a wolf note regime played with increasing $\dot{y}_{bow}$ and approximately constant F_N.

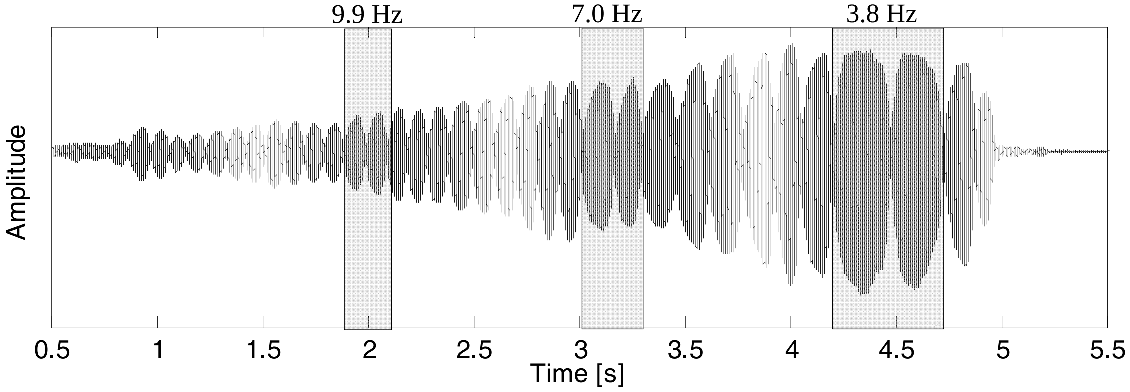

Figure 3.52 – Measured sound pressure time-history of the wolf note regime played with increasing FN and approximately constant $\dot{y}_{bow}$.

3.5. Modal behaviour of the string/body coupled system

Detailed interpretation of the numerical simulations presented in the previous sections depends on the modal behaviour of the string/body coupled system. Therefore, in this section a description of how those coupled modes may be computed is made, presenting some representative results pertaining to the violin configuration. First the string constrained by a "rigid" bridge (meaning that $y_b(x_b,t)=0$) is addressed, and the dependence of the constrained modes on the constraining parameters is investigated. Then the modal behaviour of the full string/body coupled problem is analyzed, with $y_b(x_b,t)$ given by the body motion at the bridge location, highlighting a few interesting features of the coupled modes.

3.5.1 String constrained at the bridge

The dynamical behaviour of the string constrained at the bridge is described in terms of **(3.6)** to **(3.11)** and the constraint force (3.23) with $y_b(x_b,t)=0$,

$$\left[\mathbf{M}\right]\left\{\ddot{\mathbf{Q}}(t)\right\}+\left[\mathbf{C}\right]\left\{\dot{\mathbf{Q}}(t)\right\}+\left[\mathbf{K}\right]\left\{\mathbf{Q}(t)\right\}=-C_{bs}\left[\Phi(x_b)\right]\left\{\dot{\mathbf{Q}}(t)\right\}-K_{bs}\left[\Phi(x_b)\right]\left\{\mathbf{Q}(t)\right\} \tag{3.26}$$

Where, as before, matrices $\left[\mathbf{M}\right]=\mathrm{diag}(m_1,\cdots,m_N)$, $\left[\mathbf{C}\right]=\mathrm{diag}(2\,m_1\omega_1\,\zeta_1,\cdots,2\,m_N\omega_N\,\zeta_N)$ and $\left[\mathbf{K}\right]=\mathrm{diag}(m_1\omega_1^2,\cdots,m_N\omega_N^2)$ pertain to the modal parameters of the unconstrained string, pinned at the tailpiece and the nut, while $\left\{\mathbf{Q}(t)\right\}=\left\langle q_1(t),\cdots,q_N(t)\right\rangle^T$ is the vector of modal responses. The right hand-side terms stem from the modal projections **(3.7)** of the constraining force (3.23) at the bridge, accounting for the physical response **(3.11)** of the string at the bridge location x_b, whence the coupling matrix

$$\left[\Phi(x_b)\right]=\left\{\varphi_n(x_b)\right\}\left\{\varphi_n(x_b)\right\}^T=\begin{bmatrix}\varphi_1(x_b)\varphi_1(x_b) & \varphi_1(x_b)\varphi_2(x_b) & \cdots & \varphi_1(x_b)\varphi_N(x_b)\\ \varphi_2(x_b)\varphi_1(x_b) & \varphi_2(x_b)\varphi_2(x_b) & \cdots & \varphi_2(x_b)\varphi_N(x_b)\\ \vdots & \vdots & \ddots & \vdots\\ \varphi_N(x_b)\varphi_1(x_b) & \varphi_N(x_b)\varphi_2(x_b) & \cdots & \varphi_N(x_b)\varphi_N(x_b)\end{bmatrix} \tag{3.27}$$

where $\left\{\varphi_n(x_b)\right\}\equiv\left\langle\varphi_1(x_b)\quad\varphi_2(x_b)\quad\cdots\quad\varphi_N(x_b)\right\rangle^T$ stands for the modeshapes, at the bridge location, of the unconstrained string.

From (3.26),

$$\left[\mathbf{M}\right]\left\{\ddot{\mathbf{Q}}(t)\right\}+\left[\left[\mathbf{C}\right]+C_{bs}\left[\Phi(x_b)\right]\right]\left\{\dot{\mathbf{Q}}(t)\right\}+\left[\left[\mathbf{K}\right]+K_{bs}\left[\Phi(x_b)\right]\right]\left\{\mathbf{Q}(t)\right\}=\left\{\mathbf{0}\right\} \tag{3.28}$$

And, assuming free-response solutions of the form $\left\{\mathbf{Q}(t)\right\}=\left\{\Psi_n^Q\right\}\exp(\lambda_n t)$, the following quadratic eigen-problem is obtained

$$\left[\lambda_n^2\left[\mathbf{M}\right]+\lambda_n\left[\left[\mathbf{C}\right]+C_{bs}\left[\Phi(x_b)\right]\right]+\left[\left[\mathbf{K}\right]+K_{bs}\left[\Phi(x_b)\right]\right]\right]\left\{\Psi_n^Q\right\}=\left\{\mathbf{0}\right\} \tag{3.29}$$

which can be easily converted into an equivalent first-order (state-space) form and then readily solved using standard procedures. Equation (3.30) is one possible symmetrical form, among others – see, for instance Bertolini (1998).

$$\left(\lambda_n\begin{bmatrix}\left[\left[\mathbf{C}\right]+C_{bs}\left[\Phi(x_b)\right]\right] & \left[\mathbf{M}\right]\\ \left[\mathbf{M}\right] & \left[\,\mathbf{0}\,\right]\end{bmatrix}+\begin{bmatrix}\left[\left[\mathbf{K}\right]+K_{bs}\left[\Phi(x_b)\right]\right] & \left[\,\mathbf{0}\,\right]\\ \left[\,\mathbf{0}\,\right] & -\left[\mathbf{M}\right]\end{bmatrix}\right)\begin{Bmatrix}\left\{\Psi_n^Q\right\}\\ \lambda_n\left\{\Psi_n^Q\right\}\end{Bmatrix}=\begin{Bmatrix}\left\{\mathbf{0}\right\}\\ \left\{\mathbf{0}\right\}\end{Bmatrix} \tag{3.30}$$

The eigenvalues and corresponding eigenvectors obtained from (3.30) are in general complex and, for oscillating solutions, arise in conjugate pairs $\lambda_n=\hat{\sigma}_n\pm i\hat{\omega}_n$. The (damped) modal frequencies $\hat{\omega}_n=\mathrm{Im}(\lambda_n)$ and modal dissipation values $\hat{\sigma}_n=\mathrm{Re}(\lambda_n)$ reflect the linear dynamics of the dissipative coupled system, in terms of the constraint parameters K_{bs} and C_{bs}. The undamped modal frequencies $\hat{\omega}_{n0}$ and modal damping values $\hat{\zeta}_n$ of the constrained string may be inferred from the various λ_n using the following relations

$$\hat{\omega}_{n0} = \sqrt{\hat{\sigma}_n^2 + \hat{\omega}_n^2} \qquad ; \qquad \hat{\zeta}_n = -\frac{\hat{\sigma}_n}{\sqrt{\hat{\sigma}_n^2 + \hat{\omega}_n^2}} \tag{3.31}$$

and one obtains $\hat{\omega}_n = \hat{\omega}_{n0}\sqrt{1-\hat{\zeta}_n^2}$, as usual. After obtaining the eigenvectors $\left\{\Psi_n^Q\right\}$ of the coupled system in terms of the modal amplitude coefficients of the original string modes, one can easily express the corresponding modeshapes $\left\{\Psi_n^Y\right\}$ in terms of physical amplitudes by recombination of the unconstrained modeshapes

$$\left\{\Psi_n^Y\right\} = \left[\left\{\varphi_1\right\}, \left\{\varphi_2\right\}, \ldots, \left\{\varphi_N\right\}\right]\left\{\Psi_n^Q\right\} \quad , \quad n = 1, 2, \ldots, N \tag{3.32}$$

Figure 3.53 and Figure 3.54 show the changes in the string modal frequencies and damping values respectively, as the bridge constraining stiffness K_{bs} increases in the range $10 \sim 10^7$ Nm^{-1} with no coupling dissipation ($C_{bs} = 0$), for the first nine modes. One may notice that modal frequencies behave as an almost harmonic series for very the lowest values of K_{bs}, meaning that the bridge is then barely “felt” by the string. On the opposite extreme, when $K_{bs} > 10^6$ Nm^{-1}, further increase in the constraining stiffness brings no significant changes, as for all practical purposes, the bridge is already “rigid” as far as the string is concerned. Again, the highly constrained string modal frequencies are almost harmonic, except for a mode at 1224 Hz, which will be explained later. All the modal frequencies increase with K_{bs}, as they should, system inharmonicity being maximal at about $K_{bs} \simeq 5\times10^3$ N/m, when the bridge is far from “rigid” but already a significant constraint.

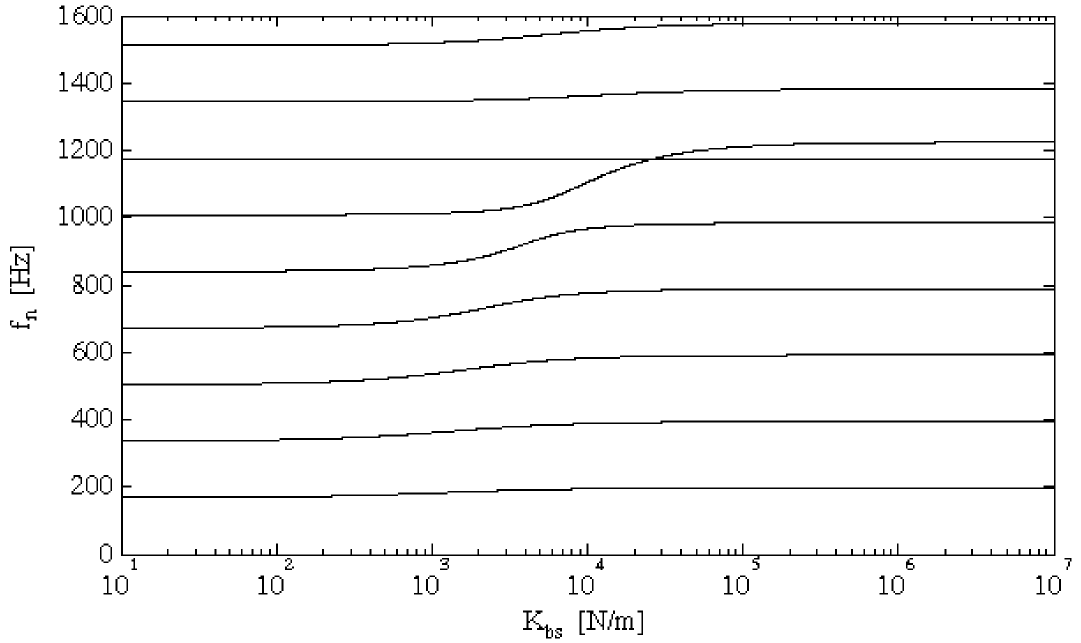

Figure 3.53 – Modal frequencies of the string modes constrained at the bridge, as a function of the stiffness coupling constant K_{bs} (with $C_{bs} = 0$)

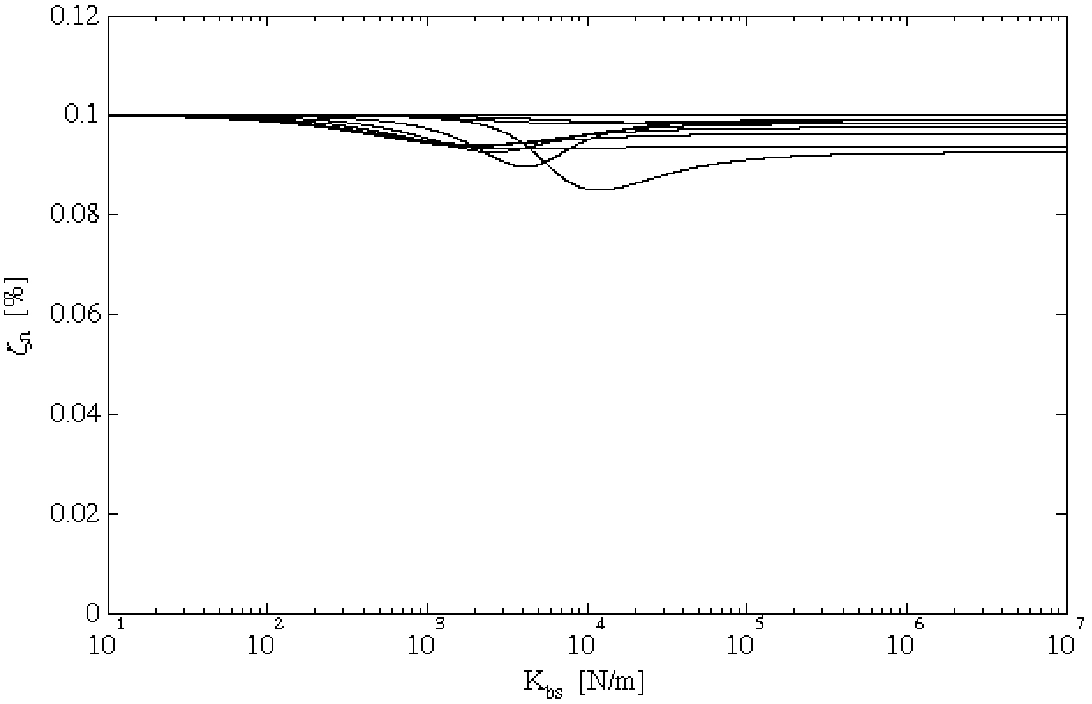

Figure 3.54 – Modal damping of the string modes constrained at the bridge, as a function of the stiffness coupling constant K_{bs} (with $C_{bs} = 0$)

From Figure 3.54 it appears that the modal damping values of the constrained modes are almost independent from K_{bs} when $C_{bs} = 0$, and always slightly lower than those of the original (unconstrained) string modes (here 0.1 % was postulated for all modes). However, as shown in Fig. A3, the scenario is considerably different when C_{bs} is not nil (here $C_{bs} = 10$ Nsm^{-1}), because significant energy is then damped out when the constraining stiffness is low enough to allow for string motions at the bridge location. Notice that, for high values $K_{bs} > 10^6$ Nm^{-1}, modal damping of the constrained modes does not depend whatsoever on C_{bs} and only reflect the modal damping values of the original modes.

To conclude this section Figure 3.55 displays the modeshapes of the first nine constrained modes, computed from (3.30) and (3.32), when the bridge behaves as an almost-rigid constraint ($K_{bs} = 10^7$ Nm^{-1}). Notice that for most modes in this frequency range the modal amplitudes are only significant between the nut and the bridge, the string length between the bridge and the tailpiece being only marginally active, which is well consistent with the near-harmonic series obtained for the constrained modal frequencies. The only exceptions (in this frequency range) being the 6th mode, with its modal frequency barely affected by the string motion on the tailpiece-side (because the bridge naturally stands at a node), and mostly the 7th mode. Indeed, this mode is strongly dominated by a localized tailpiece-side response, and hence displays a modal frequency mostly related to the bridge-tailpiece distance. Obviously, this is the mode which breaks the harmonic series of the modal frequencies displayed by the right side of Figure 3.53.

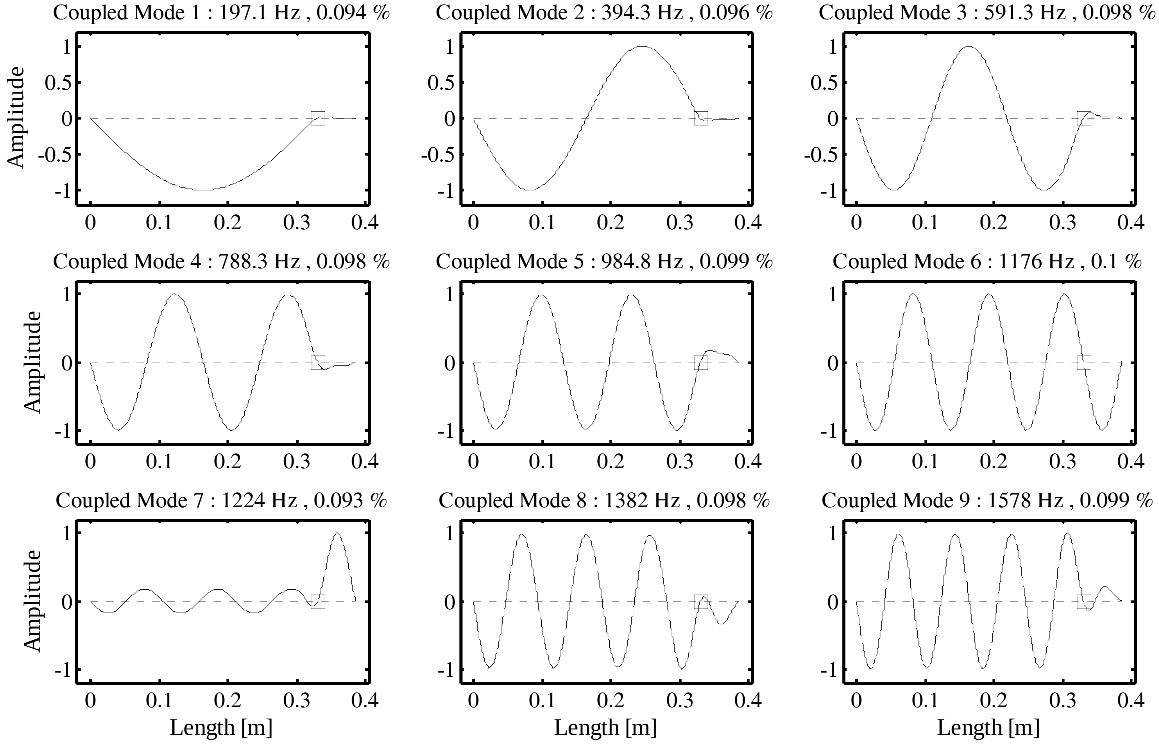

Figure 3.55 – Modeshapes of the first string modes constrained at an almost-rigid bridge, represented by a square ($K_{bs} = 10^7$ Nm^{-1}).

3.5.2 String/body coupled modes

The coupled modes of the string/body system can be addressed in a similar manner as in the previous section. Formulation follows similar lines to the previous presentation, although – because now $y_b(x_b,t) \neq 0$ – the modal parameters of the P body modes must obviously be included. Then, from equations **(3.6)-(3.11)** and **(3.21)**-(3.23), the coupled system becomes

$$\begin{bmatrix} \mathbf{M} & \mathbf{0} \\ \mathbf{0} & \mathbf{M}_B \end{bmatrix} \begin{Bmatrix} \{\ddot{\mathbf{Q}}(t)\} \\ \{\ddot{\mathbf{Q}}_B(t)\} \end{Bmatrix} + \begin{bmatrix} \mathbf{C} & \mathbf{0} \\ \mathbf{0} & \mathbf{C}_B \end{bmatrix} \begin{Bmatrix} \{\dot{\mathbf{Q}}(t)\} \\ \{\dot{\mathbf{Q}}_B(t)\} \end{Bmatrix} + \begin{bmatrix} \mathbf{K} & \mathbf{0} \\ \mathbf{0} & \mathbf{K}_B \end{bmatrix} \begin{Bmatrix} \{\mathbf{Q}(t)\} \\ \{\mathbf{Q}_B(t)\} \end{Bmatrix} =$$
$$= -C_{bs} \begin{bmatrix} \Phi_{SS}(x_b) & \Phi_{SB}(x_b) \\ \Phi_{BS}(x_b) & \Phi_{BB}(x_b) \end{bmatrix} \begin{Bmatrix} \{\dot{\mathbf{Q}}(t)\} \\ \{\dot{\mathbf{Q}}_B(t)\} \end{Bmatrix} - K_{bs} \begin{bmatrix} \Phi_{SS}(x_b) & \Phi_{SB}(x_b) \\ \Phi_{BS}(x_b) & \Phi_{BB}(x_b) \end{bmatrix} \begin{Bmatrix} \{\mathbf{Q}(t)\} \\ \{\mathbf{Q}_B(t)\} \end{Bmatrix} \tag{3.33}$$

with the coupling sub-matrices

$$\left[\Phi_{SS}(x_b)\right]=\left\{\varphi_n(x_b)\right\}\left\{\varphi_n(x_b)\right\}^T \quad ; \quad \left[\Phi_{SB}(x_b)\right]=-\left\{\varphi_n(x_b)\right\}\left\{\phi_p(x_b)\right\}^T \tag{3.34}$$
$$\left[\Phi_{BS}(x_b)\right]=-\left\{\phi_p(x_b)\right\}\left\{\varphi_n(x_b)\right\}^T \quad ; \quad \left[\Phi_{BB}(x_b)\right]=\left\{\phi_p(x_b)\right\}\left\{\phi_p(x_b)\right\}^T$$

where $\left\{\phi_p(x_b)\right\}$ is the vector of the body modeshape values at the bridge location (here taken as unity, following the normalization procedure adopted).

Equation (3.33) is of the form (3.26), although obviously the system size is now $N+P$. Therefore the corresponding eigenproblem may also be written in form (3.29) or (3.30), from which the string/body coupled modes are computed. Notice that the coupling matrix built from (3.34) is symmetrical, as it should. This, however, is no guarantee that the coupled modes will display real modeshapes – and indeed, as will be shown later, complex modes are the rule here more than the exception.

Figure 3.56 displays the change of the string/body modal frequencies as the stiffness coupling constant K_{bs} increases. These computations are based on the same unconstrained string modes as before, while Table 3.1 presents the modal frequencies and damping values used for the first few body modes used in this calculation. Notice that these body modes display damping values typically one order of magnitude higher than the uncoupled string modes.

Essentially the left side of the plot shows the string and body modes when they are almost uncoupled, while the right side of the plot shows the string and body almost rigidly coupled at the bridge. In-between, the interplay of the modal frequencies stems from increasing coupling. Understandably, the string modal frequencies change significantly as K_{bs} increases, while the body modal frequencies are hardly affected.

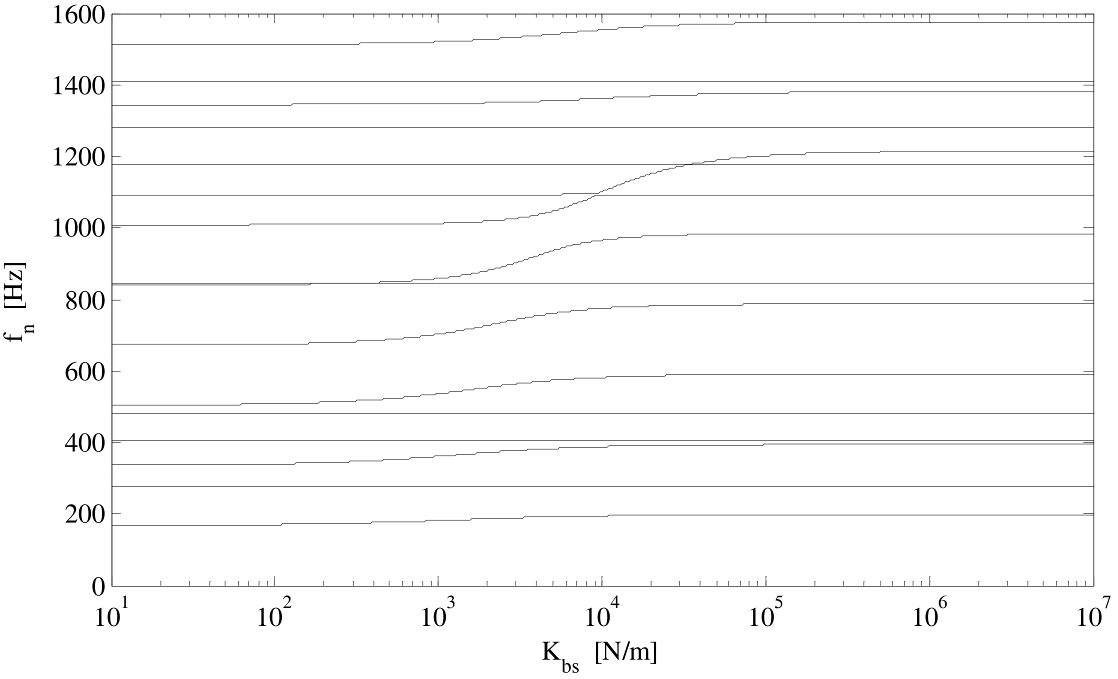

Figure 3.56 – Modal frequencies of the string/body coupled modes, as a function of the stiffness coupling constant K_{bs} at the bridge (with $C_{bs} = 0$).

At the modal frequencies controlled by the body, the bridge presents a lower impedance to the string, so that the coupled modes don’t display any more a node at the bridge location. This is demonstrated in Figure 3.57, which shows the first 9 modes of the coupled system (using $K_{bs} = 10^7$ Nm^{-1}) – see modes 2, 4, 5 and 8. Also notice that, the coupled string/body modes are complex, as the energy dissipation from the string will be mainly localized at the bridge, and hence damping is non-proportional. This is particularly significant for the coupled modes controlled by the body motion, as shown in Figure 3.57, where the modeshapes have been normalized at unity for the maxima of their real part, the corresponding imaginary part being plotted with a dotted line.

Table 3.1 – Body first modal frequencies and damping values

Mode	1	2	3	4	5
Frequency [Hz]	276.5	404.0	480.7	846.5	1093.0
Damping [%]	2	3	1	1	1

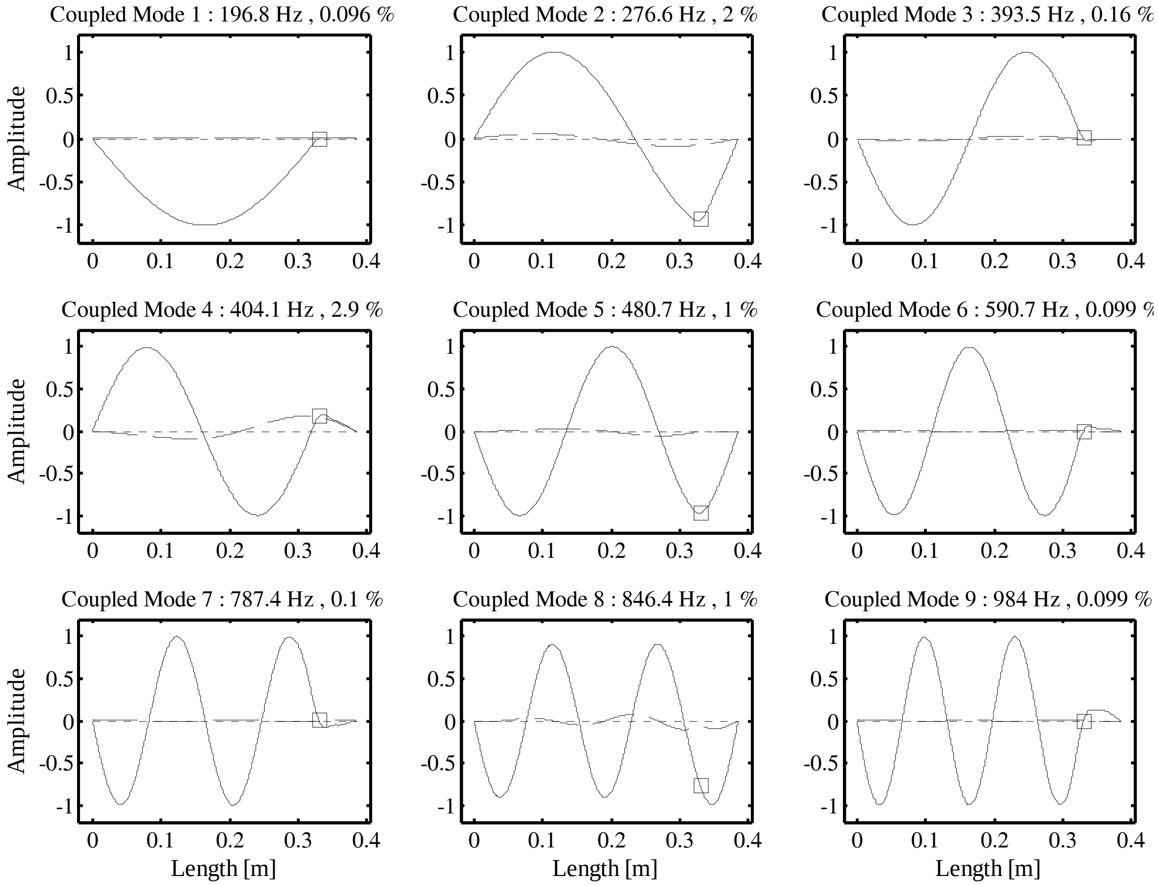

Figure 3.57 – Complex modeshapes of the first string/body coupled modes, where the square represents the bridge ($K_{bs} = 10^7$ Nm^{-1}).

Concerning the modal damping of the coupled modes on may notice that, when the bridge is almost still, the modal damping values are essentially those of the uncoupled string modes. Also understandably, when the coupled modes are controlled by the body, damping values are essentially those of the corresponding body modes. As thoroughly discussed by Woodhouse (2004), if the system damping is modelled in a satisfying manner, such typically scenario should be displayed even when two coupled “string-controlled” and “body-controlled” modes present close frequencies, as the orders of magnitude of their respective damping values should respect those of the decoupled substructures. An illustration is provided by modes 3 and 4 in Figure 3.57, even so, the 60% damping increase in the “string-controlled” mode is enough to produce some of the visible changes in the response shown in Figure 3.37(b).

Chapter 4

BOWED BARS: MARIMBAS & VIBRAPHONES

4. BOWED BARS: MARIMBAS & VIBRAPHONES

4.1. Introduction

In this chapter, a thorough description of the implementation of the simulation method for bowed bars is presented. Both tuned and constant cross-section bars are studied and the self-sustained regimes emerging from different playing conditions are presented.

4.2. Computational Model

4.2.1 Modal model for bending bars

The cross-sectional dimensions of bars used in percussion musical instruments are not usually small compared to their length. In fact, as modal frequencies increase, the Bernoulli-Euler slender beam model becomes progressively inadequate. Therefore, flexural modes are here modelled in terms of the Timoshenko thick-beam model, which corrects for the effects of rotary inertia and shear deformation (Graff, 1975). Although torsional and axial vibrations are also present in the dynamics of this system, only flexural vibration modes will be addressed in this study. Thus, for small vibratory motions, the transverse displacement $y(x,t)$ and slope $\phi(x,t)$ of the free conservative system are formulated as:

$$\rho A(x)\frac{\partial^2 y}{\partial t^2}+kGA(x)\left(\frac{\partial\phi}{\partial x}-\frac{\partial^2 y}{\partial x^2}\right)=0 \qquad (4.1)$$

$$\rho I(x)\frac{\partial^2\phi}{\partial t^2}-EI(x)\frac{\partial^2\phi}{\partial x^2}+kGA(x)\left(\phi-\frac{\partial y}{\partial x}\right)=0 \qquad (4.2)$$

where $A(x)$ and $I(x)$ are the local bar cross-section area and moment of inertia, respectively, ρ is the specific mass of the bar material, E is the Young modulus, G is the shear modulus and k is a geometric factor for shear energy (equal to $5/6$ for rectangular cross-sections). Inertial and stiffness terms can be easily recognized in equations (4.1) and (4.2).

If linear dissipation is assumed, any solution of (4.1) can be written in terms of the beam modal parameters: modal masses m_n, modal circular frequencies ω_n, modal damping ζ_n, and modeshapes $\varphi_n(x)$, $n=1,2,\cdots,N$. The order N of the modal truncation is problem-dependent and must be asserted by physical reasoning, supported by the convergence of computational results. The forced response of a damped bar can then be formulated as a set of N ordinary second-order differential equations:

$$[M]\{\ddot{Q}(t)\}+[C]\{\dot{Q}(t)\}+[K]\{Q(t)\}=\{\Xi(t)\} \tag{4.3}$$

where: $[M]=\mathrm{Diag}(m_1,\cdots,m_N)$, $[C]=\mathrm{Diag}(2m_1\omega_1\zeta_1,\cdots,2m_N\omega_N\zeta_N)$ and $[K]=\mathrm{Diag}(m_1\omega_1^2,\cdots,m_N\omega_N^2)$ are matrices of the modal parameters, and $\{Q(t)\}=\langle q_1(t),\cdots,q_N(t)\rangle^T$, $\{\Xi(t)\}=\langle\Im_1(t),\cdots,\Im_N(t)\rangle^T$ are vectors of the modal responses and the generalized forces, respectively.

The modal damping values ζ_n are usually identified from experiments; however, they may eventually be theoretically estimated (Fletcher & Rossing, 1998). The modal forces $\Im_n(t)$ are obtained by projecting the external force field on the modal basis:

$$\Im_n(t)=\int_0^L F(x,t)\,\varphi_n(x)\,dx \quad ; \quad n=1,2,\cdots,N \tag{4.4}$$

The physical motions can be computed from the modal amplitudes $q_n(t)$ by superposition:

$$y(x,t)=\sum_{n=1}^{N}\varphi_n(x)\,q_n(t) \tag{4.5}$$

and similarly concerning the velocities and accelerations. For given external excitation and initial conditions, the previous system of equations can be integrated using an adequate time-step integration algorithm. Explicit integration methods are well suited for the friction model developed here.

In this implementation, a simple Verlet integration algorithm is used (Beeman, 1976), which is a second order explicit scheme. Note that, although equations (4.3)-(4.5) obviously pertain to a linear formulation, nothing prevents us from including in $\Im_n(t)$ all nonlinear effects arising in the system. Accordingly, the system modes become coupled by the nonlinear effects.

4.2.2 Friction Model

For the present system, the same friction model as described in section 2.3.1 and 2.3.2 is used. Considering the Coulomb-type friction force arising when the bow is applied at location x_c of the bar:

$$\begin{cases} F_s(x_c,t) = -\mu_d(\dot{y}_c) F_N \,\mathrm{sgn}(\dot{y}\ ) \,; & \text{if } \left|\dot{y}_c\right| > 0 \\ \left|F_a(x_c,t)\right| < \mu_S F_N & ; \text{ if } \left|\dot{y}_c\right| = 0 \end{cases} \tag{4.6}$$

Here, the relative transverse velocity between the bow and the bar is given by (see Figure 4.1):

$$\dot{y}_c = \dot{y}(x_c,t) - \dot{y}_{bow}(t) = \sum_{n=1}^{N} \varphi_n(x_c)\, \dot{q}_n(t) - \dot{y}_{bow}(t) \tag{4.7}$$

where $F_N(t)$ is the normal force between the bow and the bar, μ_S is a “static” friction coefficient (used during surface adherence) and $\mu_d(\dot{y}_c)$ is a “dynamic” friction coefficient (used for sliding regimes).

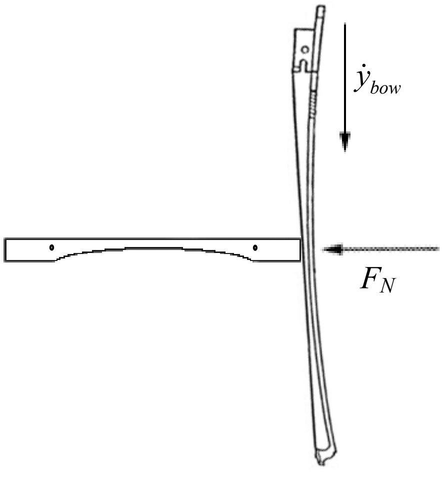

Figure 4.1 - Scheme of the bow/bar interaction: Normal force F_N ; Tangential bow velocity $\dot{y}_{bow}$

The numerical implementation of this friction model is made as described in section 2.3.2.

4.2.3 Modal and Friction Parameters

The numerical simulations presented in this chapter were performed for a *A_3 vibraphone bar* (with fundamental frequency f_1 = 220.4 Hz), with an undercut leading to approximate 1-4-10 harmonic relationships of the three first bending modal frequencies, and also for an aluminum *bar of constant cross-section*, with the same fundamental but with inharmonic modal frequency relationships. This will enable us to compare the influence of the tuning undercut on the oscillation regimes of the bowed bars.

In order to construct the modal basis for the simulations of both bars, it is necessary to calculate or measure its modal parameters m_n , ω_n , ζ_n and modeshapes $\varphi_n(x)$, $n = 1, 2, \cdots, N$.

The modal basis used in the simulations of the bars were obtained from two different procedures: 1) an experimental procedure for the identification of modal frequencies and modal damping for the vibraphone 1-4-10 bar; 2) a numerical procedure based on the finite element method for determination of modal parameters for the constant cross-section and unorthodox tuning bars.

The modal frequencies, ω_n, and modal damping, ζ_n, of the *A_3 vibraphone bar* were identified by measuring the transfer function between the acceleration response of the bar and the impulse excitation provided by an instrumented impact hammer (see section 4.4.1). The measurements were carefully performed in order to distinguish bending modes from torsion modes which are not included in the present computational model. The modeshapes $\varphi_n(x)$ were then calculated using finite element methods, as applied to the geometries of both bars. The modal masses were then computed according to:

$$m_n = \int_0^L m(x)\ \varphi_n^2(x)\ dx \tag{4.8}$$

The fundamental frequency, f_1 (220.4 Hz) and the damping values ζ_n used in all the computations (for both the constant section and the vibraphone bar) are those experimentally identified for the vibraphone bar. Modal damping is low, at an average value of 0.02 %. Table 4.1 shows the modal frequencies identified for the free-free bars in the range 0~8000 Hz.

Table 4.1- Modal frequencies for the A_3 vibraphone bar and constant section bar

Vibraphone bar A_3	f_n [Hz]	220.4	870.5	2278	3787	4960	7141	—	—
	f_n/f_1	**1**	**3.95**	**10.3**	**17.2**	**22.5**	**32.4**	—	—
Constant section bar	f_n [Hz]	220.4	606.7	1187	1956	2912	4050	5366	6855
	f_n/f_1	**1**	**2.75**	**5.38**	**8.87**	**13.2**	**18.4**	**24.3**	**31.1**

The frequency-response measurements for the vibraphone bar showed two low-frequency free oscillations (around 35 Hz), which are related to the rigid-body translation and rocking modes of the bar, when coupled with its supporting fixture. To introduce this feature in the model, two flexible and damped supports were modelled at locations $x_1 = L/5$ and $x_2 = 4L/5$. Also, the zero-frequency translation and rocking modes of the bars were included in the computational modal basis, along with 8 flexural modes (with frequencies up to about 8000 Hz). Note that the dynamic support reactions are projected on the modal basis, along with the friction bow force. The support stiffness and damping values used for each support are $K_s = 10^4$ N/m and $C_s = 20$ Ns/m, respectively, as crudely estimated from the experimental results.

The friction parameters used in all numerical simulations are $\mu_S = 1.0$, $\mu_D = 0.2$ and $C = 10$. These values lead to a friction law $\mu_d(\dot{y}_c)$ (see Figure 4.2), according to the scarce experimental results available — see Lazarus (1972), Askenfelt (1989) and Schumacher (1994).

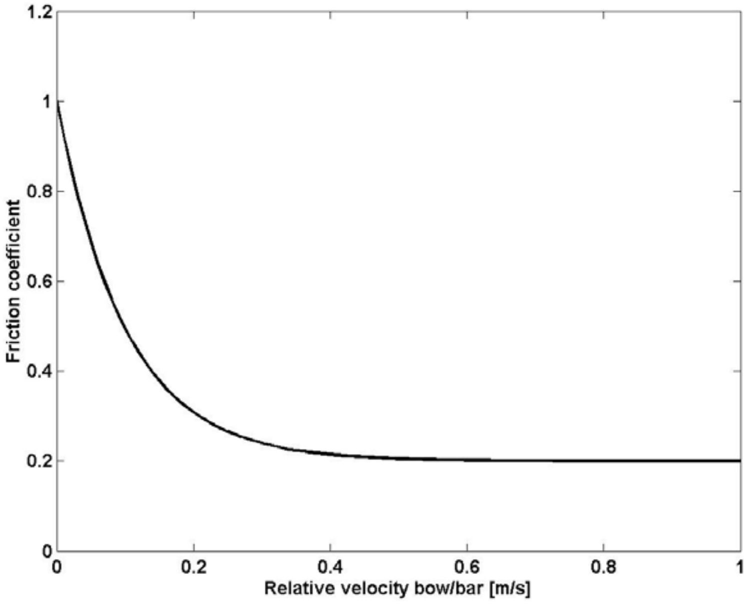

Figure 4.2 - Evolution of the friction coefficient with sliding velocity (μ_s = 1, μ_d = 0.2, C = 10)

4.3. *Numerical Simulations*

Extensive numerical simulations have been performed exploring a wide range of excitation parameters: FN = 0.05 ~ 35 N and $\dot{y}_{bow}$ = 0.002 ~ 1 m/s, which encompass the usual playing range. In order to cope with the relatively large transients that arise in these systems, 5 seconds of computed data were generated, at a sampling frequency of 20 kHz, to obtain representative realistic simulations.

The values of the bar geometrical and mechanical parameters used in the computations are shown in Table 4.2.

Table 4.2 - Geometric and mechanical characteristics of the A_3 vibraphone bar and a constant cross-section bar

	Length (cm)	Width (cm)	Max. Height (cm)	Min. Height (cm)	E (GPa)	ρ (kg/m^3)
A_3 Vibraphone bar	32.4	5	1.11	0.42	71	2700
Constant section bar	35.2	5	0.52	0.52	71	2700

4.3.1 Basic self-excited regimes

Figure 4.3 shows the simulated response of the vibraphone bar, at the bowing point, using a normal bow force $F_N = 2$ N and a bowing velocity $\dot{y}_{bow} = 0.1$ m/s. These parameters might be considered "usual" for bowed bars (however, depending on many factors, large variations from these values may be used by performers when seeking musically-effective sounds). The first graph on the top of Figure 4.3 shows the bar bowing point displacement time history during an interval of 5 seconds. The next three pairs of graphs represent, respectively, zoomed time-histories and power spectral densities of the displacement, velocity and acceleration at the bowing location. The last two graphs show, respectively, the time-history of the tangential friction force (on the left) and the time-intervals when the bar is sticking or sliding relative to the bow (on the right).

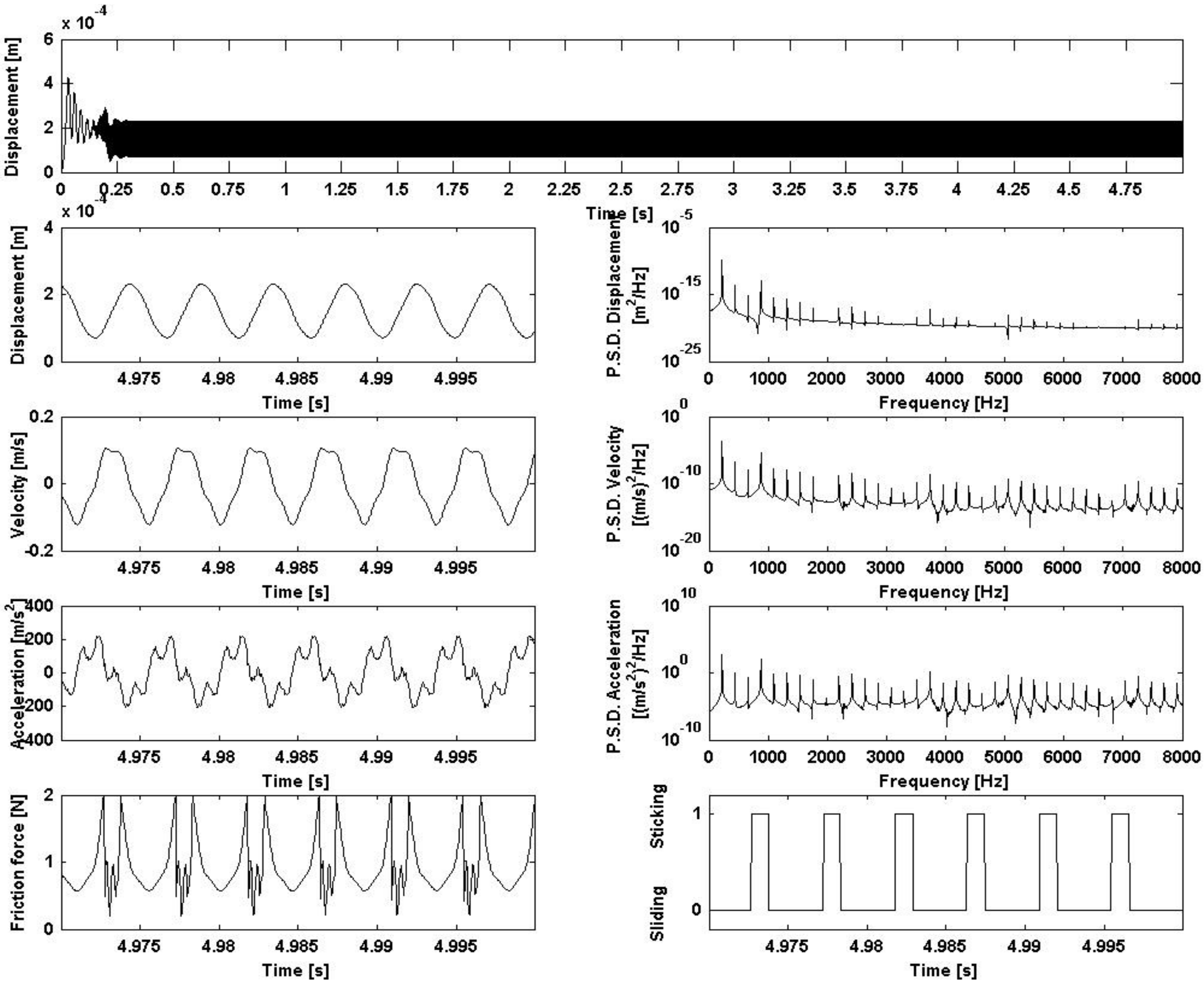

Figure 4.3 - Vibratory response at the bowing point of a tuned A3 vibraphone bar: Normal bow force $F_N = 2$ N; Bowing velocity $\dot{y}_{bow} = 0.1$ m/s ("musical" regime).

One can notice a large-amplitude low-frequency transient, which is mostly controlled by the flexible supporting conditions of the bar. Then, a steady self-excited motion develops, which is dominated by the response of the first vibratory flexural bar mode (at 220,4 Hz). This behaviour contrasts with the typical responses of bowed strings, which display very significant “activity” of the higher-order modes. Here, the spectral harmonics due to the system nonlinearity are of lower amplitude, as shown in the displacement spectrum. However, a few harmonics increase significantly, when they approach a modal frequency of the bar — for this vibraphone bar, the fourth harmonic near the 870 Hz mode (at a ratio $f_2/f_1 = 3.95$) can be clearly heard. Notice also that the friction force is quite complex, with a large portion of the cycle in the sliding regime. This also contrasts with the behaviour of bowed strings, for which most of the motion takes place in adherence conditions (Antunes et al, 2000a; Tafasca et al, 2000).

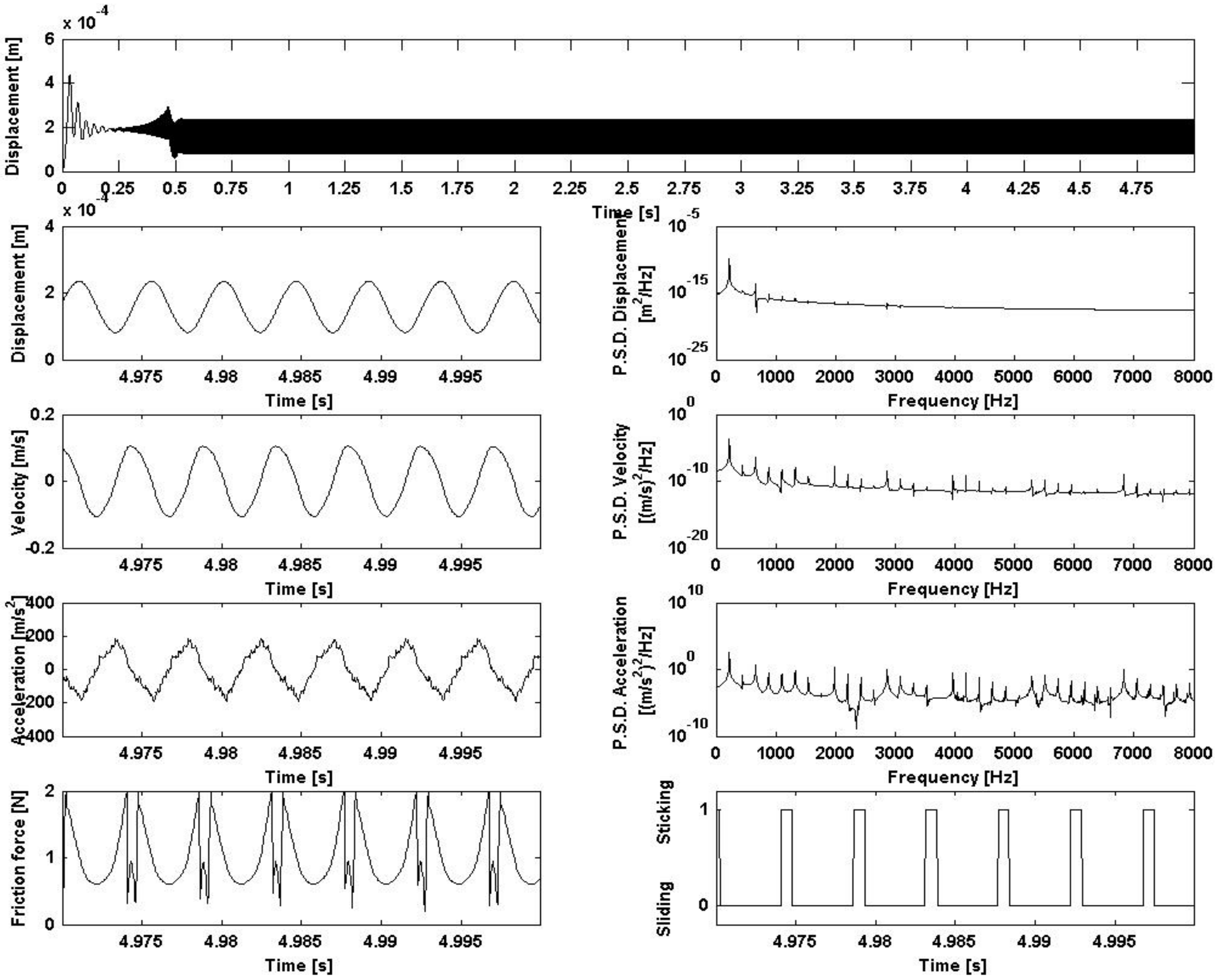

Figure 4.4 - Vibratory response at the bowing point of a bar of constant section: Normal bow force $F_N = 2$ N ; Bowing velocity $\dot{y}_{bow} = 0.1$ m/s (“musical” regime).

Figure 4.4 shows the results obtained when simulating the bowed response of the *bar with constant cross-section*, under similar bowing conditions. Again the self-excited motion is dominated by the first bar mode. However, looking at the harmonic content, it is now the *third* harmonic that is slightly enhanced, as it approaches the 607 Hz mode (at a ratio $f_2/f_1 = 2.75$). Furthermore, the higher inharmonicity of this bar leads to an even lower amplitude of the higher harmonics resulting in a distinct timbre from the tuned bar and a longer initial transient due to the difficulty of the modes to lock into a common periodicity.

4.3.2 Influence of playing conditions

The self-excited responses shown in Figure 4.3 and Figure 4.4, which are dominated by the first bending mode of the bars, are those typically aimed by musicians — and, as such, will be designated “musical” regime. Quite different solutions may appear when changing the bowing parameters F_N and $\dot{y}_{bow}$. In bowed bars, the range of values $\left(F_N\,;\dot{y}_{bow}\right)$ leading to musically-interesting sounds is more limited than for bowed strings — meaning that it is more difficult to excite musical self-excited motions with bowed bars. In fact, depending on the bowing parameters, three main response regimes may be obtained:

(a) For high values of F_N and low values of $\dot{y}_{bow}$, a low-frequency “non-musical” self-excited motion arises, where rocking motions of the (un-deformed) bar are controlled by the support stiffness — designated here as “support” regime (Figure 4.5);

(b) For low values of F_N and high values of $\dot{y}_{bow}$, no self-excited motions are displayed, because the bow slides all the time and any starting transient motion will ultimately disappear — the “decaying” regime (Figure 4.6);

(c) Between the extreme values of the input parameters $\left(F_N\,;\dot{y}_{bow}\right)$, the previously mentioned musically-interesting solution exists, where stick-slip phenomena enable self-excited motions dominated by the first bending bar mode (Figure 4.3 and Figure 4.4).

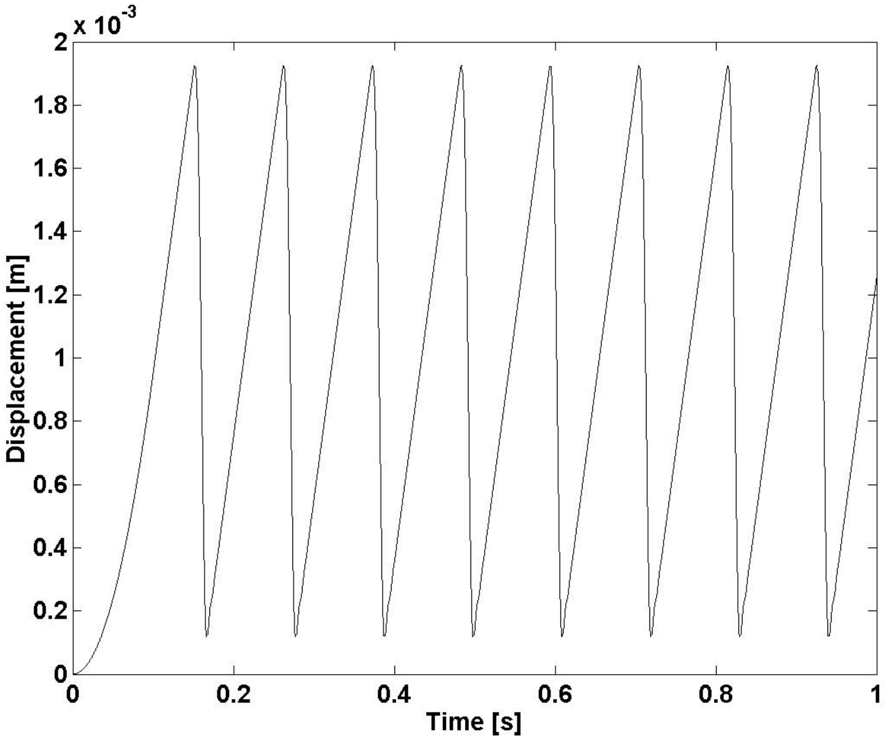

Figure 4.5 - Low-frequency self-excited oscillation. $F_N = 20$ **N and** $\dot{y}_{bow} = 0.1$ **m/s ("support" regime).**

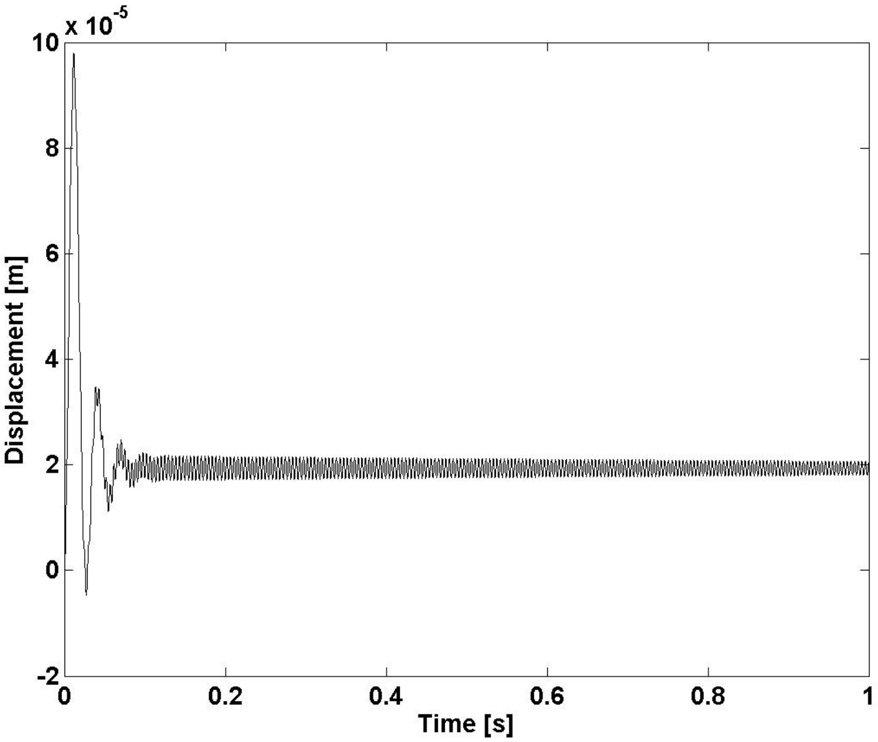

Figure 4.6 - Decaying not self-excited oscillation. $F_N = 0.2$ **N and** $\dot{y}_{bow} = 0.5$ **m/s**

(“decaying” regime).

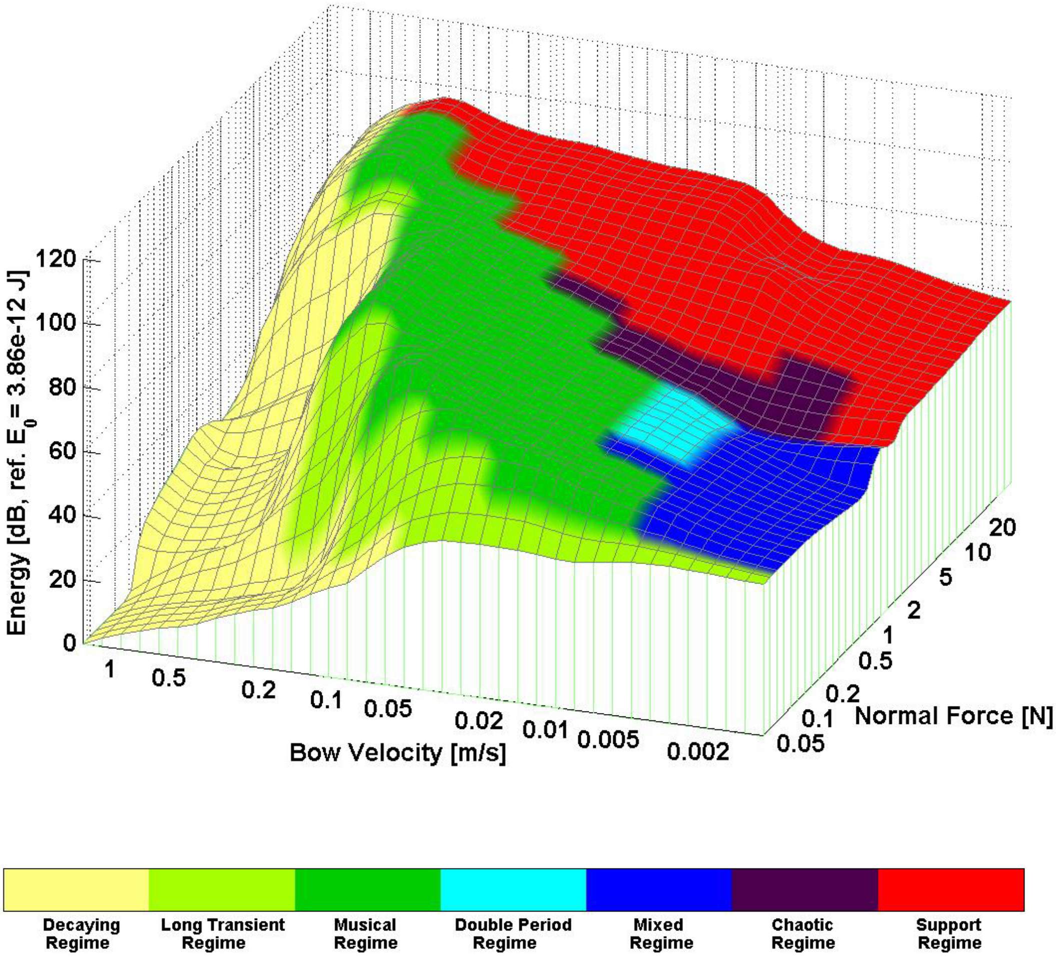

Figure 4.7 - Total energy of vibration of a 1-4-10 vibraphone bar as a function of F_N and $\dot{y}_{bow}$.

Figure 4.7 and Figure 4.8 show the various solution domains, respectively for the tuned and the constant-section bar. A set of colors was chosen to distinguish between the various dynamical regimes, when plotting the energy magnitude of the various solutions obtained from the computations. It is clear from these results that the tuned (e.g. harmonic) bending modes of the A_3 vibraphone bar allow for a larger domain of F_N and $\dot{y}_{bow}$ leading to the self-excited “musical” regime, when compared with the corresponding domain stemming from the computations performed with the inharmonic constant-section bar.

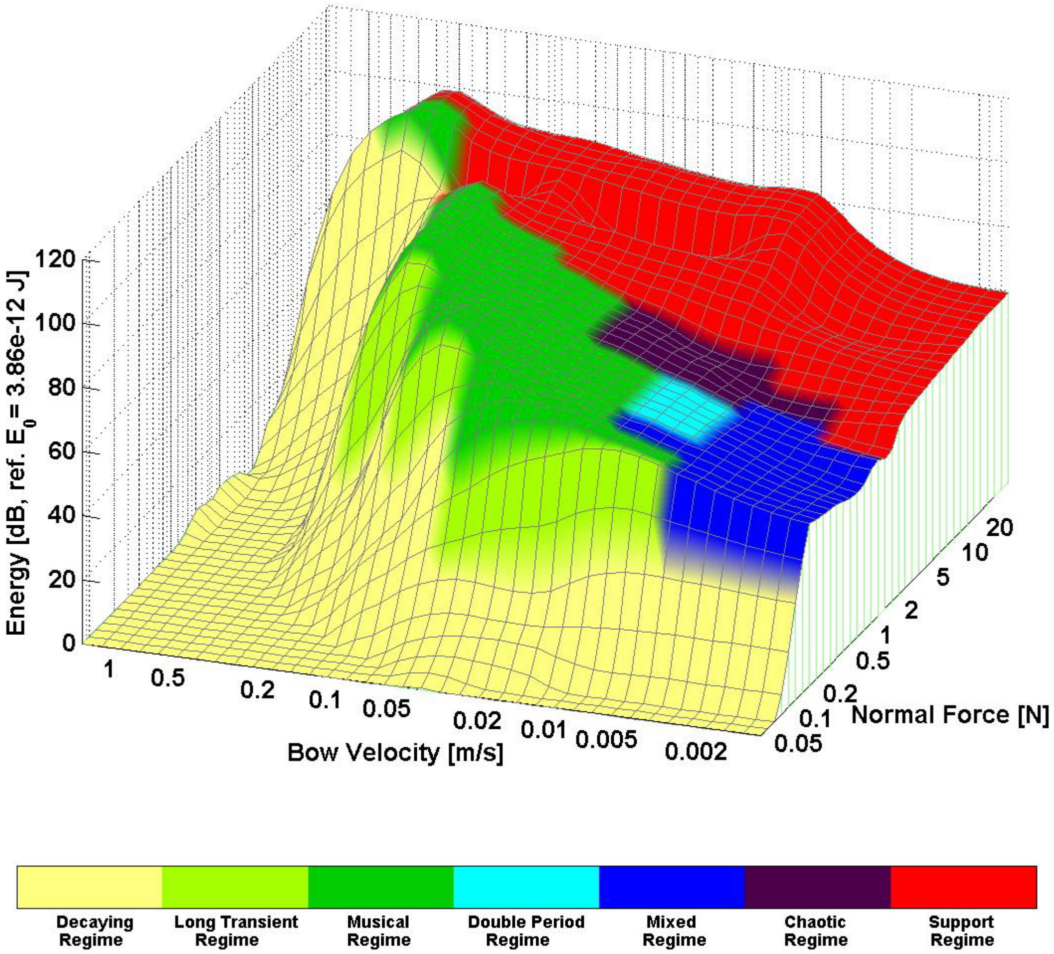

Figure 4.8 - Total energy of vibration of a constant-section bar as a function of F_N and $\dot{y}_{bow}$.

Increasing the bow velocity leads to an increase of the amplitude of the bar motion — a behaviour also displayed by bowed string instruments. When the bow velocity is far too high for any sticking to occur then the “decaying” regime prevails. The transition from the “decaying” regime to the low-frequency “support” oscillation (passing through the “musical” solution), appears to be related to the fraction of time spent in the sliding state. Figure 4.9 shows the percentage of sliding time, computed during the stationary part of the response oscillations, as a function of the applied normal force and bow velocity. The dependence of the sliding time on F_N and $\dot{y}_{bow}$ is clearly seen.

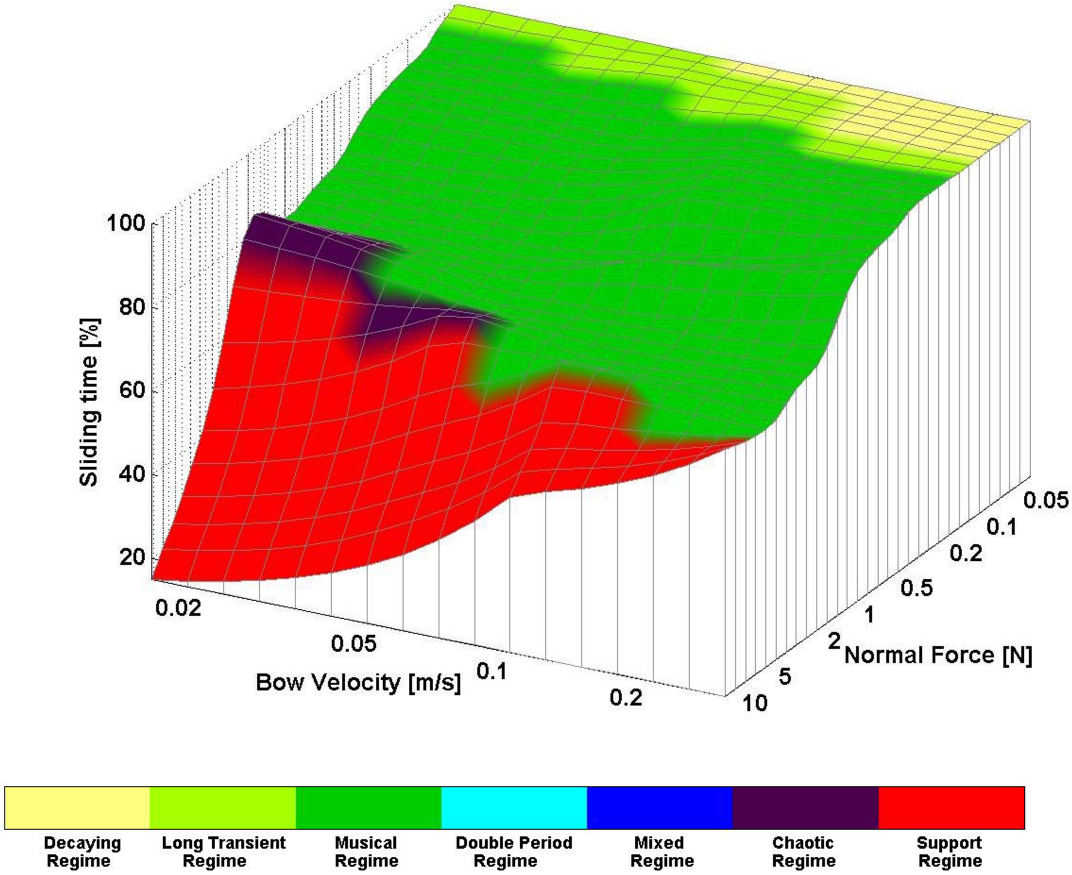

Figure 4.9 – Relative sliding time as a function of F_N and $\dot{y}_{bow}$.

For very low velocities, a “mixed” regime arises (blue color in Figure 4.7 and Figure 4.8), where a combination of the low-frequency “support” solution and of the “musical” self-excited regime appears. In these simulations, for values $\dot{y}_{bow}$ between 0.005 and 0.01 m/s the frequencies of the bar modes are clearly seen in the velocity spectra, together with other frequency components at lower amplitude, sometimes with a harmonic structure. As the applied force is increased or the bow velocity is decreased, these regimes give origin to double period and even chaotic oscillations before settling into the lower-frequency support oscillation as seen in the typical phase-trajectories and spectral plots shown in Figure 4.10. Notice that, for every motion regime, the flexural modal frequencies of the bar are always embedded in the response spectral envelopes.

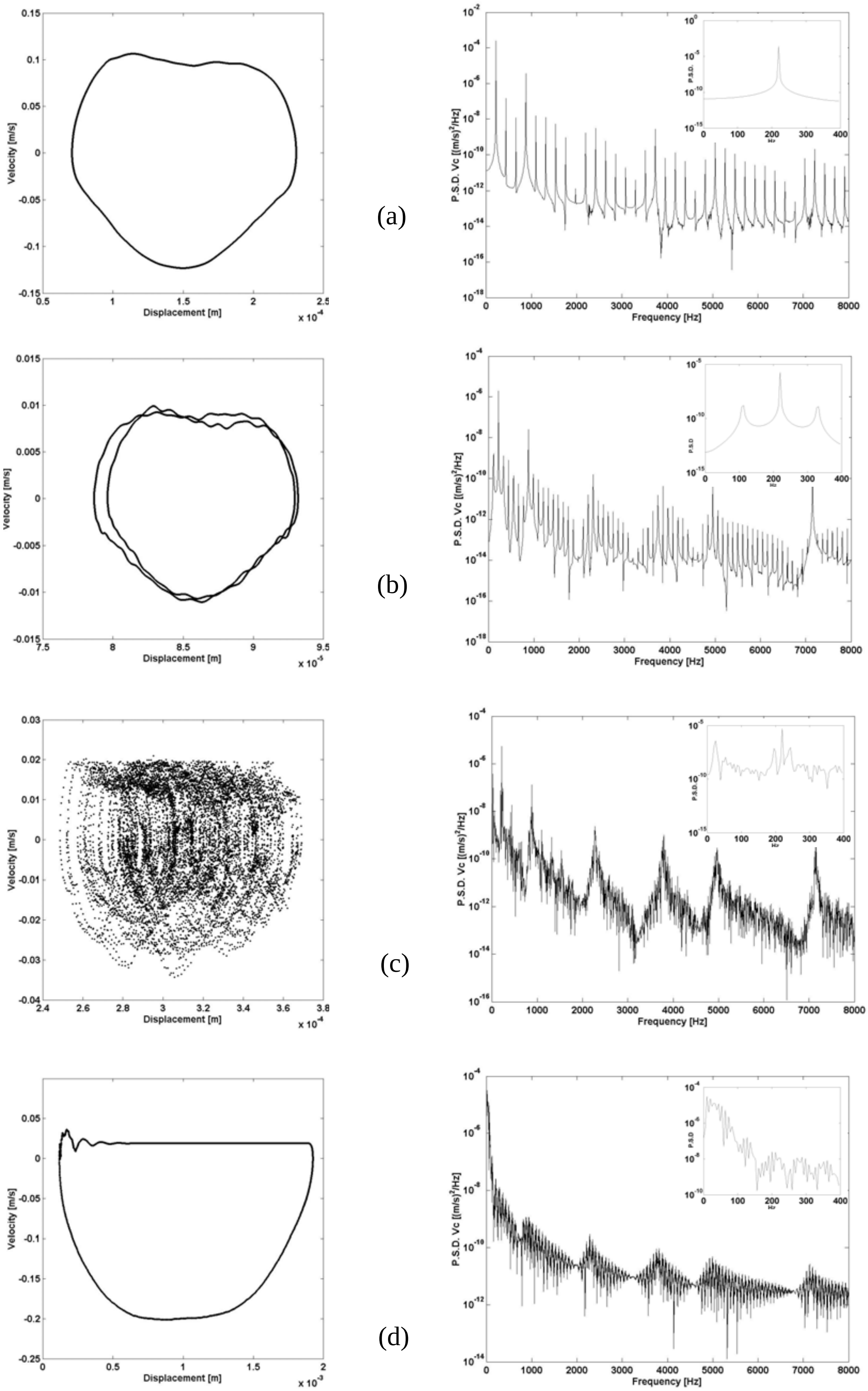

(a)

(b)

(c)

(d)

Figure 4.10 - Phase Space and Power Spectral Density representations for the: a) Musical regime -F_N = 2 N, V_b = 0.1 m/s; b) Double period regime - F_N = 0.5 N, V_b = 0.01 m/s; c) Chaotic regime - F_N = 2 N, V_b = 0.02 m/s and d) Support regime - F_N = 10 N, V_b = 0.02 m/s.

Within the green region in Figure 4.7 and Figure 4.8, the "sound quality" (e.g. the relative amplitude of the spectral peaks of the responses) changes with F_N and $\dot{y}_{bow}$ in a much less dramatic way than with bowed strings (see Antunes et al, 2000a; Tafasca *et al*, 2000; McIntyre *et al*, 1983) Although, for a given motion regime, the response amplitudes of the bars increase almost linearly with the bowing velocity (as in bowed strings), the effects of increasing the normal force are subtle, (contrasting with bowed strings, for which normal force effects are usually significant).

Another dramatic difference between these two systems is that the length of the starting transients is much longer for bowed bars than with bowed strings, emphasizing the increased difficulties in controlling this system. Figure 4.11 and Figure 4.12 show how the initial transients increase exponentially with $\dot{y}_{bow}$ and decrease inversely proportionally to F_N.

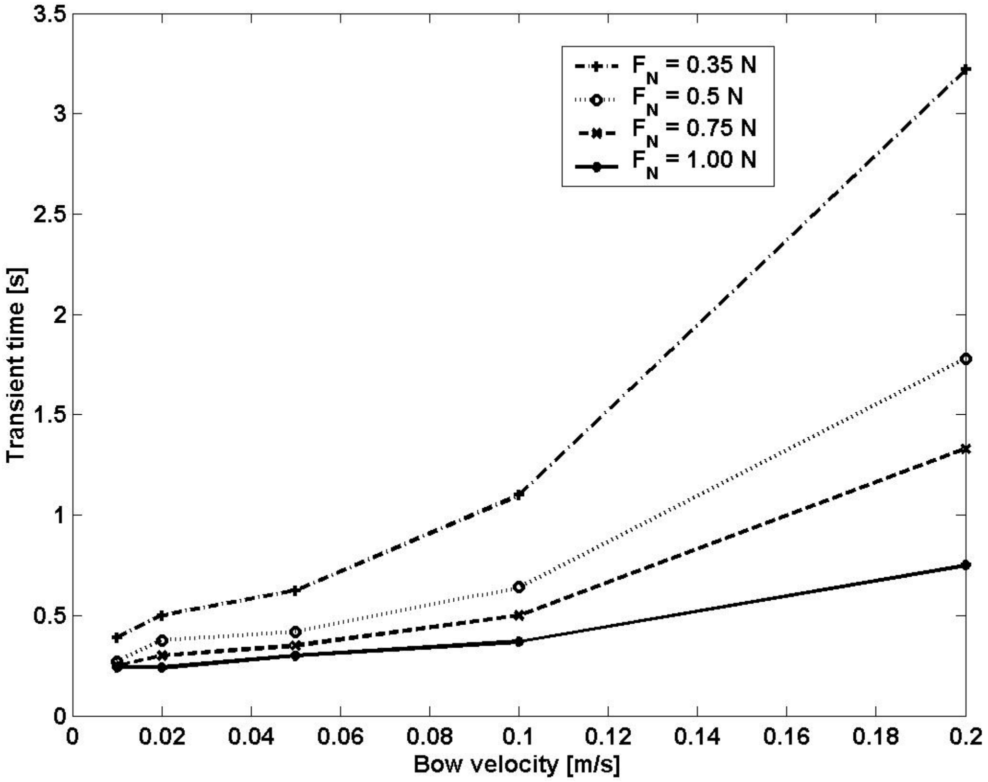

Figure 4.11 - Initial transients (1-4-10 vibraphone bar) as a function of $\dot{y}_{bow}$.

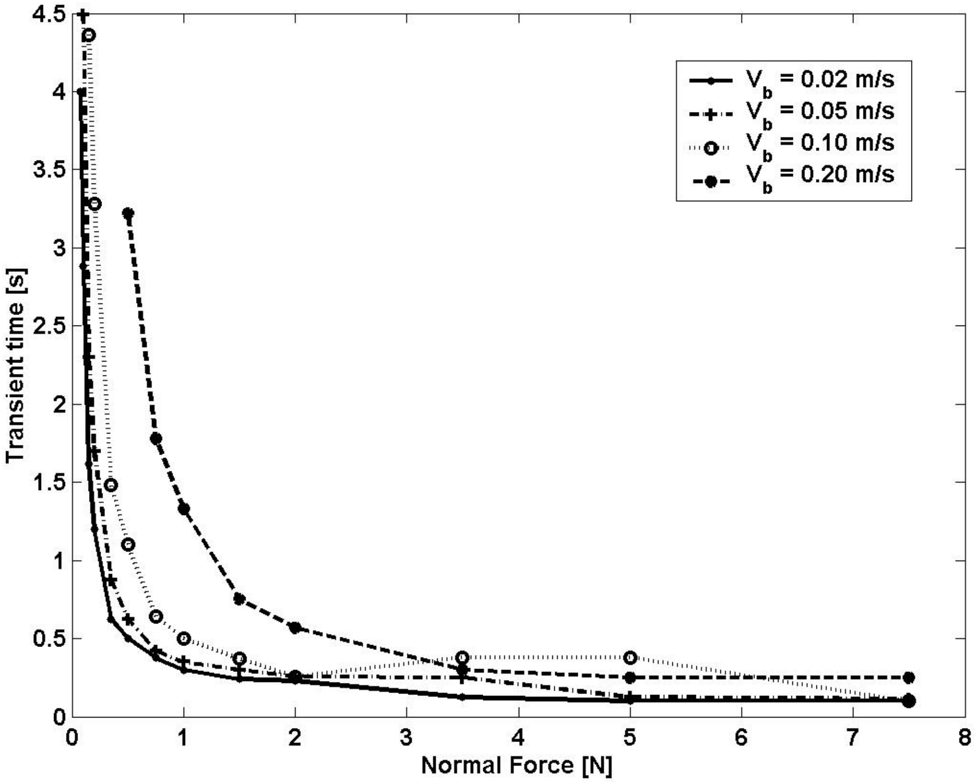

Figure 4.12 - Initial transients (1-4-10 vibraphone bar) as a function of F_N.

As already stated, the dynamics of this system are mainly controlled by the first vibratory bar mode (and by the flexible support), in clear contrast with bowed strings. This is attested by Figure 4.13, which shows the change of the modal energies of the system as a function of the normal force, for a bowing velocity of 0.02 m/s. These are computed from the temporal modal responses and represented normalized to the total energy of the system according to:

$$\bar{E}_n = \frac{1}{2} m_n \left\langle \dot{q}_n^2(t) + \omega_n^2 q_n^2(t) \right\rangle \Big/ E_T \equiv E_n / E_T \tag{4.9}$$

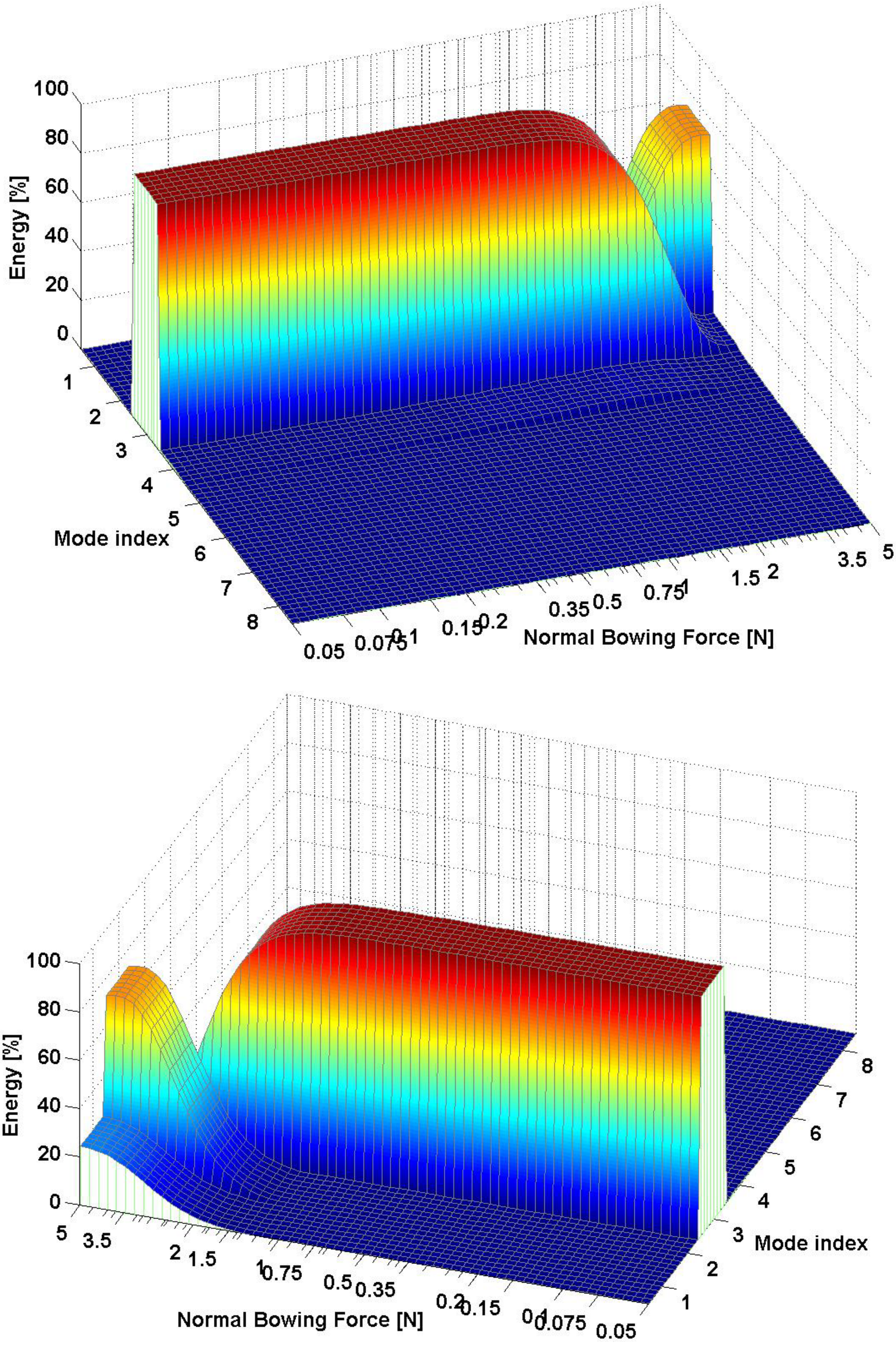

Figure 4.13 - Modal energies (1-4-10 vibraphone bar) as a function of F_N for $\dot{y}_{bow}$ =0.02 m/s

Comparing Figure 4.13 and Figure 4.7, it can be seen how changes from the musical regime to the chaotic regime and to the support self-excited oscillation are controlled by a progressive transfer of energy from the first bending mode to the low-frequency rocking and translation rigid-body bar/support modes. This behaviour is similar at other bow velocities. This fact suggests that it may be sufficient to model analytically this system using a couple of vibratory modes.

4.3.3 Responses of uniform, undercut and unorthodox bars

Figure 4.14 shows the profiles of the bars used in these simulations. The absolute and relative dimensions presented in the figure are not to scale. As can be seen from the analysis of Table 4.2, the three bars present a decreasing level of modal inharmonicity due to the shape of the tuning undercut. The optimised bar (b) is quite similar to current commercially available vibraphone bars, with their typical central undercut. However, the "harmonic" bar (c) would be a very unorthodox design, by current standards.

Table 4.3 - Natural bending frequencies and modal relationships for the three bars.

	Uniform bar		**Vibraphone bar**		**Harmonic bar**	
n	f_n [Hz]	f_n/f_1	f_n [Hz]	f_n/f_1	f_n [Hz]	f_n/f_1
1	220.4	1	220.4	1	220	1
2	606.7	2.75	870.5	3.95	440	2
3	1187	5.38	2278	10.3	660	3
4	1956	8.87	3787	17.2	1625	7.38
5	2912	13.2	4960	22.5	2448	11.1
6	4050	18.4	7141	32.4	2983	13.5
7	5366	24.3	-	-	4444	20.2
8	6855	31.1	-	-	5591	25.4
…	…	…	…	…	…	…
N	8		8		13	

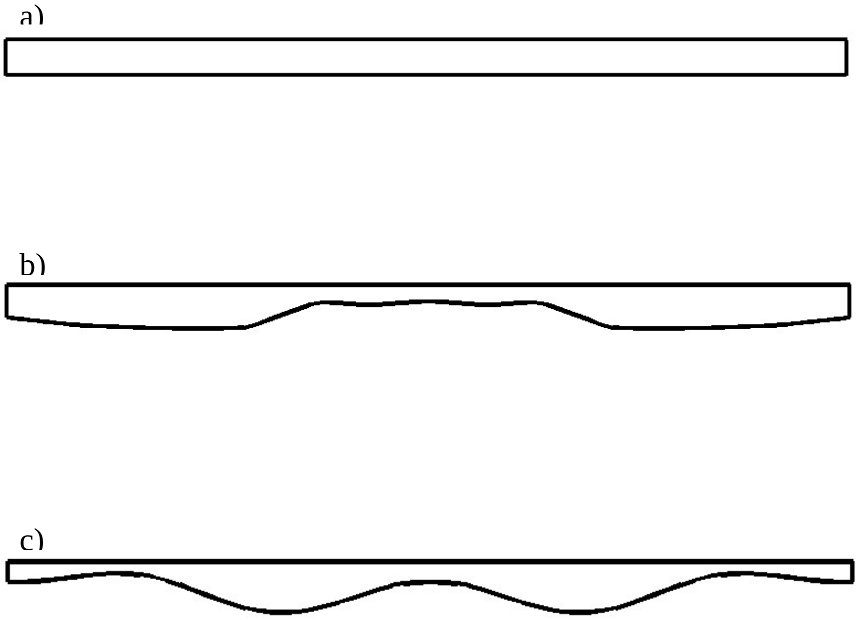

Figure 4.14 - Bar profiles: a) Uniform bar; b) Vibraphone (1-4-10) bar; c) Harmonic (1-2-3) bar.

4.3.3.1 Uniform and Vibraphone Bar

Figure 4.15a and Figure 4.15b show time-history segments of the computed dynamical responses at the bowing point (located at one of the ends of the bars) and the corresponding power spectral densities, respectively for the uniform (constant cross-section) and for the vibraphone bar, using a normal bow force F_N =2 N and a bowing velocity $\dot{y}_{bow}$ = 0.1 m/s.

In both cases the motion is dominated by the response of the first vibratory flexural mode although for the vibraphone bar there is more energy spread in higher-order modes, which have natural frequencies in approximate integer ratios with the fundamental. The high degree of inharmonicity of the uniform bar leads to a lower amplitude of the higher harmonics (which are mostly due to the system non-linearity) resulting in a distinct timbre from the tuned vibraphone bar. Also, the uniform bar usually displays longer initial transients, due to the difficulty of the modes to lock into a common periodicity. This behaviour contrasts with the typical responses of bowed strings, which display very significant “activity” of the higher-order modes and much shorter initial transients.

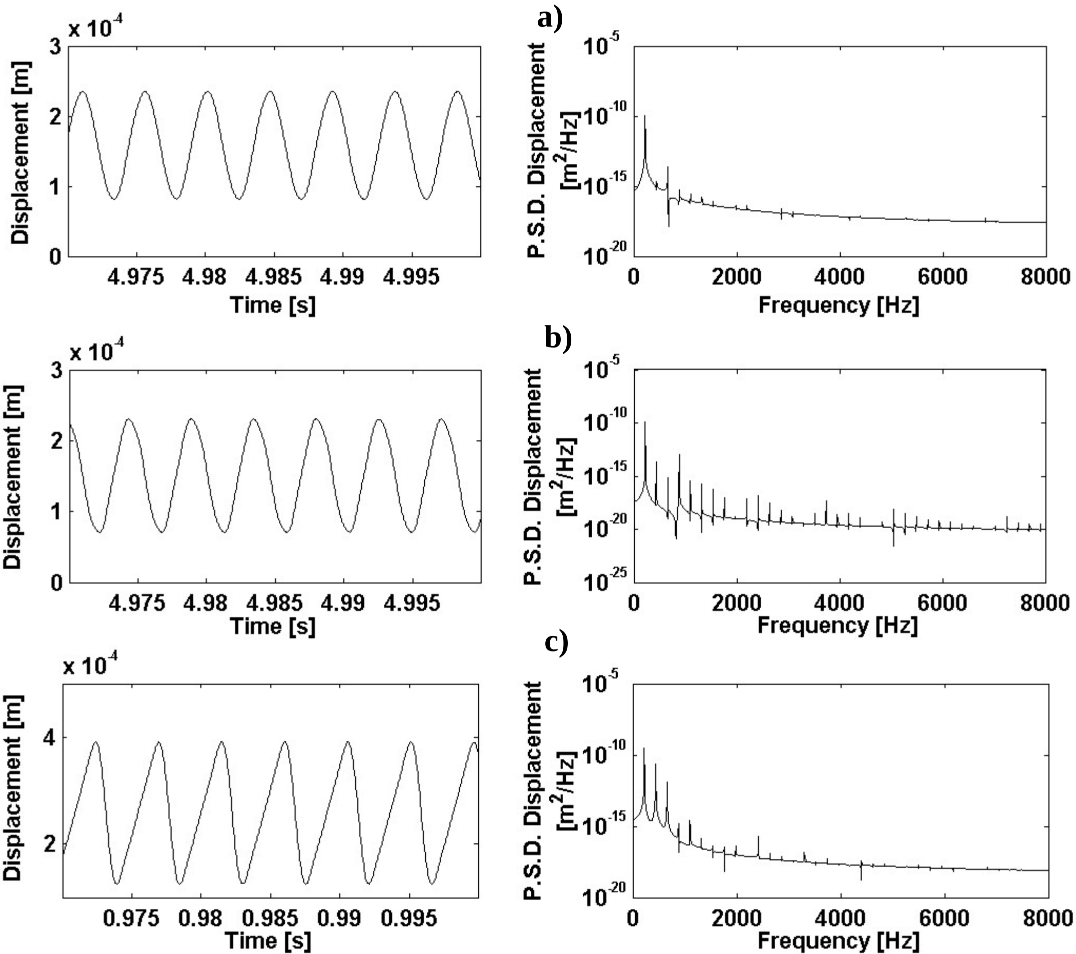

Figure 4.15 - Time history and power spectral density of the bowed response of a: a) Uniform bar (using F_N = 2 N); b) Vibraphone (1-4-10) bar (using F_N = 2 N); c) Harmonic bar (using F_N = 3.5 N).

4.3.3.2 Harmonic Bar

The simulated displacement response of a 1-2-3 harmonic bar bowed with F_N = 3.5 N and $\dot{y}_{bow}$ = 0.1 m/s is shown in Figure 4.15c. The self-excited motion of the bar is now dominated by the first three vibratory flexural modes, with low amplitude response of the higher harmonics, due to the high inharmonicity of the modal frequencies beyond the third flexural mode. However, because the three first bending modes are harmonic and respond in a very cooperative manner, the waveform of the bar displacement is almost saw-shaped, such as the Helmholtz waveform in bowed string.

Indeed, similarity between the harmonic 1-2-3 bowed bar and bowed strings is also noticed when looking at the stick-slip behaviour of the friction interaction. Figure

4.16a to Figure 4.16c show the computed frictional forces corresponding to the three case studies of Figure 4.15. The relative sticking-time (within a period) increases somewhat from the uniform bar to the tuned vibraphone bar, but significantly more for the harmonic bar (the bar sticks to the bow during 56% of the motion period). This behaviour approaches what is observed for bowed strings, which stick during a very significant part of the motion (see Antunes et al, 2000a; Tafasca et al, 2000). Also, the friction force displayed by the 1-2-3 bar (Figure 4.16c) presents similarities with typical bow/string interaction forces, in clear contrast to the results presented in Figure 4.16a and Figure 4.16b.

The results presented show that the dynamics of uniform and vibraphone bowed bars are mainly dominated by the first bending mode. This is in contrast with the much higher modal activity observed in bowed string motions. The vibraphone bar exhibits a higher level of playability when compared to the uniform bar, due to the higher harmonicity of its modal frequencies. However, the unorthodox tuning used for the harmonic (1-2-3) bar enables the emergence of waveforms which are similar to those displayed by bowed strings, as well as similar relative sticking times.

In conclusion, shaping bars so that their first few modal frequencies are harmonic, creates an interesting new “animal”, which behaves half-way between strings and common bars.

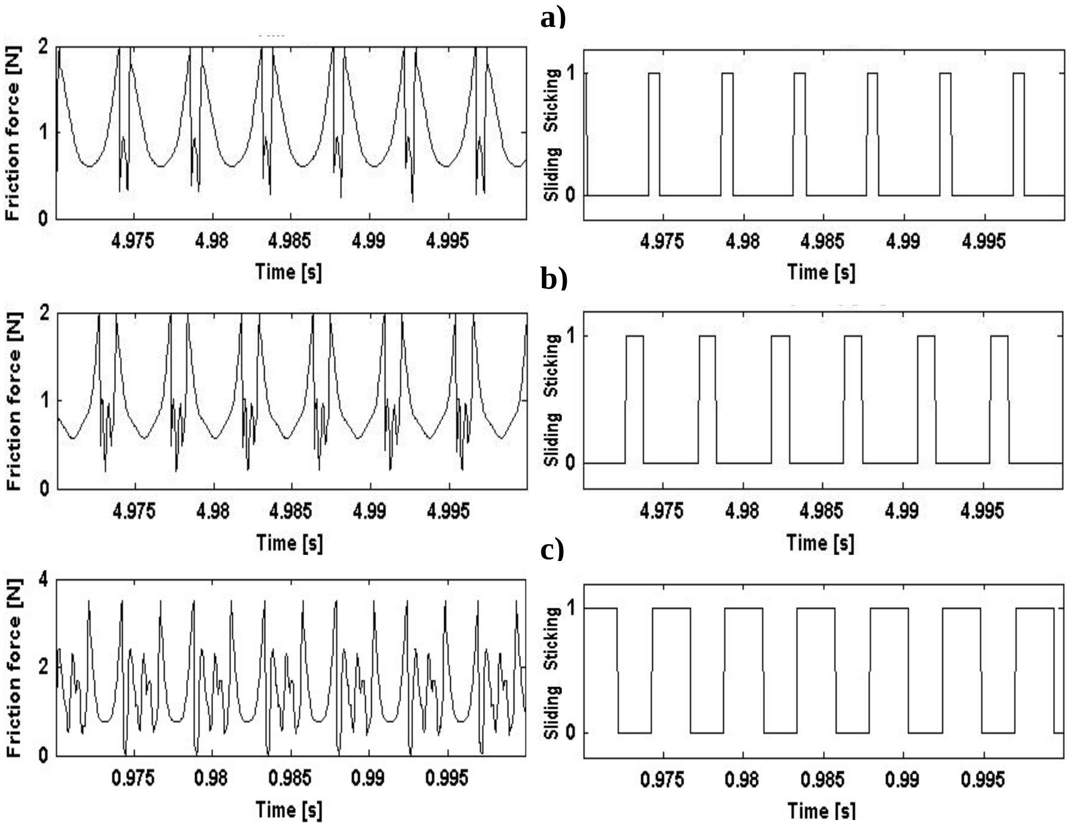

Figure 4.16 - Friction force time-history segment and slipping-time diagrams of a: a) Uniform bar (using F_N = 2 N); b) Vibraphone (1-4-10) bar (using F_N = 2 N); c) Harmonic bar (using F_N = 3.5 N).

4.4. Experimental Results

Experimental measurements on vibraphone bars were carried to fulfil two main objectives: 1) to assist the calculation of modal parameters necessary to the computations and 2) to allow a comparison of the computation results with real bowed bar oscillations.

4.4.1 Modal identification of vibraphone bars

As explained in previous sections the modal basis used in the simulations of the bars were obtained from two different procedures: 1) an experimental procedure for the identification of modal frequencies and modal damping for the vibraphone 1-4-10 bar; 2) a numerical procedure based on the finite element method for determination of all modal parameters for the constant cross-section and unorthodox tuning bars and of the modeshapes of the 1-4-10 vibraphone bar. From these procedures, the first will be summarily presented in this section.

The identification of the modal frequencies of the vibraphone bar were obtained by inspection of the frequency response functions measured between the acceleration signal of an accelerometer placed at one end of the bar (and at half the width of the bar) and the force signal induced by an impact hammer at the opposite end (see Figure 4.17). Both signals were fed to 2 input channels of a 4-channel frequency analyser which calculated the frequency response functions from the acceleration and force signals.

The bar under test was supported on the vibraphone structure by a cord, as would be in a real performance. The cord goes through two holes located at the nodal points of the first bending mode, in order to minimize damping. All the remaining bars were damped with a heavy cloth to eliminate unwanted sympathetic vibrations.

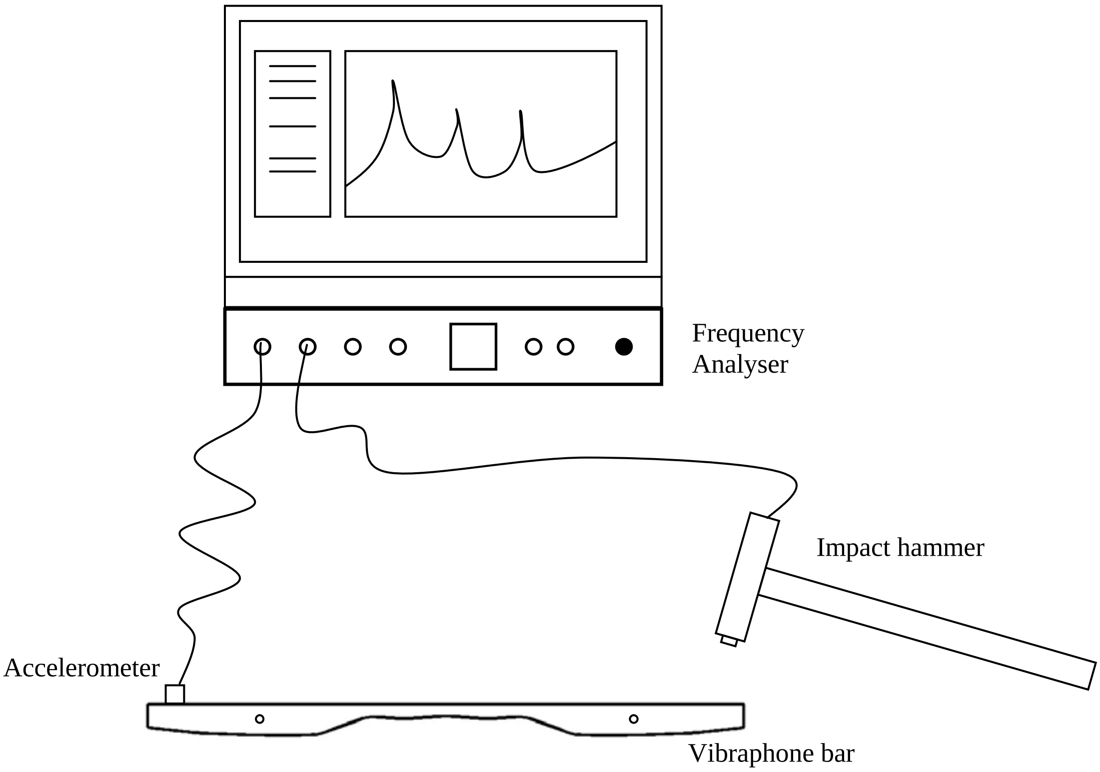

Figure 4.17 – Experimental setup used for the experimental modal identification of the bars

In order to separate flexural modes from torsion modes (the impact exerted did not excite significantly any longitudinal modes), several frequency response functions were measured with different locations of impact along the width of the bar. Figure 4.18 shows an example of a measured frequency response function with an impact location away from the middle of the bar width. On the other hand, Figure 4.19 shows another frequency response function but now with an impact location precisely in the middle of the bar width. Comparing both figures confirmed the hypothesis that both modes showing up at approximately 750 Hz and 3100 Hz were not bending modes, but torsion modes as confirmed by finite element calculations. Close inspection of the frequency response functions showed two two low-frequency free oscillations at approximately 35 Hz, in every measurement made even when damping the bar to eliminate flexural, longitudinal or torsional vibrations. These oscillations are related to the rigid-body translation and rocking modes of the bar, when coupled with its supporting fixture.

Experimental modal research on these systems has already been explored thoroughly (see Fletcher & Rossing, 1998; 2000) and the present measurements showed good agreement with the published results. Table 4.1 shows the results obtained from the modal identification on both vibraphone and constant cross-section bar.

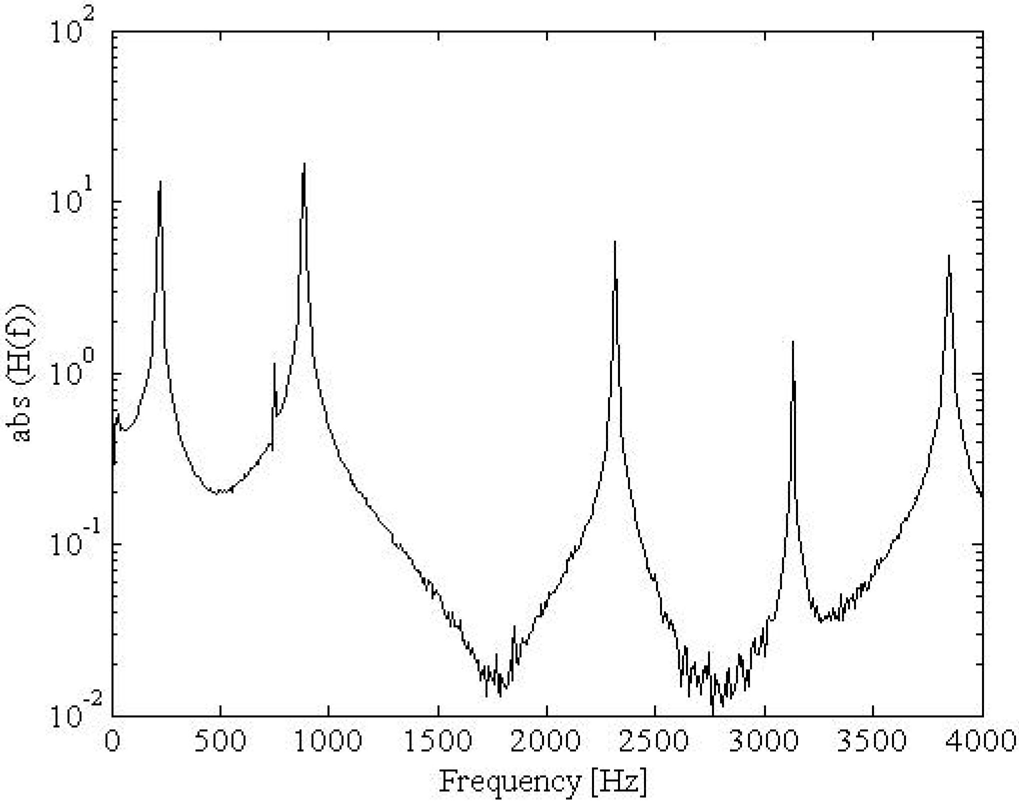

Figure 4.18 – Frequency response function of the 1-4-10 vibraphone bar with impact off-axis

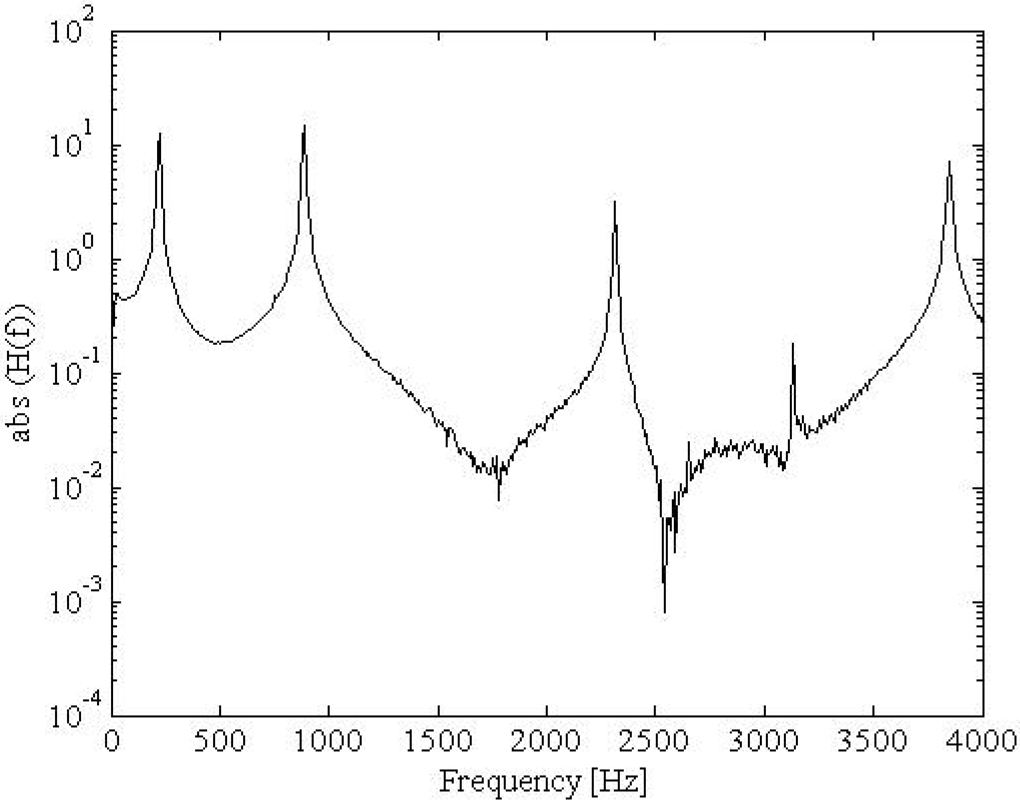

Figure 4.19 – Frequency response function of the 1-4-10 vibraphone bar with impact on-axis

4.4.2 Experimental self-excited motions

Preliminary experiments have been performed at this stage, although under uncontrolled conditions. Figure 4.20 shows a typical result measured near the bowing point of a A_3 vibraphone bar (with the modal parameters used in these simulations), as hand-bowed by a professional musician. The background noise of the measured spectrum is obviously higher than in this sample simulation – compare with Figure 4.3 or Figure 4.10a – but the similarity of the computed and experimental signals is unmistakable.

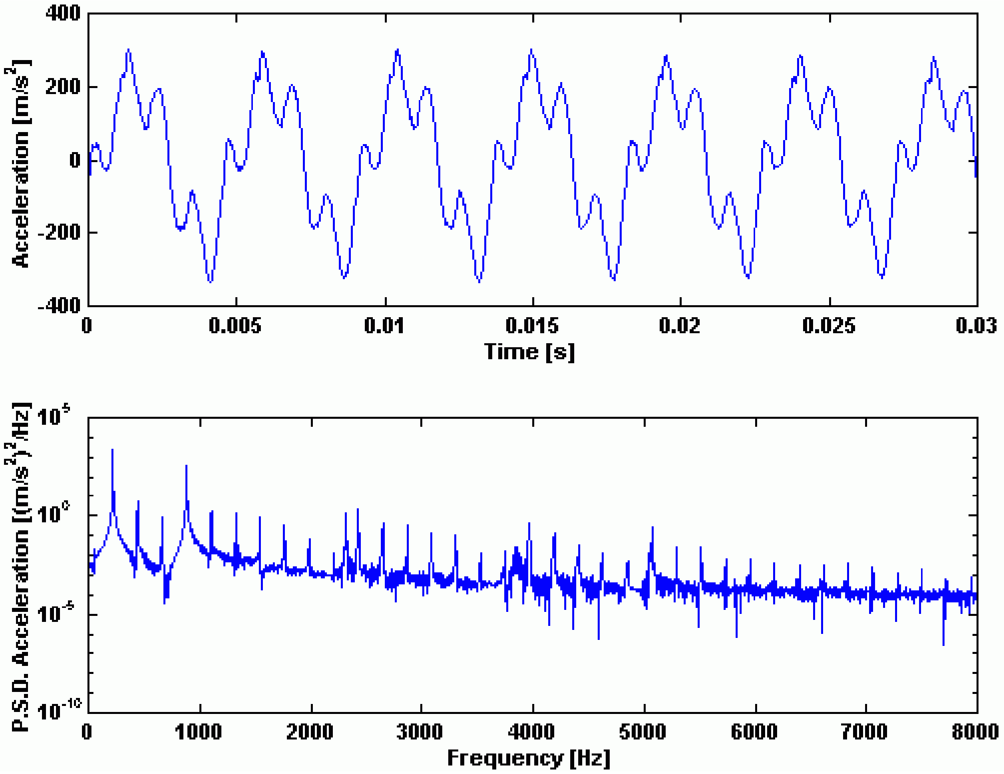

Figure 4.20 - Experimental response of a bowed A_3 vibraphone bar.

Chapter 5

BOWED SHELLS: TIBETAN BOWLS

5. BOWED SHELLS: TIBETAN BOWLS

5.1. *Introduction*

In this chapter, the modal physical modelling technique is applied to axi-symmetrical shells subjected to impact and/or friction-induced excitations. This approach is based on a modal representation of the unconstrained system – here consisting on two orthogonal families of modes of similar (or near-similar) frequencies and shapes. The bowl modeshapes have radial and tangential motion components, which are prone to be excited by the normal and frictional contact forces between the bowl and the impact/sliding stick (called *puja*). At each time step, the generalized (modal) excitations are computed by projecting the normal and tangential interaction forces on the modal basis. Then, time-step integration of the modal differential equations is performed using an explicit algorithm. The physical motions at the contact location (and any other selected points) are obtained by modal superposition. This enables the computation of the motion-dependent interaction forces, and the integration proceeds. Details on the specificities of the contact and frictional models used in these simulations are given. A detailed experimental modal identification has been performed for three different Tibetan bowls. Then, extensive series of nonlinear numerical simulations are produced, for both impacted and rubbed bowls, demonstrating the effectiveness of the proposed computational techniques and highlighting the main features of the physics of singing bowls. The influence of the contact/friction and playing parameters is discussed – the normal contact force F_N and of the tangential velocity V_T of the exciter – on the produced sounds. Many aspects of the bowl responses displayed by these numerical simulations have been observed in preliminary qualitative experiments.

5.1.1 Tibetan singing bowls and their use

Singing bowls, also designated by Himalayan or Nepalese singing bowls (Gaynor, 2002) are traditionally made in Tibet, Nepal, Bhutan, Mongolia, India, China and Japan. Although the name *qing* has been applied to lithophones since the Han Chinese Confucian rituals, more recently it also designates the bowls used in Buddhist temples (Thrasher, 2001). In the Himalaya there is a very ancient tradition of metal manufacture, and bowls have been handcrafted using alloys of several metals –

mainly copper and tin, but also other metals such as gold, silver, iron, lead, etc. – each one believed to possess particular spiritual powers. There are many distinct bowls, which produce different tones, depending on the alloy composition, their shape, size and weight. Most important is the sound producing technique used – either impacting or rubbing, or both simultaneously – as well as the excitation location, the hardness and friction characteristics of the *puja* (frequently made of wood and eventually covered with a soft skin) – see Jansen, 1993.

The origin of these bowls isn't still well known, but they are known to have been used also as eating vessels for monks. The singing bowls dates from the Bon civilization, long before the Buddhism (Huyser, 1999). Tibetan bowls have been used essentially for ceremonial and meditation purposes. Nevertheless, these amazing instruments are increasingly being used in relaxation, meditation (Huyser, 1999), music therapy (Gaynor, 2002; Gardner, 1990; Gaynor, 1999) and contemporary music.

The musical use of Tibetan singing bowls in contemporary music is a consequence of a broad artistic movement. In fact, in the past decades the number of percussion instruments used in Western music has greatly increased with an "invasion" of many instruments from Africa, Eastern, South-America and other countries. Many Western composers have included such instruments in their music in an acculturation phenomenon.

The Tibetan bowls and other related instruments used in contemporary music are referred to, in scores, by several names: temple bells, campana di templo, japonese temple bell, Buddhist bell, cup bell, dobaci Buddha temple bell. Several examples of the use of these instruments can be found in contemporary music: Philippe Leroux, *Les Uns* (2001); John Cage/Lou Harrison, *Double Music* (1941) percussion quartet, a work with a remarkable Eastern influence; Olivier Messiaen, *Oiseaux Exotiques* (1955/6); John Kenneth Tavener, cantata *Total Eclipse* (1999) for vocal soloist, boys' choir, baroque instruments, brass, Tibetan bowls, and timpani; Tan Dun Opera *Marco Polo* (1995) with Tibetan bells and Tibetan singing bowls; Joyce Bee Tuan Koh, *Lè* (1997) for choir and Tibetan bowls.

Figure 5.1. Three singing bowls used in the experiments: Bowl 1 ($\phi = 180$ mm); Bowl 2 ($\phi = 152$ mm); Bowl 3 ($\phi = 140$ mm).

Figure 5.2. Large singing bowl: Bowl 4 ($\phi = 262$ mm), and two pujas used in the experiments.

5.2. Computational Model

5.2.1 Modal model for axi-symmetrical shells

Perfectly axi-symmetrical structures exhibit double vibrational modes, occurring in orthogonal pairs with identical frequencies ($\omega_n^A = \omega_n^B$) (Rossing, 1994). However, if a slight alteration of this symmetry is introduced, the natural frequencies of these two degenerate modal families deviate from identical values by a certain amount $\Delta\omega_n$. The use of these modal pairs is essential for the correct dynamical description of axi-symmetric bodies, under general excitation conditions. Furthermore, shell modeshapes present both radial and tangential components. Figure 5.3 displays a representation of the first four modeshape pairs, near the bowl rim, where the excitations are usually exerted (e.g., $z_e \approx Z$). Both the radial (green) and tangential (red) motion components are plotted, which for geometrically perfect bowls can be formulated as:

$$\begin{cases} \varphi_n^A(\theta) = \varphi_n^{Ar}(\theta)\,\vec{r} + \varphi_n^{At}(\theta)\,\vec{t} \\ \varphi_n^B(\theta) = \varphi_n^{Br}(\theta)\,\vec{r} + \varphi_n^{Bt}(\theta)\,\vec{t} \end{cases} \tag{5.1}$$

with

$$\begin{cases} \varphi_n^{Ar}(\theta) = \cos(n\theta) \\ \varphi_n^{At}(\theta) = -\sin(n\theta)\big/n \end{cases} \tag{5.2}$$

$$\begin{cases} \varphi_n^{Br}(\theta) = \sin(n\theta) \\ \varphi_n^{Bt}(\theta) = \cos(n\theta)\big/n \end{cases} \tag{5.3}$$

where $\varphi_n^{Ar}(\theta)$ corresponds to the radial component of the A family nth modeshape, $\varphi_n^{At}(\theta)$ to the tangential component of the A family nth mode shape, etc. Figure 5.3 shows that spatial phase angles between orthogonal mode pairs are $\pi/2j$. One immediate conclusion can be drawn from the polar diagrams shown and equations (5.2) and (5.3): the amplitude of the tangential modal component decreases relatively to the amplitude of the radial component as the mode number increases. This suggests that only the lower-order modes are prone to engage in self-sustained motion due to tangential rubbing excitation by the *puja*.

If linear dissipation is assumed, the motion of the system can be described in terms of the bowl's two families of modal parameters: modal masses m_n^X, modal circular frequencies ω_n^X, modal damping ζ_n^X, and mode shapes $\varphi_n^X(\theta)$ (at the assumed excitation level $z_e \approx Z$), with $n = 1, 2, \cdots, N$, where X stands for the modal family A or B. The order N of the modal truncation is problem-dependent and should be asserted by physical reasoning, supported by the convergence of computational results.

The maximum modal frequency to be included, ω_N, mostly depends on the short time-scales induced by the contact parameters – all modes significantly excited by impact and/or friction phenomena should be included in the computational modal basis.

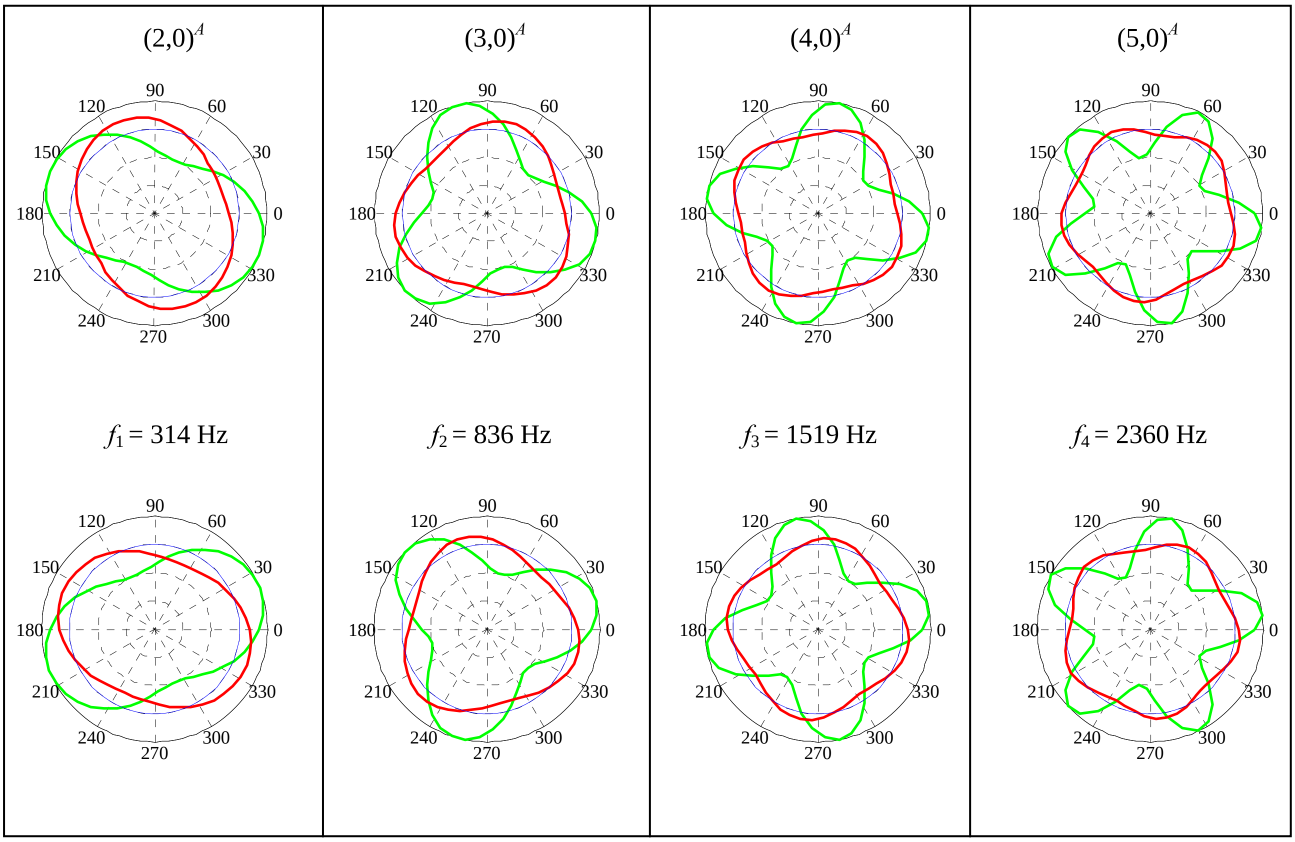

Figure 5.3. Mode shapes at the bowl rim of the first four orthogonal mode pairs (Blue: Undeformed; Green: Radial component; Red: Tangential component).

The forced response of the damped bowl can then be formulated as a set of 2N ordinary second-order differential equations

$$\left[\begin{array}{c|c} \left[M_A\right] & 0 \\ \hline 0 & \left[M_B\right] \end{array}\right]\begin{Bmatrix} \left\{\ddot{Q}_A(t)\right\} \\ \left\{\ddot{Q}_B(t)\right\} \end{Bmatrix} + \left[\begin{array}{c|c} \left[C_A\right] & 0 \\ \hline 0 & \left[C_B\right] \end{array}\right]\begin{Bmatrix} \left\{\dot{Q}_A(t)\right\} \\ \left\{\dot{Q}_B(t)\right\} \end{Bmatrix} + \left[\begin{array}{c|c} \left[K_A\right] & 0 \\ \hline 0 & \left[K_B\right] \end{array}\right]\begin{Bmatrix} \left\{Q_A(t)\right\} \\ \left\{Q_B(t)\right\} \end{Bmatrix} = \begin{Bmatrix} \left\{\Xi_A(t)\right\} \\ \left\{\Xi_B(t)\right\} \end{Bmatrix} \tag{5.4}$$

where:

$\left[M_X\right] = \text{Diag}(m_1^X, \cdots, m_N^X)$,

$\left[\,C_X\,\right] = \text{Diag}(2\,m_1^X\,\omega_1^X\,\zeta_1^X, \cdots, 2\,m_N^X\,\omega_N^X\,\zeta_N^X)$,

$\left[\,K_X\,\right] = \text{Diag}(m_1^X\,(\omega_1^X)^2, \cdots, m_N^X\,(\omega_N^X)^2)$,

are the matrices of the modal parameters (where X stands for A or B), for each of the two orthogonal mode families, while $\left\{Q_X(t)\right\} = \left\langle q_1^X(t), \cdots, q_N^X(t)\right\rangle^T$ and $\left\{\Xi_X(t)\right\} = \left\langle \Im_1^X(t), \cdots, \Im_N^X(t)\right\rangle^T$ are the vectors of the modal responses and of the generalized forces, respectively. Note that, although equations (5.4) obviously pertain to a linear formulation, nothing prevents us from including in $\Im_n^X(t)$ all the nonlinear effects which arise from the contact/friction interaction between the bowl and the *puja*. Accordingly, the system modes become coupled by such nonlinear effects.

The modal forces $\Im_n^X(t)$ are obtained by projecting the external force field on the modal basis:

$$\Im_n^X(t) = \int_0^{2\pi} \left[F_r(\theta,t)\,\varphi_n^{Xr}(\theta) + F_t(\theta,t)\,\varphi_n^{Xt}(\theta)\right] d\theta \qquad n = 1, 2, \cdots, N \tag{5.5}$$

where $F_r(\theta,t)$ and $F_t(\theta,t)$ are the radial (impact) and tangential (friction) force fields applied by the *puja* – e.g., a localised impact $F_r(\theta_c,t)$ and/or a travelling rub $F_{r,t}(\theta_c(t),t)$. The radial and tangential physical motions can be then computed at any location θ from the modal amplitudes $q_n^X(t)$ by superposition:

$$y_r(t) = \sum_{n=1}^{N}\left[\varphi_n^{Ar}(\theta)q_n^A(t) + \varphi_n^{Br}(\theta)q_n^B(t)\right] \tag{5.6}$$

$$y_t(t) = \sum_{n=1}^{N} \left[\varphi_n^{At}(\theta) q_n^A(t) + \varphi_n^{Bt}(\theta) q_n^B(t) \right] \tag{5.7}$$

and similarly concerning the velocities and accelerations.

5.2.2 Dynamics of the puja

As mentioned before, the excitation of these musical instruments can be performed in two basic different ways: by impact or by rubbing around the rim of the bowl with the *puja* (these two types of excitation can obviously be mixed, resulting in musically interesting effects). The dynamics of the *puja* will be formulated simply in terms of a mass m_P subjected to a normal (e.g. radial) force $F_N(t)$ and an *imposed* tangential rubbing velocity $V_T(t)$ – which will be assumed constant in time for all exploratory simulations – as well as to an initial impact velocity in the radial direction $V_N(t_0)$. These three parameters are the most relevant factors which allow the musician to play the instrument and control the mechanism of sound generation. Many distinct sounds may be obtained by changing them: in particular, $V_N(t_0) \neq 0$ with $F_N = V_T = 0$ will be "pure" impact, and $F_N(t) \neq 0$, $V_T(t) \neq 0$ with $V_N(t_0) = 0$ will be "pure" *singing* (see Chapter 1). The radial motion of the *puja*, resulting from the external force applied and the impact/friction interaction with the bowl is given by:

$$m_P \ddot{y}_P = -F_N(t) + F_r(\theta, t) \tag{5.8}$$

where $F_r(\theta, t)$ is the dynamical bowl/*puja* contact force.

5.2.3 Contact interaction formulation

The radial contact force resulting from the interaction between the *puja* and the bowl is simply modelled as a contact stiffness, eventually associated with a contact damping term:

$$F_r(\theta_c) = -K_c\, \tilde{y}_r(\theta_c, t) - C_c\, \dot{\tilde{y}}_r(\theta_c, t) \tag{5.9}$$

where $\tilde{y}_r$ and $\dot{\tilde{y}}_r$ are respectively the bowl/*puja* relative radial displacement and velocity, at the (fixed or travelling) contact location $\theta_c(t)$, K_c and C_c are the contact stiffness and damping coefficients, directly related to the *puja* material. Other and more refined contact models – for instance of the hertzian type, eventually with hysteretic behaviour – could easily be implemented instead of (5.9).

5.2.4 Friction interaction formulation

In previous chapter the effectiveness of a friction model used for the simulation of bowed bars has been shown. Such model enabled a clear distinction between sliding and adherence states, sliding friction forces being computed from the Coulomb model $F_t = -|F_r|\,\mu_d(\dot{y}_t)sgn(\dot{y}_t)$, where $\dot{y}_t$ is the bowl/*puja* relative tangential velocity, and the adherence state being modelled essentially in terms of a local "adherence" stiffness K_a and some damping. It was thus possible to emulate true friction sticking of the contacting surfaces, whenever $|F_t| < |F_r|\,\mu_s$, however at the expense of a longer computational time, as smaller integration time-steps seem to be imposed by the transitions from velocity-controlled sliding states to displacement-controlled adherence states.

In this chapter, the simpler approach to friction interaction described in section 2.3.3 is used, which allows for faster computation times, although it lacks the capability to emulate true friction sticking.

5.2.5 Time-step integration

For given external excitation and initial conditions, the previous system of equations is numerically integrated using an adequate time-step algorithm. Explicit integration methods are well suited for the contact/friction model developed here. As before a simple Velocity-Verlet integration algorithm is used (Beeman, 1976).

5.3. Numerical Results

The numerical simulations presented here are based on the modal data of two different sized instruments: The modal identification performed on Bowl 2 and Bowl 4, and the corresponding results will be shown in section 5.4.1. The simulations based on the smaller instrument data will be used to highlight the main features of the dynamics of these instruments, while the larger instrument simulations will serve the purpose of studying the influence of the contact/friction parameters on the oscillation regimes.

The *puja* is modelled as a simple mass of 20 g, moving at tangential velocity V_T, and subjected to an external normal force F_N as well as to the bowl/*puja* nonlinear interaction force. A significant range of rubbing parameters is explored: $F_N = 1 \sim 9$ N and $V_T = 0.1 \sim 0.5$ m/s , which encompass the usual playing conditions, although calculations were made also using impact excitation only. For clarity, the normal force and tangential velocity will be assumed time-constant, in the present simulations. However, nothing would prevent us from imposing any time-varying functions $F_N(t)$ and $V_T(t)$, or even – as musicians would do – to couple the generation of $F_N(t)$ and $V_T(t)$ with the nonlinear bowl/*puja* dynamical simulation, through well-designed control strategies, in order to achieve a suitable response regime.

The contact model used in all rubbing simulations of Bowl 2 has a contact stiffness of $K_c = 10^6$ N/m and a contact dissipation of $C_c = 50$ Ns/m , which appear adequate for the present system. However, concerning impact simulations of this instrument, contact parameters ten times higher and lower were also explored. The friction parameters used in numerical simulations of this instrument are $\mu_s = 0.4$, $\mu_\infty = 0.2$ and $C = 10$. In relation to the numerical simulations of Bowl 4, different contact/friction parameters were used to simulated friction by *pujas* made of different materials, namely rubber and wood. Its values will be described in section 5.3.4.

In section 5.2.1 a few general remarks were produced concerning the order of the modal basis to use. With respect to the present system, the choice of the modal basis order of truncation is not difficult and certainly not critical, as only a few modes are excited (in contrast with bowed strings). For easily understandable physical reasons, modes with modal stiffness much higher than the contact stiffness are not significantly excited, so a reasonable criterion to choose a minimum order of truncation N is to compare K_c with the successive K_n of the modal series. In the present study a maximum value of $K_c = 10^6 \text{ N/m}$ is used, then it is reasonable to assume that modes with K_n much higher than 10^7 N/m will be "useless". For Bowl 2, it was devided to use seven mode pairs, the maximum value K_N being of the order $K_{2\times7} \sim 10^8 \text{ N/m}$. Indeed, this is a generous modal basis, and four mode pairs would do equally well, as $K_{2\times4} \sim 10^7 \text{ N/m}$. However it is pointless to discuss on such a detail, when the number of modes is low. In relation to the larger Bowl 4, ten mode pairs were used, following the same reasoning. Both computational and experimental results confirm that the truncation criterion adopted is adequate.

As discussed before, assuming a perfectly symmetrical bowl, simulations were performed using identical frequencies for each mode-pair ($\omega_n^A = \omega_n^B$). However, a few computations were also performed for less-than-perfect systems, asymmetry being then modelled introducing a difference (or "split") $\Delta\omega_n$ between the frequencies of each mode pair. An average value of 0.005% was used for all modal damping coefficients. In order to cope with the large settling times that arise with singing bowls, 20 seconds of computed data were generated (enough to accommodate transients for all rubbing conditions), at a sampling frequency of 22050 Hz.

5.3.1 Impact responses

Figure 5.4(a, b) display the simulated responses of a perfectly symmetrical bowl to an impact excitation ($V_N(t_0)=1 \text{ m/s}$), assuming different values for the contact model parameters. The time-histories of the response displacements pertain to the impact location. The spectrograms are based on the corresponding velocity responses. Typically, as the contact stiffness increases from 10^5 N/m to 10^7 N/m, higher-order modes become increasingly excited and resonate longer. The corresponding simulated sounds become progressively brighter, denoting the "metallic" bell-like tone which is clearly heard when impacting real bowls using wood or metal *pujas*.

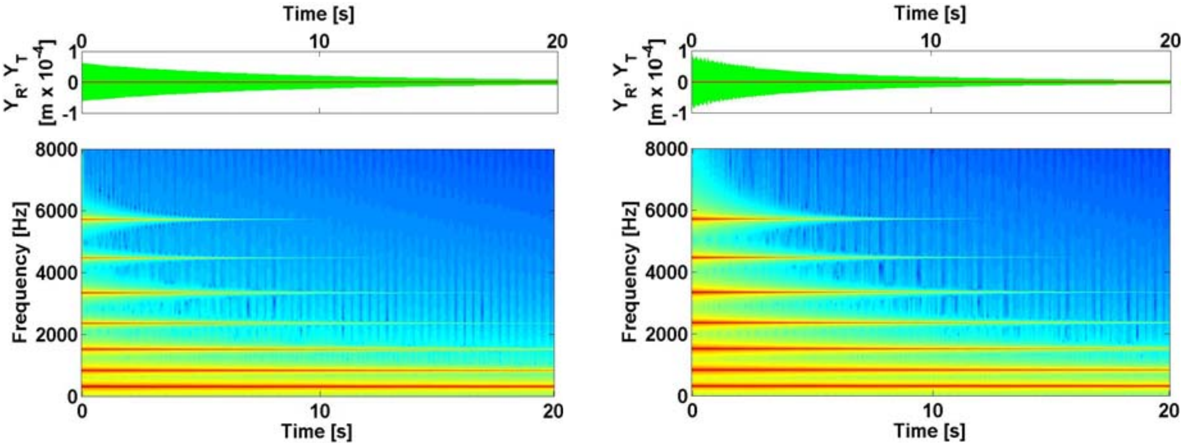

(a) **(b)**

Figure 5.4. Displacement time histories (top) and spectrograms (bottom) of the response of Bowl 2 to impact excitation with two different values of the bowl/puja contact stiffness: (a) 10^5 N/m (sound file available); (b) 10^7 N/m (sound file available).

5.3.2 Friction-excited responses

Figure 5.5 shows the results obtained when rubbing a perfectly symmetrical bowl near the rim, using fairly standard rubbing conditions: $F_N = 3\text{ N}$ and $V_T = 0.3\text{ m/s}$. The plots shown pertain to the following response locations: (a) the travelling contact point between the bowl and the *puja*; (b) a fixed point in the bowl's rim. Depicted are the time-histories and corresponding spectra of the radial (green) and tangential (red) displacement responses, as well as the spectrograms of the radial velocity responses.

As can be seen, an instability of the first "elastic" shell mode (with 4 azimuthal nodes) arises, with an exponential increase of the vibration amplitude until saturation by nonlinear effects is reached (at about 7.5 s), after which the self-excited vibratory motion of the bowl becomes steady. The response spectra show that most of the energy lays in the first mode, the others being marginally excited. Notice the dramatic differences between the responses at the travelling contact point and at a fixed location. At the moving contact point, the motion amplitude does not fluctuate and the tangential component of the motion is significantly higher than the radial component. On the contrary, at a fixed location, the motion amplitude fluctuates at a frequency which can be identified as being four times the spinning frequency of the *puja*: $\Omega_{fluct} = 4\Omega_{puja} = 4\left(2V_T/\phi\right)$. Furthermore, at a fixed location, the amplitude of the radial motion component is higher than the tangential component.

The animations of the bowl and *puja* motions enable an interpretation of these results. After synchronisation of the self-excited regime, the combined responses of the first mode-pair result in a vibratory motion according to the 4-node modeshape, which however spins, "following" the revolving *puja*. Furthermore, synchronisation settles with the *puja* interacting near a node of the radial component, corresponding to an anti-nodal region of the tangential component – see Figure 5.3 and Equations (5.2) and (5.3). In retrospect, this appears to make sense – indeed, because of the friction excitation mechanism in singing bowls, the system modes self-organize in such way that a high *tangential* motion-component will arise at the contact point, where energy is inputted.

At any fixed location, a transducer will "see" the vibratory response of the bowl modulated in amplitude, as the $2j$ alternate nodal and anti-nodal regions of the "singing" modeshape revolve. For a listener, the rubbed bowl behaves as a spinning quadropole – or, in general, a $2j$-pole (depending on the self-excited mode j) – and the radiated sound will always be perceived with beating phenomena, even for a perfectly symmetrical bowl. Therefore the sound files available were generated from the velocity time-history at a fixed point in the bowl rim.

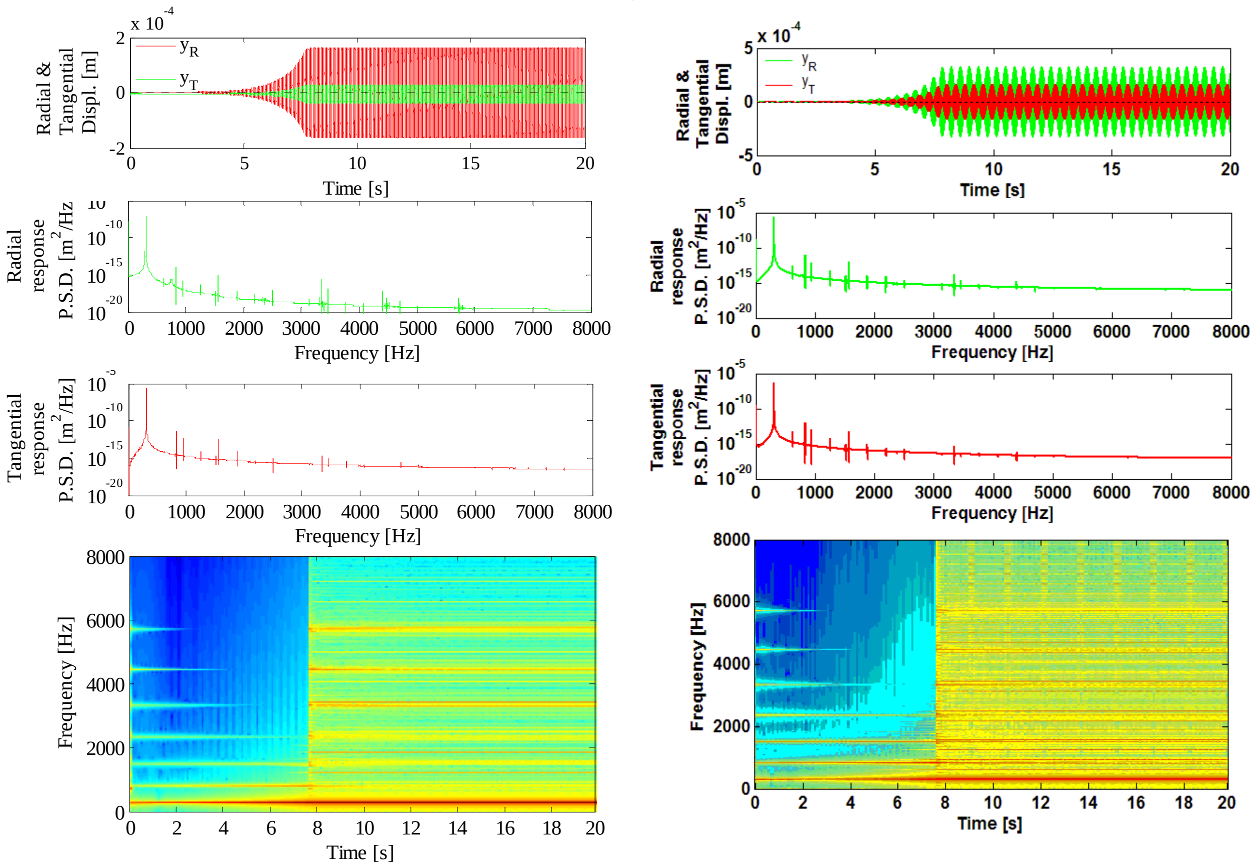

(a) (b)

Figure 5.5. Time-histories, spectra and spectrograms of the dynamical response of Bowl 2 to friction excitation when F_N = 3 N, V_T = 0.3 m/s: (a) at the bowl/puja travelling contact point; (b) at a fixed point of the bowl rim (sound file available).

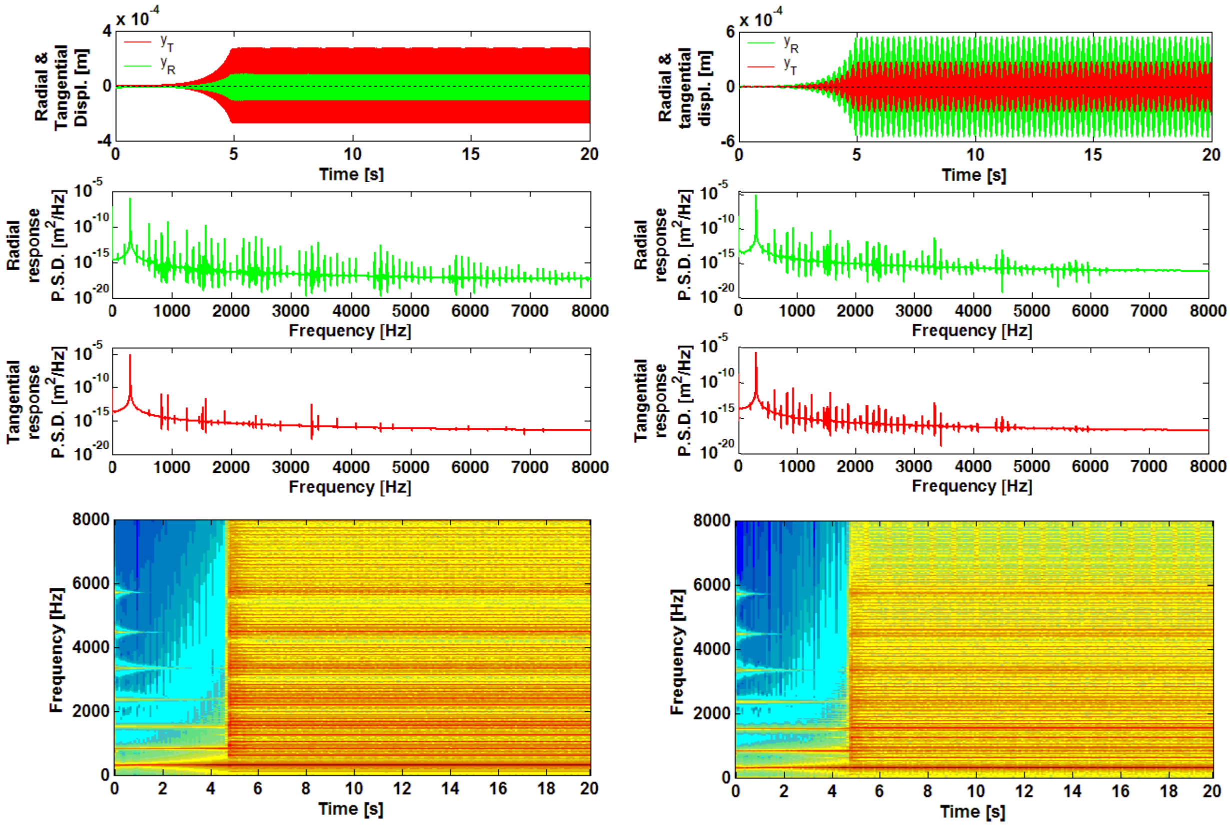

(a) **(b)**

Figure 5.6. Time-histories, spectra and spectrograms of the dynamical response of Bowl 2 to friction excitation when F_N = 7 N, V_T = 0.5 m/s: (a) at the bowl/puja travelling contact point; (b) at a fixed point of the bowl rim (sound file available).

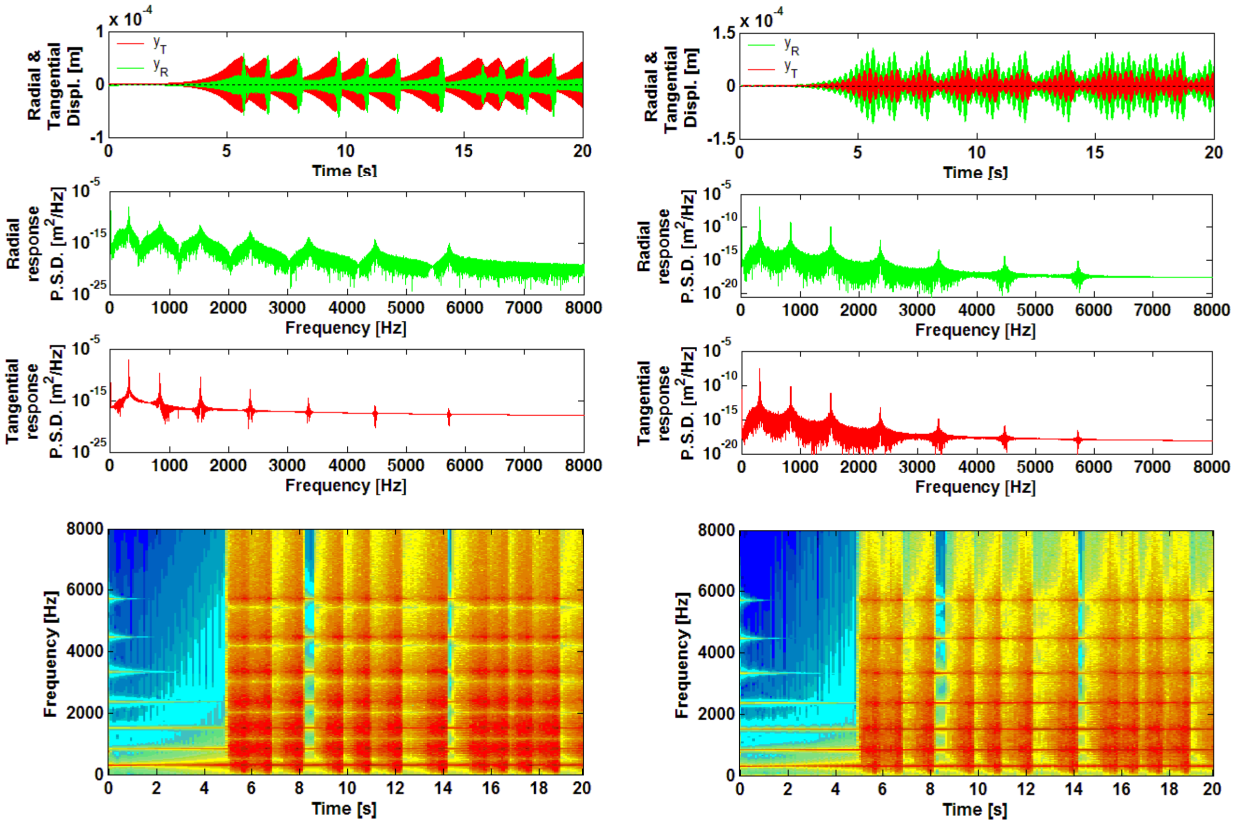

(a) **(b)**

Figure 5.7. Time-histories, spectra and spectrograms of the dynamical response of Bowl 2 to friction excitation when $F_N = 1$ N, $V_T = 0.5$ m/s: (a) at the bowl/puja travelling contact point; (b) at a fixed point of the bowl rim (sound file available).

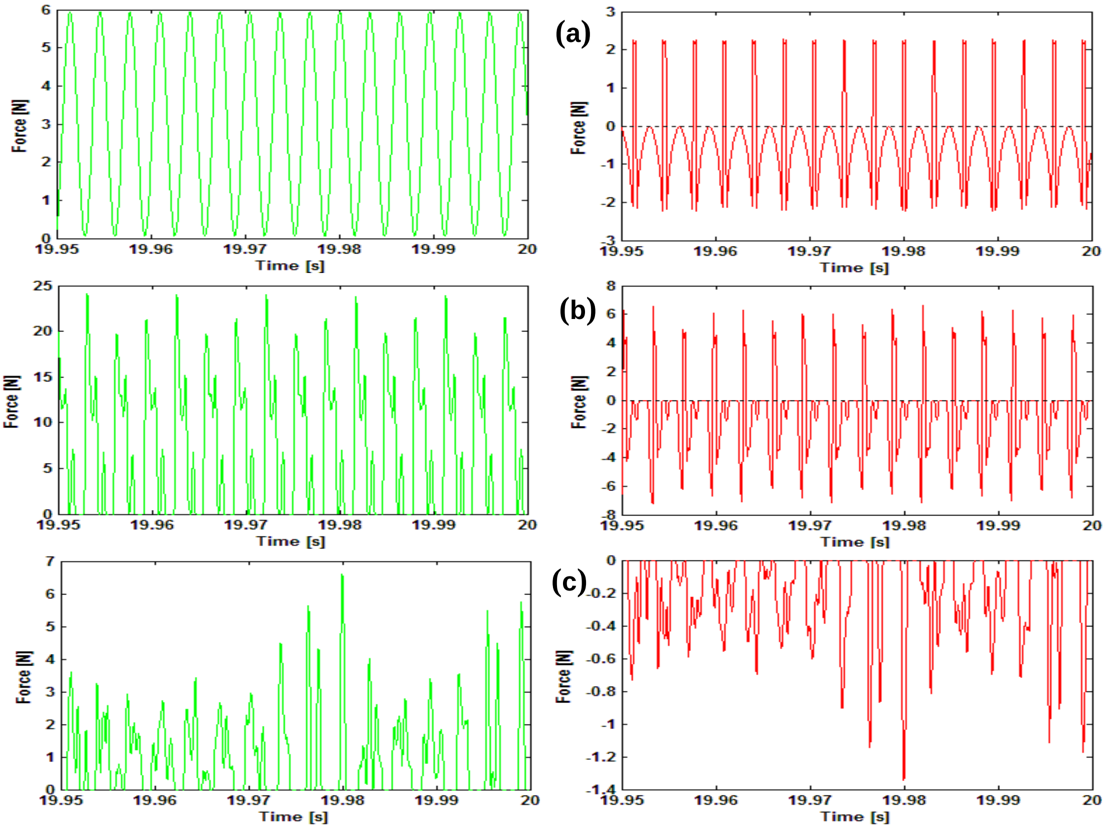

Figure 5.8. Radial (green) and tangential (red) interaction forces between the bowl and the travelling puja: (a) F_N = 3 N, V_T = 0.3 m/s; (b) F_N = 7 N, V_T = 0.5 m/s; (c) F_N = 1 N, V_T = 0.5 m/s.

Following the previous remarks, the out-of-phase envelope modulations of the radial and tangential motion components at a fixed location, as well as their amplitudes, can be understood. Indeed, all necessary insight stems from Equations(5.2) and (5.3) and the first plot of Figure 5.3.

In order to confirm the rotational behaviour of the self-excited mode a simple experiment was performed under normal playing (rubbing) conditions on Bowl 2. The near-field sound pressure radiated by the instrument was recorded by a microphone at a fixed point, approximately 5 cm from the bowl's rim. While a musician played the instrument, giving rise to a self-sustained oscillation of the first shell mode ($j = 2$, see Figures 4 and 5), the position of the rotating puja was monitored by an observer which emitted a short impulse at the puja passage by the microphone position. Since sound radiation is mainly due to the radial motion of the bowl, the experiment proves the existence of a radial vibrational nodal region at the travelling point of excitation. Between each two passages of the puja by this point (i.e. one revolution), 4 sound pressure maxima are recorded, corroborating the previous comments that the listener hears a beating phenomena (or pseudo-beating) originating from a rotating $2j$-pole source, whose "beating-frequency" is proportional to the revolving frequency of the puja. Such behaviour will be experimentally documented in section 5.4.

It should be noted that the results basically support the qualitative remarks provided by Rossing, when discussing friction-excited musical glass-instruments – see Rossing (1984) or his book Rossing (2000) pp. 185-187, the only references where some attention has been paid to these issues). However, his main point "*The location of the maximum motion follows the moving finger around the glass*" may now be further clarified: the "maximum motion" following the exciter should refer in fact to the maximum *tangential* motion component (and not the radial component, as might be assumed).

Before leaving this example, notice in Figure 5.8 the behaviour of the radial and tangential components of the bowl/*puja* contact force, on several cycles of the steady motion. The radial component oscillates between almost zero and the double of the value F_N imposed to the *puja*, and contact is never disrupted. The plot of the friction force shows that the bowl/*puja* interface is sliding during most of the time. This behaviour is quite similar to what was observed in simulations of bowed bars, and is in clear contrast to bowed strings, which adhere to the bow during most of the time – see Inácio *et al* (2003b), for a detailed discussion. The fact that sticking only occurs during a short fraction of the motion, justifies the simplified friction model which has been used for the present computations.

Figure 5.6 shows the results for a slightly different regime, corresponding to rubbing conditions: $F_N = 7\ \text{N}$ and $V_T = 0.5\ \text{m/s}$. The transient duration is smaller than in the previous case (about 5 s). Also, because of the higher tangential *puja* velocity, beating of the vibratory response at the fixed location also displays a higher frequency. This motion regime seems qualitatively similar to the previous example, however notice that the response spectra display more energy at higher frequencies, and that is because the contact between the exciter and the bowl is periodically disrupted, as shown in the contact force plots of Figure 5.8(b). One can see that, during about 25% of the time, the contact force is zero. Also, because of moderate impacting, the maxima of the radial component reach almost $3\,F_N$. Both the radial and friction force components are much less regular than in the previous example, but this does not prevent the motion from being nearly-periodic.

Figure 5.7 shows a quite different behaviour, when $F_N = 1\ \text{N}$ and $V_T = 0.5\ \text{m/s}$. Here, a steady motion is never reached, as the bowl/*puja* contact is disrupted whenever the vibration amplitude reaches a certain level. As shown in Figure 5.8(c), severe chaotic impacting arises (the amplitude of the radial component reaches almost $7\,F_N$), which breaks the mechanism of energy transfer, leading to a sudden decrease of the motion amplitude. Then, the motion build-up starts again until the saturation level is reached, and so on. As can be expected, this intermittent response regime results in curious sounds, which interplay the aerial characteristics of "singing" with a distinct "ringing" response due to chaotic chattering. Anyone who ever attempted to play a Tibetan bowl is well aware of this sonorous saturation effect, which can be musically interesting, or a vicious nuisance, depending on the context.

To get a clearer picture of the global dynamics of this system, Figure 5.9 and Figure 5.10 present the domains covered by the three basic motion regimes (typified in Figure 5.5 to Figure 5.7), as a function of F_N and V_T: (1) Steady self-excited vibration with permanent contact between the *puja* and the bowl (green data); (2) Steady self-excited vibrations with periodic contact disruption (yellow data); (3)

Unsteady self-excited vibrations with intermittent amplitude increasing followed by attenuation after chaotic chattering (orange data). Note that, under different conditions, the self-excitation of a different mode may be triggered – for instance, by starting the vibration with an impact followed by rubbing. Such issue will be discussed in subsequent sections of this chapter.

Figure 5.9(a) shows how the initial transient duration depends on F_N and V_T. In every case, transients are shorter for increasing normal forces, though such dependence becomes almost negligible at higher tangential velocities. At constant normal force, the influence of V_T strongly depends on the motion regime. Figure 5.9(b) shows the fraction of time with motion disruption. It is obviously zero for regime (1), and growing up to 30% at very high excitation velocities. It is clear that the "ringing" regime (3) is more prone to arise at low excitation forces and higher velocities.

Figure 5.10(a) and Figure 5.10(b) show the root-mean-square vibratory amplitudes *at the traveling contact point*, as a function of F_N and V_T. Notice that the levels of the radial components are much lower than the corresponding levels of the tangential component, in agreement with the previous comments. These plots show some dependence of the vibratory level on the response regime. Overall, the vibration amplitude increases with V_T for regime (1) and decreases for regime (3). On the other hand, it is almost independent of F_N for regime (1), while it increases with F_N for regime (3).

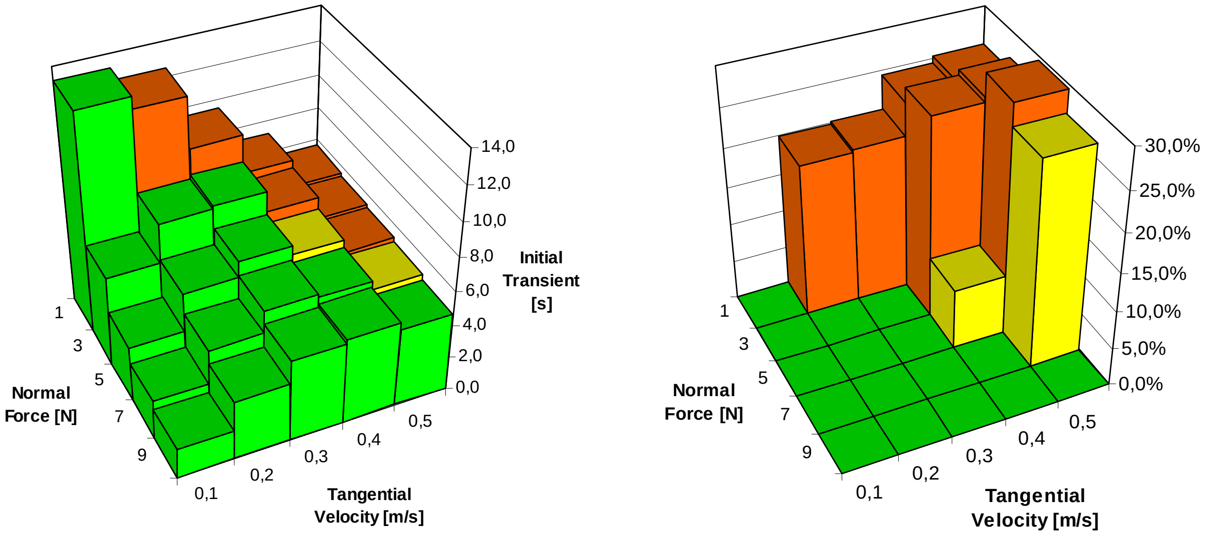

(a)

(b)

Figure 5.9. (a) Initial transient duration and (b) percentage of time with no bowl/*puja* contact, as a function of F_N and V_T.

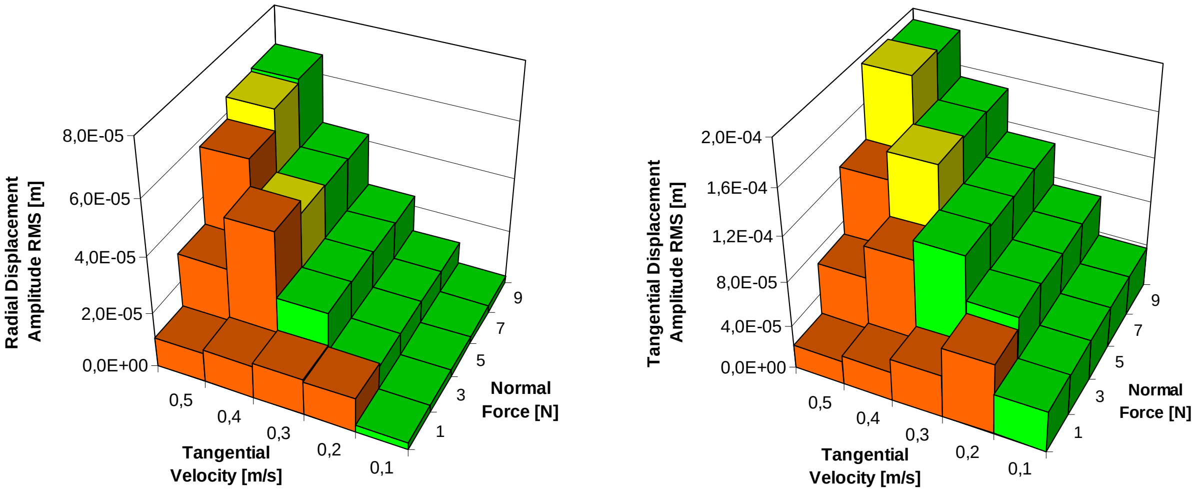

(a)

(b)

Figure 5.10. Displacement amplitude (RMS) at the bowl/*puja* travelling contact point, as a function of F_N and V_T: (a) Radial motion component; (b) Tangential motion component.

5.3.3 Non-symmetrical bowls

Figure 5.11 (a) and (b) enable a comparison between the impact responses of perfectly symmetrical and a non-symmetrical bowls. Here, the lack of symmetry has been simulated by introducing a frequency split of 2% between the frequencies of each mode-pair (e.g. $\Delta\omega_n = 0.02\omega_n$), all other aspects remaining identical – such crude approach is adequate for illustration purposes.

Notice that the symmetrical bowl only displays radial motion *at the impact point* (as it should), while the unsymmetrical bowl displays both radial and tangential motion components due to the different propagation velocities of the travelling waves excited. On the other hand, one can notice in the response spectra of the unsymmetrical system the frequency-split of the various mode-pairs. This leads to beating of the vibratory response, as clearly seen on the corresponding spectrogram.

Figure 5.12 shows the self-excited response of the symmetrical bowl, when rubbed at $F_N = 3\text{ N}$ and $V_T = 0.3\text{ m/s}$. Notice that sound beating due to the spinning of the response modeshape dominates, when compared to effect of modal frequency-split. Interestingly, the slight change in the modal frequencies was enough to modify the nature of the self-excited regime, which went from type (1) to type (3). This fact shows the difficulties in mastering these apparently simple instruments.

5.3.4 Influence of the contact/friction parameters

Playing experience shows that rubbing with *pujas* made of different materials may trigger self-excited motions at different fundamental frequencies. This suggests that friction and contact parameters have an important influence on the dynamics of the bowl regimes. Although this behaviour was present in all the bowls used in this study, it was clearly easier to establish these different regimes on a larger bowl. Therefore the illustration of the different behaviours that can be obtained is made by using Bowl 4 and parameters corresponding to two *pujas,* respectively covered with rubber and made of naked wood.

As the frequency separation between mode-pairs was relatively small for this bowl, a perfectly symmetrical bowl is assumed, and simulations using 10 mode-pairs wree performed with identical frequencies ($\omega_n^A = \omega_n^B$) – see Table 5.2. An average value of

0.005% was used for all modal damping coefficients. In order to cope with the large settling times that arise with singing bowls, 30 seconds of computed data were generated (enough to accommodate transients for all rubbing conditions).

Figure 5.13 shows a computed response obtained when using a soft *puja* with relatively high friction. Here a contact stiffness K_c = 10^5 N/m was used, assuming friction parameters $\mu_s = 0.8$, $\mu_\infty = 0.4$ and C = 10, under playing conditions F_N = 5 N and V_T = 0.3 m/s.

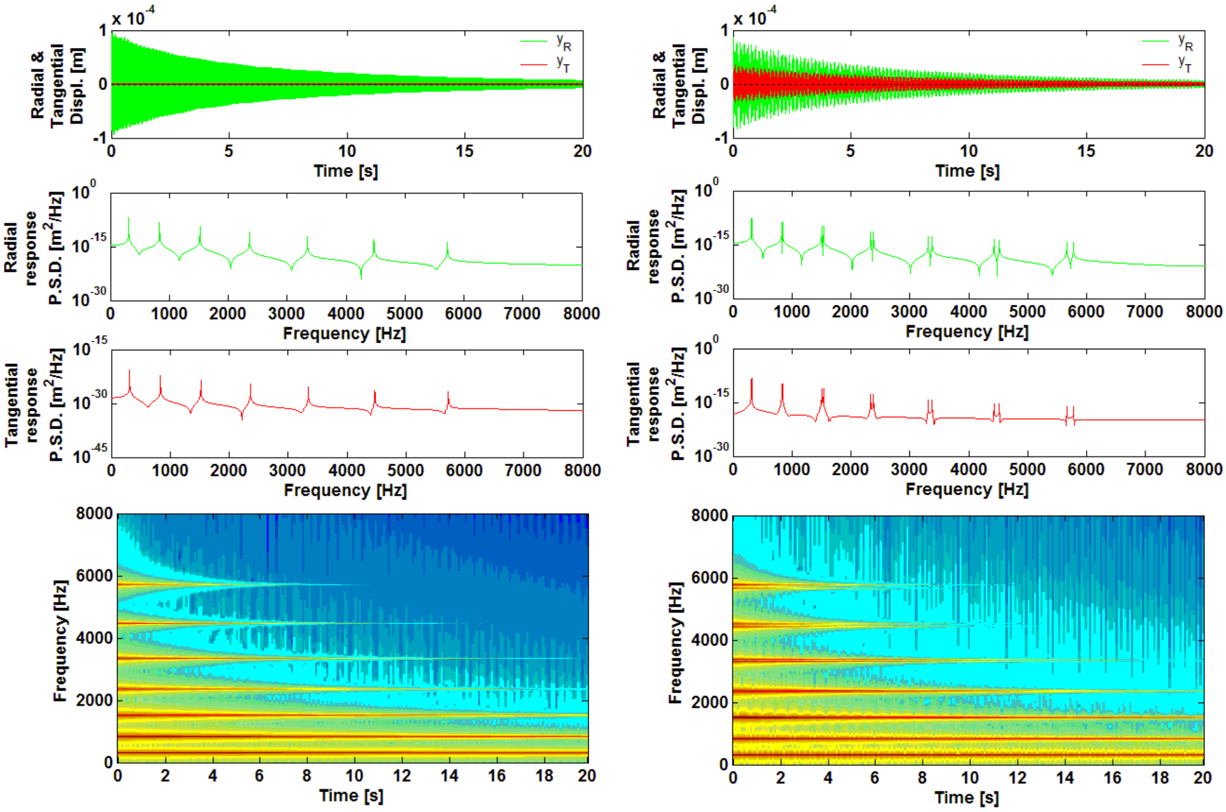

(a) (b)

Figure 5.11. Dynamical responses of an impacted bowl, at the impact location: (a) Axi-symmetrical bowl (0% frequency split); (b) Non-symmetrical bowl with 2% frequency split (sound file available).

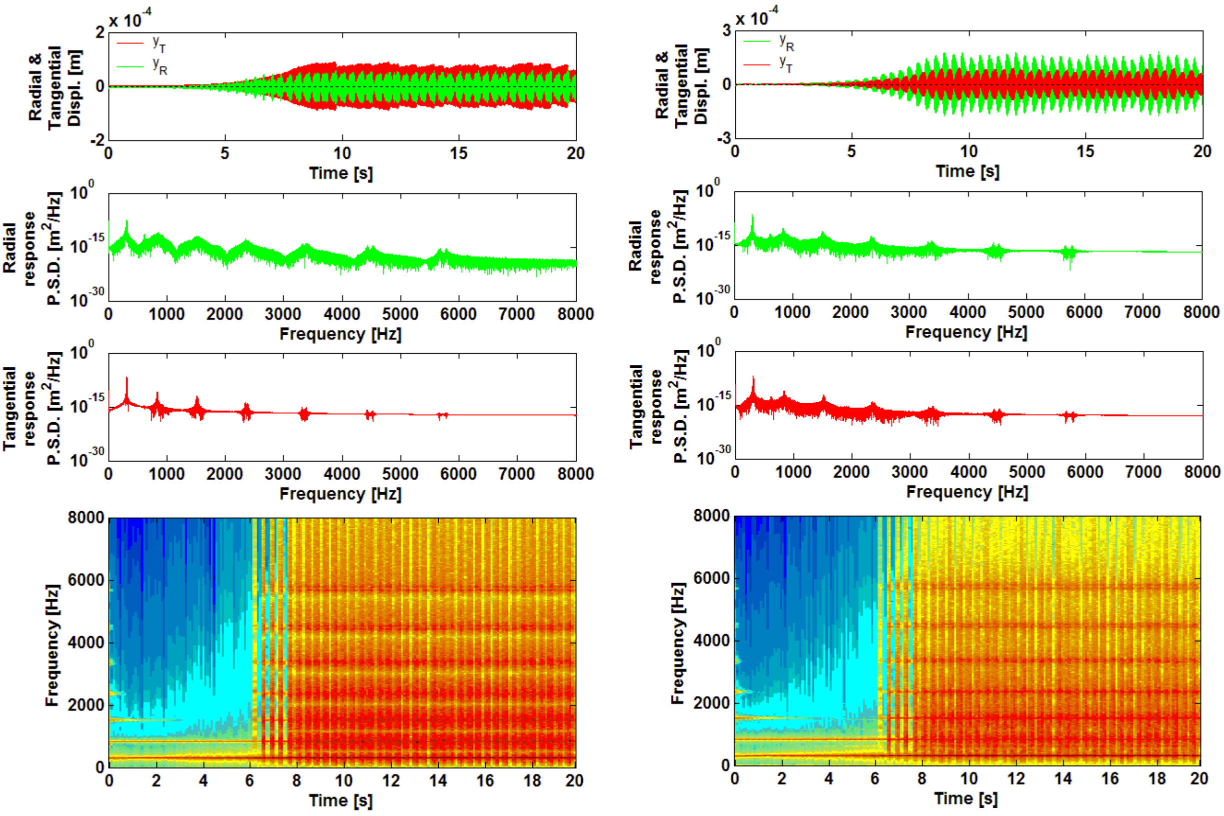

(a) **(b)**

Figure 5.12. Dynamical response of a rubbed bowl with 2% frequency split when $F_N = 3$ N, $V_T = 0.3$ m/s: (a) at the bowl/puja travelling contact point; (b) at a fixed point of the bowl rim (sound file available).

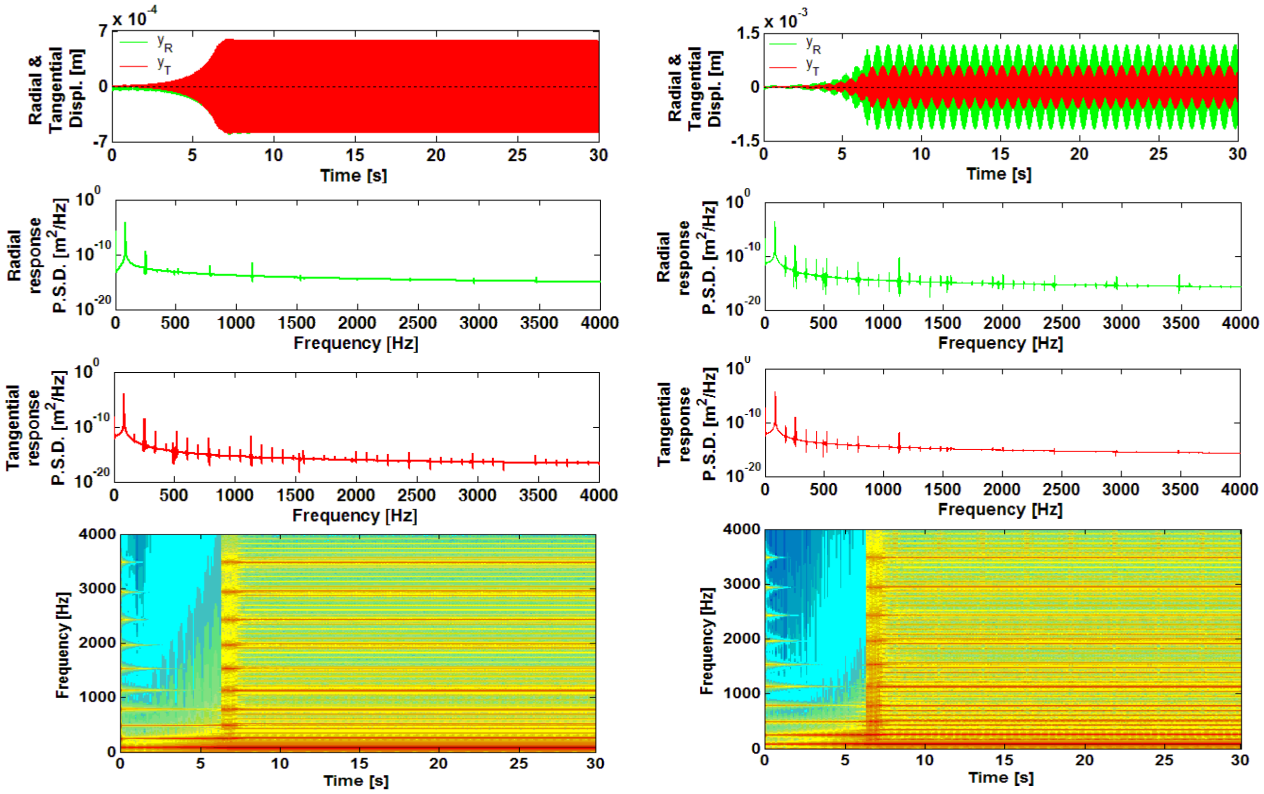

(a)

(b)

Figure 5.13. Time-histories, spectra and spectrograms of the dynamical response of Bowl 4 excited by a rubber-covered puja for F_N = 5 N and V_T = 0.3 m/s: (a) at the bowl/puja travelling contact point; (b) at a fixed point of the bowl rim (sound file available).

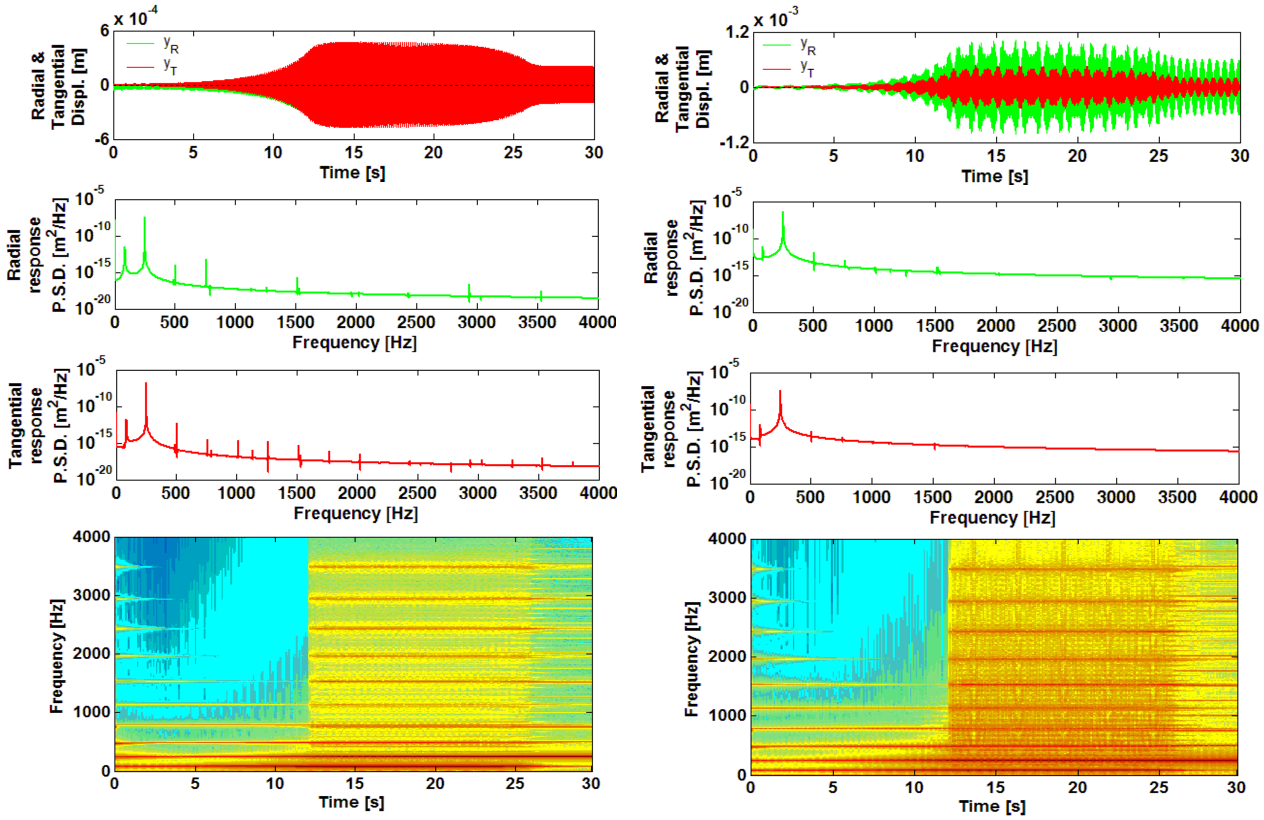

(a) (b)

Figure 5.14. Time-histories, spectra and spectrograms of the dynamical response of Bowl 4 excited by a wooden puja for F_N = 5 N and V_T = 0.3 m/s: (a) at the bowl/puja travelling contact point; (b) at a fixed point of the bowl rim (sound file available).

The plot shown in a) displays the radial (green) and tangential (red) bowl motions at the travelling contact point with the puja. These are of about the same magnitude, and perfectly steady as soon as the self-excited motion locks-in. In contrast, plot b) shows that the radial motion clearly dominates when looking at a fixed location in the bowl, with maximum amplitudes exceeding those of the travelling contact point by a factor two. Most important, beating phenomena is observed at a frequency related to the puja spinning frequency $\Omega_p = 2V_T/\phi$, as also observed in relation to Bowl 2. The spectrum shown in plot c) presents the highest energy near the first modal frequency, while the spectrogram d) shows that the motion settles after about 7 seconds of exponential divergence. Indeed, the computed animations show that the unstable first bowl mode ($\approx$87Hz) spins, following the puja motion, with the contact point located near one of the four nodes of the excited modeshape (see Figure 5.3). The bowl radiates as a quadro-pole spinning with frequency Ω_p, and beating is perceived with frequency $\Omega_{beat} = 4\Omega_p$.

Figure 5.14 shows a computed response obtained when using a harder puja with lower friction, assuming $K_c = 10^6\ \mathrm{N/m}$, $\mu_s = 0.4$ and $\mu_\infty = 0.2$, under the same playing conditions as before.

The self-excited motion takes longer to emerge and is prone to qualitative changes. However, vibration is essentially dominated by the *second* modal frequency ($\approx$253Hz), with a significant contribution of the first mode during the initial 25 seconds. This leads to more complex beating phenomena, except during the final 5 seconds of the simulation, where one can notice that, in spite of the similar value of V_T used, beating is at a higher frequency than in Figure 5.13. Indeed, because the second elastic mode is now unstable (see Figure 5.3), the bowl radiates as a hexa-pole spinning with frequency Ω_p, and beating is perceived with frequency $\Omega_{beat} = 6\Omega_p$.

5.4. *Experimental Results*

5.4.1 Modal Identification

Figures 1.1 and 1.2 in Chapter 1 show the four bowls and two *pujas* used for the experimental work in this work. In order to estimate the natural frequencies ω_n, damping values ς_n, modal masses m_n and modeshapes $\varphi_n(\theta,z)$ to be used in the numerical simulations, a detailed experimental modal identification based on impact testing was performed for Bowls 1, 2 and 3. A mesh of 120 test locations was defined for each instrument (e.g., 24 points regularly spaced azimuthally, at 5 different heights). Impact excitation was performed on all of the points and the radial responses were measured by two accelerometers attached to inner side of the bowl at two positions, located at the same horizontal plane (near the rim) with a relative angle of 55º between them, as can be seen in Figure 5.15(a). Modal identification was achieved by developing a simple MDOF algorithm in the frequency domain (Ewins, 1984). The modal parameters were optimized in order to minimize the error $\varepsilon(\omega_n,\varsigma_n,m_n,\varphi_n)$ between the measured transfer functions $H_{er}(\omega)=\ddot{Y}_r(\omega)/F_e(\omega)$ and the fitted modal model $\hat{H}_{er}(\omega;\omega_n,\varsigma_n,m_n,\varphi_n)$, for all measurements ($P_e$ excitation and P_r response locations), in a given frequency range $[\omega_{\min},\omega_{\max}]$ encompassing N modes. Hence:

$$\varepsilon(\omega_n,\varsigma_n,m_n,\varphi_n)= \\ =\sum_{e=1}^{P_e}\sum_{r=1}^{P_r}\int_{\omega_{\min}}^{\omega_{\max}}\left[H_{er}(\omega)-\hat{H}_{er}(\omega;\omega_n,\varsigma_n,m_n,\varphi_n)\right]d\omega \tag{5.10}$$

with:

$$\hat{H}_{er}(\omega;\omega_n,\varsigma_n,m_n,\varphi_n)= \\ =\sum_{n=n_1}^{n_1+N}-\omega^2\frac{A_n^{er}}{\omega_n^2-\omega^2+2i\omega\omega_n\varsigma_n}-\omega^2C_1+C_2 \tag{5.11}$$

where the modal amplitude coefficients are given as $A_n^{er}=\varphi_n(\theta_e,z_e)\varphi_n(\theta_r,z_r)/m_n$ and the two last terms in (5.11) account for modes located out of the identified frequency-range. The values of the modal masses obviously depend on how modeshapes are normalized ($|\varphi(\theta,z)|_{\max}=1$). Note that the identification is nonlinear in ω_n and ς_n but linear in A_n^{er}.

Results from the experiments on the three bowls show the existence of 5 to 7 prominent resonances with very low modal damping values up to frequencies about 4~6kHz. For these well-defined experimental modes, the simple identification scheme used proved adequate. As an illustration, Figure 5.15(b) depicts the modulus of a frequency response function obtained from Bowl 2, relating the acceleration measured at point 1 (near the bowl rim) to the force applied at the same point.

The shapes of the identified bowl modes are mainly due to bending waves that propagate azimuthally, resulting in patterns similar to some modeshapes of bells (Rossing, 2000). Following Rossing, notation (j,k) represents here the number of complete nodal meridians extending over the top of the bowl (half the number of nodes observed along a circumference), and the number of nodal circles, respectively.

Despite the high manufacturing quality of these handcrafted instruments, perfect axi-symmetry is nearly impossible to achieve. As was explained in section 5.2.1, these slight geometric imperfections lead to the existence of two orthogonal modes (hereby called modal families A and B), with slightly different natural frequencies. Although this is not apparent in Figure 5.15(b), by zooming the analysis frequency-range, an apparently single resonance often reveals two closely spaced peaks.

Figure 5.16 shows the perspective and top views of the two orthogonal families of the first 7 “sounding” (radial) modeshapes (rigid-body modes are not shown) for Bowl 2, as identified from experiments. In the frequency-range explored, all the identified modes are of the $(j,0)$ type, due to the low value of the height to diameter ratio (Z/ϕ) for Tibetan bowls, in contrast to most bells. The modal amplitudes represented are normalised to the maximum amplitude of both modes, which complicates the perception of some modeshapes. However, the spatial phase difference ($\pi/2j$) between each modal family (see section 5.2.1) is clearly seen. Although modal frequencies and damping values were obtained from the modal identification routine, it was soon realized that the accelerometers and their cables had a non-negligible influence on the bowl modal parameters, due to the very low damping of these systems, which was particularly affected by the instrumentation.

Indeed, analysis of the near-field sound pressure time-histories, radiated by impacted bowls, showed slightly higher values for the natural frequencies and much longer decay times, when compared to those displayed after transducers were installed. Hence, it was decided to use some modal parameters identified from the acoustic responses of non-instrumented impacted bowls. Modal frequencies were extracted from the sound pressure spectra and damping values were computed from the logarithm-decrement of band-pass filtered (at each mode) sound pressure decays.

Table 5.1 shows the values of the double modal frequencies (f_n^A and f_n^B) of the most prominent modes of the three bowls tested, together with their ratios to the fundamental – mode (2,0) – where f_n^{AB} represents the average frequency between the two modal frequencies f_n^A and f_n^B. These values are entirely in agreement with the results obtained by Rossing (2000). Interestingly, these ratios are rather similar, in spite of the different bowl shapes, sizes and wall thickness. As rightly pointed by Rossing (2000), these modal frequencies are roughly proportional to j^2, as in cylindrical shells, and inversely proportional to ϕ^2. Rossing explains this in simple terms, something that can be also grasped from the theoretical solution for in-plane modes for rings (Harris, 1996):

$$\omega_j = \frac{j(j^2-1)}{\sqrt{j^2+1}}\sqrt{\frac{EI}{\rho A R^4}} \text{, with } j = 1, 2, ..., N \quad (3)$$

where E and ρ are the Young Modulus and density of the ring material, I the area moment of inertia, A the ring cross section area and R the ring radius. It can be seen that as j takes higher values, the first term of equation 3 tends to j^2, while the dependency on the ring diameter is embedded in the second term.

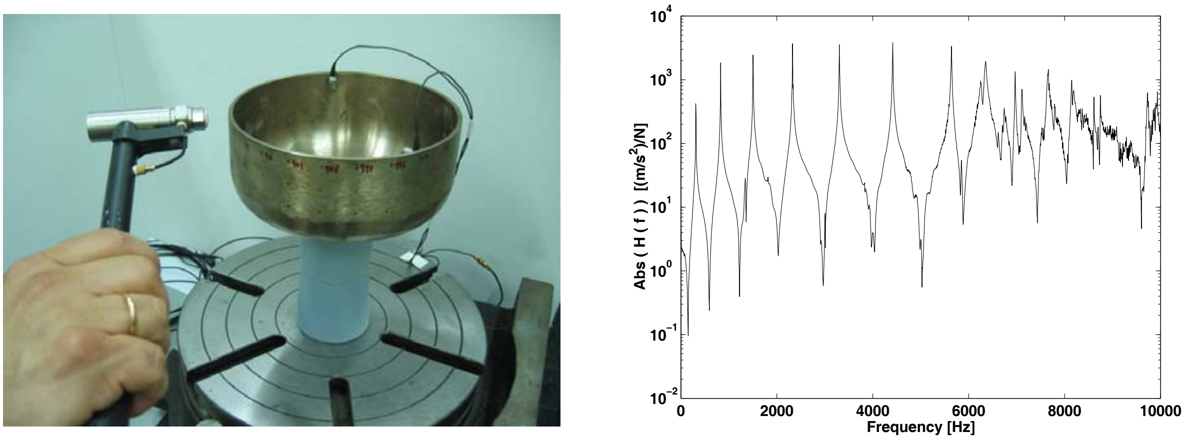

(a) **(b)**

Figure 5.15. Experimental modal identification of Bowl 2: (a) Picture showing the measurement grid and accelerometer locations; (b) Modulus of the accelerance frequency response function.

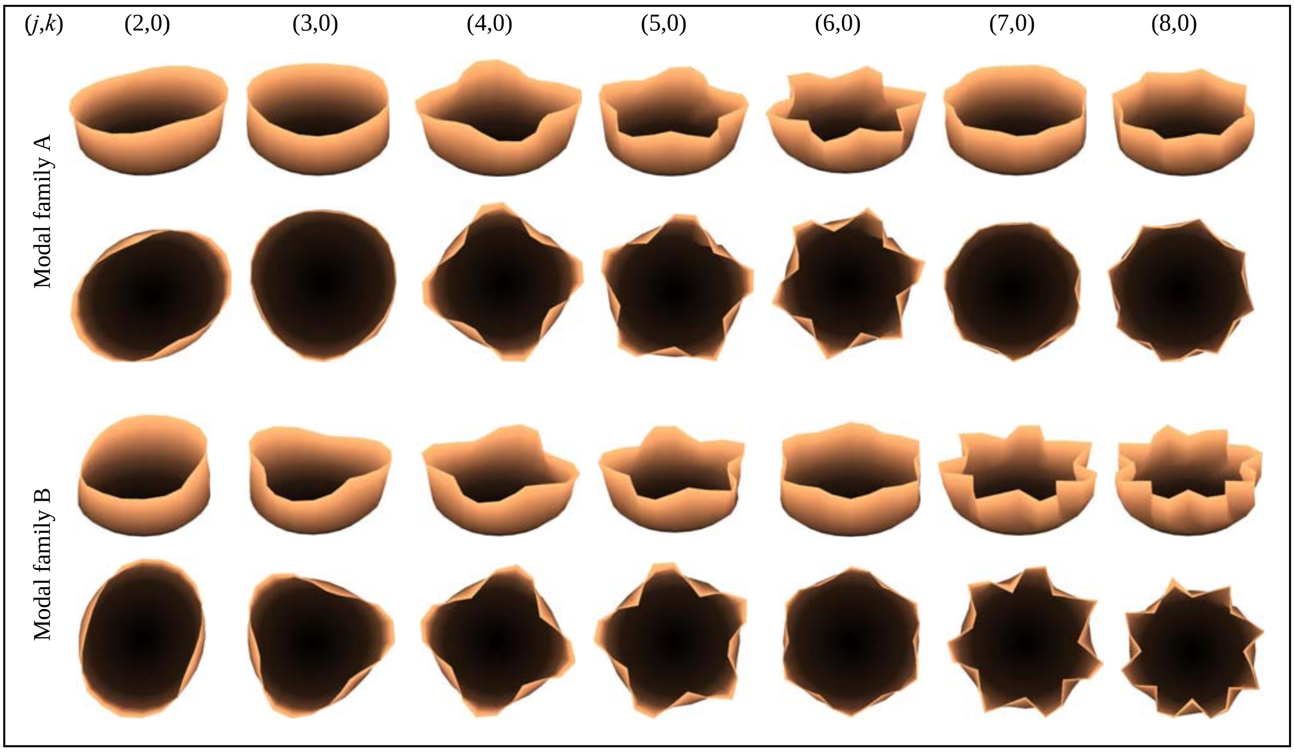

Figure 5.16. Perspective and top view of experimentally identified modeshapes (j,k) of the first 7 elastic mode-pairs of Bowl 2 (j relates to the number of nodal meridians and k to the number of nodal circles – see text).

Table 5.1 – Modal frequencies and frequency ratios of bowls 1, 2 and 3 (as well as their total masses M_T and rim diameters ϕ).

	Bowl 1			**Bowl 2**			**Bowl 3**		
Total Mass	$\boldsymbol{M_T}$ = 934 g			$\boldsymbol{M_T}$ = 563 g			$\boldsymbol{M_T}$ = 557 g		
Diameter	$\phi = 180$ mm			$\phi = 152$ mm			$\phi = 140$ mm		
Mode	f_n^A [Hz]	f_n^B [Hz]	f_n^{AB}/f_1^{AB}	f_n^A [Hz]	f_n^B [Hz]	f_n^{AB}/f_1^{AB}	f_n^A [Hz]	f_n^B [Hz]	f_n^{AB}/f_1^{AB}
(2,0)	219.6	220.6	1	310.2	312.1	1	513.0	523.6	1
(3,0)	609.1	609.9	2.8	828.1	828.8	2.7	1451.2	1452.2	2.8
(4,0)	1135.9	1139.7	5.2	1503.4	1506.7	4.8	2659.9	2682.9	5.2
(5,0)	1787.6	1787.9	8.1	2328.1	2340.1	7.5	4083.0	4091.7	7.9
(6,0)	2555.2	2564.8	11.6	3303.7	3312.7	10.6	5665.6	5669.8	10.9
(7,0)	3427.0	3428.3	15.6	4413.2	4416.4	14.2	-	-	-
(8,0)	4376.3	4389.4	19.9	5635.4	5642.0	18.1	-	-	-

The frequency relationships are mildly inharmonic, which does not affect the definite pitch of this instrument, mainly dominated by the first (2,0) shell mode. As stated, dissipation is very low, with modal damping ratios typically in the range ς_n = 0.002~0.015 % (higher values pertaining to higher-order modes). However, note that these values may increase one order of magnitude, or more, depending on how the bowls are actually supported or handled.

Further experiments were performed on the larger bowl shown in Figure 1.2 (Bowl 4), with ϕ = 262 mm, a total mass of 1533 g and a fundamental frequency of 86.7 Hz. A full modal identification was not pursued for this instrument, but ten natural frequencies were identified from measurements of the sound pressure resulting from impact tests. These modal frequencies are presented in Table 5.2, which show a similar relation to the fundamental as the first three bowls presented in this study. For this instrument all these modes were assumed to be of the (*j*,0) type.

Table 5.2 – Modal frequencies and frequency ratios of Bowl 4.

Mode (*j*,*k*)	f_n [Hz]	f_n/f_1
(2,0)	86.7	1.0
(3,0)	252.5	2.9
(4,0)	490.0	5.7
(5,0)	788.0	9.1
(6,0)	1135.0	13.1
(7,0)	1533.0	17.7
(8,0)	1963.0	22.6
(9,0)	2429.0	28.0
(10,0)	2936.0	33.9
(11,0)	3480.0	40.1

5.4.2 Experimental Self-Excited Motions

Figure 5.17(a) shows the experimental results recorded by a microphone placed near the bowl rim, while playing with a *rubber-covered* puja. As described before, timing pulses were generated at each consecutive revolution, when the puja and microphone were nearby. Vibration was dominated by an instability of the *first* mode (2,0) and, in spite of mildly-controlled human playing, it is clear that radiation is minimal near the contact point and that four beats per revolution are perceived. When a harder *naked wood* puja was used, the initial transient became longer, before an instability of the *second* mode (3,0) settled. The bowl responses tended to be less regular, as shown in Figure 5.17(b), however six beats per revolution are clearly perceived. All these features support the simulation results presented in Figure 5.13 and Figure 5.14, as well as the physical discussion presented in section 5.3.2.

The present results stress the importance of the contact/friction parameters, if one wishes a bowl to "sing" in different modes – such behaviour is easier to obtain in larger bowls. As a concluding remark, it should be emphasised that a sonorous bowl/puja rattling contact can easily arise, in particular at higher tangential velocities and lower normal forces, a feature which was equally displayed by many experiments and numerical simulations, as discussed before.

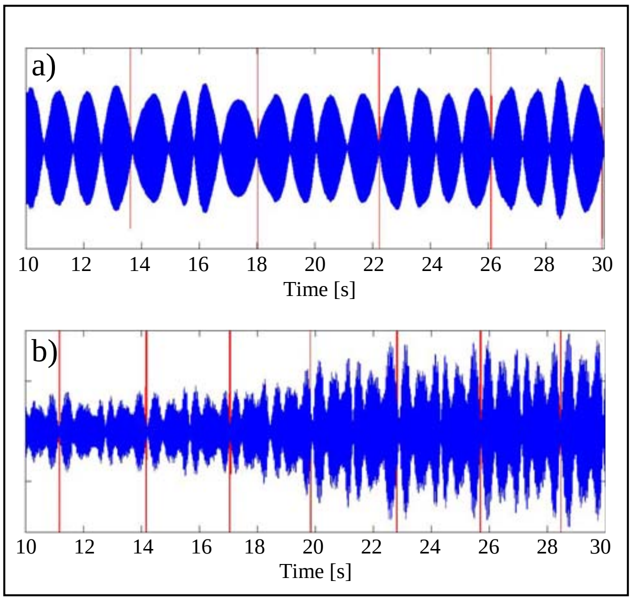

Figure 5.17 – Near-field sound pressure waveform (blue) due to friction excitation by: a) a rubber-covered *puja* and b) a wooden *puja* on Bowl 4, and electrical impulses (red) synchronized with the passage of the puja by the microphone position (sound files available).

Chapter 6

6. LINEARISED ANALYSIS OF SELF-EXCITED REGIMES

6.1. *Introduction*

As explained in the previous chapters, considerable efforts have been invested by the scientific community to produce time-domain numerical simulations of the self-excited nonlinear regimes. However, no systematic analysis of the linearized behaviour of the bowed string has ever been pursued. In this chapter the features of the linearized modal dynamics of bowed bars and bowed strings are analysed, starting from a modal formulation of the string acted by the nonlinear bowing forces, using a classic Coulomb model with velocity-dependent friction coefficient. Then the corresponding linearized formulation is developed, about an average sliding state, which enables computation of the complex eigenvalues and eigenvectors as a function of the bowing parameters, which can offer interesting information concerning the system stability behaviour, and further insight when addressing the post-instability nonlinear limit-cycle responses.

6.2. *Bowed bar*

6.2.1 Modal formulation for the bowed bar

For the purpose of the work presented in this section the simple Bernoulli-Euler model for the bar flexural vibrations is adequate. However, extension to the more realistic Timoshenko model is straightforward and merely leads to a correction in the beam modal parameters used in the following. Starting from the classic damped equation for a non-uniform beam:

$$\rho S(x)\frac{\partial^2 y}{\partial t^2}+\eta\frac{\partial y}{\partial t}+\frac{\partial^2}{\partial x^2}\left[EI(x)\frac{\partial^2 y}{\partial x^2}\right]=F(x,t) \qquad (6.1)$$

where $y(x,t)$ is the lateral bending displacement, ρ and E are the beam density and Young modulus, η is a coefficient of viscous dissipation, $S(x)$ and $I(x)$ are the cross-section area and geometric moment of inertia about the bending axis, $F(x,t)$ is the externally applied excitation, Equation (2.1) may be recast in modal form:

$$[M]\{\ddot{Q}(t)\}+[C]\{\dot{Q}(t)\}+[K]\{Q(t)\}=\{\Xi(t)\} \tag{6.2}$$

where, $[M]$, $[C]$ and $[K]$, are the matrices of modal parameters of the unconstrained system m_n, $c_n = 2m_n\omega_n\zeta_n$ and $k_n = m_n\omega_n^2$ (using N modes with frequencies ω_n and modal damping values ζ_n) while $\{Q(t)\}$ and $\{\Xi(t)\}$ are the vectors of modal amplitudes and generalised forces, respectively. For a bar with uniform cross-section and free-free boundary conditions, the modal masses, modal frequencies and modeshapes are given respectively by $m_n = \int_0^L m(x)\,\phi_n^2(x)\,dx$, $\omega_n = (\lambda_n/L)^2\sqrt{EI/\rho S}$ and $\phi_n(x) = \beta_n\{\cos(\lambda_n x/L) + \sinh(\lambda_n x/L) + \alpha_n[\sin(\lambda_n x/L) + \cosh(\lambda_n x/L)]\}$, with the parameters $\alpha_n = -(\cos\lambda_n - \sinh\lambda_n)/(\sin\lambda_n - \cosh\lambda_n)$ and β_n chosen such as to obtain a normalizing condition $\max|\phi_n(x)| = 1$. From the free-free boundary conditions of the bar – $\phi''(0) = \phi''(L) = 0$ and $\phi'''(0) = \phi'''(L) = 0$ – the bar modal frequencies and modeshapes are obtained. The first two eigen-frequencies pertain to rigid-body modes, with frequencies $\omega_1 = \omega_2 = 0$ and modeshapes $\phi_1(x) = 1$ (translational mode) and $\phi_2(x) = 1 - 2x/L$ (rocking mode).

The generalised forces $\mathscr{F}_n(t)$ of vector $\{\Xi(t)\}$ are obtained by projection of the external force field on the modal basis. For the present case, three point-forces are applied to the system at three different positions: the friction force, $F_f(t)$, induced by the bow at the edge of the bar, and the forces $F_{s1}(t)$ and $F_{s2}(t)$, applied by the elastic supports of the bar at the nodal points of the first vibratory bending mode, giving a total of:

$$F(x,t) = F_f(x_f,t) + F_{s1}(x_{s1},t) + F_{s2}(x_{s2},t) \tag{6.3}$$

where x_f, x_{s1} and x_{s2} are the locations of the applied forces. $F_{s1}(t)$ and $F_{s2}(t)$ are given by Equation (6.4) where K_s and C_s are the stiffness and damping values of the bar elastic supports.

$$F_{si}(t) = K_s y_{si}(t) + C_s \dot{y}_{si}(t), \text{ with } i = 1,2 \tag{6.4}$$

The generalized forces can then be described by:

$$\mathscr{F}_n(t) = \sum_{m=1}^{3} F_m(t)\,\phi_n(x_m),\ \text{with}\ x_1 = x_f\,,\ x_2 = x_{s1}\ \text{and}\ x_3 = x_{s2} \tag{6.5}$$

The physical and modal variables are related by modal superposition:

$$y(x,t) = \sum_{n=1}^{N} \phi_n(x)\, q_n(t) \tag{6.6}$$

and similarly when relating velocities and accelerations.

6.2.2 Friction Model

As in the previous chapters, a Coulomb-type friction model is used for the tangential contact force:

$$\begin{cases} F_f(t) = -F_N\,\mu(V_r)\,sign(V_r) & if \quad |V_r| \neq 0 \qquad \text{(sliding)} \\ |F_f(t)| \leq F_N \mu_S & if \quad |V_r| = 0 \qquad \text{(adherence)} \end{cases} \tag{6.7}$$

where F_N is the normal force which compresses the contacting surfaces and $V_r(t) = V_b - \dot{y}_f(t)$ is the relative velocity between the excited location of the vibrating bar $\dot{y}_f(t) \equiv \dot{y}(x_f, t)$ and the driving bow V_b. During sliding, the friction coefficient $\mu(V_r)$ depends on the relative velocity, which are formulated in the following convenient manner:

$$\mu(V_r) = \mu_D + (\mu_S - \mu_D)\exp(-C|V_r|) \tag{6.8}$$

where μ_S is the so-called static friction coefficient, at $V_r = 0$, μ_D is a limiting friction coefficient when $|V_r| \to \infty$ and C is a parameter defining how fast $\mu(V_r)$ decreases as V_r increases. During adherence, when $V_r = 0$ (or, more physically, $|V_r| < \varepsilon$), the friction force can take any value within the allowed range $|F_f(t)| \leq F_N \mu_S$, the actual force depending on the overall static and dynamic forces acting on the system. In any case, frictional will oppose (incipient or actual) motion of the system.

Figure 3.1(a) shows a typical plot of $\mu(V_r)$, which highlights the extreme nonlinearity of frictional forces in the vicinity of the adherence discontinuity. This feature, although of extreme significance as far as the nonlinear regimes are concerned, is only marginal in this work, as the low-amplitude vibrations pertaining to the linearized range are important, well before the nonlinear motions settle-in. Under such conditions, $V_b > \dot{y}_f(t)$, only the right half of the friction curve is "active" (e.g., $V_r > 0$) and the system is always sliding, with moderate nonlinearity. Experimental results pertaining to this kind of friction model report, for bowed strings, a decrease of the friction coefficient $\mu(V_r)$ when the sliding velocity $|V_r|$ increases. However, the opposite situation is also investigated, as shown in Figure 3.1(b), where $\mu(V_r)$ increases with $|V_r|$. In industrial friction-induced vibration problems, friction curves which mix the features of Figure 3.1(a) and Figure 3.1(b) are known to arise.

6.2.3 Linearized formulation

Within the framework of linearized theory, small amplitude vibrations $\tilde{y}(x,t)$ about a steady deformed state $\bar{y}(x)$ imply:

$$y(x,t)=\bar{y}(x)+\tilde{y}(x,t) \quad \Rightarrow \quad \dot{y}(x,t)=\dot{\tilde{y}}(x,t) \quad \Rightarrow \quad \ddot{y}(x,t)=\ddot{\tilde{y}}(x,t) \tag{6.9}$$

as well as small amplitude fluctuating forces about a steady value:

$$F(x,t)=\bar{F}(x)+\tilde{F}(x,t) \tag{6.10}$$

Then, when (6.9) and (6.10) are replaced in the dynamical formulation, two sets of equations may be extracted: the so-called zero-order equations, only depending on space, related to the mean deformed state, as well as the first-order equations, depending on both space and time, which enables computation of the system eigenproperties.

The modal formulation applies to dynamic as well as steady states. Therefore, approximation (6.9) may be applied as well to the modal amplitudes, obtaining from (6.6):

$$y(x,t)=\bar{y}(x)+\tilde{y}(x,t)=\sum_{n=1}^{N}\phi_n(x)\left[\bar{q}_n+\tilde{q}_n(t)\right] \tag{6.11}$$

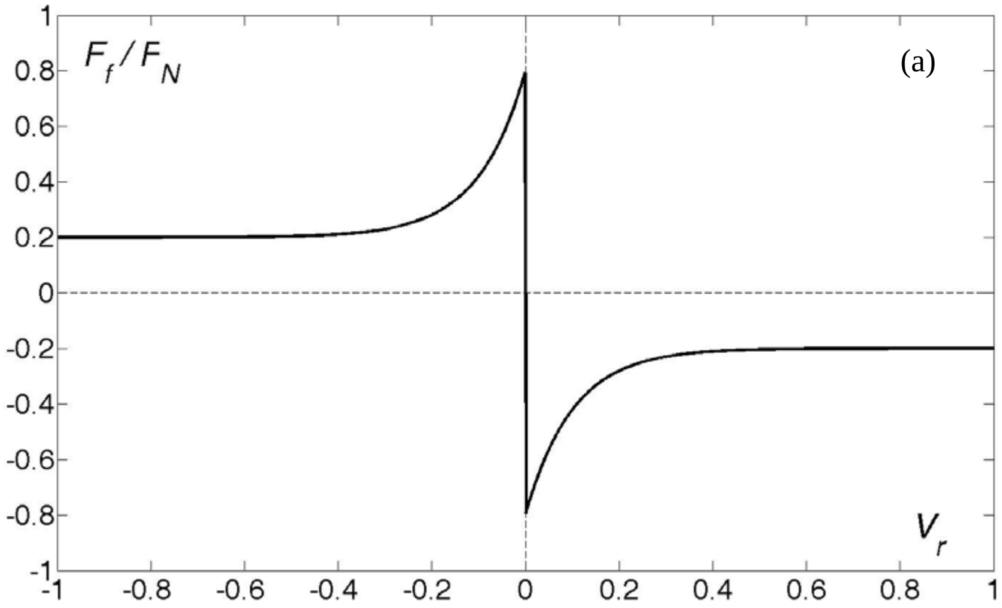

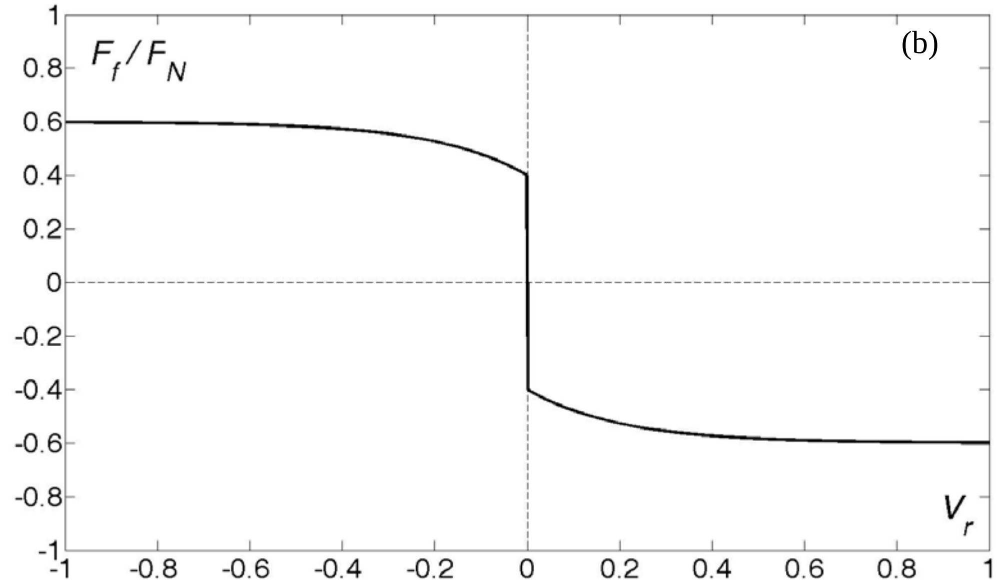

Figure 6.1 – Example of friction law with: (a) $\mu_S = 0.8$, $\mu_D = 0.2$ and $C = 10$ and (b) $\mu_S = 0.4$, $\mu_D = 0.6$ and $C = 5$.

hence the static and vibratory relations:

$$\overline{y}(x) = \sum_{n=1}^{N} \phi_n(x)\,\overline{q}_n \tag{6.12}$$

$$\tilde{y}(x,t) = \sum_{n=1}^{N} \phi_n(x)\,\tilde{q}_n(t) \tag{6.13}$$

Turning now to the nonlinear sliding friction law, under the previously discussed assumption concerning V_r , Equations (6.7) and (6.8) lead to:

$$F_f(t) = F_N\left[\mu_D + (\mu_S - \mu_D)\exp(-C\,V_r)\right] \text{ with } V_r = V_b - \sum_{n=1}^{N} \phi_n(x_f)\,\dot{\tilde{q}}_n(t) \tag{6.14}$$

since $\dot{q} = \dot{\tilde{q}}$, as the $\overline{\dot{q}}_n$ must obviously be null. From(6.14), stems the steady frictional force:

$$\overline{F}_f = F_N\left[\mu_D + (\mu_S - \mu_D)\exp(-C\,V_b)\right] \tag{6.15}$$

as well as the oscillating linearized term

$$\tilde{F}_f(t) = A\sum_{n=1}^{N} \phi_n(x_f)\,\dot{\tilde{q}}_n(t) \tag{6.16}$$

where all relevant parameters which control the system linear stability are encapsulated in the crucial coefficient:

$$A = F_N\,(\mu_S - \mu_D)\,C\,\exp(-C\,V_b) \tag{6.17}$$

which has the dimensions of a damping coefficient, as it should. Notice that in (6.17) the amplitude of the dynamical friction force increases linearly with the normal force F_N and the difference $\mu_S - \mu_D$ between the static and dynamic friction coefficients (in agreement with well-known results), but decreases with the bow velocity V_b in an exponential manner. The influence of the "steepness" parameter C of the friction law $\mu(V_r)$ is introduced through two terms of opposing nature: for low values of V_b the linear term prevails and A increases with C , while for high values of V_b the exponential term prevails and A decreases when C increases. As far as the linearized dynamics are concerned, the specific values of the individual friction parameters are irrelevant, as only the value of the global magnitude coefficient A matters. The steady and dynamical forces applied by the supports are given respectively by:

$$\bar{F}_{si} = K_s \sum_{n=1}^{N} \phi_n(x_{si})\, \bar{q}_n \tag{6.18}$$

$$\tilde{F}_{si}(t) = K_s \sum_{n=1}^{N} \phi_n(x_{si})\, \tilde{q}_n(t) + C_s \sum_{n=1}^{N} \phi_n(x_{si})\, \dot{\tilde{q}}_n(t) \text{ with } i = 1, 2. \tag{6.19}$$

6.2.4 Steady and oscillating solutions

Replacing (6.9)-(6.13) into (6.2) and obtaining the zero-order and first-order equations:

$$\left[K\right]\left\{\bar{Q}\right\} = \left\{\Xi\right\} \tag{6.20}$$

$$\left[M\right]\left\{\ddot{\tilde{Q}}\right\} + \left[C\right]\left\{\dot{\tilde{Q}}\right\} + \left[K\right]\left\{\tilde{Q}\right\} = \left\{\tilde{\Xi}(t)\right\} \tag{6.21}$$

where the generalized steady and dynamic forces are directly obtained from results (6.15) and (6.18) as well as from (6.16), (6.17) and (6.19), by modal projection:

$$\begin{Bmatrix} \bar{\mathscr{F}}_1 \\ \bar{\mathscr{F}}_2 \\ \vdots \\ \bar{\mathscr{F}}_N \end{Bmatrix} = \begin{bmatrix} \phi_1(x_f) & \phi_1(x_{s1}) & \phi_1(x_{s2}) \\ \phi_2(x_f) & \phi_2(x_{s1}) & \phi_2(x_{s2}) \\ \vdots & \vdots & \vdots \\ \phi_N(x_f) & \phi_N(x_{s1}) & \phi_N(x_{s2}) \end{bmatrix} \begin{Bmatrix} \bar{F}_f \\ \bar{F}_{s1} \\ \bar{F}_{s2} \end{Bmatrix} \tag{6.22}$$

$$\begin{Bmatrix} \tilde{\mathscr{F}}_1(t) \\ \tilde{\mathscr{F}}_2(t) \\ \vdots \\ \tilde{\mathscr{F}}_N(t) \end{Bmatrix} = \begin{bmatrix} \phi_1(x_f) & \phi_1(x_{s1}) & \phi_1(x_{s2}) \\ \phi_2(x_f) & \phi_2(x_{s1}) & \phi_2(x_{s2}) \\ \vdots & \vdots & \vdots \\ \phi_N(x_f) & \phi_N(x_{s1}) & \phi_N(x_{s2}) \end{bmatrix} \begin{Bmatrix} \tilde{F}_f \\ \tilde{F}_{s1} \\ \tilde{F}_{s2} \end{Bmatrix} \tag{6.23}$$

Proceeding now to the computation of the steady deformation under friction excitation and accounting for the supports action. From the previous equations, the steady modal displacements are given by:

$$\left\{\bar{Q}\right\} = \left\{ \left[K\right] - K_s \left[\left\{\Phi_{s1}\right\}\left\{\Phi_{s2}\right\}\right] \begin{bmatrix} \left\{\Phi_{s1}\right\}^{\mathrm{T}} \\ \left\{\Phi_{s2}\right\}^{\mathrm{T}} \end{bmatrix} \right\}^{-1} \left\{\Phi_f\right\} \bar{F}_f \tag{6.24}$$

where $\left\{\Phi_{s1}\right\}$, $\left\{\Phi_{s2}\right\}$ and $\left\{\Phi_f\right\}$ are the modeshape vectors at the supports location s_1 and s_2 and at the friction excitation point, respectively, as seen in equations (6.22) or (6.23). Using (6.6), the mean deformed state is obtained in terms of physical coordinates:

$$\{\bar{Y}\} = [\Phi]\left\{[K] - K_s\left[\{\Phi_{s1}\}\{\Phi_{s2}\}\right]\begin{bmatrix}\{\Phi_{s1}\}^{\mathrm{T}}\\ \{\Phi_{s2}\}^{\mathrm{T}}\end{bmatrix}\right\}\{\Phi_f\}\bar{F}_f \tag{6.25}$$

where $[\Phi]$ is the modal matrix built from the bar modeshapes. On the other hand, the linearized dynamics stem from (6.21) and (6.23):

$$[M]\left\{\ddot{\tilde{Q}}(t)\right\} + \left([C]-[\Psi_2]\right)\left\{\dot{\tilde{Q}}(t)\right\} + \left([K]-[\Psi_1]\right)\left\{\tilde{Q}(t)\right\} = \{0\} \tag{6.26}$$

where $[\Psi_1]$ and $[\Psi_2]$ express how bowing couples all the bar modes (with nonzero modeshapes at the bowing and support locations).

$$[\Psi_1] = \begin{bmatrix} \phi_1(x_f) & \phi_1(x_{s1}) & \phi_1(x_{s2}) \\ \phi_2(x_f) & \phi_2(x_{s1}) & \phi_2(x_{s2}) \\ \vdots & \vdots & \vdots \\ \phi_N(x_f) & \phi_N(x_{s1}) & \phi_N(x_{s2}) \end{bmatrix} \begin{bmatrix} [\ 0 & 0 & \cdots & 0\ ] \\ K_s\left[\phi_1(x_{s1})\right. & \phi_2(x_{s1}) & \cdots & \left.\phi_N(x_{s1})\right] \\ K_s\left[\phi_1(x_{s2})\right. & \phi_2(x_{s2}) & \cdots & \left.\phi_N(x_{s2})\right] \end{bmatrix} \tag{6.27}$$

$$[\Psi_2] = \begin{bmatrix} \phi_1(x_f) & \phi_1(x_{s1}) & \phi_1(x_{s2}) \\ \phi_2(x_f) & \phi_2(x_{s1}) & \phi_2(x_{s2}) \\ \vdots & \vdots & \vdots \\ \phi_N(x_f) & \phi_N(x_{s1}) & \phi_N(x_{s2}) \end{bmatrix} \begin{bmatrix} A\left[\phi_1(x_f)\right. & \phi_2(x_f) & \cdots & \left.\phi_N(x_f)\right] \\ C_s\left[\phi_1(x_{s1})\right. & \phi_2(x_{s1}) & \cdots & \left.\phi_N(x_{s1})\right] \\ C_s\left[\phi_1(x_{s2})\right. & \phi_2(x_{s2}) & \cdots & \left.\phi_N(x_{s2})\right] \end{bmatrix} \tag{6.28}$$

One should notice in both previous equations that coefficient A indeed contains all the control parameters of the friction-excited system, apart from the excitation location, and that the displacement and velocity-coupling matrices $[\Psi_1]$ and $[\Psi_2]$ carry the modal information at the excitation and support points. Equation (6.26) leads to the second-order eigenproblem:

$$\left(\lambda_n^2[M] + \lambda_n[\mathcal{C}] + [\mathcal{K}]\right)\left\{\hat{\phi}_n^q\right\} = \{0\} \tag{6.29}$$

with $[\mathcal{C}] = [C]-[\Psi_2]$ and $[\mathcal{K}] = [K]-[\Psi_1]$, where eigen solutions $\left\{\tilde{Q}(t)\right\} = \left\{\hat{\phi}^q\right\}\exp(\lambda t)$ have been assumed. The modes of the friction-coupled system may be easily computed, as a function of A, K_s and C_s, by writing (6.29) as an equivalent first-order (state-space) form, which can be readily solved using standard procedures. Equation (6.30) is one possible symmetrical form, among others (see, for instance Bertolini, 1998):

$$\left(\lambda_n \begin{bmatrix} [\mathcal{C}] & [M] \\ [M] & [\,0\,] \end{bmatrix} + \begin{bmatrix} [\mathcal{K}] & [\,0\,] \\ [\,0\,] & -[M] \end{bmatrix}\right) \begin{Bmatrix} \left\{\hat{\phi}_n^q\right\} \\ \left\{\lambda_n \hat{\phi}_n^q\right\} \end{Bmatrix} = \begin{Bmatrix} \{0\} \\ \{0\} \end{Bmatrix} \tag{6.30}$$

The eigenvalues and corresponding eigenvectors obtained from (6.30) are in general complex and, for oscillating solutions, arise in conjugate pairs $\lambda_n = \hat{\sigma}_n \pm i\hat{\omega}_n$ and $\left\{\hat{\phi}_n^q\right\} = \{\varphi_n\} \pm i\left\{\vartheta_n\right\}$. The (damped) modal frequencies $\hat{\omega}_n = \mathrm{Im}(\lambda_n)$ and modal dissipation values $\hat{\sigma}_n = \mathrm{Re}(\lambda_n)$ determine the behaviour of the bowed system, before nonlinear effects take control. In particular, self-excited regimes stem from the linear instability of a mode, whenever $\mathrm{Re}(\lambda_n) > 0$. Then, if $\mathrm{Im}(\lambda_n) \neq 0$, it is a flutter instability, otherwise $\mathrm{Im}(\lambda_n) = 0$ implies a divergence (non-oscillatory) instability. The values of the undamped modal frequencies $\hat{\omega}_n$ and modal damping $\hat{\zeta}_n$ of the friction-coupled system may be inferred from the λ_n using the following relations:

$$\hat{\omega}_{nu} = \sqrt{\hat{\sigma}_n^2 + \hat{\omega}_n^2} \tag{6.31}$$

$$\hat{\zeta}_n = -\frac{\hat{\sigma}_n}{\sqrt{\hat{\sigma}_n^2 + \hat{\omega}_n^2}} \tag{6.32}$$

and one obtains $\hat{\omega}_n = \hat{\omega}_{nu}\sqrt{1-\hat{\zeta}_n^2}$, as usual. From the modeshapes $\left\{\hat{\phi}_n^q\right\}$ in terms of the modal amplitude coefficients, one can easily compute the corresponding modeshapes in terms of the physical coordinates:

$$\left\{\hat{\phi}_n^x\right\} = \left[\{\phi_1\},\{\phi_2\},\ldots,\{\phi_N\}\right]\left\{\hat{\phi}_n^q\right\} \quad , \quad n = 1,2,\ldots,N \tag{6.33}$$

6.2.5 Results

Two types of bars were analyzed in light of this theoretical approach: bars with uniform cross-section and bars with variable cross-section $S(x)$ tuned to specific frequency ratios of the first 3 natural frequencies. As a first example, Figure 1.8 shows a typical stability plot, for a 220 Hz tuned bar (1-4-10) modelled using 8 modes (2 rigid-body and 6 flexural), as a function of coefficient A – see Equation (6.17). The friction parameters used were $\mu_S = 1.0$, $\mu_D = 0.2$ and $C = 10$. In this figure the green colour stands for stability and the red colour for instability. The first two modes of the coupled system, s_1 and s_2, which represent the transverse and rocking motions of the rigid bar, have nearly the same frequency until the first reaches instability as A increases, with a clear decrease of the oscillation frequency, under flutter instability or divergence for high enough values of A. On the other hand, the flexural modes, f_1 to f_6, reach instability for different values of A, with the first flexural mode being unstable over a wider range, in agreement with musical playing experience.

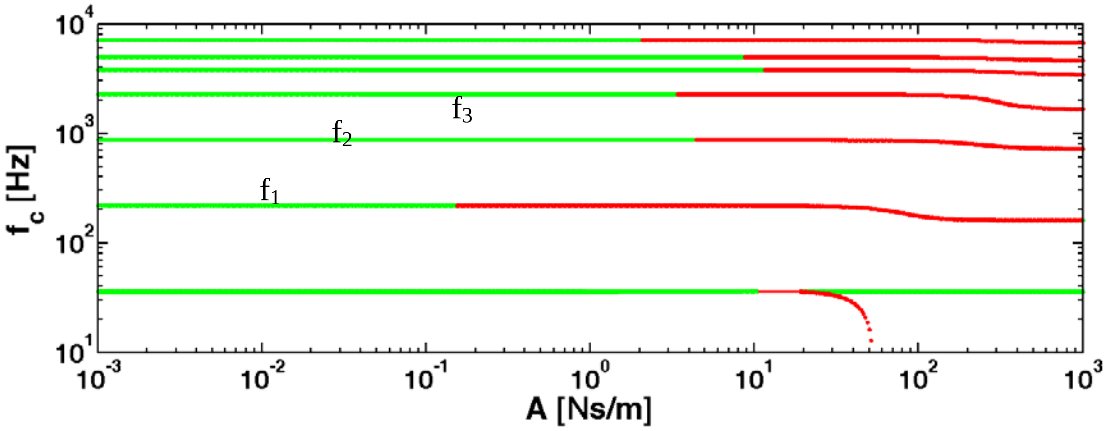

Figure 6.2 – Stability plot for a tuned 1-4-10 bar in function of coefficient A. Green – Stability; Red – Instability.

Figure 3 depicts two stability plots for the first bending mode of the tuned bar, subjected to two different friction laws (see Figure 1) where the modal frequency is plotted as a function of the bow normal force and velocity. In the first case self-sustained oscillations are expected to engage at higher values of F_N and lower values of V_b . As expected, only the friction law of Figure 1(a) allows for the appearance of unstable regimes.

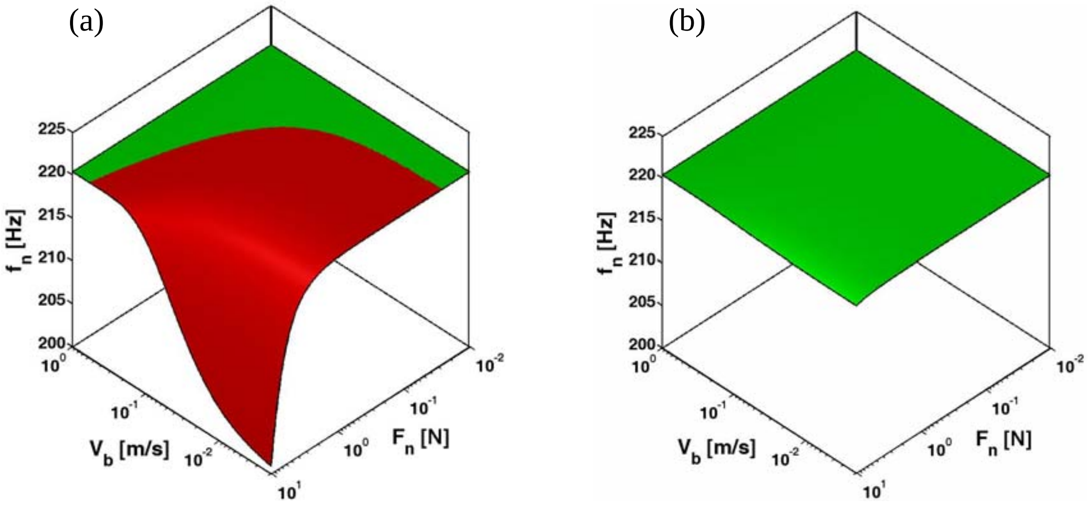

Figure 6.3 – 3D Stability plots for the first flexural mode of a tuned 1-4-10 bar for the two different friction laws in **Figure 3.1**(a) and **Figure 3.1**(b), respectively. Green – Stability; Red – Instability.

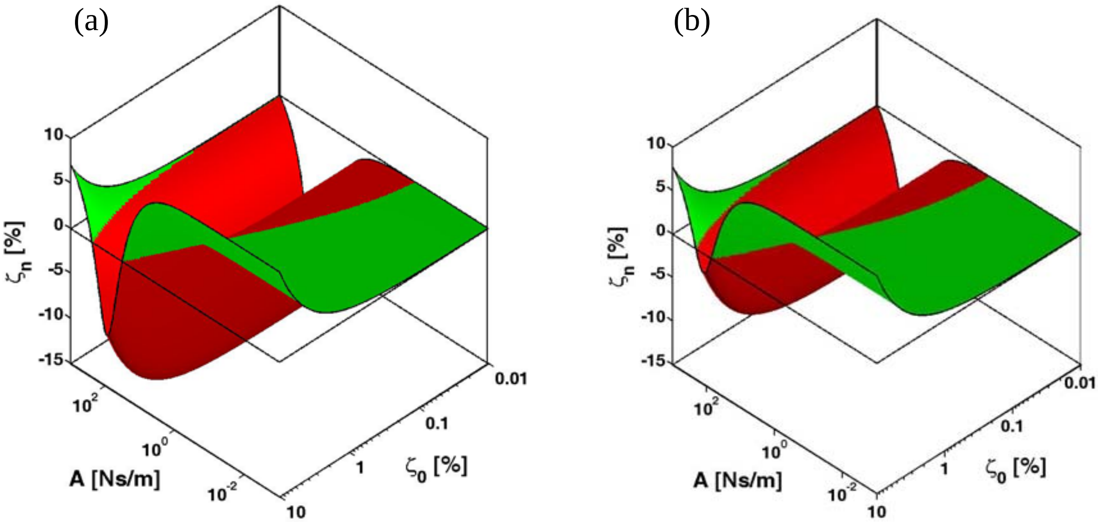

Figure 6.4 – 3D Stability plots for the first flexural mode of (a) a tuned 1-4-10 bar and (b) a uniform cross section bar. Green – Stability; Red – Instability.

As another illustration Figure 6.4(a) and Figure 6.4(b) show the first flexural mode damping ζ_n and stability as a function of the global parameter A and bar modal damping ζ_0 assumed identical for all unconstrained modes. When comparing the two bars previously discussed, the first flexural mode of the tuned bar is more prone to instability for a wide variation of A and ζ_0.

The work presented in the Chapter 3 enabled a classification of different dynamical regimes as depicted in Figure 6.5. Performing now a linear stability analysis for all modes of the two bars, and for the same playing range and friction characteristics as in Chapter 3 – see Figure 6.6 – it is possible to establish a correlation of the main regime features between the two approaches. If, using an heuristic reasoning, the unstable mode with higher negative damping value is highlighted as dominant (for each pair of bowing conditions F_N and V_b), the linear analysis predicts instability of the first rigid-body mode (support regime) and the first flexural bar mode (musical regime) in approximately the same ranges as the nonlinear simulations. Notice that the other "intermediate" self-sustained regimes, apart from the ones mentioned, are also related to self-sustained oscillation of the first flexural mode of the bar. These variations are, obviously, something that the linear approach cannot predict. Also notice that the region of stability correlates well with the non-oscillatory regimes depicted in Figure 6.5.

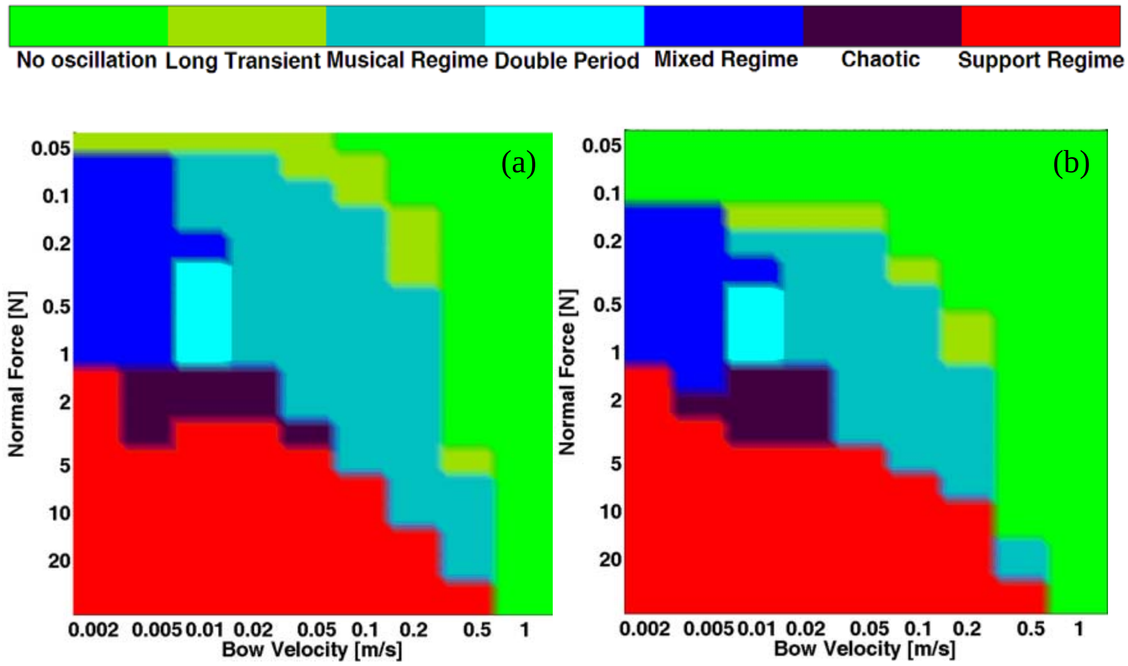

Figure 6.5 – Nonlinear dynamical regimes for (a) the 1-4-10 bar and (b) the uniform cross section bar in function of the playing parameters V_b and F_N.

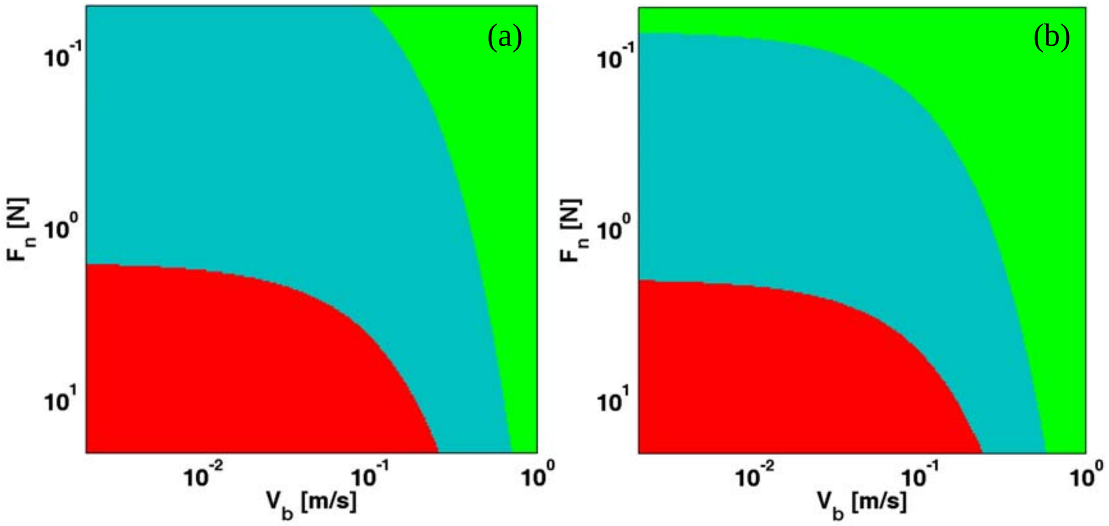

Figure 6.6 – 2D Modal stability plots for (a) a tuned 1-4-10 bar and (b) a uniform cross-section bar in function of the playing parameters. Green – Stability; Blue – 1st flexural mode instability; Red – 1st support mode instability.

6.3. Bowed String

6.3.1 Modal formulation for the bowed string

Starting from the classic damped wave equation:

$$m_0 \frac{\partial^2 y}{\partial t^2} + \eta \frac{\partial y}{\partial t} - T \frac{\partial^2 y}{\partial x^2} = F(x,t) \tag{6.34}$$

where $y(x,t)$ is the lateral displacement, m_0 is the string linear density, η is a coefficient of viscous dissipation, T is an axial tensioning force and $\mathsf{F}(x,t)$ is the externally applied excitation, Equation (6.34) may be recast in modal form:

$$\begin{bmatrix} m_1 & 0 & \cdots & 0 \\ 0 & m_2 & \cdots & 0 \\ \vdots & \vdots & \ddots & \vdots \\ 0 & 0 & \cdots & m_N \end{bmatrix} \begin{Bmatrix} \ddot{q}_1 \\ \ddot{q}_2 \\ \vdots \\ \ddot{q}_N \end{Bmatrix} + \begin{bmatrix} c_1 & 0 & \cdots & 0 \\ 0 & c_2 & \cdots & 0 \\ \vdots & \vdots & \ddots & \vdots \\ 0 & 0 & \cdots & c_N \end{bmatrix} \begin{Bmatrix} \dot{q}_1 \\ \dot{q}_2 \\ \vdots \\ \dot{q}_N \end{Bmatrix} + \begin{bmatrix} k_1 & 0 & \cdots & 0 \\ 0 & k_2 & \cdots & 0 \\ \vdots & \vdots & \ddots & \vdots \\ 0 & 0 & \cdots & k_N \end{bmatrix} \begin{Bmatrix} q_1 \\ q_2 \\ \vdots \\ q_N \end{Bmatrix} = \begin{Bmatrix} \mathscr{F}_1 \\ \mathscr{F}_2 \\ \vdots \\ \mathscr{F}_N \end{Bmatrix} \tag{6.35}$$

where $m_n = m_0 L/2 \ (\forall n)$, $c_n = 2 m_n \omega_n \zeta_n$ and $k_n = m_n \omega_n^2$ are the modal parameters of the pinned-pinned string (using N modes with frequencies $\omega_n = n\pi c/L$, with $c = \sqrt{T/m_0}$, and modal damping values ζ_n). The modeshapes of a string pinned at both the bridge ($x = 0$) and nut ($x = L$) extremities are given by $\phi_n(x) = \sin(n\pi x/L)$. For inharmonic strings with bending stiffness parameter β, the modal frequencies depart from the harmonic series for increasing modal index, and $\omega_n = (n\pi c/L)\sqrt{1+\beta n^2}$, for $n \geq 2$.

On the other hand, $q_n(t)$ are the modal amplitudes and $\mathscr{F}_n(t)$ are the generalized forces obtained by modal projection of the external force field:

$$\mathscr{F}_n(t) = \int_0^L \mathsf{F}(x,t)\, \phi_n(x)\, dx \quad , \quad n = 1, 2, ..., N \tag{6.36}$$

with the modeshapes $\phi_n(x) = \sin(n\pi x/L)$. For point-forces at F locations:

$$\mathsf{F}(x,t) = \sum_{f=1}^{F} \mathsf{F}_f(t)\, \delta(x_f - x) \tag{6.37}$$

Equation (6.36) simplifies to $\mathscr{F}_n(t) = \sum_{f=1}^{F} \mathsf{F}_f(t)\,\phi_n(x_f)$. In matrix form:

$$\begin{Bmatrix} \mathscr{F}_1 \\ \mathscr{F}_2 \\ \vdots \\ \mathscr{F}_N \end{Bmatrix} = \begin{bmatrix} \phi_1(x_1) & \phi_1(x_2) & \cdots & \phi_1(x_F) \\ \phi_2(x_1) & \phi_2(x_2) & \cdots & \phi_2(x_F) \\ \vdots & \vdots & \ddots & \vdots \\ \phi_N(x_1) & \phi_N(x_2) & \cdots & \phi_N(x_F) \end{bmatrix} \begin{Bmatrix} \mathsf{F}_1 \\ \mathsf{F}_2 \\ \vdots \\ \mathsf{F}_F \end{Bmatrix} \tag{6.38}$$

The physical and modal variables are related by the variable transformation:

$$y(x,t) = \sum_{n=1}^{N} \phi_n(x)\,q_n(t) \tag{6.39}$$

which expresses modal superposition. In matrix form, at P discrete locations:

$$\begin{Bmatrix} y_1 \\ y_2 \\ \vdots \\ y_P \end{Bmatrix} = \begin{bmatrix} \phi_1(x_1) & \phi_2(x_1) & \cdots & \phi_N(x_1) \\ \phi_1(x_2) & \phi_2(x_2) & \cdots & \phi_N(x_2) \\ \vdots & \vdots & \ddots & \vdots \\ \phi_1(x_P) & \phi_2(x_P) & \cdots & \phi_N(x_P) \end{bmatrix} \begin{Bmatrix} q_1 \\ q_2 \\ \vdots \\ q_N \end{Bmatrix} \tag{6.40}$$

and similarly when relating velocities and accelerations.

6.3.2 Friction model

Following the work presented in the previous section, a Coulomb-type friction model is used for the tangential contact force:

$$\begin{cases} \mathsf{F}_f(t) = -\mathsf{F}_N\,\mu(V_r)\,\mathrm{sign}(V_r) & \text{if} \quad |V_r| \neq 0 \qquad \text{(sliding)} \\ \left|\mathsf{F}_f(t)\right| \leq \mathsf{F}_N\,\mu_S & \text{if} \quad |V_r| = 0 \qquad \text{(adherence)} \end{cases} \tag{6.41}$$

where F_N is the normal force which compresses the contacting surfaces and $V_r(t) = V_b - \dot{y}_f(t)$ is the relative velocity between the vibrating surface $y_f(t) \equiv y(x_f,t)$ and the driving bow V_b. During sliding, the friction coefficient $\mu(V_r)$ depends on the relative velocity, which is formulated as:

$$\mu(V_r) = \mu_D + (\mu_S - \mu_D)\exp(-C|V_r|) \tag{6.42}$$

where μ_S is the so-called static friction coefficient, at $V_r = 0$, μ_D is a limiting friction coefficient when $|V_r| \to \infty$ and C is a parameter defining how fast $\mu(V_r)$ decreases as V_r increases. During adherence, when $V_r = 0$ (or, more physically, $|V_r| < \varepsilon$), the friction force can take any value within the allowed range $|F_f(t)| \le F_N \mu_S$, the actual force depending on the overall static and dynamic forces acting on the system. In any case, frictional will oppose the (incipient or actual) motion of the system.

Figure 6.7 shows a typical plot of $\mu(V_r)$, which highlights the extreme nonlinearity of frictional forces in the vicinity of the adherence discontinuity. As referred in the previous section, this feature will be neglected in this work, as the low-amplitude vibrations pertaining to the linearized range are important, well before the nonlinear motions settle-in. Under such conditions, $V_b > y_f(t)$, only the right half of the friction curve is “active” (e.g., $V_r > 0$) and the system is always sliding, with moderate nonlinearity. Experimental results pertaining to this kind of friction model report, for bowed strings, a decrease of the friction coefficient $\mu(V_r)$ when the sliding velocity $|V_r|$ increases (Cremer, 1984).

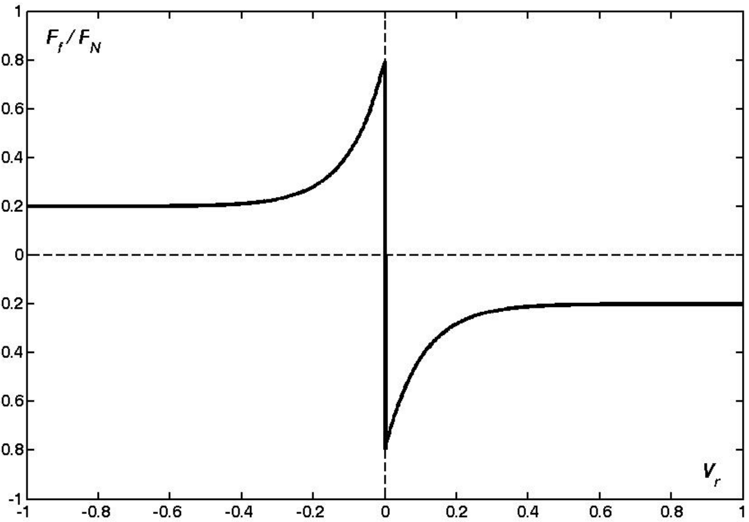

Figure 6.7 – Example of friction law with $\mu_S = 0.8$, $\mu_D = 0.2$ and $C = 10$.

6.3.3 Linearized formulation

Within the framework of linearized theory, small amplitude vibrations $\tilde{y}(x,t)$ about a steady deformed state $\bar{y}(x)$ imply:

$$y(x,t) = \bar{y}(x) + \tilde{y}(x,t) \quad \Rightarrow \quad \dot{y}(x,t) = \dot{\tilde{y}}(x,t) \quad \Rightarrow \quad \ddot{y}(x,t) = \ddot{\tilde{y}}(x,t) \tag{6.43}$$

as well as small amplitude fluctuating forces about a steady value:

$$F(x,t) = \bar{F}(x) + \tilde{F}(x,t) \tag{6.44}$$

Then, when (6.43) and (6.44) are replaced in the dynamical formulation, two sets of equations may be extracted: the so-called zero-order equations, only depending on space, which supply the mean deformed state, as well as the first-order equations, depending on both space and time, which enables computation of the system eigenproperties.

The modal formulation applies to dynamic as well as steady states. Therefore, approximation (6.43) may be applied as well to the modal amplitudes, obtaining from (6.39):

$$y(x,t) = \bar{y}(x) + \tilde{y}(x,t) = \sum_{n=1}^{N} \phi_n(x) \left[\bar{q}_n + \tilde{q}_n(t) \right] \tag{6.45}$$

hence the static and vibratory relations:

$$\bar{y}(x) = \sum_{n=1}^{N} \phi_n(x)\, \bar{q}_n \tag{6.46}$$

$$\tilde{y}(x,t) = \sum_{n=1}^{N} \phi_n(x)\, \tilde{q}_n(t) \tag{6.47}$$

Turning now to the nonlinear sliding friction law, under the previously discussed assumption concerning V_r, (6.41) and (6.42) reduce to:

$$F_f(t) = F_N \left[\mu_D + (\mu_S - \mu_D) \exp(-C\, V_r) \right] \tag{6.48}$$

hence:

$$F_f(t) = F_N \left\{ \mu_D + (\mu_S - \mu_D) \exp\left[-C \left(V_b - \sum_{n=1}^{N} \phi_n(x_f)\, \dot{q}_n(t) \right) \right] \right\} \tag{6.49}$$

Then, accounting for (6.45):

$$F_f(t) = F_N \left\{ \mu_D + (\mu_S - \mu_D) \exp\left[-C \left(V_b - \sum_{n=1}^{N} \phi_n(x_f)\, \dot{\tilde{q}}_n(t) \right) \right] \right\} \tag{6.50}$$

as the $\dot{\bar{q}}_n$ must obviously be null. From (6.50), stems the steady frictional force:

$$\bar{F}_f = F_N \left[\mu_D + (\mu_S - \mu_D) \exp(-C\, V_b) \right] \tag{6.51}$$

as well as the oscillating linearized term:

$$\tilde{F}_f(t) = A \sum_{n=1}^{N} \phi_n(x_f)\, \dot{\tilde{q}}_n(t) \tag{6.52}$$

where all relevant parameters which control the system stability are encapsulated in the important coefficient:

$$A = F_N\, (\mu_S - \mu_D)\, C \exp(-C\, V_b) \tag{6.53}$$

which has the dimensions of a damping coefficient, as it should.

Notice that the amplitude of the dynamical friction force increases linearly with the normal force F_N and the difference $\mu_S - \mu_D$ between the static and dynamic friction coefficients (which are well-known results), but decreases with the bow velocity V_b in an exponential manner. The influence of the "steepness" parameter C of the friction law $\mu(V_r)$ is introduced through two terms of opposing nature: for low values of V_b the linear term prevails and A increases with C, while for high values of V_b the exponential term prevails and A decreases when C increases. As far as the linearized dynamics are concerned, the specific values of all these parameters are irrelevant, as only the value of the amplitude coefficient A matters.

6.3.4 Steady and oscillating solutions

Replacing (6.43)-(6.47) into (6.35) and obtaining the zero-order and first-order equations:

$$\begin{bmatrix} k_1 & 0 & \cdots & 0 \\ 0 & k_2 & \cdots & 0 \\ \vdots & \vdots & \ddots & \vdots \\ 0 & 0 & \cdots & k_N \end{bmatrix} \begin{Bmatrix} \bar{q}_1 \\ \bar{q}_2 \\ \vdots \\ \bar{q}_N \end{Bmatrix} = \begin{Bmatrix} \bar{\mathscr{F}}_1 \\ \bar{\mathscr{F}}_2 \\ \vdots \\ \bar{\mathscr{F}}_N \end{Bmatrix} \tag{6.54}$$

$$\begin{bmatrix} m_1 & 0 & \cdots & 0 \\ 0 & m_2 & \cdots & 0 \\ \vdots & \vdots & \ddots & \vdots \\ 0 & 0 & \cdots & m_N \end{bmatrix} \begin{Bmatrix} \ddot{\tilde{q}}_1 \\ \ddot{\tilde{q}}_2 \\ \vdots \\ \ddot{\tilde{q}}_N \end{Bmatrix} + \begin{bmatrix} c_1 & 0 & \cdots & 0 \\ 0 & c_2 & \cdots & 0 \\ \vdots & \vdots & \ddots & \vdots \\ 0 & 0 & \cdots & c_N \end{bmatrix} \begin{Bmatrix} \dot{\tilde{q}}_1 \\ \dot{\tilde{q}}_2 \\ \vdots \\ \dot{\tilde{q}}_N \end{Bmatrix} + \begin{bmatrix} k_1 & 0 & \cdots & 0 \\ 0 & k_2 & \cdots & 0 \\ \vdots & \vdots & \ddots & \vdots \\ 0 & 0 & \cdots & k_N \end{bmatrix} \begin{Bmatrix} \tilde{q}_1 \\ \tilde{q}_2 \\ \vdots \\ \tilde{q}_N \end{Bmatrix} = \begin{Bmatrix} \tilde{\mathscr{F}}_1 \\ \tilde{\mathscr{F}}_2 \\ \vdots \\ \tilde{\mathscr{F}}_N \end{Bmatrix} \tag{6.55}$$

where the generalized steady and dynamic forces are directly obtained from results (6.51) and (6.52)-(6.53), by modal projection:

$$\begin{Bmatrix} \bar{\mathscr{F}}_1 \\ \bar{\mathscr{F}}_2 \\ \vdots \\ \bar{\mathscr{F}}_N \end{Bmatrix} = \begin{bmatrix} \phi_1(x_f) \\ \phi_2(x_f) \\ \vdots \\ \phi_N(x_f) \end{bmatrix} \bar{F}_f \tag{6.56}$$

$$\begin{Bmatrix} \tilde{\mathscr{F}}_1(t) \\ \tilde{\mathscr{F}}_2(t) \\ \vdots \\ \tilde{\mathscr{F}}_N(t) \end{Bmatrix} = \begin{bmatrix} \phi_1(x_f) \\ \phi_2(x_f) \\ \vdots \\ \phi_N(x_f) \end{bmatrix} \tilde{F}_f(t) \tag{6.57}$$

Proceeding now to the computation of the steady deformation under friction excitation, from (6.54) and (6.56):

$$\begin{Bmatrix} \bar{q}_1 \\ \bar{q}_2 \\ \vdots \\ \bar{q}_N \end{Bmatrix} = \begin{bmatrix} k_1 & 0 & \cdots & 0 \\ 0 & k_2 & \cdots & 0 \\ \vdots & \vdots & \ddots & \vdots \\ 0 & 0 & \cdots & k_N \end{bmatrix}^{-1} \begin{bmatrix} \phi_1(x_f) \\ \phi_2(x_f) \\ \vdots \\ \phi_N(x_f) \end{bmatrix} \bar{F}_f \tag{6.58}$$

and, using (6.40), the mean deformed state in terms of physical coordinates is obtained:

$$\begin{Bmatrix} \bar{y}_1 \\ \bar{y}_2 \\ \vdots \\ \bar{y}_P \end{Bmatrix} = \begin{bmatrix} \phi_1(x_1) & \phi_2(x_1) & \cdots & \phi_N(x_1) \\ \phi_1(x_2) & \phi_2(x_2) & \cdots & \phi_N(x_2) \\ \vdots & \vdots & \ddots & \vdots \\ \phi_1(x_P) & \phi_2(x_P) & \cdots & \phi_N(x_P) \end{bmatrix} \begin{bmatrix} k_1 & 0 & \cdots & 0 \\ 0 & k_2 & \cdots & 0 \\ \vdots & \vdots & \ddots & \vdots \\ 0 & 0 & \cdots & k_N \end{bmatrix}^{-1} \begin{bmatrix} \phi_1(x_f) \\ \phi_2(x_f) \\ \vdots \\ \phi_N(x_f) \end{bmatrix} \bar{F}_f \tag{6.59}$$

On the other hand, the linearized dynamics stem from (6.55) and (6.57):

$$\begin{bmatrix} m_1 & 0 & \cdots & 0 \\ 0 & m_2 & \cdots & 0 \\ \vdots & \vdots & \ddots & \vdots \\ 0 & 0 & \cdots & m_N \end{bmatrix} \begin{Bmatrix} \ddot{\tilde{q}}_1 \\ \ddot{\tilde{q}}_2 \\ \vdots \\ \ddot{\tilde{q}}_N \end{Bmatrix} + \begin{bmatrix} c_1 & 0 & \cdots & 0 \\ 0 & c_2 & \cdots & 0 \\ \vdots & \vdots & \ddots & \vdots \\ 0 & 0 & \cdots & c_N \end{bmatrix} \begin{Bmatrix} \dot{\tilde{q}}_1 \\ \dot{\tilde{q}}_2 \\ \vdots \\ \dot{\tilde{q}}_N \end{Bmatrix} + \begin{bmatrix} k_1 & 0 & \cdots & 0 \\ 0 & k_2 & \cdots & 0 \\ \vdots & \vdots & \ddots & \vdots \\ 0 & 0 & \cdots & k_N \end{bmatrix} \begin{Bmatrix} \tilde{q}_1 \\ \tilde{q}_2 \\ \vdots \\ \tilde{q}_N \end{Bmatrix} = \begin{bmatrix} \phi_1(x_f) \\ \phi_2(x_f) \\ \vdots \\ \phi_N(x_f) \end{bmatrix} \tilde{F}_f(t) \tag{6.60}$$

and, accounting that (6.52) is equivalent to:

$$\tilde{F}_f(t) = A \begin{bmatrix} \phi_1(x_f) & \phi_2(x_f) & \cdots & \phi_N(x_f) \end{bmatrix} \begin{Bmatrix} \dot{\tilde{q}}_1 \\ \dot{\tilde{q}}_2 \\ \vdots \\ \dot{\tilde{q}}_N \end{Bmatrix} \tag{6.61}$$

one obtains:

$$\begin{aligned} &\begin{bmatrix} m_1 & 0 & \cdots & 0 \\ 0 & m_2 & \cdots & 0 \\ \vdots & \vdots & \ddots & \vdots \\ 0 & 0 & \cdots & m_N \end{bmatrix} \begin{Bmatrix} \ddot{\tilde{q}}_1 \\ \ddot{\tilde{q}}_2 \\ \vdots \\ \ddot{\tilde{q}}_N \end{Bmatrix} + \begin{bmatrix} c_1 & 0 & \cdots & 0 \\ 0 & c_2 & \cdots & 0 \\ \vdots & \vdots & \ddots & \vdots \\ 0 & 0 & \cdots & c_N \end{bmatrix} \begin{Bmatrix} \dot{\tilde{q}}_1 \\ \dot{\tilde{q}}_2 \\ \vdots \\ \dot{\tilde{q}}_N \end{Bmatrix} + \begin{bmatrix} k_1 & 0 & \cdots & 0 \\ 0 & k_2 & \cdots & 0 \\ \vdots & \vdots & \ddots & \vdots \\ 0 & 0 & \cdots & k_N \end{bmatrix} \begin{Bmatrix} \tilde{q}_1 \\ \tilde{q}_2 \\ \vdots \\ \tilde{q}_N \end{Bmatrix} = \\ &\qquad = A \begin{bmatrix} \phi_1(x_f)\phi_1(x_f) & \phi_1(x_f)\phi_2(x_f) & \cdots & \phi_1(x_f)\phi_N(x_f) \\ \phi_2(x_f)\phi_1(x_f) & \phi_2(x_f)\phi_2(x_f) & \cdots & \phi_2(x_f)\phi_N(x_f) \\ \vdots & \vdots & \ddots & \vdots \\ \phi_N(x_f)\phi_1(x_f) & \phi_N(x_f)\phi_2(x_f) & \cdots & \phi_N(x_f)\phi_N(x_f) \end{bmatrix} \begin{Bmatrix} \dot{\tilde{q}}_1 \\ \dot{\tilde{q}}_2 \\ \vdots \\ \dot{\tilde{q}}_N \end{Bmatrix} \end{aligned} \tag{6.62}$$

which clearly expresses how bowing couples all the string modes with nonzero modeshapes at the bowing location.

Writing now (6.62) in condensed notation:

$$[\mathcal{M}]\left\{\ddot{\tilde{Q}}(t)\right\}+[\mathcal{C}]\left\{\dot{\tilde{Q}}(t)\right\}+[\mathcal{K}]\left\{\tilde{Q}(t)\right\}=A\left[\Phi(x_f)\right]\left\{\dot{\tilde{Q}}(t)\right\} \tag{6.63}$$

where one should notice that coefficient A encapsulates all the control parameters of the friction-excited system, apart from the excitation location, while the velocity-coupling matrix $\left[\Phi(x_f)\right]$ carries the modal information at the excitation point x_f . Equation (6.63) reduces to the homogeneous form:

$$[\mathcal{M}]\left\{\ddot{\tilde{Q}}(t)\right\}+\left([\mathcal{C}]-A\left[\Phi(x_f)\right]\right)\left\{\dot{\tilde{Q}}(t)\right\}+[\mathcal{K}]\left\{\tilde{Q}(t)\right\}=\{0\} \tag{6.64}$$

leading to a second-order eigenvalue/eigenvector problem:

$$\left(\lambda_n^2[\mathcal{M}]+\lambda_n\left[\mathcal{C}(A,x_f)\right]+[\mathcal{K}]\right)\left\{\hat{\phi}_n^q\right\}=\{0\} \quad \text{with} \quad \left[\mathcal{C}(A,x_f)\right]=[\mathcal{C}]-A\left[\Phi(x_f)\right] \tag{6.65}$$

where solutions $\left\{\tilde{Q}(t)\right\}=\left\{\hat{\phi}^q\right\}\exp(\lambda t)$ have been assumed. The modes of the friction-coupled system may be easily computed, as a function of A and x_f, by writing (6.65) in an equivalent first-order (state-space) form, which can be readily solved using standard procedures. Equation (6.66) is one possible symmetrical form, among others (see, for instance, Bertolini, 1998):

$$\left(\lambda_n\begin{bmatrix}\left[\mathcal{C}(A,x_f)\right] & [\mathcal{M}]\\ [\mathcal{M}] & [\,0\,]\end{bmatrix}+\begin{bmatrix}[\mathcal{K}] & [\,0\,]\\ [\,0\,] & -[\mathcal{M}]\end{bmatrix}\right)\begin{Bmatrix}\left\{\hat{\phi}_n^q\right\}\\ \left\{\lambda_n\hat{\phi}_n^q\right\}\end{Bmatrix}=\begin{Bmatrix}\{0\}\\ \{0\}\end{Bmatrix} \tag{6.66}$$

The eigenvalues and corresponding eigenvectors obtained from (6.66) are in general complex and, for oscillating solutions, arise in conjugate pairs $\lambda_n=\hat{\sigma}_n\pm i\hat{\omega}_n$ and $\left\{\hat{\phi}_n^q\right\}=\{\hat{\varphi}_n\}\pm i\{\hat{\psi}_n\}$. The (damped) modal frequencies $\hat{\omega}_n=\mathrm{Im}(\lambda_n)$ and modal dissipation values $\hat{\sigma}_n=\mathrm{Re}(\lambda_n)$ determine the behaviour of the bowed system, before nonlinear effects take control. In particular, self-excited regimes stem from the linear instability of a mode, whenever $\mathrm{Re}(\lambda_n)>0$. Then, if $\mathrm{Im}(\lambda_n)\neq 0$, it is a flutter instability, otherwise $\mathrm{Im}(\lambda_n)=0$ implies a divergence (non-oscillatory) instability. The values of the undamped modal frequencies $\hat{\omega}_{n0}$ and modal damping $\hat{\zeta}_n$ of the friction-coupled system may be inferred from the λ_n using the following relations:

$$\hat{\omega}_{nu} = \sqrt{\hat{\sigma}_n^2 + \hat{\omega}_n^2} \tag{6.67}$$

$$\hat{\zeta}_n = -\frac{\hat{\sigma}_n}{\sqrt{\hat{\sigma}_n^2 + \hat{\omega}_n^2}} \tag{6.68}$$

and one obtains $\hat{\omega}_n = \hat{\omega}_{nu}\sqrt{1-\hat{\zeta}_n^2}$, as usual. After the modeshapes $\left\{\hat{\phi}_n^q\right\}$ in terms of the modal amplitude coefficients of the original string modes have been obtained, one can easily compute the modeshapes in terms of the physical coordinates:

$$\left\{\hat{\phi}_n^x\right\} = \left[\{\phi_1\},\{\phi_2\},\ldots,\{\phi_N\}\right]\left\{\hat{\phi}_n^q\right\} \quad , \quad n = 1,2,\ldots,N \tag{6.69}$$

or, in extended notation:

$$\begin{Bmatrix} \hat{\phi}_n(x_1) \\ \hat{\phi}_n(x_2) \\ \vdots \\ \hat{\phi}_n(x_P) \end{Bmatrix} = \begin{bmatrix} \phi_1(x_1) & \phi_2(x_1) & \cdots & \phi_N(x_1) \\ \phi_1(x_2) & \phi_2(x_2) & \cdots & \phi_N(x_2) \\ \vdots & \vdots & \ddots & \vdots \\ \phi_1(x_P) & \phi_2(x_P) & \cdots & \phi_N(x_P) \end{bmatrix} \begin{Bmatrix} \hat{\phi}_n(q_1) \\ \hat{\phi}_n(q_2) \\ \vdots \\ \hat{\phi}_n(q_N) \end{Bmatrix} \quad , \quad n = 1,2,\ldots,N \tag{6.70}$$

6.3.5 Results

Calculations using the previously described approach were made for a violin string with length, L = 33 cm, a linear density of 3.1×10^{-3} kg/m, and a fundamental frequency of 196 Hz. A modal damping of 0.1% was used for all modes and no string inharmonicity was included in the present calculations (inclusion of the string bending stiffness presents no difficulty). The string was modelled using 50 modes and the friction parameters used were μ_S = 0.4, μ_D = 0.2 and C = 5.

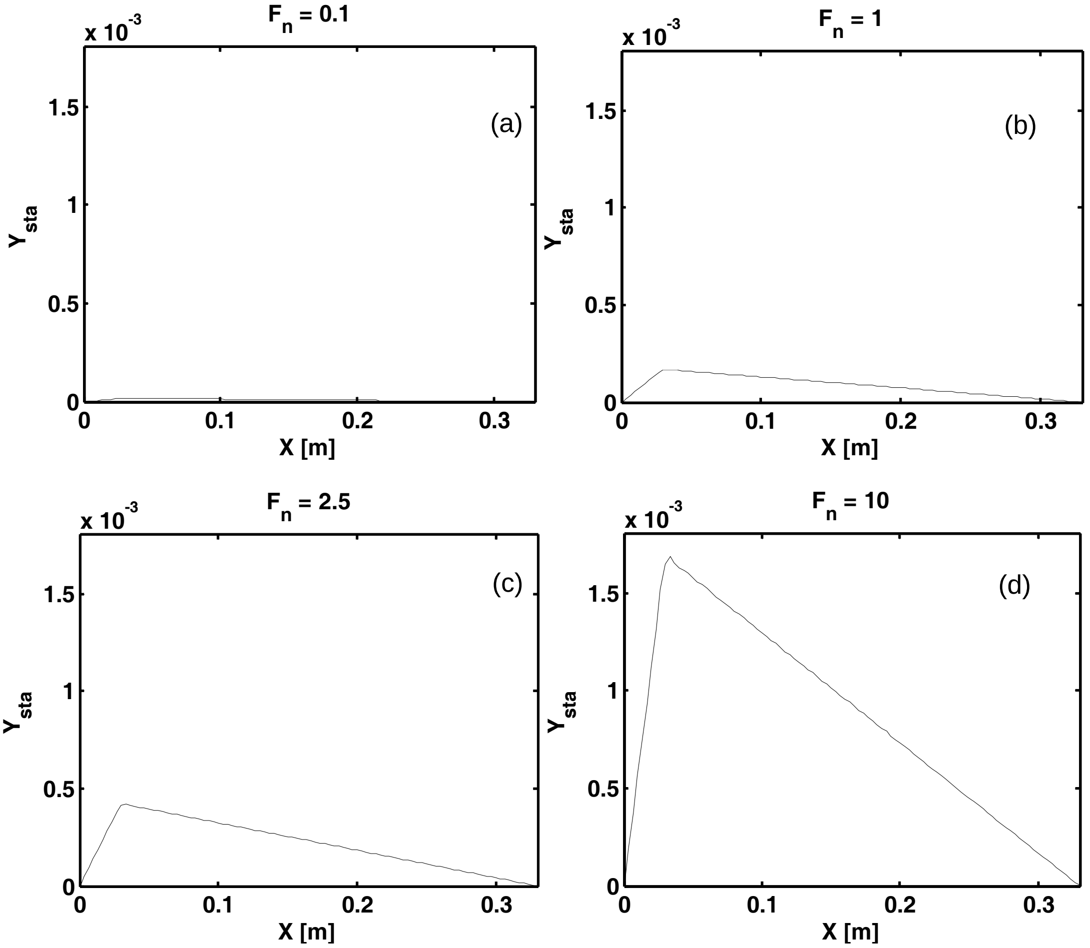

Figure 6.8 – Static string deformation for: (a) F_N = 0.1 N; (b) F_N = 1 N, (c) F_N = 2.5 N and (d) F_N = 10 N

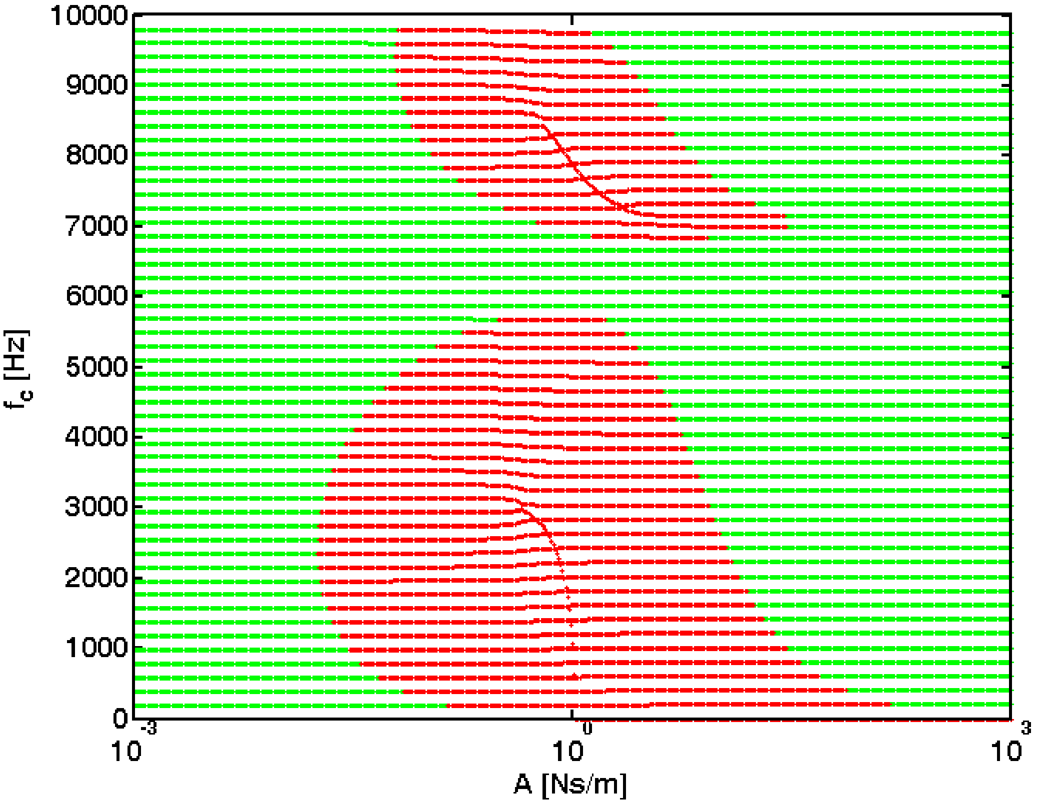

Figure 6.9 – Stability plot in function of A, for x_f = 10 mm.

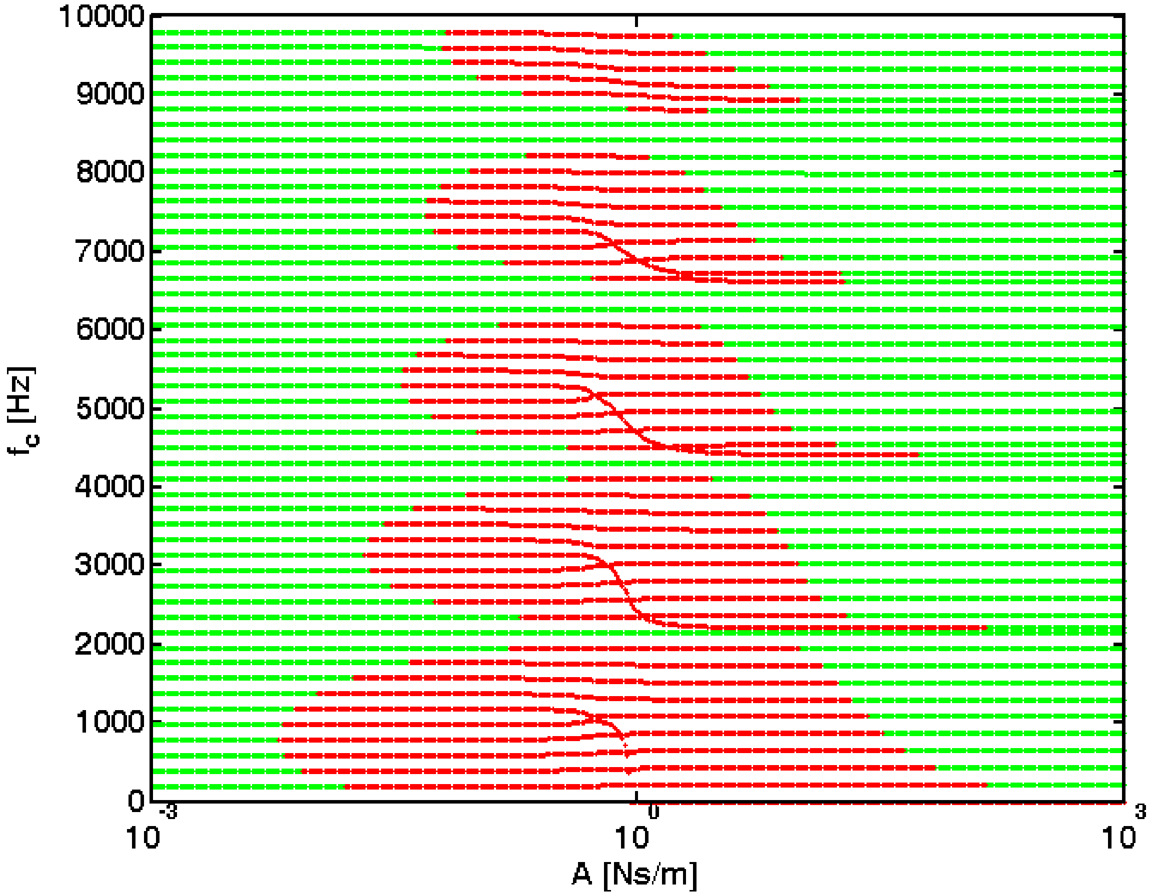

Figure 6.10 – Stability plot in function of A, for x_f = 30 mm

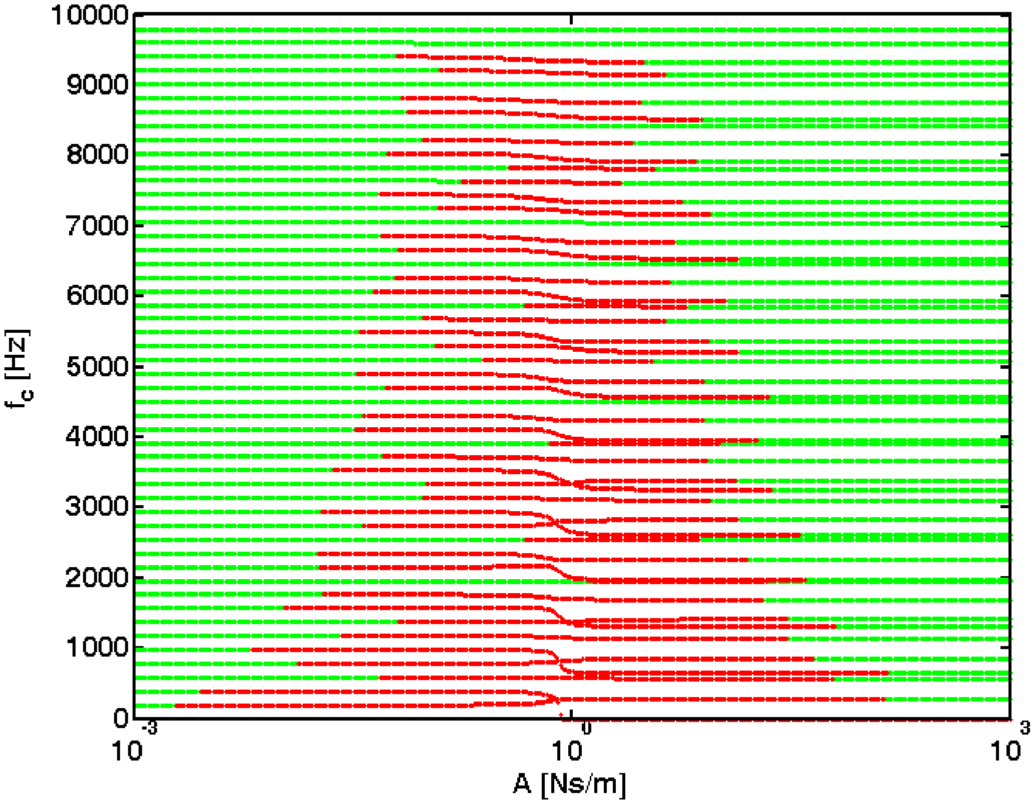

Figure 6.11 – Stability plot in function of A, for x_f = 100 mm

As a first and plausible illustration, Figure 6.8 shows the zero-order solutions obtained from equation (6.59), for three values of the normal force F_N, when bowing at location x_f = 30 mm. Dynamical results from the first-order solution (6.63) are shown in the stability plots of Figure 6.9 to Figure 6.11, where the friction-coupled modal frequencies of the bowed string are displayed as a function of the excitation coefficient A, for three locations x_f of the bow. For each mode, the green colour stands for stability and the red colour for instability. Notice that many modes become linearly unstable simultaneously, however a few of them – those with nodal regions near the bowing location – never become unstable. On the other hand, it is well known from playing experience and confirmed by nonlinear numerical simulations that playing near the bridge brings increased energy from higher-order modes. The counterpart to this fact, from the point of view of this linearized analysis, is that an increased number of higher-order modes become unstable at lower values of parameter A when bowing near the bridge.

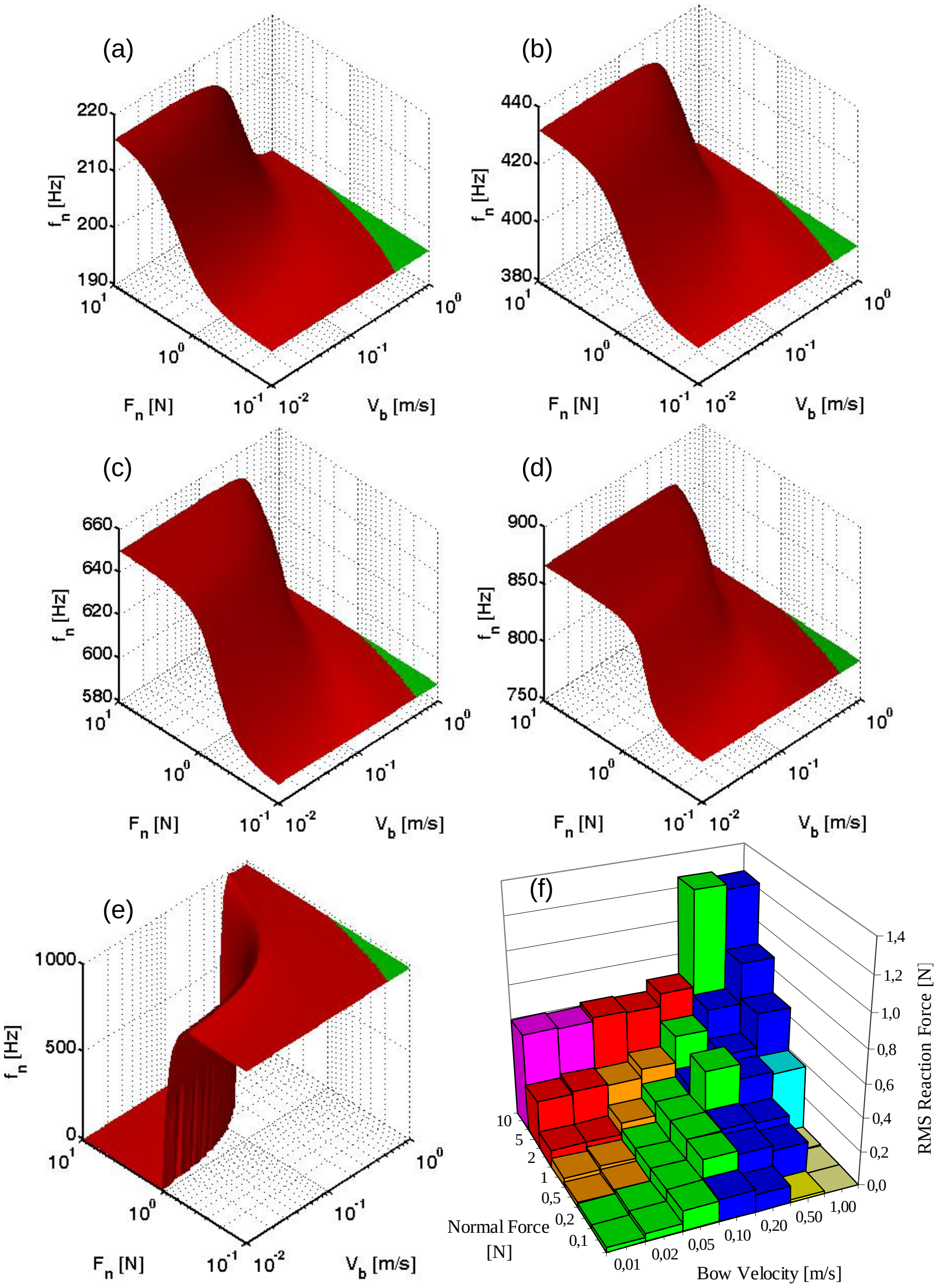

Figure 6.12 – (a)-(e): Modal frequencies and stability maps of the first five string modes as a function of F_N and $\dot{y}_{bow}$ (bowing at x_c = 30 mm); (f) Dynamical bridge reaction force and nonlinear motion regimes from time-domain numerical simulations of the bowed string (decaying regime – light yellow; Helmholtz regime – green; higher-order regime – blue; raucous regime – red; anomalous low-frequency regime – magenta).

A last and very interesting aspect deserving to be mentioned concerns the linear instability of those modes which present antinodes near the bow. For high enough values of A, their modal frequencies decrease drastically, so that the first of them in fact becomes unstable by *divergence* (and not by flutter, as usual). It is tempting to connect such behaviour with the trigging of chaotic “raucous” motions, which arise when bowing the string with excessive normal forces. Figure 6.12 displays the stability maps of the first bow-coupled string modes, when x_f = 30 mm, as a function of the bow normal force and tangential velocity. For this bow location, it is the 5th mode which becomes unstable by divergence, and the corresponding stability map may be compared with the nonlinear motion regimes computed from time-domain simulations also shown in Figure 6.12. The similarity of the qualitative behaviour is striking.

Chapter 7

CONCLUSIONS

7. CONCLUSIONS

The work described in this thesis aimed to develop a general computational methodology for the simulation of bowed musical instruments dynamics, based on a modal approach. The main objective was to obtain results that could be comparable to the behaviour of real instruments, in particular bowed strings such as the violin or cello, bowed bars as the vibraphone or marimba and bowed shell structures as the Tibetan singing bowls or the glass harmonica. The conclusions of each chapter, mainly from Chapter 3 to Chapter 5 show that this objective has been fulfilled. Furthermore, a linearized approach to the nonlinear problem was developed using the same basic methodology, which showed coherent results with those obtained from the nonlinear computations. The main achievements presented in this thesis are described in the following paragraphs, divided into the subsection related to each of the three instruments studied.

7.1. Main achievements

The main contributions to scientific knowledge brought by the contents of this thesis are presented in the following paragraphs. For all three systems studied, animations and sounds have been produced which enable a good interpretation of the results obtained and understanding of the occurring physical phenomena.

7.1.1 Bowed strings

- A numerical modal model was implemented which incorporates the measured dynamics of real-life instrument bodies, coupled to the string motions;

- A systematic study was made of the effect of torsion modes on the string dynamics was made revealing the different types of behaviour that the string motion can acquire for a wide range of torsion to transverse frequency ratios;

- A demonstration was made that differences between point-model and finite-width simulations can be more pronounced outside the range of bowing parameters leading to the Helmholtz motion;

- Effective simulation of a realistic wolf-note on a cello was obtained, establishing also the range of the playing parameters where this phenomenon emerges, for a particular friction law and instrument body characteristics;

- Demonstration was made of the beating dependence of the wolf-note with bowing velocity and applied bow force, with good agreement with experimental results;

Apart from the numerical model implementation, the results relating to the coupling between the body of the instrument and the string are, according to the literature review made, the most detailed published up to the present date.

7.1.2 Bowed bars

- A numerical modal model was developed which includes the force generated by the supports acting on the nodal points of the first flexural mode of the bar;

- The numerical modal model developed allows the introduction of bars of arbitrary shape and pre-defined (calculated or identified) modal basis;

- The results of the simulation of the vibration time history of bowed vibraphone bars are in good agreement with measured time-history on these instruments;

- Different vibratory regimes of bowed vibraphone and constant cross-section bars, for different playing conditions of bow velocity and applied force were simulated.

7.1.3 Bowed shells

- A numerical modal model was developed that allows the introduction of orthogonal vibratory modes pairs, including their tangential and radial components, essential to the correct description of the instrument dynamics;

- The results of the simulations of the time-history of the vibrations of bowed Tibetan bowls are in good agreement with the measured time-history;

- Different vibratory transients and self-sustained regimes of bowed Tibetan bowls were simulated, for different playing conditions of the exciting stick velocity and applied force, in good agreement with real instrument playing experience;

- An important clarification was made on the radial and tangential vibratory behaviour of bowed Tibetan bowls and of the beating phenomena associated with perfectly axi-symmetrical instruments;

- Demonstration was made of the strong dependence of the Tibetan bowls self-sustained regime order of oscillation on the contact/friction parameters, with a clear support from measured results;

According to the literature review made, the results presented on Tibetan bowls seem to be, currently, the most detailed and illuminating ever published.

7.2. Perspectives for future work

The main objective of future research that can be proposed based on the theme of this thesis is the improvement of the numerical model in order to achieve better quality simulations when compared to measured results. This can be accomplished by refining the method in two of its main pillars: the friction model and the description of the dynamical system. Both of these aspects imply numerical and experimental work, the main points of which are detailed in the following paragraphs.

7.2.1 Numerical

7.2.1.1 Improving the description of the system

The modal method presented in this thesis allows the incorporation of different components of the system in study. In the case of the cello, for example, the body of the instrument as well as the moving finger pressing the string along the fingerboard (glissando effect) were successfully implemented, something not easily accomplished – if ever – with the current computational techniques. However, further aspects can be included, not only for bowed strings but also for bars and bowls.

In the case of bowed strings, the coupling between the in-plane transverse motion of the string (where in-plane means in a plane parallel to the top plate of the instrument body) and the out-of-plane motion (perpendicular to the top plate) should be implemented. This can be easily achieved with most computational approaches, including the one presented in this thesis. This fact seems important because this vertical motion of the string can have a strong influence on the motion of the bow hairs, which will influence the string motion, etc. Longitudinal modes also couple with transverse modes of the string, and its effect on the sound experienced by a player is more pronounced if bowing with the bow in a position not perpendicular to the string. Bow hair compliance is another important issue that should be addressed by introducing the longitudinal and transverse dynamical properties of the bow hair, for a certain rod tension.

Bowed bars and shells are much simpler systems with very few components. The main improvement comes from an adequate definition of the support dynamics which can have some influence on the resulting system motion. Since bowed bars are usually excited by a bow, the supports should have some compliance and damping in the direction of the normal force applied by the player and not only on the direction of the applied friction force. This motion can probably couple with oscillations of the bow which can be one of the reasons for the difficulty experience by players when trying to obtain sounds from this instrument.

7.2.1.2 Comparison of friction models

As described in this work, several friction models can be used to simulate bowed instruments. Recent research with the bowed strings (Woodhouse, 2003; Galluzzo & Woodhouse, 2003; Serafin *et al*, 2003; Woodhouse & Galluzzo, 2004) has proposed the use of thermal related friction models as a more reliable alternative to the classic Coulomb friction model used in this thesis. Implementing the different friction models in the modal method described in this thesis is the natural next step in this research work. This implementation will allow a clear comparison between the behaviour of the different models. The implementation and the results obtained must be accompanied experimental measurements of the frictional behaviour of the system analyzed (see section 7.2.2).

7.2.1.3 Friction-modelling refining

Apart from the comparisons described in the previous section, the refining of the present friction model should be considered, in order to incorporate the features that can be considered indispensable to the realistic simulation of the system dynamics. These features, which should originate from the results of friction force measurements on both string, bars, bowls and respective exciters (see section 7.2.2), would preferably be implemented in such a way that the friction model behaves well for the different systems, by incorporating shaping variables to the friction law, that will approximate it to real measurement results. Notice that the friction interfacefor the *puja*/bowl excitation is not of the same type as the bow/string interface. There is no rosin melting in such interaction and therefore the tribological aspects should be quite different.

7.2.1.4 Implementing sound radiation

The generation of realistic sounds from the simulations obtained by the present method, which relies solely on physics, is still a challenge. All sounds that were extracted from the present simulation method were simply related to the vibratory velocity of the surface of the instrument. From the three systems studied the Tibetan bowl was the one that gave strikingly realistic results. However, this approach should be now complemented by the implementation of a set of transfer functions relating vibratory variables in several points of the instrument to the far field sound pressure at some point in space. Otherwise, use of the integral Helmholtz-Kirchoff radiation equations may be adopted. Both approaches present quite distinct advantages and drawbacks.

7.2.1.5 Improving numerical efficiency

The numerical efficiency of the model implementation presented in this thesis is not optimized. The comparatively large computation times described as one of the main disadvantages of this method – but notice that, contrary to faster computation methods, the modal approach easily provides information on the dynamical response of the full system – may certainly be decreased. Different approaches on integration methods and on the code building should allow a decrease of computation times of at least an order of magnitude.

7.2.2 Experimental

7.2.2.1 Identification of friction parameters

The work carried by Woodhouse & Galluzzo (2003), showed good resemblance of simulated bowed string initial transient with measured results, by using the thermal modelled developed by Smith & Woodhouse (2000). Although, as stated by the authors of that work, further work is needed to find a more accurate friction law, since the one used could not represent accurately some important features such as the flattening effect. To improve the friction model, experimental work on the identification of the friction force, and its relation with its governing quantities, whether it is the bow/string relative velocity, temperature or other, is needed. A possible path to continue this work is using remote identification techniques by inverse algorithms, first on more rigid structures such as the bowed bar which has a more simple geometry than the Tibetan bowl, and then on the string. One of the major difficulties with this technique (apart from noise presence in the measurements) is the influence of the transducer on the dynamical properties of the system. Therefore, non-contact transducers are preferred. An interesting approach would be to try friction force identification not from measurements on the instrument, but on the bow itself (at the frog, for example) using the same inverse techniques. A major step on the use of inverse methods for the identification of bow/string interaction forces was recently provided by Woodhouse *et al* (2000) and Schumacher *et al* (2005).

7.2.2.2 Quantitative validation of numerical results

As obvious as it may seem, the use of measurements to validate the numerical results is very important. In this thesis only qualitative comparisons have been made between simulations and measurements. In following work one should aim for quantitative comparisons. This will not only allow testing of the method itself but also helping the improvement of the friction laws. Again in this case, the main difficulty is the presence of the transducer, which has a great influence on the instrument sound, and therefore non-contact transducers should be used.

Chapter 8

REFERENCES

8. REFERENCES

Akay, A. (2002), Acoustics of Friction, Journal of the Acoustical Society of America, 111: 1525-1547.

Amontons, G. (1699), De la Resistance Causé dans les Machines, Mémoires de l'Académie Royale A., 275-282.

Antoniou, S.S., Cameron, A., Gentle, C.R. (1976), The Friction-Speed Relation From Stick-Slip Data, Wear, 36: 235-254.

Antunes, J., Axisa, F., Beaufils, B., Guilbaud, D. (1990), Coulomb Friction Modelling in Numerical Simulations of Vibration and Wear Work Rate of Multispan Tube Bundles, Journal of Fluids and Structures, 4: 287-304.

Antunes, J., Tafasca, M., Borsoi, L. (2000a), Simulation des Régimes Vibratoires Non-Linéaires d'Une Corde de Violon, Bulletin de la Société Française de Mécanique, 2000-3: 193-202.

Antunes, J., Tafasca, M., L. Henrique, L. (2000b), Simulation of the Bowed-String Dynamics: Part 1 – A Nonlinear Modal Approach, Proceedings of the 5th French Acoustics Congress, Lausanne.

Antunes, J., Henrique, L., Inácio, O. (2001), Aspects of Bowed-String Dynamics, Proceedings of the 17th International Congress on Acoustics, Roma, Italy.

Antunes, J., Henrique, L. (2002), Conception optimale des instruments à percussion: 2 – Synthese sonore par modèle physique, 6ème Congrès Français d'Acoustique, Lille.

Armstrong-Hélouvry, B., Dupont, P. and Canudas de Wit, C. (1994), Friction in Servo Machines: Analysis and Control Methods, Applied Mechanics Revues, 47(7): 275-305.

Askenfelt, A. (1989), Measurement of the Bowing Parameters in Violin Playing: Part 2: Bow-Bridge Distance, Dynamic Range, and Limits of Bow Force, Journal of the Acoustical Society of America, 86: 503-516.

Axisa, F., Trompette, P. (2005), *Modelling Mechanical Systems (Volume 2) – Structural Elements*, Elsevier, Oxford.

Bathe, K. J., Wilson, E. L. (1973), Stability and Accuracy Analysis of Direct Integration Methods, Earthquake Engineering and Structural Dynamics, 1: 283-291.

Beeman, D. (1976), Some Multistep Methods for Use in Molecular Dynamics Calculations, Journal of Computational Physics, 20: 130-139.

Bell, R., Burdekin, M. (1969), A Study of the Stick-Slip Motion of Machine Tool Feed Drives, Proceedings of the Institution of Mechanical Engineers, 184 (part 1, n. 29): 543-557.

Benade, H. (1975), The wolf tone on violin family instruments, Catgut Acoustical Society Newsletter, 24: 21-23.

Bernard, J.E. (1980), The Simulation of Coulomb Friction in Mechanical Systems, Simulation, 34(1): 11-16.

Bertolini, A. F. (1998), Review of eigensolution procedures for linear dynamic finite element analysis, Applied Mechanics Reviews 51: 155-172.

Bilbao, S. (2007), Modal Representations and Computational Complexity in Physical Modelling Sound Synthesis Applications, Proceedings of the 19th International Congress on Acoustics, Madrid.

Bliman, P.-A., Sorine, M. (1991), Friction modelling by hysteresis operators. application to Dahl, stiction and Stribeck effects, Proceedings of the Conference "Models of Hysteresis", Trento, Italy.

Bliman, P.-A. (1992), Mathematical study of the Dahl's friction model, European Journal of Mechanics. A/Solids, 11H6I, 835–848.

Bo, L.C., Pavalescu, D. (1982), The Friction-Speed Relation and Its Influence of the Critical Velocity of the Stick-Slip Motion, Wear 82(3): 277-289.

Boutillon, X. (1991), Analytical investigation of the flattening effect - the reactive power balance rule, Journal of the Acoustical Society of America, 90: 754-763.

Bowden, E.E., Tabor, D. (1964), *The Friction and Lubrication of Solids*, Parts I and II, Clarendon Press, Oxford.

Brockley, C.A., Ko, P.L. (1970), Quasi-Harmonic Fiction-Induced Vibration, ASME Hournal of Lubrication Technology, 92: 550-556.

Burwell, J.T., Rabinowicz, E. (1953), The Nature of the Coefficient of Friction, Journal of Applied Physics 24(2): 136-139

Chapuis, J.-C., (2000) Ces Si Délicats Instruments de Verre, Pour la Science, 272: 68-74.

Cook, P. (2002), *Real Sound Synthesis for Interactive Applications*, A. K. Peters, Natick, Massachusetts, USA.

Coulomb, C. (1785), Théorie de Machines Simples, Mémoire de Mathématique et de Physique de l'Académie Royale, 161-342.

Craig, R.R. (1981), *Structural Dynamics*, Wiley, New York.

Cremer, L. (1984), *The physics of the violin*, MIT Press, Cambridge, MA.

Dahl, P. (1968), A solid friction model, Technical Report TOR-0158H3107–18I-1, The Aerospace Corporation, El Segundo, CA.

Dahl, P. (1976), Solid friction damping of mechanical vibrations, AIAA Journal, 14H12I:1675–82.

Derveaux, G., Chaigne, A., Joly, P., Bécache, E. (2003), Time-domain simulation of a guitar: Model and Method, Journal of the Acoustical Society of America, 114: 3368-3383.

Desaguliers, J.T. (1725), Some Experiments Concerning the Cohesion of Lead, Philos. Trans. R. Soc. Lond., 33: 345.

Deuflhard, P., Hermans, J., Leimkuhler, B., Mark, A.E. Reich, S. Skeel, R.D. (Eds.), (1999), Computational Molecular Dynamics: Challenges, Methods, Ideas - Series: Lecture Notes in Computational Science and Engineering, Vol. 4, Springer-Verlag, Berlin.

Dupond, P.E. (1993), The Effect of Friction on the Forward Dynamics Problem, International Journal Robotics Research, 12(2): 164-179.

Essl, G., Cook, P. (2000), Measurement and Efficient Simulations of Bowed Bars, Journal of the Acoustical Society of America, 108: 379-388.

Euler, L. (1748), Sur le Frottement des Corps Solides, Histoire de l´Académie Royale a Berlin IV, 122-132.

Ewins, D. J. (1984), *Modal Testing Theory and Practice,* Wiley, New York, USA.

Fahy, F., Gardonio, P. (2007), *Sound and Structural Vibration – Radiation, Transmission and Response,* Academic Press, Oxford, 2nd Edition, 2007

Faure, C. -A. and Boutillon, X. (1993), Détermination et étude expérimentale de la fréquence d’oscillation d’une corde frottée, C. R. Acad. Sci. Paris, 317: 1377-1382.

Fenny, B., Guran, A., Hinrichs, N., Popp, K. (1998), A historical review on dry-friction and stick–slip phenomena, Applied Mechanics Review 51: 321–341.

Firth, I. M., Buchanan, J. M. (1973), The wolf in the cello, Journal of the Acoustical Society of America, 53: 457-463.

Fletcher, N., Rossing, T. (1998), *The Physics of Musical Instruments,* 2nd ed., Springer, New York.

Fletcher, N. (1999), The Nonlinear Physics of Musical Instruments, Reports on Progress in Physics, 62: 723-764.

French, A. P. (1983), In Vino Veritas: A Study of Wineglass Acoustics, American Journal of Physics 51: 688-694.

Friedlander, F. G. (1953), On the Oscillations of the Bowed String, Proceedings of the Cambridge Philosophical Society, 49: 516-530.

Galluzzo, P.M., Woodhouse, J. (2003), Experiments with an Automatic Bowing Machine, Proceedings of the Stockholm Music Acoustics Conference (SMAC2003), Stockholm, Sweden.

Gardner, K. (1990), *Sounding the Inner Landscape: Music as Medicine*, Element, Rockport.

Gaynor, M.L. (1999), *Sounds of Healing: A Physician Reveals the Therapeutic Power of Sound, Voice, and Music*, Bantam Dell Pub Group.

Gaynor, M.L. (2002), *The Healing Power of Sound: Recovery from Life-threatening Illness Using Sound, Voice and Music*, Shambhala Publications.

Gough, C. (1980), The Resonant Response of a Violin G-String and the Excitation of the Wolf Note, Acustica, 44: 113-123.

Graff, K.F. (1975), *Wave motions in elastic solids*, Dover Publications, New York.

Grosh, K.A. (1963), The Relation Between Friction and the Visco-Elastic Properties of Rubber, Proceeding of the Royal Society of London, Ser. A: 21-39

Guettler, K., Askenfelt, A. (1997), Acceptance Limits for the Duration of Pre-Helmholtz Transients in Bowed String Attacks, Journal of the Acoustical Society of America, 101: 2903-2913.

Guettler, K. (2002), The Bowed String: On the Development of Helmholtz Motion and On the Creation of Anomalous Low Frequencies, Doctorate thesis, Royal Institute of Technology - Speech, Music and Hearing, Stockholm.

Haessig Jr., D.A., Friedland, B. (1985), On the Modelling and Simulation of Friction, Journal of Dynamic Systems, Measurements and Control, 107: 100-103.

Haessig Jr., D.A., Friedland, B. (1991), On the Modelling and Simulation of Friction, Transactions of the ASME, 113: 354-362.

Hanson, R.J., Schneider, A.J., Halgedahl, F.W. (1994), Anomalous Low-Pitched Tones From a Bowed Violin String, Catgut Acoustical Society Journal, 2(6), Series II.

Harris, C. M. (1996), *Shock and Vibration Handbook*, McGraw Hill, New York.

Helmholtz, H. L. F. (1877), *On the Sensations of Tone*, 4th Ed. (1954), Transl. A. J. Ellis, Dover Publilcations, New York.

Henrique, L., Antunes, J. (2002), Conception Optimale des Instruments a Percussion: 1 – Stratégie D'optimisation Topologique, Proceedings of the 6ème Congrès CFA 2002, Lille.

Henrique, L., Antunes, J. (2003), Optimal Design and Physical Modelling of Mallet Percussion Instruments (Parts 1 and 2), Proceedings of the 6th French Acoustics Congress (CFA 2002), Lille, France.

Henrique, L., Antunes, J., Carvalho, J. S. (2002), Shape Optimisation Techniques for Musical Instruments Design, 144th Meeting of the Acoustical Society of America / First Pan-American/Iberian Meeting on Acoustics, Cancun.

Hess, D.P., Soom, A. (1990), Friction at a Lubricated Line Contact Operating at Oscillating Sliding Velocities, Journal of Tribology, 112(1): 147-152.

Hirschberg, A., Kergomard, J., Weinreich, G. (1995), *Mechanics of Musical Instruments*, Springer.

Huang, P., Serafin, S., Smith, J.O. (2000), A Waveguide Mesh Model of High-Frequency Violin Body Resonances, Proceedings of the International Computer Music Conference (ICMC 2000), Berlin, 86-89.

Hunt, J.B., Torbe, I., Spencer, G.C. (1965), The Phase-Plane Analysis of Sliding Motion, Wear 8: 455-465

Huyser, A. (1999), *Singing Bowl Exercises for Personal Harmony*, Binkey Kok Publications, Havelte.

Ibrahim, R.A. (1994a), Friction-Induced Vibration, Chatter, Squeal, and Chaos - Part I: Mechanics of Contact and Friction, ASMEApplied Mechanics Reviews, 47(7): 209-226.

Ibrahim, R.A. (1994b), Friction-Induced Vibration, Chatter, Squeal, and Chaos - Part II: Dynamics and Modeling, ASME Applied Mechanics Reviews, 47(7): 227–253.

Inácio, O., Henrique, L., Antunes, J. (2001a), “Dynamical Analysis of Bowed Bars”, Proceedings of the 8th International Congress on Sound and Vibration (ICSV8), Hong Kong, China.

Inácio, O., Henrique, L., Antunes, J. (2001b): Influence des Modes de Torsion sur les Régimes Dynamiques des Cordes Frottées, Journée Instruments à Cordes, Groupe Spécialisé d’Acoustique Musicale, Lisboa, Portugal.

Inácio, O. (2002), Largeur d’Archet et Régimes Dynamiques de la Corde Frottée, Proceedings of the 6th French Acoustics Congress (CFA 2002), Lille, France.

Inácio, O., Antunes, J., Henrique, L. (2002), Influence of Torsion Modes in Bowed String Dynamics, 144th Meeting of the Acoustical Society of America, Cancun, Mexico.

Inácio, O., Henrique, L., Antunes, J. (2003a), Nonlinear Dynamics and Playability of Bowed Instruments: From the Bowed String to the Bowed Bar, Proceedings of the 11th International Conference on Computational Methods and Experimental Measurements (CMEM 2003), Halkidiki, Greece.

Inácio, O., Henrique, L., Antunes, J. (2003b), Simulation of the Oscillation Regimes of Bowed Bars: A Nonlinear Modal Approach, Communications in Nonlinear Science and Numerical Simulation, 8: 77-95.

Inácio, O., Henrique, L., Antunes, J. (2003c), The Physics of Tibetan Singing Bowls – Part 1: Theoretical Model and Part 2: Numerical Simulations, 34th National Acoustics Congress and Acoustics Iberian Meeting (TecniAcustica 2003), Bilbao, Spain.

Inácio, O., Henrique, L., Antunes, J. (2004a): The Physics of Tibetan Singing Bowls, Revista de Acústica, Sociedad Española de Acústica, 35 (1 & 2): 33-39.

Inácio, O., Antunes, J. (2004b), Dynamical Responses of a Large Tibetan Singing Bowl, Proceedings of the International Symposium on Musical Acoustics (ISMA2004), Nara, Japan.

Inácio, O., Antunes, J., Wright, M.C.M. (2004c), On the Violin Family String/Body Dynamical Coupling, Proceedings of the Spring Conference of the Institute of Acoustics, Southampton, United Kingdom.

Inácio, O., Antunes, J., Wright, M.C.M. (2004d), Bowing the Wolf: Simulations and Experiments on a Cello, Proceedings of the IV Ibero-American Acoustics Congress, Guimarães, Portugal.

Inácio, O., Antunes, J. (2005), Dynamical Regimes of Bowed-String Instruments with Body-Coupling, Proceedings of the 12th ICSV, Lisbon, Portugal.

Inácio, O., Antunes, J., (2006), A Linearized Analysis of Friction-Excited Musical Bars, Proceedings of the 8éme Congrès CFA 2006, Tours, France.

Inácio, O., Henrique, L., Antunes, J. (2006), The Dynamics of Tibetan Singing Bowls, Acta Acustica United with Acustica, 92, 637-653.

Jansen, E.R. (1993), *Singing Bowls: a Practical Handbook of Instruction and Use*, Red Wheel.

Jansson, E. (2002), Acoustics for violin and guitar makers: Chap. 4 – Properties of the violin and guitar string, (4th Edition), KTH, Stockholm, Sweden. Online at http://www.speech.kth.se/music/acviguit4.

Johnson, K.L. (1985), *Contact Mechanics*, Cambridge University Press, Cambridge.

Juang, J. N. (1994), *Applied System Identification*, Prentice Hall PTR, New Jersey, USA.

Juang, J. N., Pappa, R. S. (1985), An Eigensystem Realization Algorithm for Modal Parameter Identification and Model Reduction, Journal of Guidance, Control, and Dynamics, 8(5): 620-627.

Karnopp, D. (1983), Computer Simulation of Stick-Slip Friction in Dynamic Systems, ASME Journal of Dynamic Systems, Measurement and Control, 50: 67-76.

Klamechi, B.E. (1985), A Catastrophe Theory Description of Slip-Stick Motion in Sliding, Wear, 101: 325-332.

Kragelsky, I., Dobychin, M., Kombalov, V. (1982), *Friction and Wear: Calculation Methods*, Pergamon Press, Oxford.

Lazarus, H. (1972), Die Behandlung der Selbsterregten Kippschwingungen der Gestrichenen Saite mit Hilfe der Endlichen Laplace Transformation, Dissertation, Tech. Univ. Berlin 1972.

Leine, R.I., Campen, D.H., Kraker, A., Steen, L. (1998), Stick-Slip Vibrations Induced by Alternate Friction Models, Nonlinear Dynamics, 16: 41-54.

Lord Rayleigh (1894), *The Theory of Sound, Vol. 1 and 2*, MacMillan, New York. Reprinted by Dover, New York, 1945.

Martins, J.A.C., Oden, J.T., Simões, F.M.F. (1990), A Study of Static and Kinetic Friction, Journal of Engineering Science, 28: 29-92.

McIntyre, M., Schumacher, R., Woodhouse, J. (1981), Aperiodicity in Bowed-String Motion, Acustica, 49: 13-32.

McIntyre, M., Schumacher, R., Woodhouse, J. (1982), Aperiodicity in Bowed-String Motion: on the Differential-Slipping Mechanism, Acustica, 50: 294-295.

McIntyre, M., Schumacher, R., Woodhouse, J. (1983), On the Oscillation of Musical Instruments, Journal of the Acoustical Society of America, 74: 1325-1345.

McIntyre, M., Woodhouse, J. (1979), On the Fundamentals of Bowed-String Dynamics, Acustica, 43: 93-108.

Meirovich, L. (1997), *Principles and Techniques of Vibrations*, Prentice Hall International, New Jersey.

Newmark, N. M. (1959), A Method of Computation for Structural Dynamics, ASCE Journal of the Engineering Mechanics Division, 85, EM3.

Oden, J.T., Martins, J.A.C. (1985), Models and Computational Methods for Dynamic Friction Phenomena, Computer Methods in Applied Mechanics and Engineering 52: 527-634.

Pitteroff, R., Woodhouse, J. (1998a), Mechanics of the Contact Area between a Violin Bow and a String: Part 1 – Reflection and Transmission Behaviour, Acustica, 84: 543-562.

Pitteroff, R., Woodhouse, J. (1998b), Mechanics of the Contact Area between a Violin Bow and a String: Part 2 – Simulation of the Bowed String, Acustica, Vol. 84:744-757.

Pitteroff, R., Woodhouse, J. (1998c), Mechanics of the Contact Area between a Violin Bow and a String: Part 3 – Parameter Dependence, Acustica, 84: 929-938.

Puaud, J., Caussé, R., Gibiat, V. (1991), Quasi-Périodicité et Bifurcations dans la Note de Loup, J. Acoustique, 4: 253-259.

Rabinowicz, E. (1958), The Intrinsic Variable Affecting the Stick-Slip Process, Proc. Phys. Soc. London 71: 668-675.

Rabinowicz, E. (1965), *Friction and Wear of Materials*, John Wiley & Sons, New York.

Raman, C. V. (1918), On the mechanical theory of the vibrations of bowed strings and of musical instruments of the violin family, with experimental verification of the results, Indian Association for the Cultivation of Science, 15: 1-158.

Rice, J.R., Ruina, A.L. (1983), Stability of steady frictional slipping, J. Appl. Phys., 50: 343-349.

Rossing, T. (1994), Acoustics of the Glass Harmonica, Journal of the Acoustical Society of America, 95: 1106-1111.

Rossing, T. (1994), Acoustics of the Glass Harmonica, Journal of the Acoustical Society of America, 95: 1106-1111.

Rossing, T. (2000), *The Science of Percussion Instruments*, Singapore, World Scientific.

Sakamoto, T. (1985), Normal Displacements of the Sliding Body in a Stick-Slip Friction Process, Proc. Of JSLE Intl. Trib. Conf. Tokyo, 141-146

Sakamoto, T. (1987), Normal Displacements and Dynamic Friction Characteristics in a Stick-Slip Process, Tribology International 20(1): 25-31

Sampson, J.B., Morgan, F., Reed, D.W., Muskat, M. (1943), Friction Behaviour During the Slip Portion of the Stick-Slip Process, Journal of Applied Physics 14(12): 689-700.

Schelleng, J. C. (1973), The Bowed String and the Player, Journal of the Acoustical Society of America, 53: 26-41.

Schelleng, J. (1963), The Violin as a Circuit, Journal of the Acoustical Society of America, 35: 326-338.

Schoonderwaldt, E., Guettler, K., Askenfelt, A. (2003), Effect of the Width of the Bow Hair on the Violin String Spectrum, Proceedings of the Stockholm Music Acoustics Conference (SMAC2003), Stockholm, Sweden (2003).

Schumacher, R.T. (1979), Self-Sustained Oscillations of the Bowed String, Acustica, 43: 109-120.

Schumacher, R.T. (1994), Measurement of Some Parameters of Bowing, Journal of the Acoustical Society of America, 96: 1985-1998.

Schumacher, R.T., Garoff, S., Woodhouse, J. (2005), Probing the Physics of Slip–Stick Friction using a Bowed String, The Journal of Adhesion, 81:723–750.

Serafin, S., Avanzini, F., Rocchesso, D. (2003), Bowed String Simulation Using an Elasto-Plastic Model, Proceedings of the Stockholm Music Acoustics Conference (SMAC2003), Stockholm, Sweden.

Serafin, S., Wilkerson, C., Smith III, J. (2002), Modelling Bowl Resonators Using Circular Waveguide Networks, Proceedings of the 5th International Conference on Digital Audio Effects (DAFx-02), Hamburg, Germany.

Serafin, S., Young, D. (2003), Bowed String Physical Model Validation through Use of a Bow Controller and Examination of Bow Strokes, Proceedings of the Stockholm Music Acoustics Conference (SMAC2003), Stockholm, Sweden.

Singer, I.L., Pollack, H.M., Eds. (1992), Fundamentals of Friction: Macroscopic and Microscopic Processes, Kluwer, Dordrecht, 37-54.

Smith, J. H., Woodhouse, J. (2000), The Tribology of Rosin, Journal of the Mechanics and Physics of Solids, 48: 1633-1681.

J. O. Smith (2003), Digital waveguide modeling of musical instruments, CCRMA, Stanford University, http://www-ccrma.stanford.edu/~jos/waveguide/.

Suh, N.P. (1986), Tribophysics, Prentice-Hall, Englewood Cliffs, NJ.

Swope, W. C., Andersen, H. C., Berens, P. H., Wilson, K. R. (1982), A Computer Simulation Method for the Calculation of Equilibrium Constants for the Formulation of Physical Clusters of Molecules: Application to Small Water Clusters, Journal of Chemical Physics, 76: 637-649.

Tabor, D. (1981), Friction, The Present State of Our Understanding, ASME journal of Lubrication Technology, 103: 169-179.

Tafasca, M., Antunes, J., Henrique, L. (2000), Simulation of the Bowed-String Dynamics: Part 2 – Parametric Computations, Proceedings of the 5th French Acoustics Congress (CFA 2000), Lausanne, Switzerland.

Thrasher, A. R. (2001), Qing, in Stanley Sadie (ed.), The New Grove Dictionary of Music and Musicians, 2nd ed., New York, Macmillan, 20: 652.

Threlfall, D.C. (1978), The Inclusion of Coulomb Friction in Mechanisms Programs with Particular Reference to DRAM, Mechanics and Machine Theory, 13(4): 475-483.

Tolstoi, D.M., Borisova, G.A., Grigorova, S.R. (1971), Role of Intrinsic Contact of Oscillation in Normal Directions During Friction, in Nature of the Friction in Solids, Nauka I Tekhnica, Minsk.

Tworzydlo, W.W., Becker, E. (1991), Influence of Forced Vibrations on the Static Coefficient of Friction - Numerical Analysis, Wear, 43: 175-196.

Woodhouse, J. (1993), On the Playability of Violins: Part 2 – Minimum bow force and transients, Acustica, 78: 137-153.

Woodhouse, J., (2000), Reconstruction of Bowing Point Friction Force in a Bowed String, Journal of the Acoustical Society of America, 108(1): 357-368.

Woodhouse, J. (2003), Bowed String Simulation Using a Thermal Friction Model, Acustica, 89: 355-368.

Woodhouse, J. (2004), On the synthesis of guitar plucks, Acta Acustica United with Acustica, 90: 928-944.

Woodhouse, J., Galluzzo, P.M. (2004), The Bowed String As We Know It Today, Acustica, 90: 579-589.

Young, D., Essl, G. (2003), HyperPuja: A Tibetan Singing Bowl Controller, Proceedings of the Conference on New Interfaces for Musical Expression (NIME-03), Montreal, Canada.